Restrained shrinkage behaviour of rapid hardening fibre reinforced concrete repairs

By:

Hajir Abdulhussein Al-musawi

(BSc, MSc)

A thesis submitted in partial fulfilment of the requirements for the degree of
Doctor of Philosophy

The University of Sheffield

Department of Civil and Structural Engineering

Sheffield

February 2019

Abstract

The functionality and durability of concrete overlays is compromised by delamination and large cracks that result from excessive shear and tensile stresses due to restrained shrinkage. Expansive cements could mitigate shrinkage problems, but as they are usually brittle, they still develop cracks under mechanical loads. Manufactured Steel fibres (MSF) can be used to control crack widths of repairs. However, to promote the sustainability of repairs, recycled fibres extracted from un-vulcanised rubber belt off-cuts can be used. They are also more cost effective than MSF. Currently, there is no accepted design approach to limit crack widths or to accurately quantify the effect of fibres on crack widths and crack spacings of overlays.

The aim of this study is to contribute to the understanding of flexural performance and restrained shrinkage and subsequent deterioration of plain and recycled fibre reinforced rapid hardening overlays, especially the fibre effect on crack widths of overlays, and to promote more sustainable, yet efficient solutions. A combination of experimental, analytical and numerical investigation is employed to study: a) the effect of recycled clean steel fibres (RCSF) on the compressive and flexural behaviour of rapid hardening mixes, b) the effect of RCSF on the crack development of overlays and shear stresses at the interface and c) the effect of non-uniform shrinkage distribution across the depth of overlays on the tensile stress development, and therefore, on the risk of cracking in overlays.

It was found that the RCSF are efficient in bridging cracks, resulting in flexural hardening properties. The RCSF reduce crack widths in overlays by about 60%. The available methods for predicting crack widths are found to be inaccurate. Therefore, a modified crack width equation is proposed and validated, and a new equation for estimating crack spacing is derived. The fibres are also found to positively contribute in reducing the risk of delamination. They are shown to enhance the shear strength and proven to reduce the shear stress development after crack development and reduce the level of deterioration of shear interface by controlling crack widths. The assumption of uniform shrinkage distribution in overlays underestimates the extent of hygral tensile stresses. An empirical equation to consider this effect is proposed.

This work is expected to enable better and more sustainable designs for overlay repairs and strengthening.

Acknowledgements

I would first like to thank my supervisor Prof. Kypros Pilakoutas for his continuous support, inspiration, patience, encouragement, especially during the difficult times, and for his valuable advices over the past four years.

I also would like to acknowledge my second supervisor Dr. Maurizio Guadagnini for his support, assistance and the detailed correction of my thesis and my third supervisor Dr. Susan Bernal for her valuable discussions and suggestions.

I appreciate the financial support provided by the Higher Committee for Education Development in Iraq (HCED Iraq) and the EC collaborative FP7-ENV-2013 project "ANAGENNISI — Innovative Reuse of All Tyre Components in Concrete" under grant number 603722.

Great thanks and appreciations to the technicians in concrete and heavy structures laboratories, for their help and understanding, and to all members in Concrete and Earthquake Engineering (CEE) group for their support and valuable helps.

Finally, infinite thanks to all members of my family for their encouragement, patience and hope over my entire life.

Table of Contents

List of Figures

List of Tables

LIST OF ABBREVIATIONS AND SYMBOLS

ABBREVIATIONS

3D	three dimensional
A	Absorption
ACI	American Concrete Institute
AF	Amplification factor
ASTM	American Society for Testing and Materials
BC	Brittle Cracking
BS	British Standard CA
CA	Calcium aluminate cement
CDP	Concrete Damage Plasticity
CFRP	Carbon fiber reinforced polymer
CMOD	Crack Mouth Opening Displacement
CSA	Plain mortar mix with calcium sulfoaluminate cement
CSC	Concrete Smeared Cracking
DIC	Digital Image Correlation
EC	Eurocode
FCSA	Fibre reinforced mortar with calcium sulfoaluminate cement
FE	Finite Element

FEA	Finite Element Analysis
FM	Fineness modulus of sand
FRC	Fibre reinforced concrete
FRSC	Fibre reinforced mortar with calcium aluminate cement
HMA	Hot mixed asphalt
ISB	Inner softening band
JCI	Japanese Concrete Institute
LoP	Limit of Proportionality
LVDT	Linear Variable Differential Transformer
MC	Model Code
MSF	Manufactured steel fibres
OPC	Ordinary Portland Cement
PC	Plain Concrete
RC	Reinforced Concrete
RCSF	Recycled Clean Steel Fibres
RSC	Plain mortar mix with calcium aluminate cement
RTSF	Recycled tyre steel fibres
SFRC	Steel Fibre Reinforced Concrete
SG	Specific Gravity
SP	Superplasticiser

Sub	Substrate concrete
USDFLD	User defined field subroutine

GREAK SYMBOLS

α	ratio of h_o/H
α_0	ratio D_0/D_1
α_1	Parameter for ACI equation for free shrinkage estimation
αbs	factor depends on cement type
α_t	coefficient of thermal expansion of FRC
$\beta_{(C)}$	contraction coefficient
$\beta_{cc}(t)$	function that describes the strength development with time
ΔT	temperature gradient
γ_{sh}	cumulative product of the correction parameters
λL	bond constant
μ	coefficient of friction
μ_0	viscosity
$\mu\varepsilon$	microstrain
Ψ_0	dilation angle
ψ	Degree of restraint
ε	strain

ε_0	flow potential eccentricity
ε_{cr}	creep strain
ε_{cs}	concrete free shrinkage
ε_l	losses (unrestrained) strain
ε_{re}	restrained shrinkage strain
$(\varepsilon_{sh})_M$	free shrinkage strain
σ	Stress
σ_1	actual tensile stress obtained from inverse analysis
σ_2	flexural stress of the lower layer of composite prism
σ_{b1}	nominal average stress of the base layer at the cracked section
σ_{b2}	average stress of the base layer at the crack-free section
σ_o	average stress of the overlay at the crack-free section
σ_{b0}/σ_{c0}	ratio of biaxial to uniaxial compressive strength
σ_x	overlay normal stress
$\sigma_{x,max}$	maximum tensile stress in overlay
τ	average shear stress at the interface between overlay and base
τ_{max}	maximum shear stress that interface can carry before sliding begins
τ_{xz}	average shear stress along the interface of composite prism
$\tau_{xz,max}$	maximum shear stress

SYMBOLS

A_o	cross-sectional area of the overlay
$A_{o,eff}$	effective area of overlay layer
A_b	cross-sectional area of the base
b	width of the overlay
b_b	width of the beam
C	moisture content
C_0	reference moisture content
C_b	adjustment factor to account for the subgrade restraint effect
C_c	normalised moisture concentration at $D(C_{norm}) = 0.5D_1$
C_h	coefficient of cohesion
C_{norm}	normalized moisture content
d_f	diameter of fibre
D	moisture diffusion coefficient
D_0	minimum moisture diffusion coefficient
D_1	max diffusion coefficient
E_o	modulus of elasticity of overlay layer
E_b	modulus of elasticity of base layer
E_c	modulus of elasticity

E_{fm}	flexural modulus of elasticity
f	surface factor
f_{cm}	mean compressive strength at the age of 28 days
f_{ctd}	design tensile strength
f_{ctm}	concrete mean tensile strength
$f_{ctm,fl}$	first cracking strength
f_{cu}	concrete compressive strength
f_{Ftsm}	average value of the residual strength of FRC
$f_{mor,FRC}$	flexural strength of mortar
f_R	Residual flexural strength
f_{R1}	Residual flexural strength at CMOD$_1$
f_{R2}	Residual flexural strength at CMOD$_2$
f_{R3}	Residual flexural strength at CMOD$_3$
f_{R4}	Residual flexural strength at CMOD$_4$
$f_{res,FRC}$	Residual strength of FRC
f_{Ri}	Residual flexural strength at CMOD$_i$
$f_{(w)}$	residual tensile strength
F_l	Load corresponding to LoP
h	prism depth
h_o	overlay depth

h_{sp}	depth of a notched prism
H	total depth of composite prism
I_1	moments of inertia of the top layer materials of composite prism with respect to the neutral axis
I_2	moments of inertia of the bottom layer materials of composite prism with respect to the neutral axis
k	converting factor
K	initial stiffness
K_c	compressive meridian
K_{nn}	normal stiffness component
K_{ss}	tangential stiffness component
K_{tt}	tangential stiffness component
l	distance along the length of composite prism
l_b	span length
l_f	fibre length
l_t	distance along the length of composite prism form free edge to constant stress level in overlay
L	length of concrete prism
m	ratio of E_b/E_o
M	applied bending moment
n	moisture diffusivity parameter
N_x	normal force
P	percent of maximum crack spacing to average crack spacing

P_s	factor for shrinkage
P_{peak}	Peak load in flexure
$R_{10,20}$	residual strength factor at a given equivalent ductility value
s	coefficient depends on the class of cement
shr_{Auto}	autogenous shrinkage
S	crack spacing
S_m	average crack spacing
S_{max}	maximum crack spacing
S_{avg}	average crack spacing
t	time
T_{peak}	peak temperature
$T_{1/2\ \mathrm{peak}}$	time half way to the peak temperature
U_3	horizontal deformation
V_f	Volume of fibres
V_u	ultimate shear strength
w_{cr}	crack width
w_u	maximum value of crack width
W	water loss percent
X_2	shear distance
y	distance from the bottom fibre to the neutral axis of composite prism

Chapter 1: Introduction

This chapter provides the background to the research problem and scientific challenges, the aim and objective of the research, as well as methodology and thesis layout.

1.1 Background

Deterioration of infrastructure, particularly pavements, is progressive and without appropriate interventions, serious service disruptions and high costs can result. Concrete overlays are increasingly used in repairs of deteriorated elements and strengthening of concrete structures. Drying shrinkage is expected to develop swiftly in overlays, as the fresh layer not only loses moisture to the environment, but also to the concrete substrate. Repair mortars are usually rich in cement, often with rapid hardening cements, and thus their autogenous and drying shrinkage is expected to be high as well. As the substrate layer restrains the ability of the overlay to shrink, tensile and interfacial shear stresses develop which can lead to cracking and/or delamination if they exceed the material capacity [1].

Cracking and delamination are the main structural issues that affect repairs. Cracks provide easy access passages for deleterious agents like water to penetrate concrete, leading to early saturation, freeze–thaw damage, scaling, and steel corrosion, which accelerate the rate of deterioration [2]. Shrinkage induced cracks can propagate and coalesce into wider cracks under the effect of mechanical loads, compromising the integrity of repaired structures. Repaired elements are in general designed to behave as monolithic elements.

Early age deterioration was reported by Lin and Wang [3] when concrete overlays, with high cement content and low w/c ratio, were used to achieve high early strength, sufficient to quickly reopen a repaired asphalt pavement in Taiwan. Nevertheless, the thin concrete overlay, which was used to restore the structural capacity of the asphalt pavement, suffered from early deterioration and distresses after being in service for just two months, due to restrained shrinkage which led to large cracks, as illustrated in (Figure 1.1).

Figure 1.1. Failure of UTW in Taiwan (After Lin & Wang [3])

Restrained shrinkage strain can also impact the structural capacity of repaired structures. Lampropoulos et al. [4] studied the effect of restrained shrinkage strain on the compressive strength of jacketed concrete columns. They found that the strength of a jacket is reduced by 30-40% due to the tensile stress development in the jacket. Jafarifar et al. [5] found that the tensile capacity at the top of a concrete pavement can be reduced by up to 50 % due to drying shrinkage. They also found that when ignoring shrinkage distress, the load bearing capacity of SFRC pavements can be overestimated by twofold in short-term calculations as well as when including fatigue loading. Younis [6] experimentally investigated the effect of end restrained shrinkage strain on the flexural strength of concrete mixes with different w/c ratios. He found that shrinkage induced cracks lowers the flexural strength of concrete by approximately 2-24% depending on the w/c ratio, with higher reductions in specimens with lower w/c ratios, possibly due to high autogenous shrinkage of these specimens and lower creep compliance.

Expansive cements can mitigate shrinkage and subsequent cracking problems in overlays. However, due to the inherent brittleness of these materials, cracks can still develop under applied loads. Manufactured Steel fibres (MSF) can be used to control crack widths [7] and increase the toughness of a concrete layer [8-13], thus, preventing deterioration and enhancing the durability of repairs. Nonetheless, Carlsward [8] points out that fibres may not play a vital role in concrete overlays as multiple narrow cracks developed in both well bonded plain (PC I and PC II as shown in Figure 2.1) and fibre reinforced overlays (FRSC 30 I, FRSC 60 I, FRSC 30 II and FRSC 60 II). However, in delaminated areas of overlays (shown as gray areas in Figure 1.2), fibre were found to reduce the crack widths, Figure 1.2.

Steel fibres can be obtained from end of life tyres. Since 1999, extensive experimental and analytical work has been conducted at the University of Sheffield [14-21] to investigate the mechanical properties of post-consumer recycled Tyre Steel Fibres (RTSF) obtained from end of life tyres and their potential applications. These fibres are found to control cracks well at serviceability limits, however, due to their short and variable lengths, they are less effective than MSF in controlling bigger cracks. Though using such materials in repairs can increase the sustainability of repairs, they may not offer an excellent performance compared to MSF.

About 1.5 billion tyres are produced per annum worldwide [22]. During the process of tyre manufacturing, roughly 5% (by weight) of un-vulcanised rubber belt offcuts which contain a large amount of steel cords is generated. Each steel cord consists of a number of steel filaments twisted together with a filament helically wound around them. Despite being high quality material, most of steel cords are disposed of as waste or used for energy recovery together with rubber. Recently, the industry of tyre recycling has developed a novel cryogenic process to extract the steel cords undisturbed from un-vulcanised offcuts, and these cords are cut to predetermined lengths suitable for concrete reinforcement, called Recycled Clean Steel Fibres (RCSF) as they are not contaminated with rubber [23]. Therefore, the cost of their production is expected to be less than the cost of MSF.

Hu et al. [24] showed that concrete mixes reinforced with different dosages of RCSF exhibited flexural hardening properties. This indicates their potential efficiency in controlling cracks of materials with high shrinkage values. Therefore, to further promote the sustainability of repairs and enhance their durability, RCSF could be used in concrete repairs.

It is known that bond strength of repairs is mainly affected by interface cleanliness, absence of weak loose substances and surface roughness [8, 25, 26]. It is also understood that the strength of the weaker layer of a composite structure provides the upper limit for the interfacial shear strength [25]. Kim et al. [27] studied the effect of fibre reinforcement on the tensile and shear bond strength of mortar overlays by using wedge splitting test and bi-surface shear test, respectively. They found that the failure load is not affected by fibre addition to the mix, though the tensile debonding energy is increased with the increase in fibres content especially when the failure path crosses the mortar layer.

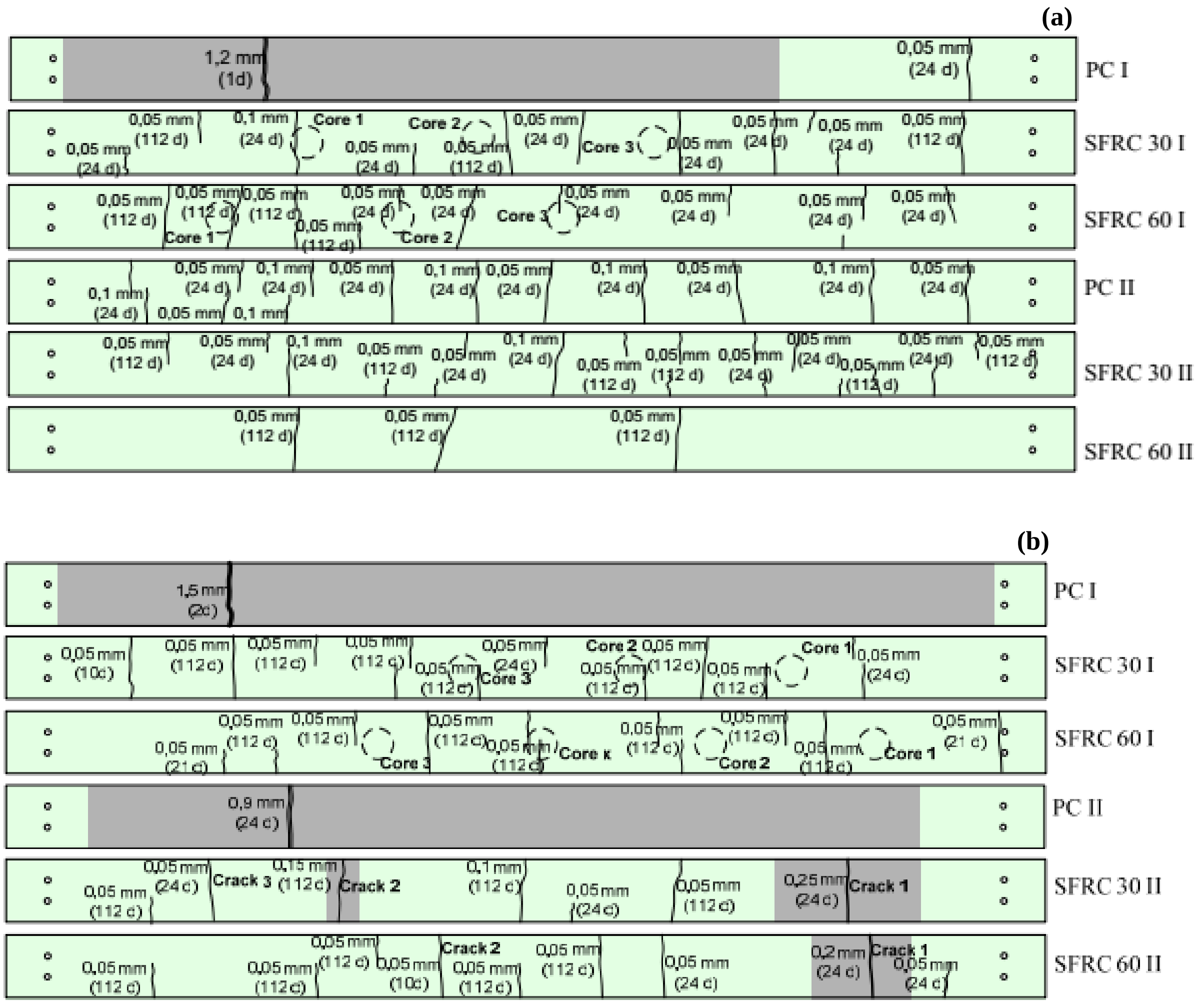

Figure 1.2. Cracking and de-bonding (shaded areas) with the final width of cracks and time to cracking in overlay strips cast on: (a) Smooth and dry substrate slab; (b) Rough and moistened substrate slab (After Carlward [8]).

1.2 Scientific Challenges

Cracking is one of the main challenges in concrete repairs that can impact not only the functionality of repairs, but also their durability. To predict crack widths in plain overlays, concrete free shrinkage ε_{cs} is multiplied by the crack spacing. The free shrinkage strain of overlays made with conventional cement types can be estimated using code procedures [25, 28, 29] with a good accuracy. However, these procedures do not consider rapid hardening cements or fibres in their predictive equations. Using total free shrinkage provides un upper limit for the estimated crack widths of overlays as the restraint level does not reach 100% for most practical applications.

Currently, there is no widely accepted design approach to limit crack widths in overlays or accurately quantify the effect of fibres on crack width and crack spacing of overlays. The available procedures in literature [30, 31] use fracture properties in fibre reinforced overlays, in particular, the residual strength parameters to consider the effect of industrial fibres. However, such procedures can lead to negative crack width in fibre reinforced overlays with deflection hardening properties. Furthermore, the few existing methods to calculate crack spacings in overlays rely mainly on experience and experimental observations. Hence, as there are no experimental data or analytical models that show the effect of rapid hardening cements and recycled clean steal fibres (RCSF) on cracks, it is uncertain whether those methods can still be applied. Furthermore, the effect of restrained shrinkage distress on the strength of concrete overlays with and without fibres is not well understood. There is also a need to understand the role of fibres on interfacial shear stress and strength and the risk of delamination.

Cracking and delamination due to restrained shrinkage in overlays depends on several overlay, base and interface properties as well as their interactions and it can be quite expensive and time consuming to investigate all the parameters experimentally. Likewise, analytical procedures may not be very accurate in predicting their behaviour as restrained shrinkage and its subsequent cracking and/or delamination are rather complex. Thus, a fracture-based analysis with appropriate time dependent material properties is needed to provide more accurate and in-depth insight into the behaviour of overlays under restrained shrinkage.

Analytical equations for calculating the tensile stresses of overlays assume uniform shrinkage distribution [32]. In overlays, the top layer tends to shrink faster than the lower layer as the top layer loses moisture to the environment while the lower layer loses moisture to the substrate, and thus the rate of drying at the interface is smaller. This shrinkage gradient is expected to affect the stress state of overlays and should be quantified and considered into account to provide better estimation of the risk of cracking in overlays.

1.3 Aims and Objectives

This study aims to contribute to the understanding of restrained shrinkage in overlays made with plain and RCSF reinforced rapid hardening mixes with special attention towards quantifying the fibre effect on crack widths of overlays and to promote more sustainable solutions. This aim will be achieved through the following objectives:

1. To characterise the flexural and compressive behaviour of mortars made with different rapid hardening cements with special focus on the effect of RCSF and development of their properties with time and quantify the residual strength parameters for the tested fibre reinforced mixes.
2. Assess the suitability of available procedures given by codes and by others to model the flexural behaviour of rapid hardening RCSF materials and compare their results with inverse analysis results. Using inverse analysis to derive σ-ε models that facilitate the modelling of such materials.
3. Investigate the time dependent moisture movement and free shrinkage behaviour of rapid hardening materials.
4. Evaluate the available code procedures to estimate the shrinkage evolution of these mixes over time and propose new factors for each cement type. Determine essential hygral and moisture transfer properties for computational modelling including moisture diffusion coefficient, surface factor and

shrinkage hygral coefficient.

5. Compare the values of shrinkage strain predicted by computational models over time with code predicted values. Validate the hygral numerical stresses by using simple analytical procedures.
6. Assess the risk of cracking and delamination for overlays made with rapid hardening materials.
7. Investigate experimentally and analytically the restrained shrinkage of overlays made with rapid hardening materials.
8. Propose crack spacing prediction equations for overlays under restrained shrinkage.
9. Review crack widths models and modify them to consider RCSF effect.
10. Examine the effect of fibres on interfacial shear strength of overlays.
11. Perform computational modelling of composite prisms under restrained shrinkage.
12. Undertake parametric investigations to study the effect of base and interface properties on the performance of overlays.
13. Quantify the effect of stress gradient on tensile stresses of overlays and include this effect into stress predictions.

1.4 Research Methodology

To address the above objectives, a combination of experimental, analytical and numerical investigations is used. To investigate the tensile properties of SFRC, uniaxial tension tests could be used. However, as performing the direct tests and interpreting results are difficult [14,17, 25, 33], flexural tests are adopted in this study. The first experimental study involves flexural testing of notched and unnotched mortar prisms at different ages. It also includes measuring the compressive strength of those mixes as well as determining their flexural modulus., By using inverse analysis, the tensile characteristics of fibre reinforced mortars (σ-ε models) are back calculated using results of the first experimental study.

The second experimental study deals with moisture measurement and free shrinkage tests. By using inverse analysis, moisture diffusivity, surface factor and hygral contraction coefficient are back calculated using data from the second experimental study.

The third experimental study involves restrained shrinkage evaluation of 16 composite prisms overlaid with rapid hardening plain and fibre reinforced mixes. After shrinkage stabilisation, the prisms are tested in four-point bending to understand the effect of cracking on the bearing capacity of repaired prisms. Benefiting from equilibrium concepts, a simple analytical model for crack spacing estimation is developed and validated and used in calculations of crack widths of overlays. Overlaid prisms are numerically modelled using material properties obtained from inverse analysis. Based on the analysis results, the analytical equations for predicting tensile stresses in overlays are modified to consider this effect.

The last experimental study examines the effect of fibres on interfacial shear strength of overlays. Bi-surface shear tests are performed on composite cube prisms of 120 × 120 ×150 mm. The Shear test was also numerically modelled to have a better understanding on the interfacial shear behaviour of different mixes.

1.5 Thesis layout

This thesis comprises six chapters and four appendices. Chapter one and six are written in normal thesis format while other the chapters are written in journal paper format. A brief description of each chapter is given as follows:

Chapter 2 entitled "Performance of rapid hardening recycled clean steel fibre materials" is based on Al-musawi et al. [34], published in Construction and Building Materials. It addresses objectives 1,2 and 9. It presents extensive experimental and numerical studies on the flexural performance of recycled clean steel fibres (RCSF) on rapid hardening mortars produced using two commercial cement types; calcium sulfo-aluminate cement and calcium aluminate cement as sole cementitious materials. The chapter describes the compressive and flexural behaviour of these mixes tested at different ages, ranging from one hour to one year. Constitutive equations based on the RILEM [35] and Model Code 2010 [25] recommendations and suggested by others [36, 37] are used to predict flexural behaviour of the tested mixes. The analytical results are compared with predictions obtained from inverse analysis.

Chapter 3 entitled "Shrinkage properties of plain and recycled steel–fibre-reinforced rapid hardening mortars for repairs" is based on Al-musawi et al. [38], published in Construction and Building Materials and addresses objectives 3-6 and 11. It comprises experimental and numerical investigations of the time dependent transport properties and shrinkage behaviour of the mixes that develop in the first experimental study described in chapter 2. Inverse analysis using finite element method is used to determine the moisture diffusivity and the hygral contraction coefficient of each mix. The available code predictive procedures are evaluated and new factors for each cement type are proposed. A comparison is made between the predicted values of shrinkage strain over time, for different depths, using these procedures and obtained values from the numerical models.

Chapter 4 entitled "Effect of shrinkage on rapid hardening plain and recycled steel fibre concrete overlays" is based on Al-musawi et al. [39], submitted to Cement and Concrete Composites and addresses objectives 7-10. This chapter presents experimental and analytical studies on restrained shrinkage of overlays made with rapid hardening mortar mixes reinforced with recycled fibres. A simple analytical model for predicting crack spacing is developed and the results are compared with experimental values. The available methods in literature for predicting the crack width are reviewed and a modified crack width predictive model for plain and RCSF reinforced overlays is proposed and evaluated.

Chapter 5 entitled "A numerical study on the effect of shrinkage on rapid hardening plain and recycled steel fibre concrete overlays" is based on Al-musawi et al. [40], submitted to Construction and Building Materials and addresses objectives 11-13. This chapter focuses on numerical analysis and examines the performance of overlays under restrained shrinkage. The experimental results presented in chapter 4 were modelled in Abaqus. The FE analysis results are validated by comparing the numerical stresses to the predictions of the Silfwerbrand analytical procedure [32]. Parametric studies are preformed to investigate the shrinkage behaviour of rapid hardening overlays. The studied parameters include overlay depth, interface properties and moisture content of the substrate with special attention on the effect of non-uniform shrinkage distribution on the hygral stresses in overlays. Based on the analysis results, an empirical method to consider this effect is proposed. Finally, the experimental results of interfacial shear specimens are modelled.

Chapter Six includes concluding remarks and recommendations for future work.

References

1. Beushausen, H., Alexander, M.G., (2006). Failure mechanisms and tensile relaxation of bonded concrete overlays subjected to differential shrinkage. *Cem. Concr. Res.* 36 (10), 1908-1914. Available at: https://www.sciencedirect.com/science/article/pii/S0008884606001608.
2. Banthia, N., Zanotti, C., Sappakittipakorn, M., (2014). Sustainable fibre reinforced concrete for repair applications. *Constr. Build. Mater.*, 67(PART C), 405–412. Available at: http://dx.doi.org/10.1016/j.conbuildmat.2013.12.073.
3. Lin, D.F., Wang, H.Y., (2005). Forensic investigation of ultra-thin whitetopping failures in Taiwan. *J. PERFORM. CONSTR. FAC.*, 19(2), pp.165–171. Available at: http://www.scopus.com/inward/record.url?eid=2-s2.0-18744371584&partnerID=40.
4. Lampropoulos, A.P., Tsioulou, O.T. and Dritsos, S.E., (2012). Biaxial Stress due to Shrinkage in Concrete Jackets of Strengthened Columns. *ACI Mater. J.*, 109(3), 331-340.
5. Jafarifar, N., Pilakoutas, K., Bennett, T., (2016). The effect of shrinkage cracks on the load bearing capacity of steel-fibre-reinforced roller-compacted-concrete pavements. *Mater. Struct.*, 49(6), 2329-2347. Available at:

https://link.springer.com/article/10.1617/s11527-015-0652-0.

6. Younis, K.H., (2014). *Restrained shrinkage behaviour of concrete with recycled materials*. PhD thesis. University of Sheffield. UK.
7. Turatsinze, A., Granju, J.L., Bonnet, S., (2006). Positive synergy between steel-fibres and rubber aggregates: Effect on the resistance of cement-based mortars to shrinkage cracking. *Cem. Concr. Res.*, 36 (9), 1692-1697.
8. Carlsward, J., (2006). *Shrinkage Cracking of Steel Fibre Reinforced Self Compacting Concrete Overlays*. Doctoral Thesis. Lulea University of Technology. Department of Civil and Environmental Engineering, Sweden.

9. Gopalaratnam, V.S., Gettu, R., (1995). On the characterization of flexural toughness in fiber reinforced concretes. *Cem. Concr. Compos.*, 17 (1995) 239–254, Available at:
https://doi.org/10.1016/0958-9465(95)99506-O.
10. ACI 544.1R, (1996). State-of-the-Art Report on Fibre-Reinforced Concrete. American Concrete Institute, Detroit, USA.
11. Banthia, N., Sheng, J., (1996). Fracture toughness of micro-fiber reinforced cement composites. *Cem. Concr. Compos.*, 18, 251–269, Available at:
https://doi.org/10.1016/0958-9465(95)00030-5.
12. Bernard, E.S., (2006). Influence of toughness on the apparent cracking load of fiber reinforced concrete slabs, *J. Struct. Eng.*, 132, 1976–1983, Available at:
https://doi.org/10.1061/(ASCE)0733-9445(2006)132:12(1976).
13. Rashiddadash, P., Ramezanianpour, A.A., Mahdikhani, M., (2014). Experimental investigation on flexural toughness of hybrid fiber reinforced concrete (HFRC) containing metakaolin and pumice. *Constr. Build. Mater.*, 51, 313–320, Available at:
https://doi.org/10.1016/j.conbuildmat.2013.10.087.
14. Tlemat, H., (2004). Steel Fibres from Waste Tyres to Concrete, Testing, Modelling and Design. PhD thesis, The University of Sheffield, Sheffield, UK.
15. Tlemat, H., Pilakoutas, K. and Neocleous, K., (2006). Stress-strain characteristic of SFRC using recycled fibres. *Mater. Struct.*, 39(3),365-377. Available at: https://link.springer.com/article/10.1007/s11527-005-9009-4.
16. Tlemat, H., Pilakoutas, K. and Neocleous, K., (2006). Modelling of SFRC using inverse finite element analysis. *Mater. Struct.*, 39(2), 221-233. Available at: https://link.springer.com/article/10.1617/s11527-005-9010-y.
17. Graeff, A.G., (2011). Long-Term Performance of Recycled Steel Fibre Reinforced Concrete for Pavement Applications. PhD thesis, The University of Sheffield, UK.
18. Graeff, A.G., Pilakoutas, K., Neocleous, K. and Peres, M.V.N., (2012). Fatigue resistance and cracking

mechanism of concrete pavements reinforced with recycled steel fibres recovered from post-consumer tyres. *Eng. Struct.*, 45, 385–395. Available at: https://www.sciencedirect.com/science/article/pii/S0141029612003392.

19. Jafarifar, N., (2012). *Shrinkage Behaviour of Steel Fibre Reinforced Concrete Pavements*. PhD thesis, The University of Sheffield, Sheffield, UK.
20. Younis, K.H. and Pilakoutas, K., (2013). Strength prediction model and methods for improving recycled aggregate concrete. *Constr. Build. Mater.*, 49, 688-701. Available at: https://www.sciencedirect.com/science/article/abs/pii/S0950061813008404.
21. Angelakopoulos, H., (2016). *Reused Post-Consumer Tyre Steel Fibres in Roller Compacted Concrete*. PhD thesis, The University of Sheffield, Sheffield, UK.
22. ETRA, (2013). Introduction to tyre recycling. The European Tyre Recycling Association, Brussels, Belgium.
23. Hu, H., (2018). *Mechanical properties of blended steel fibre reinforced concrete using manufactured and recycled fibres from tyres*. PhD thesis, The University of Sheffield, Sheffield, UK.
24. Hu, H., Papastergiou, P., Angelakopoulos, H., Guadagnini, M., Pilakoutas K., (2018). Mechanical properties of SFRC using blended recycled tyre steel cords and recycled tyre steel fibres, *Constr. Build. Mater.*, 187, 553-564. Available at: https://www.sciencedirect.com/science/article/pii/S0950061818318750?via%3Dihub.
25. F.I. du Béton, (2013). Fib Model Code for Concrete Structures 2010, Wilhelm Ernst & Sohn, Berlin, Germany.
26. Santos, P.M., Julio, E.N., (2007). Correlation between concrete-to-concrete bond strength and the roughness of the substrate surface. *Constr. Build. Mater.*, 21(8), 1688-1695. Available at: https://www.sciencedirect.com/science/article/pii/S0950061806002005.
27. Kim, M.O., Bordelon, A., (2016). Fiber effect on interfacial bond between concrete and fiber-reinforced mortar. Transportation Research Record: Journal of the Transportation Research Board, (2591), 11-18.
28. CEN, (2004). Eurocode 2: Design of concrete structures, Part 1-1: General rules and rules for buildings.

European Committee for Standardization. Brussels, Belgium.

29. ACI, (2008). ACI 209.2R-08: guide for modeling and calculating shrinkage and creep in hardened concrete. American Concrete Institute, Farmington Hills.
30. Concrete Report No. 13, (2006). Draft version of the Swedish Concrete Society report on Industrial Floors (In Swedish). Swedish Concrete Society, Report no 13. Cited in: Carlsward, J., (2006*).* *Shrinkage Cracking of Steel Fibre Reinforced Self Compacting Concrete Overlays*. Doctoral Thesis. Lulea University of Technology. Department of Civil and Environmental Engineering, Sweden.
31. Kim, M.O., Bordelon, A.C., Lee, N.K., (2017). Early-age crack widths of thin fiber reinforced concrete overlays subjected to temperature gradients. *Constr*. *Build*. *Mater*., 148, 492-503.
32. Silfwerbrand, J., (1997). Stresses and strains in composite concrete beams subjected to differential shrinkage. *ACI Struct*. *J*., 94(4), 347-353.
33. ACI 544.1R-96, (2002). State-of-the-art report on fiber reinforced concrete. American Concrete Institute, Michigan, US.
34. Al-musawi, H., Figueiredo, F., Bernal, S.A., Guadagnini, M., Pilakoutas, K., (2019). Performance of rapid hardening recycled clean steel fibre materials. *Constr. Build. Mater*.,195, 483-496.
35. RILEM TC 162-TDF, (2003). σ-ε-design method, *Mater. Struct*. 36(8), 560–567. https://doi.org/10.1007/BF02480834.
36. Barros J.A.O., Cunha V.M.C.F., Ribeiro A.F., Antune J.A.B., (2005). Post-Cracking Behaviour of Steel Fibre-Reinforced Concrete. *Mater. Struct*. 38, 47-56.
37. Hu H., Wang Z., Figueiredo F., Papastergiou P., Guadagnini M., P., Pilakoutas, (2018). Post-cracking tensile behaviour of blended steel fibre-reinforced concrete. *Struct. Concr*., 1-13. Available at: https://doi.org/10.1002/suco.201800100.
38. Al-musawi, H., Figueiredo, F., Guadagnini, M., Pilakoutas, K., (2019). Shrinkage properties of plain and recycled steel–fibre-reinforced rapid hardening mortars for repairs. *Constr*. *Build*. *Mater*., 197, 369-384. Available at:

https://doi.org/10.1016/j.conbuildmat.2018.11.099.

39. Al-musawi, H., Huang, H., Benedetti, M., Guadagnini, M., Pilakoutas, K., (2019). Effect of shrinkage on rapid hardening plain and recycled steel fibre concrete overlays, part A: Experimental and analytical work. *Mater. Struct.*, submitted for publication.
40. Al-musawi, H., Huang, H., Benedetti, M., Guadagnini, M., Pilakoutas, K., (2019). Effect of shrinkage on rapid hardening plain and recycled steel fibre concrete overlays, part B: Numerical work. *Mater. Struct.*, submitted for publication.

Chapter 2: Performance of rapid hardening recycled clean steel fibre materials

Al-musawi, H., Figueiredo, F., Bernal, S.A., Guadagnini, M., Pilakoutas, K., (2019). Performance of rapid hardening recycled clean steel fibre materials. *Constr. Build. Mater.*, 195, 483-496.

Abstract

To minimise disruption due to repairs of concrete pavements, rapid hardening and tough materials need to be used. This paper investigates the flexural performance of rapid hardening mortar mixes made with two commercial cement types, calcium sulfo-aluminate cement and calcium aluminate cement, for thin concrete repair applications. Three-point bending tests are performed on plain and steel fibre reinforced concrete specimens containing 45 kg/m^3 of recycled clean steel fibres to characterise the flexural performance of notched and unnotched prisms at different ages, ranging from one hour up to one year. The recycled fibers are shown to enhance both the flexural strength and toughness of FRC prisms, leading to hardening behaviour. Constitutive equations based on the RILEM and Model Code 2010 recommendations are found to overestimate the loading capacity of the bending tests. FE analyses using multilinear $\sigma - \varepsilon$ tensile curves obtained by employing inverse analysis can capture better the post cracking strength and cracking pattern of the tested prisms.

This chapter consists of a "stand alone" journal paper and includes a relevant bibliography at the end of the chapter. Additional information and details are presented in Appendix A.

2.1 Introduction

Progressive deterioration of infrastructure, particularly pavements, occurs due to increasing vehicular axle loads, worsening environmental conditions (due to climate change) and higher traffic volumes. Excessive deterioration can lead to serious service disruptions and higher costs for infrastructure owners and road users. Conventional ordinary Portland cement (OPC) based repair materials attain their strength rather slowly and need between 12h to 24h to develop sufficient strength before roads can be back in service, adding to delays and disruption during maintenance. To minimise disruption, rapid hardening cements can be used in repairs. There are several special rapid hardening Portland-free cements available in the market; such as calcium sulfo-aluminate (CSA) cement and calcium aluminate (CA) cement. CSA can achieve early rapid strength development and can have expansive properties [1]. It is reported to have good durability in aggressive environments, particularly when exposed to sulfates [2]. Furthermore, this cement requires less energy for its production compared to OPC [1], thus it is considered to be environmentally friendly. However, despite its lower energy demand, it is still more expensive due to the cost of its raw materials.

CA cements are characterised by high early strength development and high resistance to elevated temperatures, depending on their aluminum content. An important aspect for the rapid strength development of this cement is the substantial amount of heat of hydration which can result in high heat generation [3]. Self-heating may be a concern in sections thicker than 100 mm [3], but not necessarily for thinner repair layers. Despite the high temperature rise during hydration, CA concretes do not seem to be overly susceptible to thermal cracking. This may be due to creep relaxation of thermally induced strains, facilitated by a conversion reaction, during which some metastable phases of this cement convert to stable phases of lower volume [3, 4]. As porosity increases, the densification due to conversion causes loss of strength [3]. Hence, when used for repairs, the key concern to be addressed is cracking due to restrained shrinkage.

Restrained shrinkage is one of the main factors that govern the serviceability and durability of concrete repairs [5,6]. Shrinkage in concrete results due to moisture diffusion from the new concrete to the environment and to the concrete substrate [7] if not adequately saturated. However, shrinkage deformation (of the new layer) is restrained by the substrate layer leading to the development of tensile and interfacial shear stresses. If these stresses exceed the material capacity at any time, cracking will develop in the repair material and/or debonding along the interface between the repair material and the substrate. Micro-cracks induced by shrinkage can propagate and coalesce into macro-cracks under the effect of applied loads.

Cracks beyond a certain width can adversely affect the durability of repair materials by creating easy access for deleterious agents leading to early saturation, freeze–thaw damage, scaling, and steel corrosion, which promote further internal and external cracking and accelerate the rate of deterioration [8]. This issue can be worsen with rapid hardening (non-expansive) materials due to the rapid hydration rate which accelerates shrinkage development. Furthermore, due to the rapid stiffness development and decrease in creep compliance of rapid hardening cements [9], their ability to redistribute stresses may be affected, thereby increasing cracking potential. To address this issue, fibres can be added to control crack widths [10] as well as increase the tensile strength and fatigue resistance [11], thus resulting in more durable layers. To reduce the environmental impact of manufactured steel fibres (MSF), recycled clean steel fibres (RCSF) can be used as alternative fibre reinforcement.

During the manufacture of tyres, parallel steel cords are embedded in continuous thin rubber belts. After being cut to shape, these are placed in overlapping layers to provide flexible reinforcement within the tread and side walls of the tyre. The complex configuration of each layer generates significant levels of waste (approximately 5% by mass). The available amount of waste steel cord is therefore around 100,000 tonnes per year worldwide. The steel reinforcement used in tyre manufacture typically consists of parallel filaments of very fine wire (0.1-0.4 mm dia.) twisted together to form a cord about 0.5-1.0 mm in diameter [12]. Recycled clean steel fibre (RCSF) filaments extracted from pre-vulcanised rubber belt offcuts have become available recently and were adopted in this study. However, knowledge on their use in concrete is scarce and it is limited to research at the University of Sheffield [13]. Knowledge of the effect of industrial fibres on CSA and CA matrices is also rather limited [9,14-16] and no published data exist regarding the effect of RCSF. A study on the effect of CSA matrix on pullout performance of steel fibres [9] suggests that the synergetic effect of a stiff matrix like ettringite and high modulus steel fibres can increase crack propagation resistance in the composite material, evidenced by an increase in debonding energy density.

Since cracking is the main concern for repairs, understanding the effect of fibres in controlling crack widths under mechanical and hygral loads, as well as the complex interaction of shrinkage, stiffness and tensile strength evolution are of paramount importance. For this purpose, finite element analysis can be a useful tool. However, appropriate material parameters need to be determined experimentally and the tensile σ-ε curves of the repair materials need to be derived from direct tension or bending results. Although there are several procedures in the literature to derive the σ-ε of SFRC in tension [17-20], they may not be entirely suitable for modelling mortars reinforced with RCSF due to the different fracture energies of the two concretes. Matrices reinforced with MSF usually show deflection softening performance while concretes reinforced with RCSF are reported to have hardening performance [13]. In numerical studies performed by Hu et al. [20] and Neocleous et al. [21], it was found that RILEM proposed σ-ε equations overestimate the predicted capacity of FRC. As a result, a simplified σ-ε model was suggested to overcome issues in the other methods and to include the post-consumer tyres steel fibres (RTSF) effect.

This paper presents experimental and numerical work on the flexural performance of RCSF on rapid hardening mortars produced using CSA or CA as sole cementitious materials. Constitutive relationships derived based on code recommendations and by others [19, 20] are used to predict flexural behaviour and the results are compared with predictions obtained from inverse analysis.

This chapter addresses objectives 1,2 and 9 of the thesis.

2.2 Experimental details and methodology

2.2.1 Materials

Two commercial cement types were used in this study; calcium sulfoaluminate cement[1] (CSA) and rapid setting calcium aluminate cement[2] (RSC). According to the manufacturer, RSC consists of hydrated alumina, oxides of iron and titanium, with small amounts of silica. For production of mortars, fine aggregates, medium grade river washed sand (0-5mm sourced from Shardlow in Derbyshire, UK, SG=2.65, A = 0.5, FM = 2.64), were used. Recycled clean steel fibres (RCSF) were obtained from tyre cords extracted from un-vulcanised rubber belts (see Figure 2.1). The length of the RSCF used in this study was 21 mm and the diameter 0.2 mm. They are uniform as MSF. The strength of these fibres is reported to exceed 2600 MPa [13]. Superplasticiser[3] was added to enhance the workability and adjust the setting time.

Figure 2.1. Photograph of the RCSF used in this study

---

[1] provided by Kershin International Co., Ltd

[2] sourced from Instarmac

[3] Sika Viscoflow 2000

2.2.2 Mortar mix design

A total of 600 kg/m^3 of cement was used with low w/c ratios to obtain high early strength. For durability requirements, w/c should be kept lower than 0.4 [22]. However, as CSA cement consumes more water to form hydration products than ordinary Portland cement [23], this limit can be relaxed slightly for this cement. As a result, two different w/c ratios and superplasticiser (SP) dosages were tested. The w/c ratios for mixes with CSA cement were 0.4 and 0.41, and 0.35 and 0.36 for RSC mixes. The water content and SP were carefully selected to achieve a workable mix with setting time of no longer than 15 minutes. Fibre dosage of 45 kg/m^3 (V_f = 0.57%) was investigated as is commonly used in European practice for structural applications. The plain and fibre reinforced mortar mixes for each cement type are almost identical, to reliably investigate the effect of fibres on the mechanical properties. The details of the optimised mortar mixes that meet the setting, durability and workability requirements are summarised in Table 2.1.

The specimens were cured for one hour before demoulding and exposure to standard laboratory conditions.

Table 2.1 Mortar mix composition

mix	Cement (kg/m^3)	w/c	Sand (kg/m^3)	SP^a	Fibre dosage (kg/m^3)
CSA	600	0.40	1420	0.60	0
FCSA	600	0.41	1420	0.61	45
RSC^b	600	0.35	1300	0.20	0
FRSC	600	0.36	1300	0.21	45

^{a} % by cement mass. ^{b} mixes containing CA cement are called RSC in this study.

2.2.3 Fresh state properties

2.2.3.1 Vicat test

The setting time of cement pastes was assessed using an automatic Vicat apparatus according to ASTM C191 (2013) [24]. As the cements used in this study are fast setting, the instrument was set to take measurements every 30 seconds.

2.2.3.2 Semi-adiabatic calorimetry

The semi-adiabatic calorimeter records the temperature evolution and key temperature related properties for a tested mix, such as time to peak heat, peak heat, and cumulative heat [25]. Since the mortar mixes are designed for thin repairs, heat loss due to dissipation is expected to take place and hence, the semi-adiabatic test could reveal a temperature evolution that is close to practical applications. After mixing the required quantity for each mix, the mortar was directly placed in an insulated thermal flask cylinder of 0.5 l and a thermocouple was inserted inside the mortar to record the temperature.

2.2.4 Flexural tests

To characterise the flexural performance, mortar prisms of 40 × 40 × 160 mm were tested according to BS EN 13892-2 [26]. To obtain the load deflection curve after the peak load, displacement control was adopted rather than load control as required by the standard [26]. The rate of loading was 0.25 mm/min until 1 mm deflection, and 1 mm/min after that. To eliminate errors due to machine stiffness, spurious support displacements and local concrete crushing, a specially designed aluminum yoke (based on the Japanese standard JSCE-SF4 [27]) was mounted on the specimens. To assess the flexural behaviour over time, the prisms were tested at one hour, three hours, one day, seven days, 28 days and 365 days as the strength evolves fast for rapid hardening materials. The test was also performed on notched prisms (the notch depths range from 3.57 to 4.94 mm) to assess crack development. The Crack Mouth Opening Displacement (CMOD) was measured at mid span with a 12.5 mm clip gauge (mounted across the bottom part of the notch, Figure 2.2). For practical reasons (time limitations), this test was performed at 2 days (at the earliest age) and up to one year.

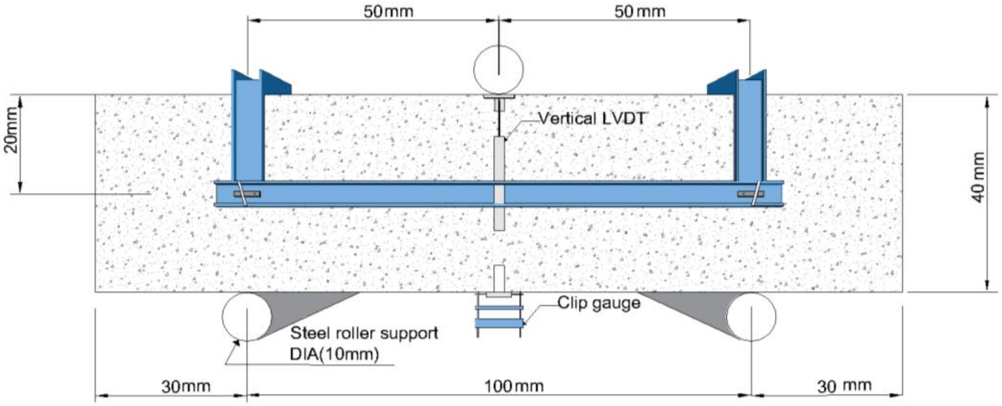

Figure 2.2. Flexural test set up

2.2.5 Compressive strength

Directly after flexural testing, the halves of the fractured prisms were tested in uniaxial compression according to BS EN 13892-2 [26]. Only the one-hour compressive strength of FRC specimens was examined separately due to practical time constrains.

2.3 Experimental Results and Discussion

2.3.1 Fresh state properties of rapid hardening materials

The water content and SP dosage were optimised for each mix to achieve a workable mix with setting time of no longer than 15 minutes. As shown in Table 2.2, the CSA cement had a relatively shorter setting time compared to the RSC cement. Slightly higher water content and SP dosages for the fibre reinforced mixes lead to a slight increase of the setting time for these mixes.

Table 2.2 Setting time and maximum temperature (T_{peak}) for different mixes

Mixes	*Vicat setting time (min.)*		*T_{peak} (C°)*
	Initial	*Final*	
CSA	9.5	10.5	68
FCSA	9.5	11.0	68
RSC	12.0	14.5	91
FRSC	12.5	15.0	88

The results of the semi-adiabatic calorimetry test (for the first 36 hours) are shown in Figure 2.3. For mixes with CSA cement, the peak temperature (T_{peak}) was about 68° C (see Table 2.2) occurring during the first hour regardless of fibre content. The temperature rise in RSC mixes was much higher than in mixes with CSA cement, with T_{peak} at 91° and 88° C for RSC and FRSC, respectively. The time half way to the peak ($T_{1/2\ peak}$) can be taken as an indication of the initial setting time of cementitious mixes [28]. For CSA and FCSA, $T_{1/2\ peak}$ was achieved at around 11 minutes, whilst for RSC and FRSC, it was recorded at around 16 minutes. These results agree well with the results of the vicat test. The temperature achieved for these cements upon hydration dropped to laboratory temperature in less than 24 hours. Heat dissipation is expected to occur faster onsite than in the semi-adiabatic test and, therefore, no major thermal cracking is expected for thin repairs, especially when curing is applied during the first two hours when T_{peak} occurs.

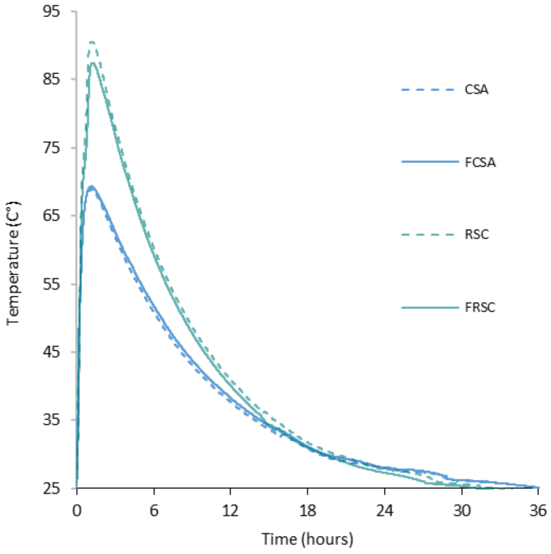

Figure 2.3. Temperature rise for mixes in semi-adiabatic test

2.3.2 Mechanical performance of rapid hardening mortars

2.3.2.1 Compressive strength

The average compressive strength f_{cu} (from six specimens) and standard deviation developed over time is shown in Figure 2.4. At one hour, FCSA achieved the highest compressive strength of 26.1 MPa while RSC achieved 17.2 MPa. This behavior changes at later ages as RSC achieves a higher strength than FCSA by approximately 6% after one-year. The fibres seem to have a positive effect on the compressive strength of both mortars, with the highest strength increase noticed at one hour (24% increase in f_{cu}). At later ages, this increase ranges from 10% to 17%. The strength increase at early ages might be attributed to the fact that stiff steel fibres contributes to the strength of FRC mixes that are not fully mature.

There is no consensus in literature on the effect of fibers on compressive strength. While some researchers [29-31] report a strength enhancement of up to 20% for Portland cement-based specimens containing recycled fibres with dosages less than 50 kg/m^3, others [32-34] found only a marginal effect due to air entrainment.

No strength reduction has been observed for any of the mixes at the age of one-year, indicating that there were no significant conversion issues. It should be noted that for fully cured rapid hardening CSA mortar-based samples (tested at 28 days), a compressive strength of 31.4 – 52.6 MPa for w/c ratios 0.4 – 0.5 was reported in literature [35] and this agrees well with the results of this study.

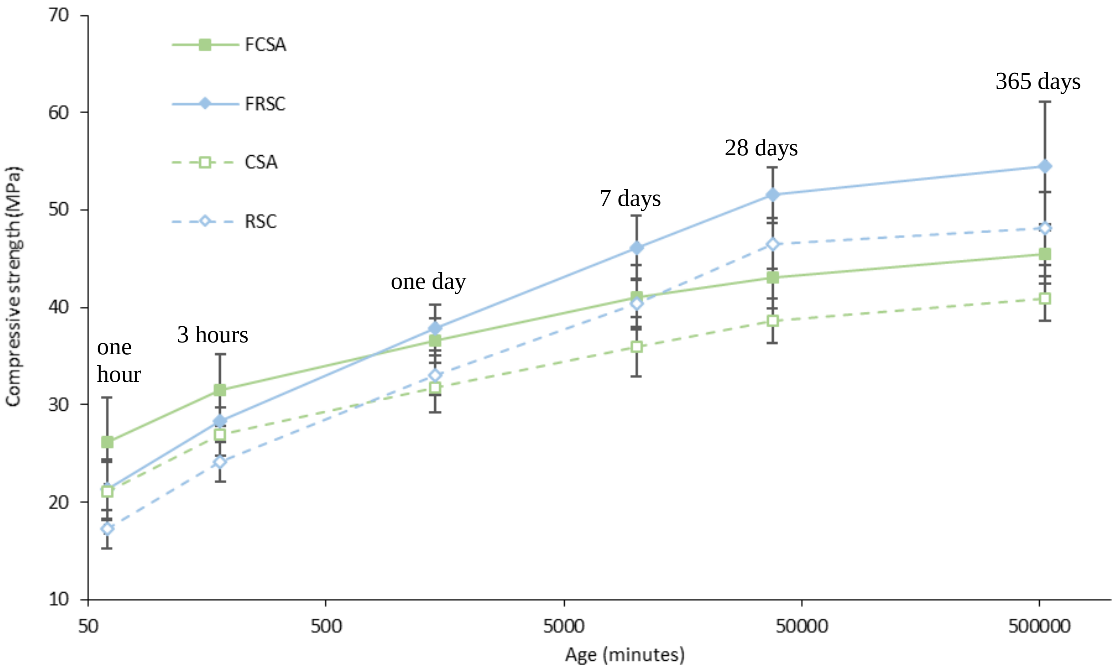

Figure 2.4. Development of f_{cu} as a function of time

To describe the compressive strength development with time, the $\beta_{cc}(t)$ function that describes the strength development with time used in Model Code 2010 [18] is followed (Equation 2.1).

$$\beta_{cc}(t) = \exp\{s.\,[1-(28/t)^{0.5}]\}$$

Equation 2.1

where, t is the concrete age in days, s is a coefficient that depends on the class of cement which ranges from 0.2 – 0.38 for $f_{cm} \leq 60$ MPa. As the cements used in this study are rapid hardening, a 0.2 value for s was adopted (as recommended by the Model Code 2010 [18]). To obtain the strength at various ages, $\beta_{cc}(t)$ is multiplied by the mean compressive strength at the age of 28 days (f_{cm}). The estimated compressive strength (-MC) at various ages is shown against the experimental results in Figure 2.5. As expected, the function underestimates the strength at the early ages by approximately 100% for the different rapid hardening mixes. As the strength evolves very rapidly at the early ages and then it slows down, smaller s values could offer a better representation for strength development with time. The s values of 0.024 and 0.044 for mixes with CSA and RSC cements, respectively, were found by regression analysis for experimental results (-MC-NR) to represent well the strength evolution with time (Figure 2.5).

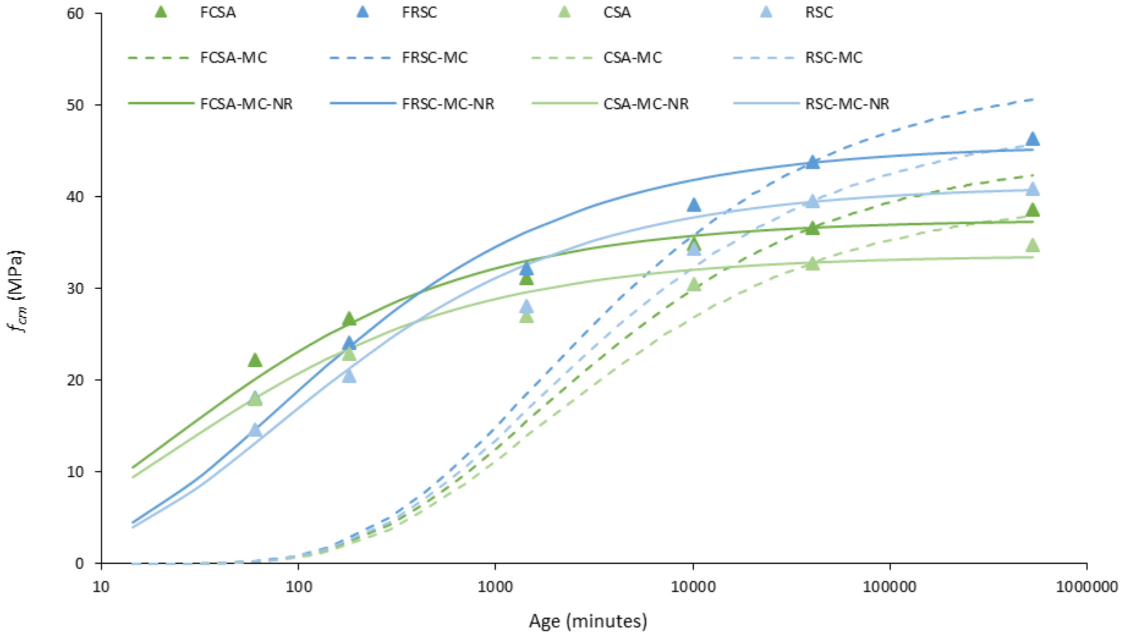

Figure 2.5. Development of experimental and estimated f_{cm} as a function of time using s = 0.2 (dashed lines) and suggested s values (solid lines-NR)

2.3.2.2 Flexural behaviour

The average flexural strength development over time (and standard deviation) is illustrated in Figure 2.6. Data points given in this figure represent the limit of proportionality (LOP), or first cracking strength ($f_{ctm,fl}$), determined according to BS EN 14651:2005 [36] as given in Equation 2.2

$$f_{ctm,fl} = \frac{3\, F_l\, l_b}{2\, b_b\, h^2} \qquad \text{Equation 2.2}$$

where, F_l is the load corresponding to LOP [36] (taken from Figure 2.7); l_b is the span length; b_b is the width of the beam; h is the beam depth.

It is noted that strength develops very fast and both plain and fibre reinforced specimens achieved 90% of their one-year strength in one day. The specimens made with CSA cement showed higher flexural strength than those with CA cement tested at the same age, probably due to the rigid dense crystal microstructure of the CSA cement [9]. RSC mixes have lower w/c ratio, hence, their compressive strength is expected to be higher in the long term. Due to high shrinkage in RSC mixes, their flexural strength is reduced. The effect of RCSF on the flexural strength enhancement of the mixes is evident at all ages. Compared to their plain counterparts, FCSA and FRSC mixes showed a flexural strength increase of approximately 36% to 70% and 24% to 41%, respectively. This agrees well with Hu et al. [34], who reported an increase of 45% - 70% in $f_{ctm,fl}$ of concrete reinforced with blends of manufactured and post-consumer recycled fibres.

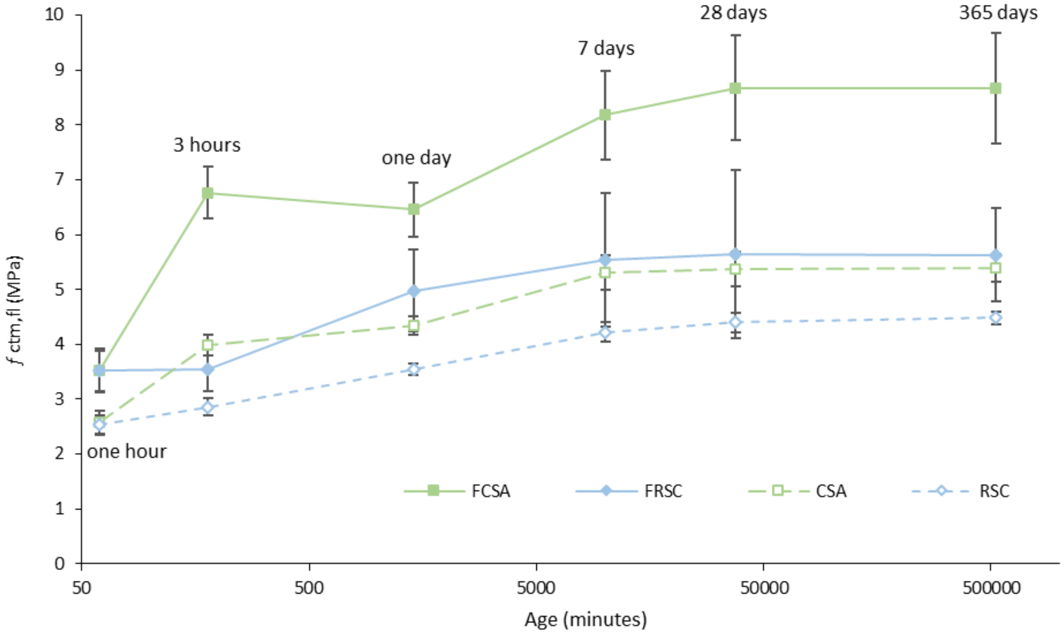

Figure 2.6. The flexural strength $f_{ctm,fl}$ development as a function of time

The load-deflection curves for FCSA and FRSC prisms are shown in Figure 2.7. The behaviour of the specimens made with the unreinforced mixes is not shown as they failed suddenly after peak load without any post cracking strength, highlighting the poor toughness of plain mortars in tension. The deflection hardening shown by reinforced mixes can be attributed to the high number of fibres spanning the cracked section and the excellent bond between steel fibres and dense matrix systems, like the CSA cement. This hypothesis is supported by the fact that in the current study, many specimens developed more than one principal crack, confirming the excellent load transfer by the RCSF. It should be noted that the preferential alignment of the fibres in the direction of stress due to the small mould size (40 × 40 × 160 mm) may have contributed to this. Deflection hardening was also reported in a study by Bordelon [37] for concrete specimens cut from prisms of 150 × 150 × 450 mm and tested using a 50 mm beam depth (to simulate a thin overlay). Deflection hardening performance for notched concrete prisms reinforced with 45kg/m^3 of blends of recycled post-consumer and manufactured steel fibres was also reported in a recent study published by Hu et al. [34].

At large deflections (greater than 2 mm), the FCSA specimens show a slight reduction in load resistance compared to FRSC specimens, possibly due to the inherent brittleness of the CSA cement. However, in most repair applications, it is not expected that the mortar will reach such high level of deformation and as a result, minimal cracking is expected.

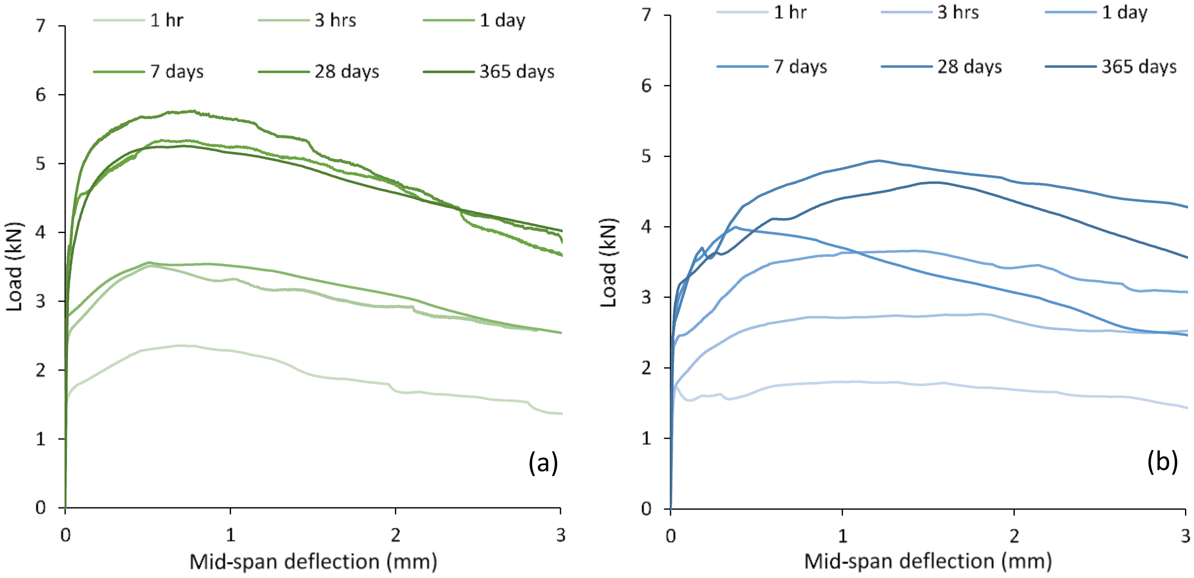

Figure 2.7. Load-deflection response of rapid hardening fibre reinforced mortars tested at different ages: (a) FCSA; (b) FRSC

2.3.2.3 Flexural modulus of elasticity (E_{fm})

The flexural modulus of elasticity (E_{fm}) was determined from load-deflection curves using elastic analysis and ignoring shear deformations. E_{fm} is the maximum flexural modulus between 30 – 60% of the peak load (P_{peak}) [38]. Figure 2.8 shows the development of E_{fm} and related standard deviations over time for all mixes.

The plain mortar mixes are shown in dotted lines. As with flexural strength, the stiffness of the mixes develops quickly and reaches around 90% of the one year modulus within 7 days.

The fibres have a remarkable effect on the modulus of elasticity. FCSA and FRSC have higher E_{fm} compared to CSA and RSC mixes respectively with the highest noticeable increase (29.7%) for FCSA occurring at one-hour of age. This behaviour was not reported in [34] and [39] who only noticed a marginal effect on the modulus of concrete with fibre addition. The remarkable increase in modulus of elasticity, though also reflected in the flexural strength, is beyond what is expected from a perfect composite. This may be partially due to fibre alignment, but also to the slightly longer mixing time that was necessary to integrate the fibres. This may increase the density of FRC mixes and affect the modulus results. An increase of approximately 36% in the modulus of elasticity of OPC based mortars reinforced with 2% (by volume) industrial steel fibres was reported in literature [40].

To estimate the modulus of elasticity of the mixes, based on compressive strength, equations from Model code [18], ACI 318-05 [22] and Kosaka et al. [41] were used. The latter equation was developed specifically for mortars. The estimated modulus of elasticity (E_c) for CSA (using the above equations) is presented in Figure 2.9. As shown, these equations overestimate E_c for CSA mix, especially at the early ages as the equations are usually used to determine the modulus of elasticity of concretes, not mortars. It should be noted that both Model code and ACI code adopt equations that use the 1/3 and 1/2 power of f_{cm} respectively. However, the results show that for these mortars, the linear relationship is more appropriate and the constant values of 720, 580, 640 and 520 were determined by regression analysis for FCSA, FRSC, CSA and RSC mixes respectively.

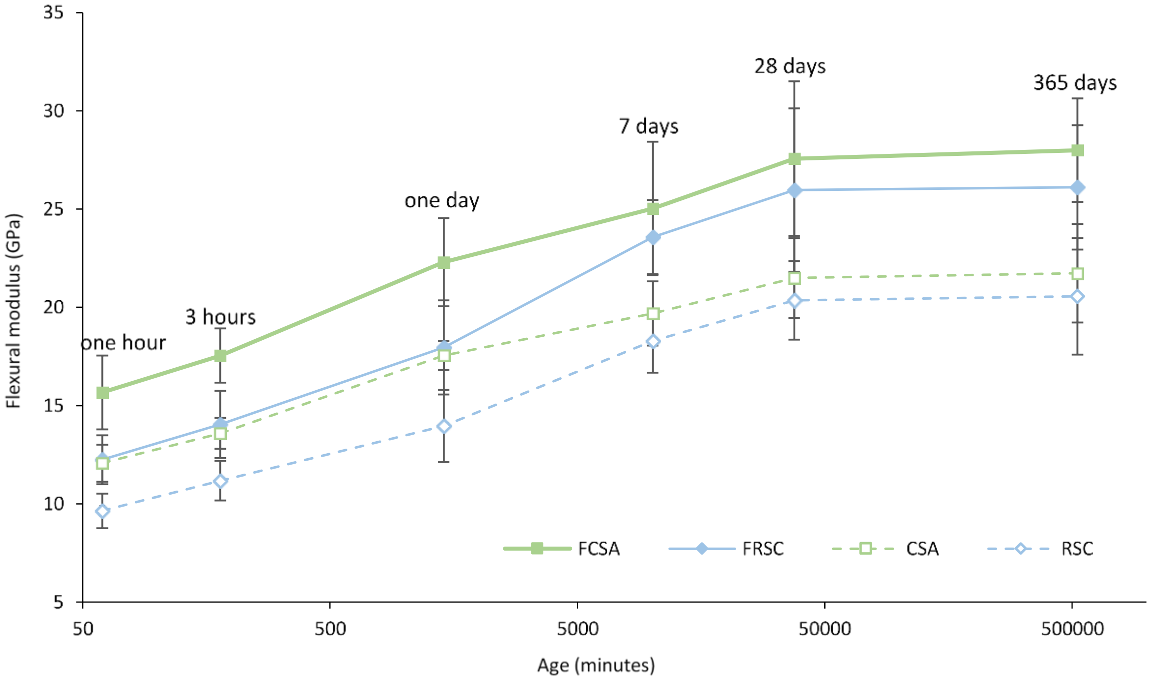

Figure 2.8. Flexural modulus (E_{fm}) of fast setting fibre reinforced mortars as a function of time

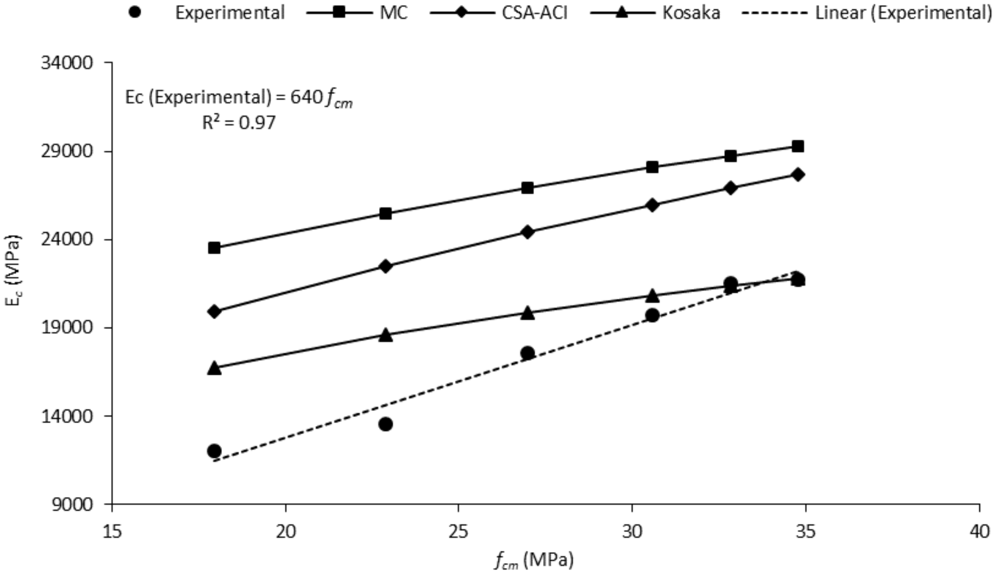

Figure 2.9. The relationship between f_{cm} and E_c using different equations for CSA mix

2.3.2.4 Relationship between measured deflection and CMOD values

A linear relationship between CMOD and average deflection is suggested in BS EN 14651:2005 [36], as given below (Equation 2.3),

$$\text{Average deflection (mm)} = k \times \text{CMOD (mm)} + 0.04\ \text{mm},\ k = 0.85 \qquad \textit{Equation 2.3}$$

This linearity has also been confirmed for FCSA and FRSC at all ages tested with coefficients of determination $R^2 > 0.99$, but as expected with lower K values, between 0.55 and 0.65, due to the different geometry of the testing arrangement. It should be noted that the CMOD measured by the clip gauge is corrected for the position of the clip gauge using the BS EN 14651:2005 [36].

A relationship between deflection and CMOD can facilitate the testing of such materials by using clip gauges only to measure the CMOD as accurate measurement of deflection requires the use of a special frame (yoke) to obtain net deflection. It also provides a benchmark for comparisons.

2.3.2.5 Residual flexural tensile strength (f_R)

RILEM TC 162-TDF [42] presents a methodology to calculate the residual flexural tensile strength of SFRC prisms, which was later adopted by BS EN 14651:2005 [36]. Residual flexural stresses (f_{R1}, f_{R2}, f_{R3} and f_{R4}) are calculated from the load-CMOD curves at 0.5, 1.5, 2.5 and 3.5 mm of CMOD, respectively. However, these CMODs are suggested for concrete prisms of 500 mm span length. For this study, the residual stresses are calculated at CMOD equal to 1/5 of those used for 500 mm span specimens; i.e. 0.1, 0.3, 0.5 and 0.7.

Figure 2.10 shows the f_{Ri} values of all FCSA and FRSC mixes tested at different ages. The f_R values for FCSAs are shown in solid lines while FRSCs are shown in dashed lines. It is noticed that for both mixes the f_R values continue to increase from CMOD 0.1 mm to 0.7 mm which shows the high efficiency of the RCSF in carrying the loads across cracks. This is also evidenced by the multiple cracks that form in some samples at, or more than, seven days of age. The residual strengths of FCSA are higher than those of FRSC for the same crack width, which implies better bond strength for RCSF in FCSA matrices.

The f_R values continue to increase with time for both FRC mixes and reach their peak values at 28 days. However, there is a slight strength reduction at one year compared to 28 days. This could be attributed to the effect of the conversion reaction occurring in the RSC cement. This is unlikely, however, as there was no reduction in compression strength at one-year of age. Another possible explanation is the effect of shrinkage on the bond strength of RCSF. This reduction in f_R is more obvious at higher CMOD levels (for f_{R2} to f_{R4}), which means that the frictional resistance along the fibres reduces slightly at one year.

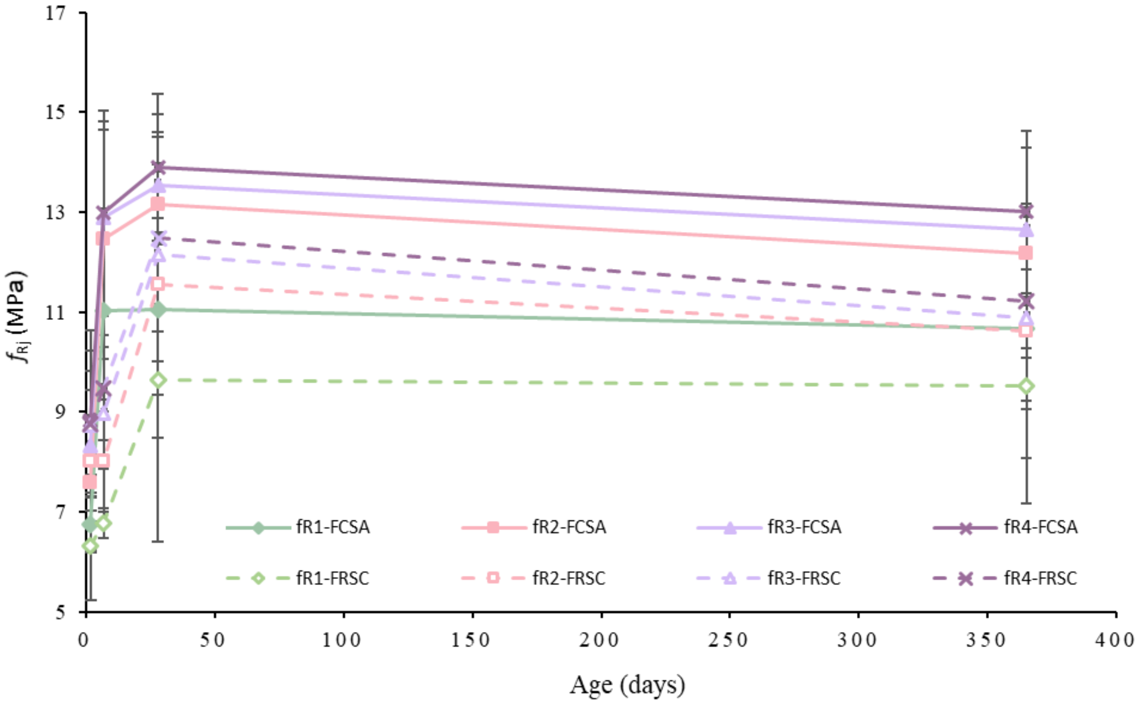

	FCSA				FRSC			
Time	—◆— fR1	—■— fR2	—▲— fR3	—✕— fR4	- ◇ - fR1	- □ - fR2	- △ - fR3	- ✕ - fR4
2	6.8 (0.6)	7.6 (1.8)	8.3 (0.4)	8.8 (1.6)	6.3 (1.1)	8.0 (0.3)	8.7 (3.2)	8.8 (2.3)
7	11.0 (0.6)	12.5 (2.2)	12.9 (0.8)	13.0 (2.1)	6.8 (1.8)	8.0 (1.0)	9.0 (3.1)	9.5 (2.5)
28	11.1 (0.6)	13.2 (1.9)	13.5 (1.0)	13.9 (2.0)	9.6 (1.9)	11.5 (1.1)	12.1 (2.8)	12.5 (1.7)
365	10.7 (0.6)	12.2 (2.1)	12.7 (1.5)	13.0 (1.6)	9.5 (1.5)	10.6 (1.1)	10.9 (2.5)	11.2 (0.9)

Figure 2.10. f_R values of FCSA and FRSC prisms (in MPa) development with age and standard deviation (given in brackets).

Figure 2.11 and Figure 2.12 show the relationship of f_{R1} vs f_{R2}, f_{R1} vs f_{R3} and f_{R1} vs f_{R4} for FCSA and FRSC, respectively. The values of f_{R2}, f_{R3} and f_{R4} correlate very well with f_{R1} for FCSA prisms with $R^2 \geq 0.98$. A similar trend was also found for FRSC prisms, however, with a relatively smaller coefficient of determination ($R^2 \geq 0.92$). A linear relationship between f_{R1} vs f_{R3}, f_{R1} vs f_{R4} were also reported by Zamanzadeh et al. [43] for unclassified RTSF. The strong correlation between the f_R values can lead to simpler design guidelines.

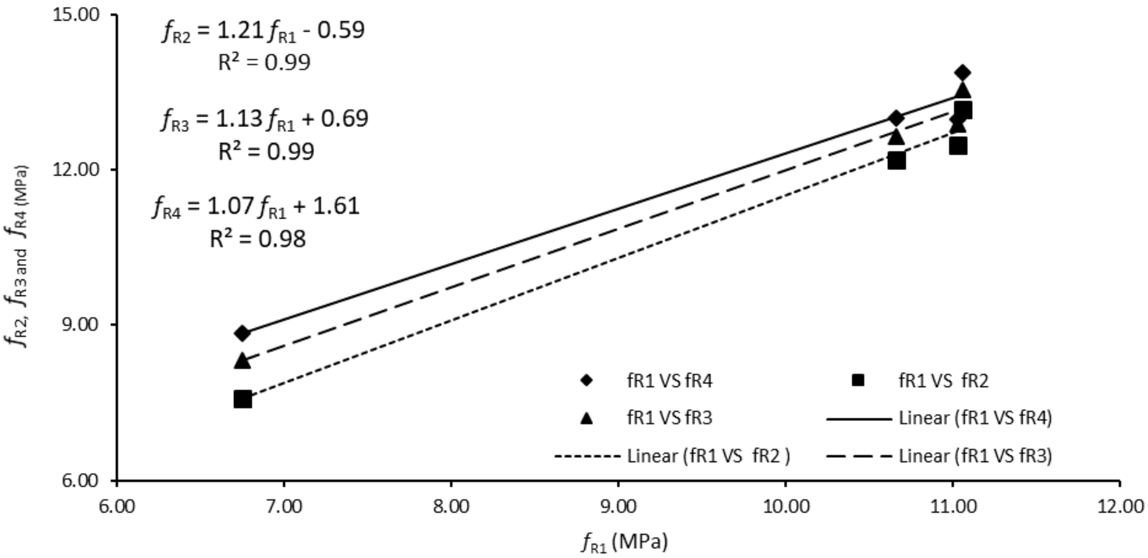

Figure 2.11. Correlation between f_{R1} *and* f_{R2}, f_{R1} *and* f_{R3}, f_{R1} *and* f_{R4} *of FCSA prisms*

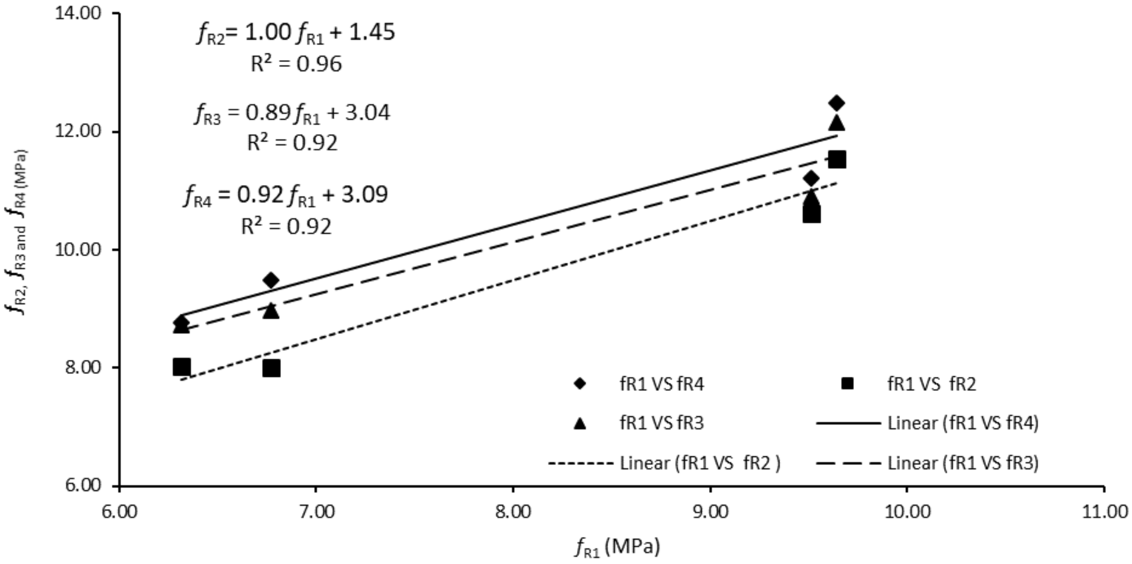

Figure 2.12. Correlation between f_{R1} *and* f_{R2}, f_{R1} *and* f_{R3}, f_{R1} *and* f_{R4} *of FRSC prisms*

Model code 2010 [18] suggests that if the value of $f_{R1}/f_L > 0.4$ and $f_{R3}/f_{R1} > 0.5$, then the fibre reinforcement can substitute (also partially) some of the required steel reinforcement. By looking at the results of this study, it can be seen that these requirements are fulfilled and, thus, the RCSF can be used to substitute some of the reinforcement in concrete structures.

2.4 Numerical study

2.4.1 FE modelling

To model the flexural performance of these materials, the FE package ABAQUS is used, which offers three material models for concrete simulation; Concrete Smeared Cracking (CSC), Brittle Cracking (BC) and Concrete Damaged Plasticity (CDP) [44]. It was found that, for this application, CSC is prone to numerical instabilities soon after crack development. Similar issues were also reported in [45] when modelling SFRC prisms using CSC. Although the BC model was applied successfully to model FRSC [46], it was considered unsuitable for the current study as it assumes that the concrete remains elastic in compression. Since, due to the high flexural strength of the mortars, in this study, the material is expected to become non-linear in compression. Therefore, the analysis was performed by using the concrete damage plasticity (CDP) model for which the user can define the tensile and compression behavior of concrete in as many steps as required. In CDP, the ratio of biaxial to uniaxial compressive strength (σ_{b0}/σ_{c0}) and the ratio of the second stress invariant on tensile meridian to that on the compressive meridian (K_c) characterise the failure surface of concrete. The dilation angle (ψ_0) and flow potential eccentricity (ε_0) are used to define the flow rule [44]. σ_{b0}/σ_{c0} was taken as 1.2 (slightly higher than the value usually assigned for plain concrete due to presence of fibres), K_c was 0.667, ψ_0 was 31° and after a sensitivity analysis for ε_0, the default value of 0.1 was adopted. The CDP model can be regularised by using viscoplasticity to assist in overcoming convergence issues, that occur in materials exhibiting softening behaviour in implicit analysis computations, by permitting the stress to be outside the yield surface. Since high values of viscosity (μ_0) compared to characteristic time increment can compromise the results, a value of zero was adopted.

Unnotched beams under 3-point bending were modelled in Abaqus with the same dimensions as tested. The mesh was kept constant at 10 mm size (two times the maximum aggregate size) (Figure 2.13) and a 3D 20-noded quadratic brick element with reduced integration (C3D20R) was chosen, as second-order elements are very effective in bending-dominated problems [44]. Uniform displacement control loading was applied to minimise convergence problems and to better simulate the experimental loading conditions.

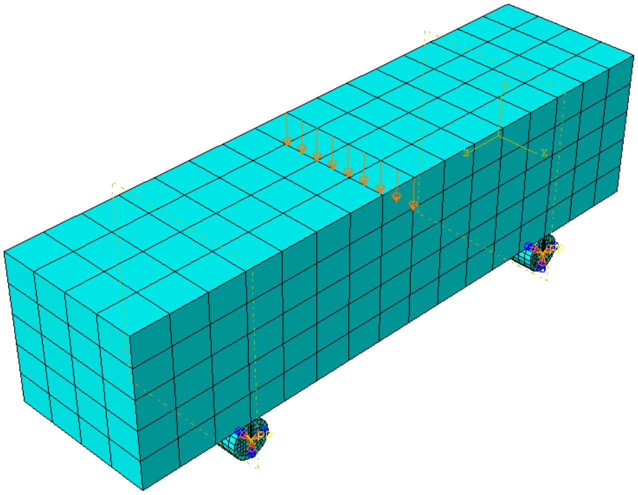

Figure 2.13. Prism assembly in Abaqus

2.4.2 Evaluation of tensile constitutive equations

RILEM TC 162-TDF (RILEM) [17], MODEL CODE 2010 (MC) [18], Barros et al. (Barros) [19] and Hu et al. (Hu) [20] procedures were selected to derive the tensile constitutive equations. Although MC allows the use of stress-crack width relationship, RILEM, Barros and Hu models all use stress-strain relationships, and since stress-crack width relationship also leads to mesh dependency in CDP, it was decided to the use stress-strain approach in modelling, to be able to make a direct comparison between different models. The derived tensile σ-ε relationships (see Table 2.3) using the aforementioned procedures were implemented in Abaqus to determine the load-deflection response of FCSA and FRSC prisms (at 28 days). MC requires the maximum value of crack width (w_u) to calculate the stress at ultimate strain. The value 0.5 mm was used for the max crack width as it corresponds to $CMOD_3$.

The predicted numerical load-deflection curves are compared against the experimental results for FCSA in Figure 2.14. It can be seen that all the approaches fail to model the full behaviour of the prisms and for most of them the analysis does not converge beyond 0.6 mm (even after using high values of μ_0). At 0.2 mm deflection, RILEM, MC and Barros overestimate the loading capacity by 29.44%, 16.65% and 7.11% while Hu underestimates the loading by 14.88% respectively. Barros's model, however, can capture the post-cracking behaviour of FCSA up to a certain extent. The models are even less effective in predicting the flexural behaviour of FRSC (see Figure 2.14). Overall, none of the above models seem to be able to capture the complete load-deflection behaviour of the tested specimens.

Table 2.3 σ-ε relationships for FCSA and FRSC at 28 days using different approaches

Mixes	*RILEM*		*MC*		*Barros*		*Hu*	
	σ	ε	σ	ε	σ	ε	σ	ε
FCSA	9.473	0	2.980	0	7.037	0	4.771	0
	4.977	0.000263	3.311	0.000030	3.981	0.001056	2.986	0.001892
	5.140	0.024814	4.977	0.002319	3.751	0.103864	3.929	0.024857
	0.095	0.025000	4.561	0.012335	0.080	0.104000	0.050	0.025000
	0.090	0.500000	0.030	0.012500	0.074	0.500000	0.048	0.500000
			0.029	0.500000				
FRSC	6.165	0	3.354	0	4.580	0	3.105	0
	4.340	0.00017	3.727	0.000006	3.472	0.001066	2.604	0.002019
	4.619	0.024822	4.340	0.002333	3.370	0.103870	3.523	0.024864
	0.070	0.025000	4.145	0.012340	0.050	0.104000	0.040	0.025000
	0.065	0.500000	0.040	0.012600	0.046	0.500000	0.035	0.500000
			0.035	0.500000				

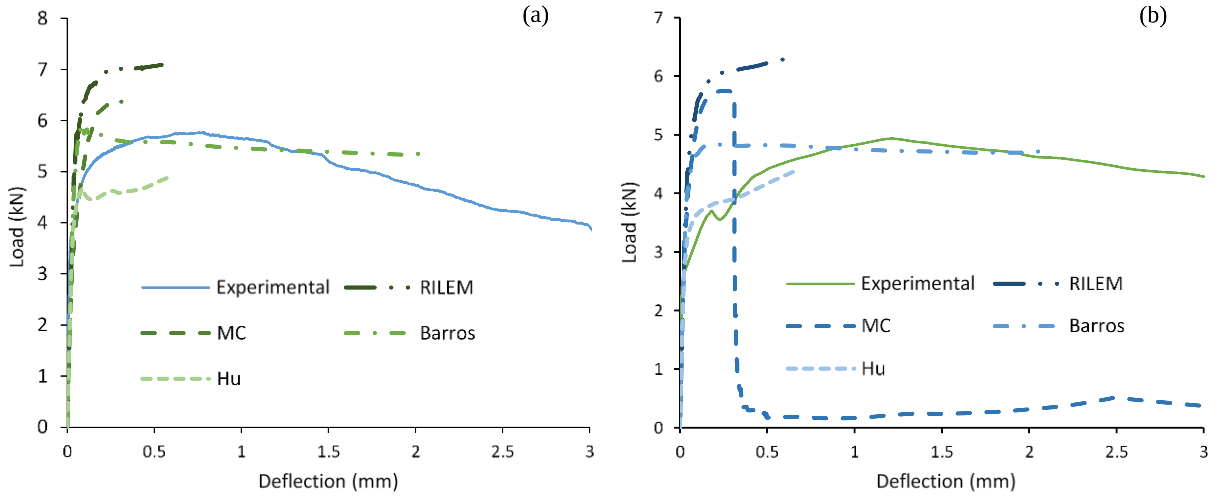

Figure 2.14. Comparison between experimental and numerical load-deflection curves at 28 days for: (a) FCSA; (b) FRSC

2.4.3 Numerical approach using inverse analysis

Inverse analysis was adopted to determine the post-cracking $\sigma - \varepsilon$ relationships for the different SFRC mixes and obtain a better prediction of the flexural performance of the tested specimens. The tensile properties are defined by using multilinear $\sigma - \varepsilon$ curves. The analysis is repeated while adjusting the tensile parameters until the numerical load-deflection curve matches the experimental response in capacity and energy dissipation within 2%.

The determined tensile $\sigma - \varepsilon$ curves shown in Figure 2.15 are then used to predict the structural behaviour of the FRC tested specimens. To better capture the flexural performance at larger displacements, the strain at failure should be accurately determined. The failure strain is calculated by dividing the ultimate width of crack (which is considered to be equal to half of the fibre length (l_f)) by the characteristic length. It was shown in a previous study on SFRC [45] that using a characteristic length of $h_{sp}/2$ (the depth of a notched prism divided by 2) gives good results when converting displacements into equivalent strains. Thus, for this study, a value of 0.5 was adopted as a strain failure which is fairly close to $l_f/2$ divided by half of the prism depth. It should be noted though that most tests were stopped at 5 mm deflection as not to damage the

LVDTs and thus, complete failure was never reached. For design purposes, a max strain of 0.025 is deemed sufficient so as to prevent the development of large crack widths.

The predicted curves are shown together with the experimental results in Figure 2.16 through Figure 2.16. As expected, the predictions match well the results.

The results for FCSA at 28 days was further analysed (using the same material model for the 10mm mesh size) with two mesh sizes; 16.6 mm and 5 mm to examine the effect of mesh size. The results (Figure 2.17) confirm that there is a slight mesh dependence when using this approach.

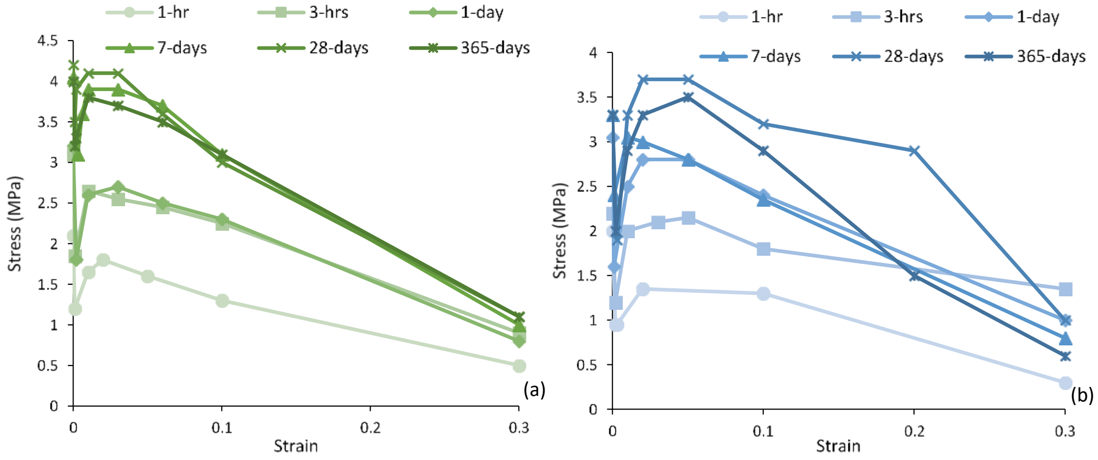

Figure 2.15. Tensile $\sigma - \varepsilon$ curves for mixes at different ages for: (a) FCSA; (b) FRSC

2.4.4 Cracking

In the CDP model, cracking can be assumed to initiate at points where the tensile equivalent plastic strain is greater than zero and the maximum principal plastic strain is positive. The direction of the vector normal to the crack plane is assumed to be parallel to the direction of the maximum principal plastic strain [44]. Figure 2.18 shows maximum principal strain contours for FCSA prism at 28 days. It is clear that the failure of the prisms is characterised by tensile cracking at the midspan of the beam as occurred in the experiments.

The crack width at the bottom of the specimens can be determined from the analysis by examining the spreading of the beam using the horizontal deformation (U_3) as shown in Figure 2.19. The crack width determined at 3 mm of deflection are compared with CMOD values measured by the clip gauge in Table 2.4. The predicted values are slightly lower than the experimental values with the biggest error of 14.66% (presented in brackets) for FCSA at 28 days. This confirms that the numerical models were not only successful in predicting the flexural capacity, but also the crack widths of the tested prisms and as a result, they could be used for further studies on repair layers.

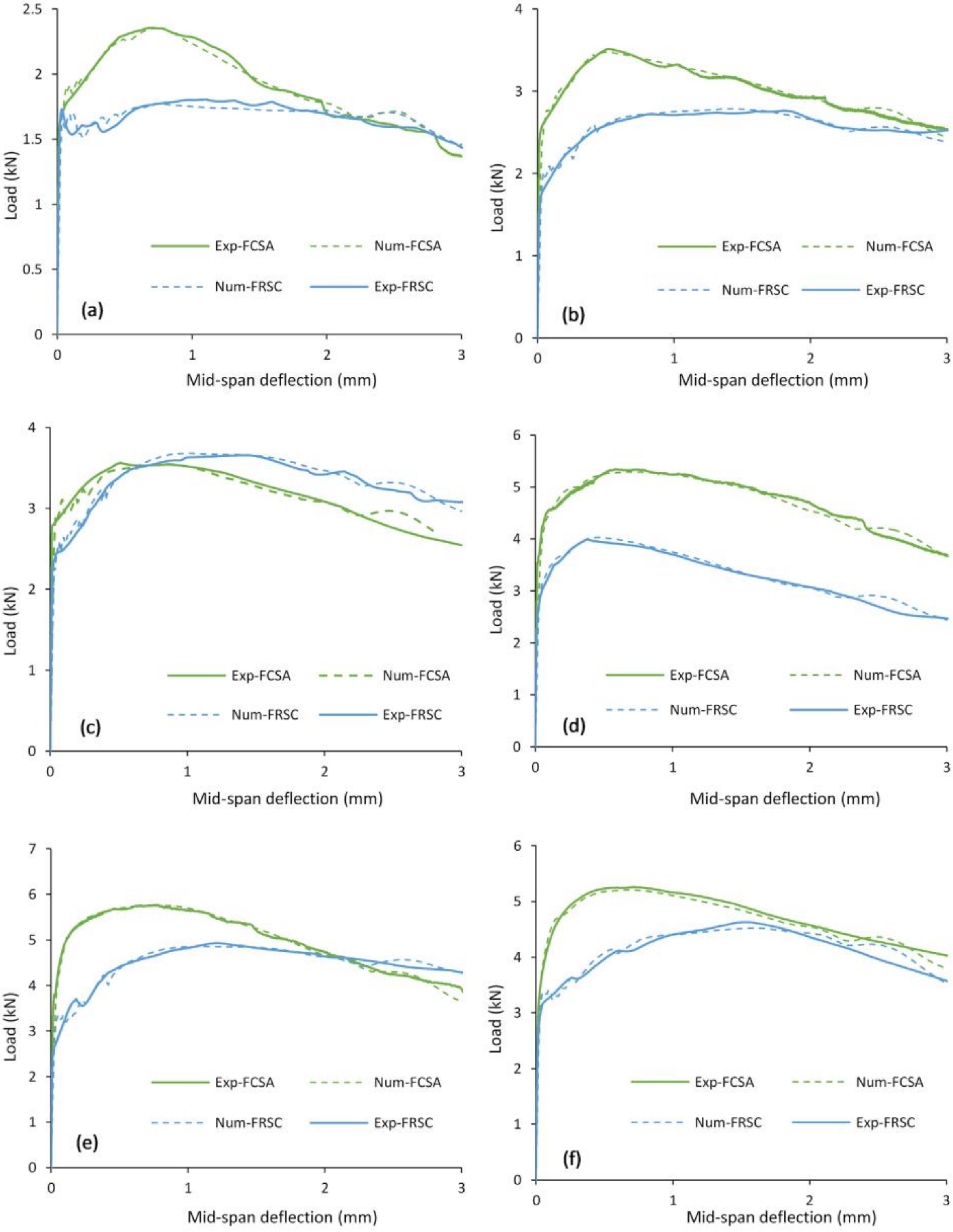

Figure 2.16. Experimental load-deflection versus numerical curves of FCSA and FRSC prisms at age of: (a) one-hour; (b) three hours; (c) one-day; (d) seven days; (e) 28 days; (f) 365 days

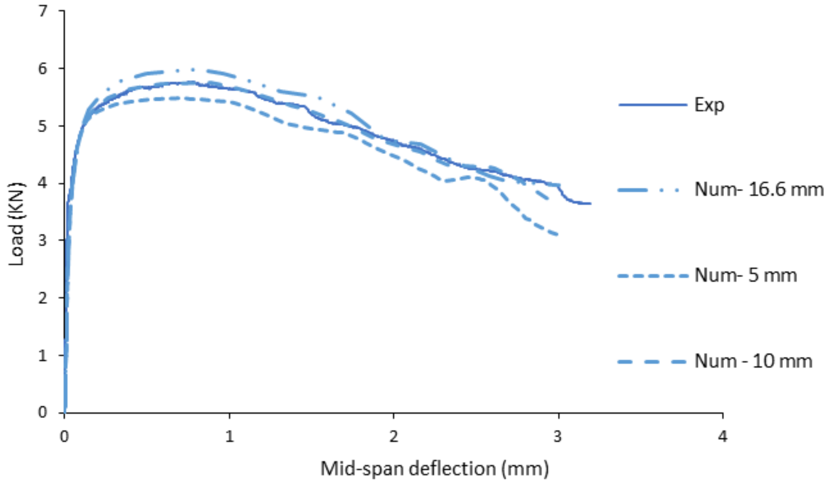

Figure 2.17. Experimental load-deflection curve of FCSA at 28 days versus numerical curves using three different mesh sizes

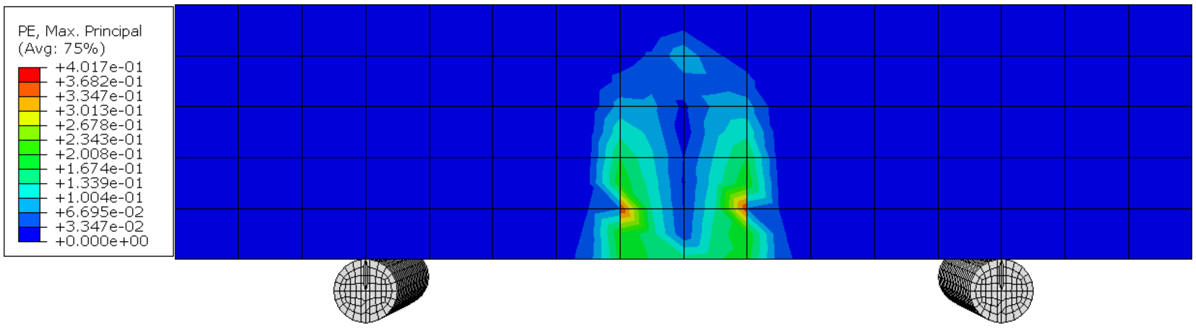

Figure 2.18. Max principal strain contour for FCSA prisms at 28 days at the end of analysis

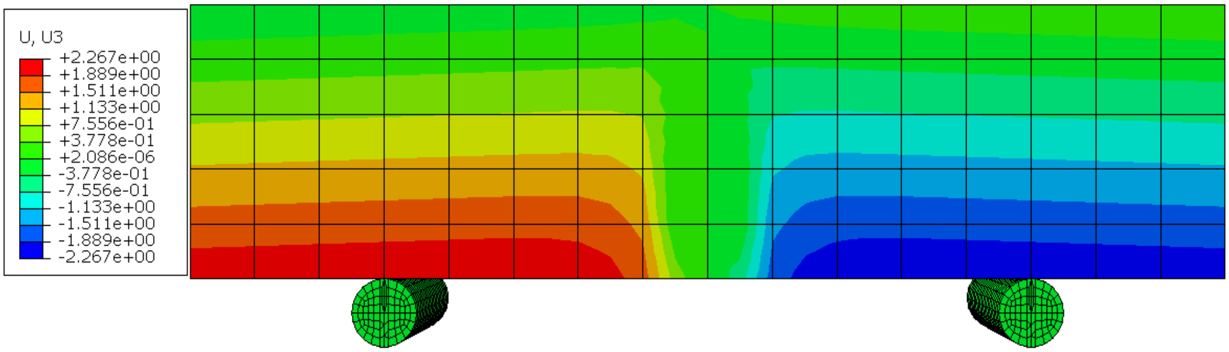

Figure 2.19. Horizontal displacement (U_3) contour for FCSA prisms at 28 days at the end of analysis

Table 2.4 The measured and predicted crack widths for fibre reinforced mixes

Mix	*Age*	*1hour*	*3 hours*	*1 day*	*7 days*	*28 days*	*365 days*
FCSA	*Numerical*	4.68 (4.10)	4.64 (5.60)	4.68 (5.45)	4.52 (8.87)	4.54 (14.66)	4.64 (9.02)
	Experimental	4.88	4.903	4.953	4.96	5.32	5.10
FRSC	*Numerical*	4.37 (12.07)	4.60 (8.18)	4.59 (9.82)	4.71 (9.25)	4.57 (12.45)	4.6 (13.21)
	Experimental	4.97	5.01	5.09	5.19	5.22	5.3

Note: Values in brackets represent the error (%) between experimental and numerical crack width

2.5 Conclusions

Experimental and numerical investigations were performed on plain and fibre reinforced rapid hardening mortars. The main findings of this study are:

- Flexural strength evolves rapidly and both plain and fibre reinforced specimens achieved 90% of their one-year strength in one day. The specimens made with CSA cement showed higher flexural strength than those made with RSC cement tested at the same age due to the rigid dense crystal microstructure of the CSA cement.
- For compressive strength, the highest strength increase of around 24% was observed at one hour. No compressive strength reduction was noticed for any of the mixes tested in this study up to the age of one-year.
- The flexural residual strength for both FCSA and FRSC specimens continued to increase up to 0.7 mm, which corresponds to $CMOD_4$. FCSA prisms show higher f_R than FRSC prisms for the same crack width. The values of f_R continue to increase with time for both FRC mixes and reach their peak values at 28 days. However, there is a slight strength reduction at one year compared to 28 days.
- Strong correlations exist between f_{R1} and f_{R2}, f_{R1} and f_{R3}, f_{R1} and f_{R4} with $R^2 \geq 0.98$ and $R^2 \geq 0.92$ for

FCSA and FRSC, respectively. They can facilitate developing $\sigma - \varepsilon$ design relationships.

- FE-predictions using CDP overestimate the loading capacity of FCSA and FRSC when using the tensile constitutive laws based on RILEM TC 162-TDF, CEB FIB MODEL CODE 2010, Barros et al. Conversely, the use of the models proposed by Hu et al. leads to underestimation.
- Inverse analysis was used successfully to obtain multilinear $\sigma - \varepsilon$ tensile curves and model the global load-displacement behaviour.
- Numerical analyses using the refined $\sigma - \varepsilon$ curves were successful in capturing the cracking widths of FRC tested prisms.

References

1. Winnefeld, F., Lothenbach, B., (2010). Hydration of calcium sulfoaluminate cements – experimental findings and thermodynamic modeling. *Cem. Concr. Res.*, 40(8), 1239–1247.
2. Ioannou, S., Paine, K., Quillin, K., (2010). Strength and durability of calcium sulfoaluminate based concretes. In International Conference on Non-Conventional Materials and Technologies: Ecological Materials and Technologies for Sustainable Building. University of Bath.
3. Scrivener, K., (2003). Calcium Aluminate Cement. In J. Newman, Advanced Concrete Technology. 2/1-2/29. Oxford: ButterworthHeinemann.
4. Campas, A., Scrivener, K. (1998). Calcium Aluminate Cements. In A. Campas, & K. Scrivener, Lea's Chemistry of Cement and Concrete, 709-771. Wobum: ButterworthHeinemann.
5. Banthia, N., Gupta, R., (2009). Plastic shrinkage cracking in cementitious repairs and overlays. *Mater. Struct.*, 42(5), 567–579.
6. Beushausen, H., Alexander, M.G., (2006). Failure mechanisms and tensile relaxation of bonded concrete overlays subjected to differential shrinkage. *Cem. Concr. Res.*, 36 (10), 1908-1914. Available at: https://www.sciencedirect.com/science/article/pii/S0008884606001608.
7. Beushausen, H., Chilwesa, M., (2013). Assessment and prediction of drying shrinkage cracking in bonded mortar overlays. *Cem. Concr. Res.*, 53, 256–266. Available at: http://dx.doi.org/10.1016/j.cemconres.2013.07.008.
8. Banthia, N., Zanotti, C. and Sappakittipakorn, M., (2014). Sustainable fibre reinforced concrete for repair applications. *Constr. Build. Mater.*, 67 (PART C), 405–412. Available at: http://dx.doi.org/10.1016/j.conbuildmat.2013.12.073.
9. Jewell, R., (2015). Influence of Calcium Sulfoaluminate Cement on the Pullout Performance of Reinforcing Fibres: An Evaluation of the Micro-Mechanical Behavior. PhD Thesis. University of Kentucky. Available at: http://uknowledge.uky.edu/ce_etds/27. [Accessed March 28, 2018].

10. Swamy, R.N., Stavrides, H., (1979). Influence of fiber reinforcement on restrained shrinkage and cracking. In *Journal Proceedings*. *ACI J.*, 76(3), 443-460.
11. Graeff, A.G., Pilakoutas, K., Neocleous, K., Peres, M.V.N.N., (2012). Fatigue resistance and cracking mechanism of concrete pavements reinforced with recycled steel fibres recovered from post-consumer tyres. *Eng. Struct.*, 45, 385–395. https://doi.org/10.1016/j.engstruct.2012.06.030.
12. Pilakoutas, K., Guadagnini, M., (2013). Re-use of steel cord from tyres as reinforcement in sustainable construction – TSB Proposal. The University of Sheffield, Sheffield.
13. Hu, H., Papastergiou, P., Angelakopoulos, H., Guadagnini, M., Pilakoutas, K., (2018). Mechanical properties of SFRC using blended recycled tyre steel cords and recycled tyre steel fibres, *Constr. Build. Mater*., 187, 553-564.
14. Frantzis, P., Baggott, R., (2000). Bond between reinforcing steel fibers and magnesium phosphate/calcium aluminate binders. *Cem. Concr. Compos*., 22, 187–192.
15. Frantzis, P., Baggott, R., (2003). Transition points in steel fiber pullout tests from magnesium phosphate and accelerated calcium aluminate binders. *Cem. Concr. Compos.*, 25, 11–17.
16. Frantzis, P., (2006). Effect of Early-Age Temperature Rise on the Stability of Rapid-Hardening Cement Fibre Composites. *J. Mater. Civil Eng*., 18, 568–575.
17. RILEM TC 162-TDF, (2003). σ-ε-design method, *Mater. Struct*., 36(8), 560–567. https://doi.org/10.1007/BF02480834.
18. F.I. du Béton, (2013). Fib Model Code for Concrete Structures 2010, Wilhelm Ernst & Sohn, Berlin, Germany.
19. Barros, J.A.O., Cunha, V.M.C.F., Ribeiro, A.F., Antune J.A.B., (2005). PostCracking Behaviour of Steel Fibre-Reinforced Concrete. *Mater. Struct*., 38, 47-56.
20. Hu, H., Wang, Z., Figueiredo, F., Papastergiou, P., Guadagnini, M., Pilakoutas, K., (2018). Post-cracking tensile behaviour of blended steel fibre reinforced concrete. *Struct. Concr*. Submitted for publication.
21. Neocleous, K., Tlemat, H., Pilakoutas, K., (2006). Design issues for concrete reinforced

with steel fibers, including fibers recovered from used tires. *J. Mater. Civ. Eng.*, 18(5), 677–685. https://doi.org/10.1061/(ASCE)0899-1561(2006).

22. American Concrete Institute (ACI), (2011). Building code requirements for structural concrete and commentary. (ACI 318M-11) Farmington Hills, MI.
23. Georgin, J.F., Ambroise, J., Péra, J., Reynouard, J.M., (2008). Development of self-leveling screed based on calcium sulfoaluminate cement: Modelling of curling due to drying. *Cem. Concr. Compos.*, 30(9), 769-778.
24. ASTM C191, (2013). Standard Test Method for Time of Setting of Hydraulic Cement by Vicat Needle. *ASTM International*, (May), 1-8.
25. RILEM, T.C., 119-TCE, (1997). Avoidance of thermal cracking in concrete at early ages. *Mater. Struct.*, 30 (202), 451-464.
26. BS EN 13892-2, (2002). Methods of test for screed materials — Part 2: Determination of flexural and compressive strength.
27. JSCE-SF4, (1984). Standard for Flexural Strength and Flexural Toughness, Method of Tests for Steel Fiber Reinforced Concrete, Concrete library of JSCE, Japan Concrete Institute (JCI), Japan.
28. Cost, T., (2008). Practical Semi-Adiabatic Calorimetry for Concrete Mixture Evaluation. In *TTCC/NCC Conference*.
29. Aiello, M.A., Leuzzi, F., Centonze, G., Maffezzoli, A., (2009). Use of steel fibres recovered from waste tyres as reinforcement in concrete: pull-out behaviour, compressive and flexural strength, *Waste Manage.*, 29, 1960–1970. https://doi.org/10.1016/j.wasman.2008.12.002.
30. Centonze, G., Leone, M., Aiello, M.A., (2012). Steel fibers from waste tires as reinforcement in concrete: a mechanical characterization. *Constr. Build. Mater.*, 36, 46–57. https://doi.org/10.1016/j.conbuildmat.2012.04.088.
31. Younis, K.H., Pilakoutas, K., (2013). Strength prediction model and methods for improving recycled aggregate concrete. *Constr. Build. Mater.*, 49, 688–701, https://doi.org/10.1016/j.conbuildmat.2013.09.003.

32. Bjegovic, D., Baricevic, A., Lakusic, S., Damjanovic, D., Duvnjak, I., (2013). Positive interaction of industrial and recycled steel fibres in fibre reinforced concrete, *J. Civ. Eng. Manage.*, 19, S50–S60. https://doi.org/10.3846/13923730.2013.802710.
33. Martinelli, E., Caggiano, A., Xargay, H., (2015). An experimental study on the postcracking behaviour of hybrid industrial/recycled steel fibre-reinforced concrete. *Constr. Build. Mater.*, 94, 290–298. https://doi.org/10.1016/j.conbuildmat.2015.07.007.
34. Hu, H., Papastergiou, P., Angelakopoulos, H., Guadagnini, M. and Pilakoutas, K., (2018). Mechanical properties of SFRC using blended manufactured and recycled tyre steel fibres. *Constr. Build. Mater.*, 163, 376-389. Available at: https://www.sciencedirect.com/science/article/pii/S0950061817325230.
35. Herrmann, P., (2014). Investigation of fresh and hardened properties of Calcium sulfoaluminate (CSA) cement blends. *Mag. Civ. Eng.*, (3), 63-70. Available at: http://www.engstroy.spb.ru/index_2014_03/07.pdf.
36. BS EN 14651, (2005). Test method for metallic fibre concrete – Measuring the flexural tensile strength (limit of proportionality (LOP), residual). British Standards Institution, London, UK.
37. Bordelon, A., (2011). *Flowable fibrous concrete for thin pavement inlays*. PhD Thesis. University of Illinois at Urbana-Champaign.
38. Younis, K.H., (2014). *Restrained Shrinkage Behaviour of Concrete with Recycled Materials*. PhD Thesis. University of Sheffield.
39. Jafarifar, N., (2012). *Shrinkage behaviour of steel fibre reinforced concrete pavements*. PhD Thesis. University of Sheffield.
40. Dawood, E.T., Ramli, M., (2011). High strength characteristics of cement mortar reinforced with hybrid fibres. *Constr. Build. Mater.*, 25 (5), 2240-2247.
41. Kosaka, Y., Takeshi, T., Ota, F., (1975). Effect of coarse aggregate on fracture behavior of concrete (part1). *J.A.C.*, 228, 1-11. Cited in Che, Y., (2010). *The development and behaviour of premix GRC suitable for mass produced structural elements*. PhD Thesis, Department of Civil and Structural Engineering, The University of Sheffield.

42. RILEM. (2002). RILEM TC 162-TDF: Test and design methods for steel fibre reinforced concrete - Bending test, final recommendation. *Mater. Struct.*, 35(253), 579–582.
43. Zamanzadeh, Z., Lourenço, L. and Barros, J., (2015). Recycled steel fibre reinforced concrete failing in bending and in shear. *Constr. Build. Mater.*, 85, 195–207. Available at: https://doi.org/10.1016/j.conbuildmat.2015.03.070.
44. ABAQUS 2017 Documentation, [Online].
45. Tlemat, H., (2004). *Steel fibres from waste tyres to concrete; testing, modelling and design*. PhD Thesis, Department of Civil and Structural Engineering, The University of Sheffield.
46. Mohsin, S.M.S., (2012). *Behaviour of fibre-reinforced concrete structures under seismic loading*. PhD Thesis. Imperial College London.

Chapter 3: Shrinkage properties of plain and recycled steel–fibre-reinforced rapid hardening mortars for repairs

Al-musawi, H., Figueiredo, F., Guadagnini, M., Pilakoutas, K., (2019). Shrinkage properties of plain and recycled steel–fibre-reinforced rapid hardening mortars for repairs. *Constr*. *Build*. *Mater*., 197, 369-384.

Abstract

This article investigates the time dependent transport properties and shrinkage performance of rapid hardening plain and fibre reinforced mortars for repair applications. Two plain and two SFRC mixes with 45 kg/m^3 of recycled clean steel fibers made with rapid hardening cements (CSA - calcium sulfoaluminate cement and RSC - calcium aluminate cement) are studied. It is found that mixes with CSA cement have much lower shrinkage values (around 220 and 365 microstrains) compared to mixes with RSC cement (around 2690 and 2530 microstrains), but most of the shrinkage in these mixes is autogenous. Nonetheless, fibres reduce the drying shrinkage of RSC cement mixes by approximately 12%. Model code 2010 and ACI equations can be used to estimate the shrinkage development with time for these mixes provided suitable parameters for each cement type are adopted. Inverse analysis using finite element method is successfully employed to determine the moisture diffusivity and the hygral contraction coefficient of each mix. A comparison is made between the values of shrinkage strain predicted by the numerical models over time, for different depths, and code equations. A simple analytical procedure is used to assess cracking and/or delamination risks due to restrained shrinkage for these materials in overlay applications.

This chapter consists of a "stand alone" journal paper and includes a relevant bibliography at the end of the chapter. Additional information and further test results are presented in Appendix B.

3.1 Introduction

Concrete overlays are extensively used in the repair and strengthening of concrete structures either to replace damaged concrete or directly cast as a new layer. In both applications, moisture from the fresh layer does not only diffuse to the environment, but also to the concrete substrate, resulting in faster drying shrinkage. Shrinkage is restrained by the substrate layer leading to tensile and interfacial shear stresses in the repair layer. These stresses, if they exceed material capacity, can lead to cracking and/or debonding, accelerating the deterioration of the repairs [1]. The cracking potential of repairs increases in rapid hardening materials that are often used to minimise disruption during repair works, due to faster shrinkage rate [2] and lower creep compliance [3].

Although fibres are reported to have a marginal effect in preventing shrinkage strains from developing in concrete, they are used to control crack widths [4] as well as increase tensile strength and fatigue resistance [5] in an attempt to achieve more durable repair layers. To reduce the environmental impact of manufactured steel fibres (MSF), recycled clean steel fibres can also be used as alternative fibre reinforcement [6, 7].

Recycled clean steel fibres (RCSF) were obtained by recycling steel fibre cords, left over from the manufacture of tyres. As a result, they have a consistent length as opposed to recycled tyre steel fibres (RTSF) which are extracted mechanically from post-consumer tyres and, thus, have more variable lengths.

Since crack width is one of the main parameters that governs the durability of repairs [8], a thorough understanding of the effect of moisture movement and restraint from the substrate is needed to predict crack development in concrete, a material which has widely varied and dynamic porosity systems [9]. The moisture transport mechanism of cementitious mixes is complex and is the subject of extensive research [9-17]. FRC mixes, however, have been studied to a lesser extent [15, 18]. It is known that w/c ratio, cement content and cement type, directly affect moisture diffusion. Fibres may also affect the moisture transport properties of concrete by changing the porosity structure and thus their effect needs to be better understood.

Silfwerbrand [19] provided an analytical procedure to calculate the tensile and shear stresses that develop in overlaid concrete layers and determine the risk of cracking and/or delamination. However, this procedure does not calculate cracking widths, a vital aspect in predicting concrete performance. Eurocode 2 (EC) [20], Model Code 2010 (MC) [21] and ACI 209.2R-08 (ACI) [22] provide procedures to predict shrinkage strain evolution for concrete structures of certain cement types with good accuracy. However, they do not account for rapid hardening cements for which often little information is provided by manufacturers other than setting time and strength. They also do not consider the effect of fibres on concrete shrinkage strain in the predictive equations.

This paper presents a detailed investigation on the time dependent transport properties and shrinkage performance of rapid hardening plain and fibre reinforced mortars for repair applications. It starts by reviewing the factors involved in diffusion and shrinkage of both plain and FRC mixes. It then presents experimental work on moisture movement and shrinkage. The results are used in inverse analysis to determine the moisture diffusion coefficient, surface factor and shrinkage hygral coefficient which are needed to predict shrinkage performance. The available code procedures to predict the shrinkage of these mixes over time are also evaluated and new factors for each cement type are proposed. The Silfwerbrand procedure is then used to determine cracking and delamination risks.

This chapter addresses objectives 3-6 and 11 of the thesis.

3.2 Moisture diffusion and shrinkage

Moisture movement during drying of concrete is characterised by two stages; a constant drying rate stage which is succeeded by a falling drying rate [12, 15, 23], depending on the degree of continuity between liquid and vapour phases and on driving force variations [16]. At the beginning of drying, the evaporation rate is constant and is approximately equal to the rate of evaporation of water exposed to the same conditions

[24-25]. As the cementitious material is fully saturated, there is no hydraulic potential gradient to drive the moisture movement inside the porous medium and the internal vapour pressure is equivalent to the saturated vapour pressure. However, at the boundary layer, there is a pressure variation from saturated vapour pressure to ambient vapour pressure, driving moisture out to the surrounding air. Moisture evaporation at the surface causes a slight reduction in vapour pressure [16]. This small vapour pressure gradient is sufficient to cause moisture flow towards the surface, since at this stage the hydraulic diffusivity is high [26]. As drying continues, moisture decreases inside the material. Drying is still considered to be in stage one as long as the capillary system is saturated. When the liquid phase becomes discontinuous upon further drying, a transition from stage one to stage two takes place, at which diffusion of water vapour becomes the dominant mechanism for moisture transport [26]. During this stage, the evaporation rate drops, as moisture is only limited to movement of water vapour rather than liquid water diffusion [27] as is the case in the first stage, and the vapour pressure falls below the saturation vapour pressure value. The moisture content continues to decrease until vapour pressure reaches ambient level. Figure 3.1 shows a typical cumulative moisture loss and evaporation rate during stage one and stage two for a cement paste sample [15]. It is shown that during stage one, the drying behaviour is independent of capillary microstructure [26]. In a study performed by Bakhashi & Mobasher [15] to investigate the effect of curing time on the diffusion characteristics of cement paste, it was found that the moisture loss was substantially reduced by curing the cement paste for 24 hours and the transition from stage one to stage two took place quicker compared to non-cured samples. This can be attributed to microstructural and pore distribution changes with additional hydration. It can be argued that for fast setting materials, stage one is expected to be much shorter than for conventional mortar, as most hydration takes place during the first few hours and phase transition happens faster. This will be investigated in this paper to understand the role of cement type on diffusion properties.

Fick’s second law (Equation 3.1) can be used to model moisture movement in concrete for various stages of drying, with a moisture diffusivity that represents liquid and vapour diffusion [16].

$$\frac{\partial C}{\partial t} = D\frac{\partial^2 C}{\partial X^2}$$ *Equation 3.1*

where, C is the moisture concentration (kg/m^3), D is the moisture diffusion coefficient (m^2/s) and t is time (s).

As the moisture transfer equations are analogous to heat transfer equations and heat transfer analysis is readily available in FEA packages, this analogy is often exploited for moisture transfer studies [16, 18, 28].

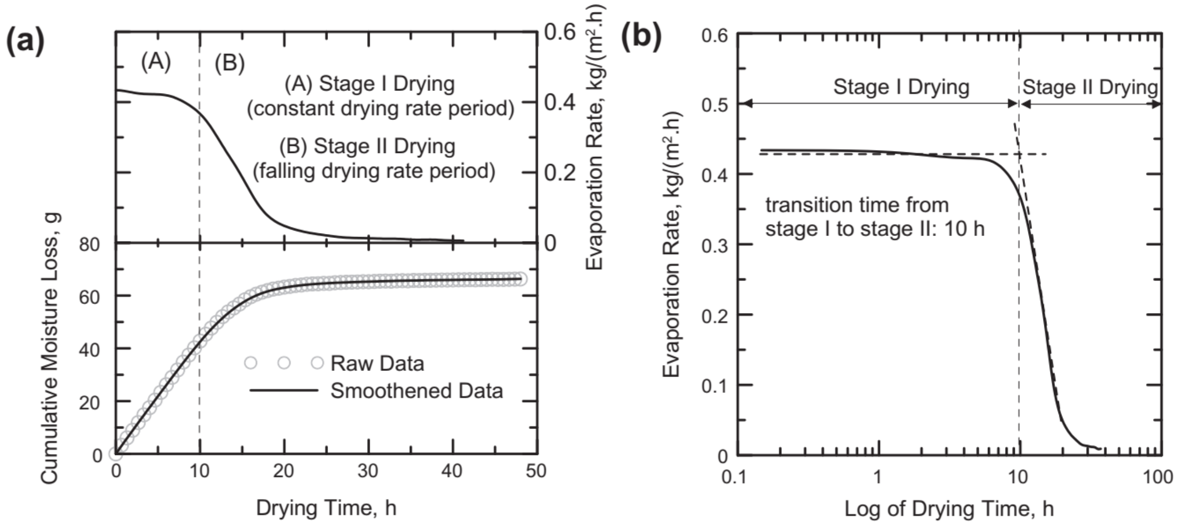

Figure 3.1. Typical cumulative moisture loss and evaporation rate of a cement paste sample versus time: (a) in linear scale; (b) in log scale [15]

Another important factor in moisture distribution problems is the surface factor or convective factor (f). This factor determines the moisture exchange between the concrete surface and the atmosphere. It depends on several other factors like the w/c ratio [11] and wind speed [29]. A wide range of surface factors is reported in literature [(0.75-7.5 mm/day [11]), 18, 29]. However, this parameter can be determined by inverse analysis for specific mortar mixes to improve the accuracy of the predicted moisture distribution.

The hydro-shrinkage coefficient (also called hygral contraction coefficient) is a factor that links free shrinkage strain to moisture content. It is a unique material property for each mix type. An exponential relationship was found by Ayano and Wittmann [13] while Huang et al. [28] used a linear relationship to simulate non-linear shrinkage in box girders. This factor can also be obtained through inverse analysis.

3.3 Experimental program

3.3.1 Mix proportions

Two plain and two SFRC mixes with 45 kg/m^3 (V_f = 0.57%) of recycled clean steel fibres (RCSF) were investigated in this study, details of which are given in Table 3.1. Two commercial cement types were used: calcium sulfoaluminate cement (CSA); and rapid setting calcium aluminate cement (RSC). River washed sand (0-5mm, SG=2.65) was used as fine aggregates. The length of the RCSF used in this study is 21 mm and the diameter is 0.2 mm. Further details on the mixes and material characteristics are given elsewhere [6].

Table 3.1 Mix proportions

Mix	Cement (kg/m^3)	w/c	SP^a	Sand (kg/m^3)	Fibre dosage (kg/m^3)
CSA	600	0.40	0.6	1420	0
FCSA	600	0.41	0.61	1420	45
RSC	600	0.35	0.2	1300	0
FRSC	600	0.36	0.21	1300	45

% by cement mass.

3.3.2 Flexural and Compressive strength

To characterize the flexural performance, mortar prisms of 40*40*160 mm were tested according to BS EN 13892-2, (2002) [30] in displacement control to better capture the post-peak behaviour. A specially designed aluminum yoke (based on the Japanese standard JSCE-SF4 [31]) was mounted on the specimens. The prisms were tested at different ages ranging from one hour up to one year to assess the flexural behaviour over time. After flexural testing, the two parts of the fractured prisms were tested under uniaxial compressive loading according to BS EN 13892-2, (2002) [30]. The results in terms of first cracking strength ($f_{ctm,fl}$) and compressive strength (f_{cu}) (associated standard deviation is given in brackets) are shown in Table 3.2.

Table 3.2 Flexural strength ($f_{ctm,fl}$) and compressive strength (f_{cu}) for all mixes (MPa)

Time (Days)	*FCSA*		*FRSC*		*CSA*		*RSC*	
	$f_{ctm,fl}$	f_{cu}	$f_{ctm,fl}$	f_{cu}	$f_{ctm,fl}$	f_{cu}	$f_{ctm,fl}$	f_{cu}
(1hr) 0.0417	3.52	26.13 (4.61)	3.52	21.3 (3.04)	2.58	21.14 (2.96)	2.53	17.23 (1.92)
(3hrs) 0.125	6.76	31.55 (3.69)	3.54	28.29 (3.54)	3.98	26.92 (2.78)	2.86	24.16 (2.04)
1	6.46	36.60 (2.27)	4.98	37.92 (2.40)	4.34	31.75 (2.51)	3.54	33.01 (2.00)
7	8.18	41.05 (3.27)	5.54	46.16 (3.20)	5.30	35.97 (3.02)	4.22	40.38 (2.43)
28	8.67	43.13 (3.23)	5.65	51.52 (2.88)	5.37	38.62 (2.30)	4.39	46.51 (2.61)
365	8.67	45.47 (3.03)	5.63	54.49 (6.64)	5.40	40.90 (2.27)	4.48	48.09 (3.74)

3.3.3 Moisture measurement in mortars

To obtain the time history of the moisture profile, needed to obtain the moisture diffusivity of the repair layers, the modified gravimetric method was adopted following the approach of Jafarifar [18]. It involves casting all specimens at the same height and then cutting them at different depths before putting them back together. Thus, the boundary condition from the underlying depth of the concrete specimens is preserved by keeping both segments in contact for the duration of the measurements.

The specimens were cast in 200*50*50 mm steel moulds. After around the expected setting time, water was added to the samples, while still in the moulds and they were covered with plastic sheets to prevent moisture evaporation. The setting time of cement pastes was assessed by the authors [6] using an automatic Vicat apparatus according to ASTM C191 (2013) [32]. The final setting time for CSA, FCSA, RSC and FRSC were 10.5, 11, 14.5 and 15 minutes. After around 40 minutes of curing, the samples were demoulded. Each prism was then immediately sliced into two segments at the prescribed depths of 10, 20, 30 mm, under wet conditions. Their weights were recorded, and the specimens were directly wrapped with cling film and sealed using a high performance ply laminated plastic foil tape. The surfaces 1-5 for the bottom segment and 1-4 for the upper part of the sliced specimens were sealed separately (Figure 3.2), creating one dimensional drying conditions.

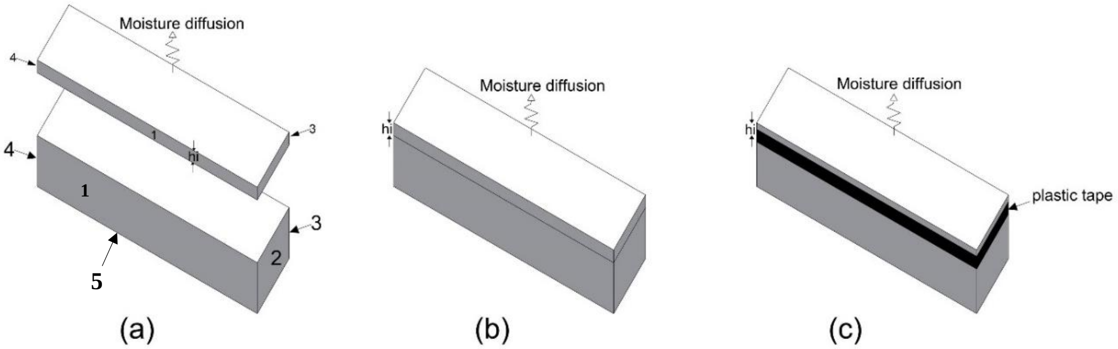

Figure 3.2. Sealing specimens for the modified gravimetric method

After each weight measurement, the two segments were assembled back together (Figure 3.2) and the joint was sealed using a new plastic tape (Figure 3.2). The weight measurements were taken at one hour and a half, three hours, one day and every day for one week. They were then recorded every week for one month and monthly for four months. After four months, the specimens were unwrapped and dried in the oven for ten days at 70 C^0. After that, the two parts of each prism were weighed. The details of how to determine the moisture content at each depth over time are given in [11,18].

3.3.4 Free shrinkage measurement

The ASTM C157/C157M (2008) standard [33] for measuring shrinkage of mortars adopts prisms of dimension of 25*25*285 mm. However, due to the use of fibres with a length of 21 mm and to minimize the boundary effects, it was decided to use bigger prisms of 40*40*160 mm instead. As for the specimens used for moisture transport studies, the specimens were cured for around 40 minutes in the moulds. After the curing, the specimens were demolded and demec points were attached to them. The total number of shrinkage samples for each mix was six prisms. Three prisms were kept in an environmental chamber with a relative humidity of 40±3% and temperature of 21±2 C^0 to measure the total shrinkage while the other three prisms were wrapped in cling film and left in a mist room to measure their autogenous shrinkage. After that, they were only unwrapped to take measurements. Shrinkage was measured on both faces of each prism using a 100 mm Demec gauge. The shrinkage measurements started at one hour and a half and continued at frequent time intervals up to 120 days.

3.4 Experimental results and discussion

3.4.1 Moisture measurements

The time history of moisture content for each mix is shown in Figure 3.3 (the moisture content at actual depths rather than prescribed depths are shown in this Figure). Each curve represents the mean value of two samples. The results confirm that drying is non-uniform across the depth of the specimens with faster drying at the top. For all the mixes, the water content of the upper layer ranges between 0.59 – 0.62 compared with 0.67 – 0.78 for the lower layers.

At the beginning of drying, the rate of drying is relatively faster for RSC and FRSC mixes compared to specimens with CSA and FCSA mixes. However, the rate of drying slows down towards the end of the drying period. The experimental moisture profiles are used in the following section to back calculate moisture diffusivity and surface factor for each mix.

Although literature states that fibres may affect the moisture transport properties of concrete, in this article, however, the fibres inclusion was confirmed not to have a major role on the moisture transport properties of rapid hardening mortar mixes, which allows the use of the MC equation [21], that is usually used to estimate the moisture diffusivity of plain concrete, to calculate their moisture diffusivities.

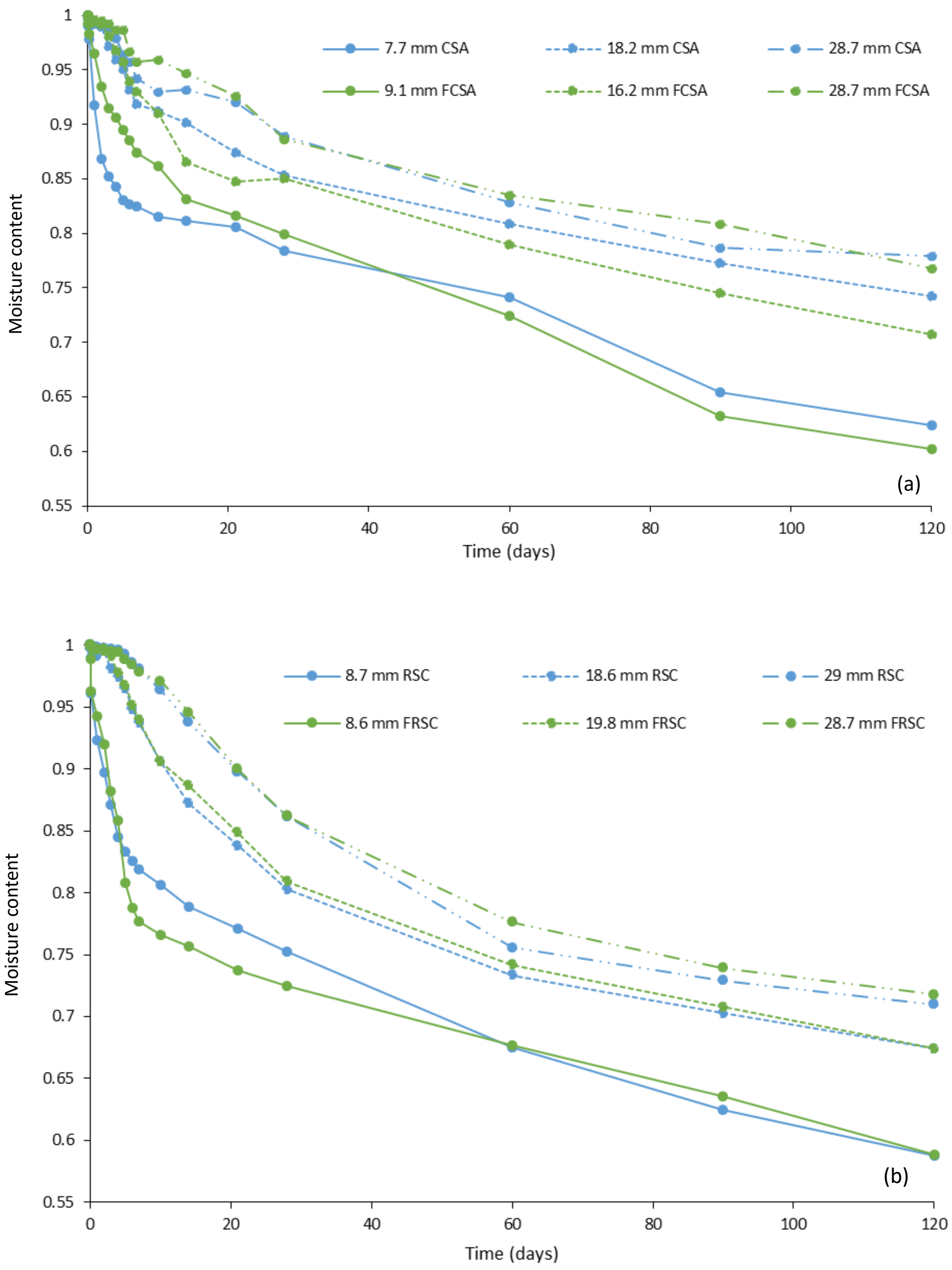

Figure 3.3. Experimentally measured change of moisture overtime: (a) CSA and FCSA mixes; (b) RSC and FRSC mixes

3.4.2 Free shrinkage results

The shrinkage evolution with time for all mixes is shown in Figure 3.4. Although a direct comparison between the shrinkage of CSA and RSC mixes is not possible due to differences in w/c ratio, superplasticizer dosage and aggregate content, the substantial difference in their shrinkage values can mainly be attributed to the different cement types. As expected, mixes with CSA cement showed much lower shrinkage strains than mixes with RSC cement. This is due to the expansive nature of their hydration products [34] and their higher water consumption during hydration [35]. For RSC cement, the reaction of its main component, monocalcium aluminate (CA), with water results in CAH_{10} and C_2AH_8 as the main hydration products as Equation 3.2 in Equation 3.3 and [2]:

$$CA + 10H \rightarrow CAH_{10}$$ *Equation 3.2*

$$2CA + 16H \rightarrow C_2AH_8 + AH_3$$ *Equation 3.3*

The subsequent conversion reactions of the metastable phases to the stable phases are:

$$2CAH_{10} \rightarrow C_2AH_8 + AH_3 + 9H$$ *Equation 3.4*

$$3C_2AH_8 \rightarrow 2C_3AH_6 + AH_3 + 9H$$ *Equation 3.5*

While for CSA cement, the main crystalline hydration products (ettringite and monosulfate) require more water to form as per Equation 3.6 and Equation 3.7 [35]:

$$C_4A_3S + 18H \rightarrow C_3A.CS.12H + 2AH_3$$ *Equation 3.6* *(monosulfate formation)*

$$C_4A_3S + 2CSH_2 + 34H \rightarrow C_3A.3CS.32H + 2AH_3$$ *Equation 3.7* *(ettringite formation)*

If less free water is available for drying, then less drying shrinkage can occur.

FCSA develops higher shrinkage strains compared to CSA at all ages. It is known that fibre inclusion introduces air in the mix [18, 36]. Also, the water content and SP dosage are higher for FCSA compared to CSA mix which can contribute to the higher recorded shrinkage values.

The provisions of EC, MC and ACI code were followed to obtain the shrinkage development of CSA and FCSA mixes with time. Both EC and MC require defining parameters αds_1 and αds_2 which depend on cement type. For the cements used, these parameters were obtained by nonlinear regression analysis. The ACI requires defining the ultimate shrinkage strain ε_{shu}. This value was obtained by multiplying the cumulative product of the correction parameters (γ_{sh}, as defined in [22]) by a factor P_s, obtained by non-linear regression analysis. The predicted and experimental free shrinkage strain for CSA and FCSA are given in Figure 3.5. As shown, the codes can predict the shrinkage evolution of these mixes reasonably well provided suitable parameters for cement type are used.

The autogenous shrinkage strains obtained for both CSA and FCSA sealed specimens were very small which indicates that some expansive reactions took place and, hence, not shown in Figure 3.4. On the other hand, both RSC and FRSC mixes showed considerable autogenous shrinkage, 1644 με and 1722 με at the age of 60 days respectively, which accounts for about 64 % and 71% of their total shrinkage at this age, respectively. Mixes with RSC cement has higher compressive strength compared to CSA cement mixes. Autogenous shrinkage is known to be directly related to compressive strength. In addition to, RSC has higher cement fineness that can increase the shrinkage [37]. High autogenous shrinkage can also be attributed to conversion of RSC cement. Nevertheless, no compressive strength reduction was noticed for RSC and FRSC specimens stored in the same conditions [6].

By examining further the RSC and FRSC results, it can be seen that drying shrinkage cannot be obtained by simply deducting autogenous shrinkage from the total shrinkage as the autogenous shrinkage continues at a faster rate than drying, possibly because drying affects the nature of the hydration reactions [38]. Therefore, less autogenous shrinkage develops in drying samples. Thus, an alternative method is needed to derive the drying shrinkage. MC relates the autogenous shrinkage (shr_{Auto}) to the compressive strength at 28 days and to the type of cement. As the hydration reactions directly affect the strength development, these methods can be used to predict Shr_{Auto} for RSC and FRSC using the compressive strength of the sealed specimens, provided that αbs (a factor that is a function of cement type) is accurately calculated. The resulting shr_{Auto} for RSC and FRSC, following the MC approach and regression analysis is shown in Figure

3.6. The optimised *αbs* along with the compressive strength at 28 days of drying samples were used to predict the autogenous shrinkage component from the total shrinkage strain. FRSC has slightly higher autogenous shrinkage (4.79 %) than RSC prisms, likely due to its higher compressive strength.

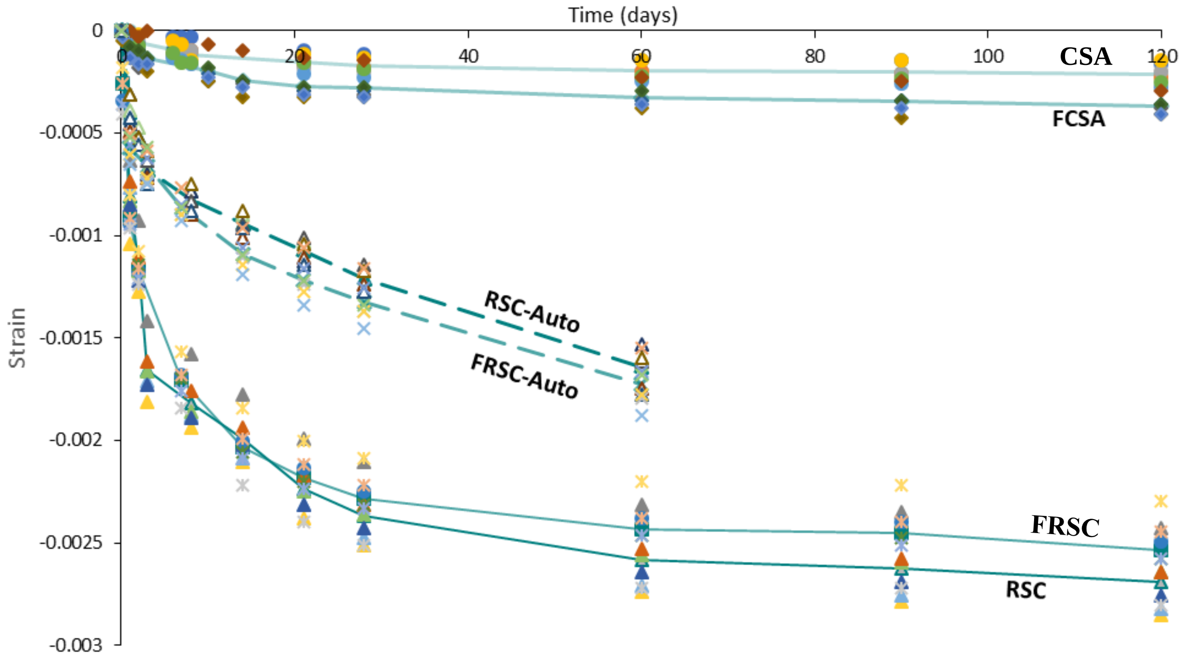

Figure 3.4. Experimental shrinkage development for all mixes with time

The drying shrinkage is obtained by subtracting shr_{Auto} from the total strain. The MC was also used to predict the drying shrinkage by assigning suitable αds1 and αds2 for RSC and FRSC, see Figure 3.7. Although the ACI code does not consider separate components of shrinkage, it can also be used to predict the total shrinkage (Figure 3.7). The shrinkage parameters used to estimate shrinkage for each mix based on the different codes are listed in Table 3.3.

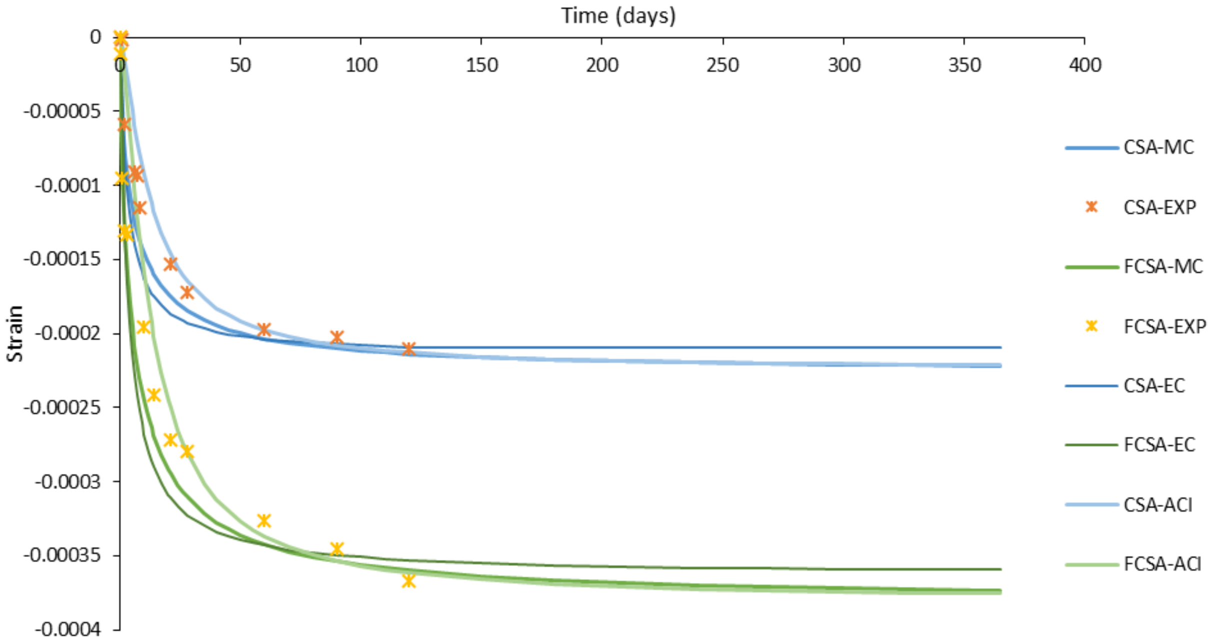

Figure 3.5. Experimental shrinkage of CSA and FCSA prisms and their predicted values based on MC, EC and ACI code

Table 3.3 Shrinkage parameters for various mixes

Mixes	*Codes*					
	MC		*EC*		*ACI*	
	αds_1	αds_2	αds_1	αds_2	P_s	α_1
CSA	0.1	0.012	0.29	0.11	108	1.32
FCSA	1.7	0.012	0.77	0.009	180	1.32

Mixes	*Codes*				
	MC			*ACI*	
	Shr_{Auto}	Shr_{Dry}		Shr_{Total}	
	αbs	αds_1	αds_2	P_s	α_1
RSC	17900	7	0.004	1320	1.65
FRSC	16780	5	0.004	1260	1.63

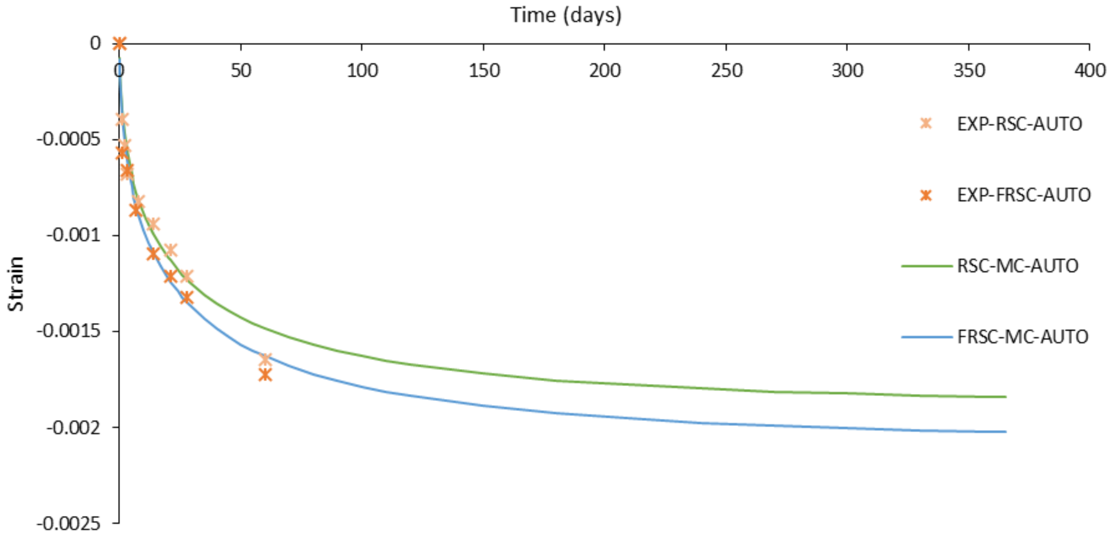

Figure 3.6. Experimental and predicted MC autogenous shrinkage of RSC and FRSC

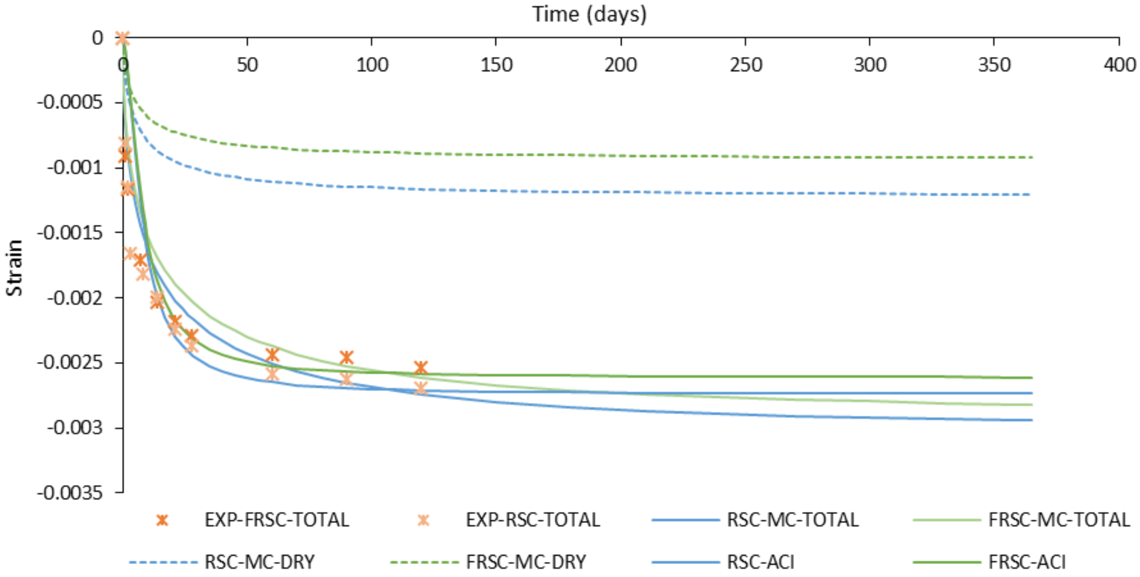

Figure 3.7. Experimental and predicted total and drying shrinkage of RSC and FRSC

It is interesting to note that the drying shrinkage of FRSC prisms seems to be smaller than RSC by around 12.6 % at the age of 365 days. This may be due to the fibre restraining effect. However, it should be noted that there is no consensus in the literature about the role of fibres on the free shrinkage strain.

3.4.3 Relationship between water loss and shrinkage

During the period of shrinkage monitoring, the weight of the prisms was recorded periodically. Figure 3.8 shows the relationship between water loss percent (W) and shrinkage for CSA and FCSA and RSC and FRSC respectively. It is clear that all mixes have a linear relationship between shrinkage and water content loss with strong correlations, although, as expected, with different multipliers.

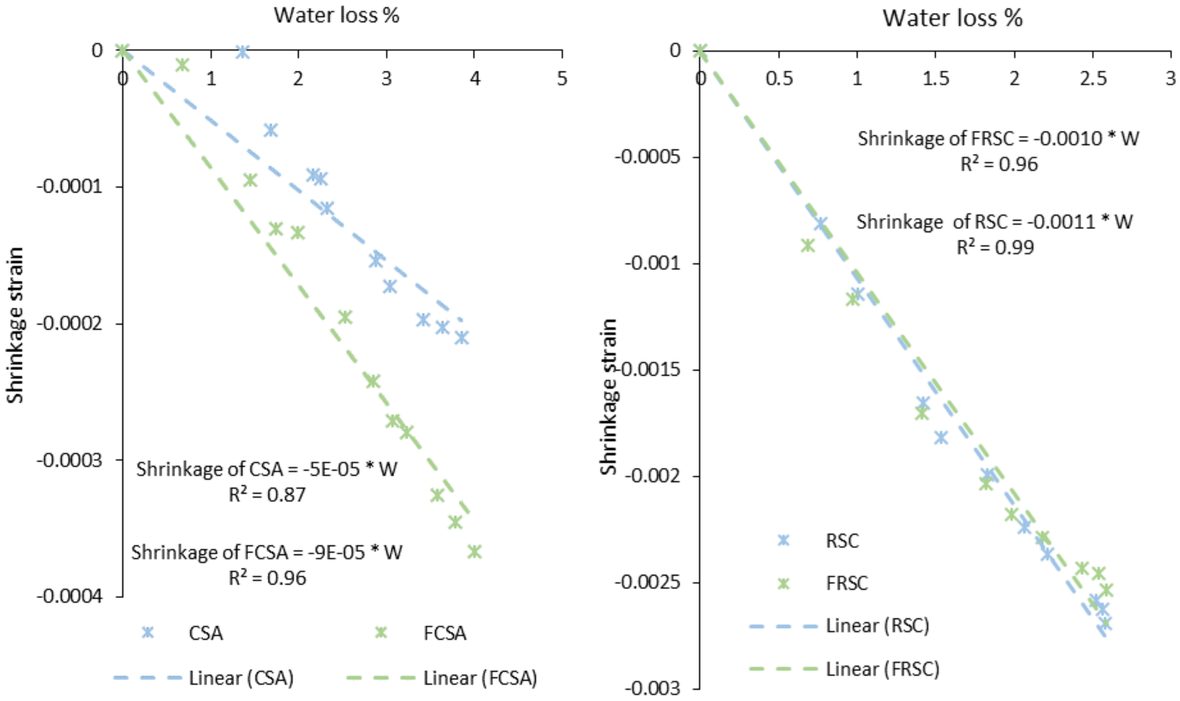

Figure 3.8. Experimental shrinkage versus measured water loss percent for: (a) CSA and FCSA; (b) RSC and FRSC prisms

Such linearity was also reported in [36] for concrete reinforced with post-consumer recycled steel fibres. In general, CSA and FCSA have more water loss than RSC and FRSC as they have higher initial water content (w/c = 0.4, 0.41 for CSA and FCSA respectively). The relationship also clearly highlights the effect of cement type on the shrinkage behaviour of the mixes. For example, for a 2.5 % water loss, the equivalent shrinkage for the mixes is 0.000125, 0.000225, 0.00275 and 0.0025 for CSA, FCSA, RSC and FRSC respectively. The water loss is also plotted against the calculated drying shrinkage for RSC and FRSC specimens (Figure 3.9). This relationship is essential when introducing shrinkage in FE modeling through the hygral contraction coefficient.

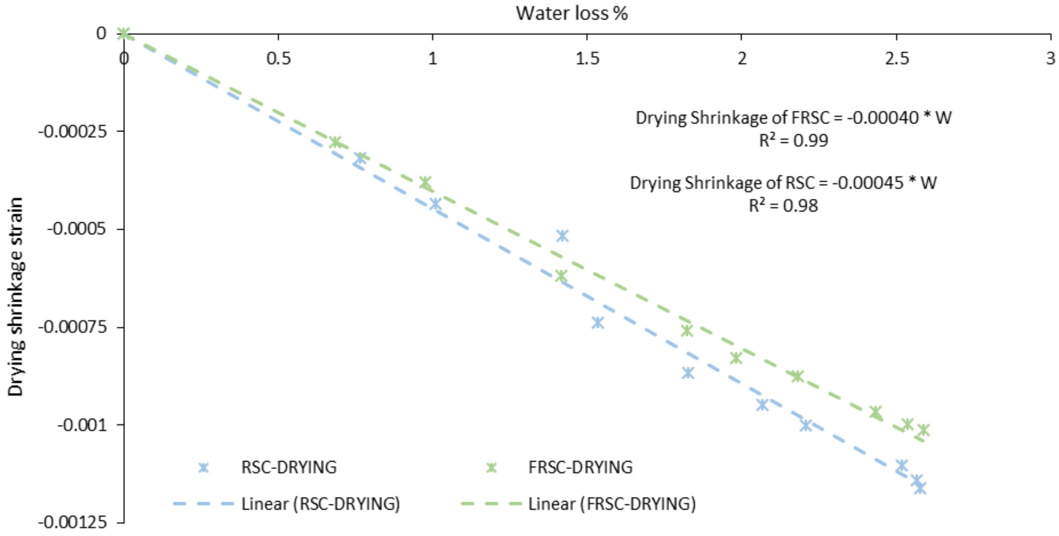

Figure 3.9. Calculated drying shrinkage versus measured water loss percent for RSC and FRSC prisms

3.5 Numerical studies

3.5.1 Numerical analysis approach

Heat transfer analysis available in FE package Abaqus was used to model moisture diffusion during drying. For this analysis, two parameters are essential; moisture diffusion and surface factor. The MC uses an equation that relates moisture diffusivity to relative humidity. As from the measurements taken only the normalised moisture content (C_{norm}) can be determined, this parameter is adopted instead of relative humidity as shown in Equation 3.8.

$$D(C_{norm}) = D_1\left(\alpha_0 + \frac{1-\alpha_0}{1+\left(\frac{1-C_{norm}}{1-C_c}\right)^n}\right) \qquad \text{Equation 3.8}$$

where, $D(C_{norm})$ is the moisture diffusivity, D_1 is the max diffusion coefficient when C_{norm} equals 1.0 and the samples are fully saturated ($D_1 = 1 \times 10^{-8}/f_{ck}$, f_{ck} = characteristic concrete strength), α_0 represents the ratio D_0/D_1; D_0 is the minimum D, C_c is the normalised moisture concentration at $D(C_{norm}) = 0.5D_1$.

The MC suggested values of α_0 = 0.05, C_c = 0.8 and n = 15 were initially used to calculate the diffusion coefficient. The resultant $D(C_{norm})$ for each mix was then adopted in the heat transfer analysis. Diffusive heat transfer 20-node quadratic brick elements (DC3D20) were used for the thermal analysis. As in the experiments, drying was only permitted through the top surface, which was assigned a surface factor, and the other surfaces were considered sealed having no moisture interaction with the environment. At the beginning of the drying, the normalised moisture concentration was 100% and the ambient relative humidity was considered constant at 40%. Initial values of the parameters for model code model of $D(C_{norm})$ as well as surface factors were optimized (Table 3.4) to minimize the difference between numerical and experimental moisture profile of each mix.

To calculate shrinkage deformations, the thermal analysis was coupled with a structural analysis in which the thermal expansion is replaced by a hygral contraction coefficient. C3D20R element type was used for the structural analysis. The tensile and compressive material characteristics were obtained from the experimental results and inverse analysis studies; further details on the procedures used are given elsewhere [6]. To accurately predict the shrinkage history, the development of the material properties with time was incorporated into the structural analysis through the implementation of the user subroutine, USDFLD. This allows the use of solution-dependent material properties and thus the user can define the field variables at a material point as a function of time [39]. The hygral coefficient was optimised to minimise the difference between measured experimental and FE predicted shrinkage strain.

3.5.2 Numerical results and discussion

3.5.2.1 Determination of moisture diffusivities and surface factor

The set of parameters implemented in MC equation (Equation 3.8) [21] to determine the moisture diffusivity coefficient for each mix are listed in Table 3.4. The calculated moisture diffusivities for different mixes, as functions of normalized moisture content, C_{norm}, are shown in Figure 3.10. The results show that CSA has the highest moisture diffusion at the beginning of drying (34.8 mm^2/day) while FRSC has the lowest moisture diffusion (24.1 mm^2/day). The diffusivity is almost constant at the beginning of drying (for 1 - 0.77 moisture content), and then decreases sharply before stabilizing again. This behaviour is congruent with the mechanism of drying reported for conventional cementitious materials [12, 15, 16, 18]. For RSC and FRSC, to minimize the difference between measured and numerical moisture profiles, a slight change to MC approach was adopted. The slope of the tail of the moisture diffusivity against moisture content was reduced to zero (from C_{norm} = 0.66 downwards) instead of being almost constant as predicted by the MC equation.

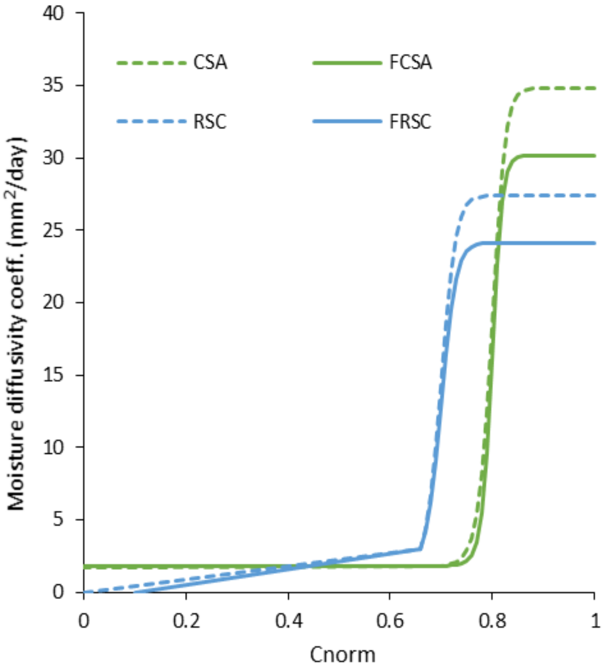

Figure 3.10. Moisture diffusivity versus normalized moisture content C_{norm}

A wide range of values is reported for moisture diffusivity (25.92 – 4665.6 mm^2/day) for well cured concrete specimens [29, 40, 41] and the results of this study seem to agree well with the lower bound of this range.

The back calculated surface factors for the tested mixes range from 4 – 6 mm/day. In addition, it was found that this factor only affects the moisture profiles near the drying surface and its effect diminishes quickly far from the top surface [18].

Table 3.4 Optimised parameters for MC equation and inverse analysis

Mix	*Optimised parameters of Equation 3.8*				*SF*	$\beta_{(C)}$
	D_1	α_0	C_c	n		
CSA	34.801	0.05	0.8	15	5	0.00038
FCSA	30.146	0.06	0.8	20	6	0.00065
RSC	27.399	0.035	0.7	20	4	0.0048
FRSC	24.139	0.05	0.7	20	4	0.0045

3.5.2.2 Determination of the hygral contraction coefficient

The hygral contraction coefficients for the mixes were back-calculated as functions of moisture content, *C*, using the free shrinkage test results. It was found that there is a strong linear relationship between shrinkage strain and moisture loss (Section 3.4.3), Equation 3.9.

$$(\varepsilon_{sh})_M = \beta_{(C)} \times (C_0 - C) \qquad \textit{Equation 3.9}$$

where, $(\varepsilon_{sh})_M$ is the free shrinkage strain, $\beta_{(C)}$ is the contraction coefficient and C_0 is the reference moisture content, 1.0. It should be noted that since both the total and drying shrinkage of RSC and FRSC show a linear relationship with water loss, the total shrinkage for samples of these mixes was modeled using a single hygral contraction coefficient. The calculated values of $\beta_{(C)}$ are listed in Table 3.4. As expected, mixes with calcium aluminate cement (CSA and FCSA) have much smaller contraction coefficient compared to the other mixes. However, for FCSA, $\beta_{(C)}$ is approximately 70% higher than that of CSA. This increase of shrinkage due to fibre addition is much higher than reported in literature. Nonetheless, those studies are only limited to Portland cement with/without pozzolanic additions. The value of $\beta_{(C)}$ for FRSC is slightly lower than that of RSC, possibly due to the restraining effect of the fibres at the large shrinkage strains developed.

3.5.2.3 Numerical moisture profiles: Results and Discussion

The numerical and experimental moisture profiles are compared in Figure 3.11. As it can be seen, the heat transfer analysis based on moisture diffusivities, calculated based on MC equation, predicts well the experimental moisture profiles with less than 5% difference.

3.5.2.4 Numerical shrinkage strain

The development of shrinkage strain with time, using parameters calculated in the previous sections, is compared to the experimental curves in Figure 3.12. As seen in Figure 3.12, the FE analysis satisfactorily represents the measured shrinkage, validating the factors adopted in the analysis.

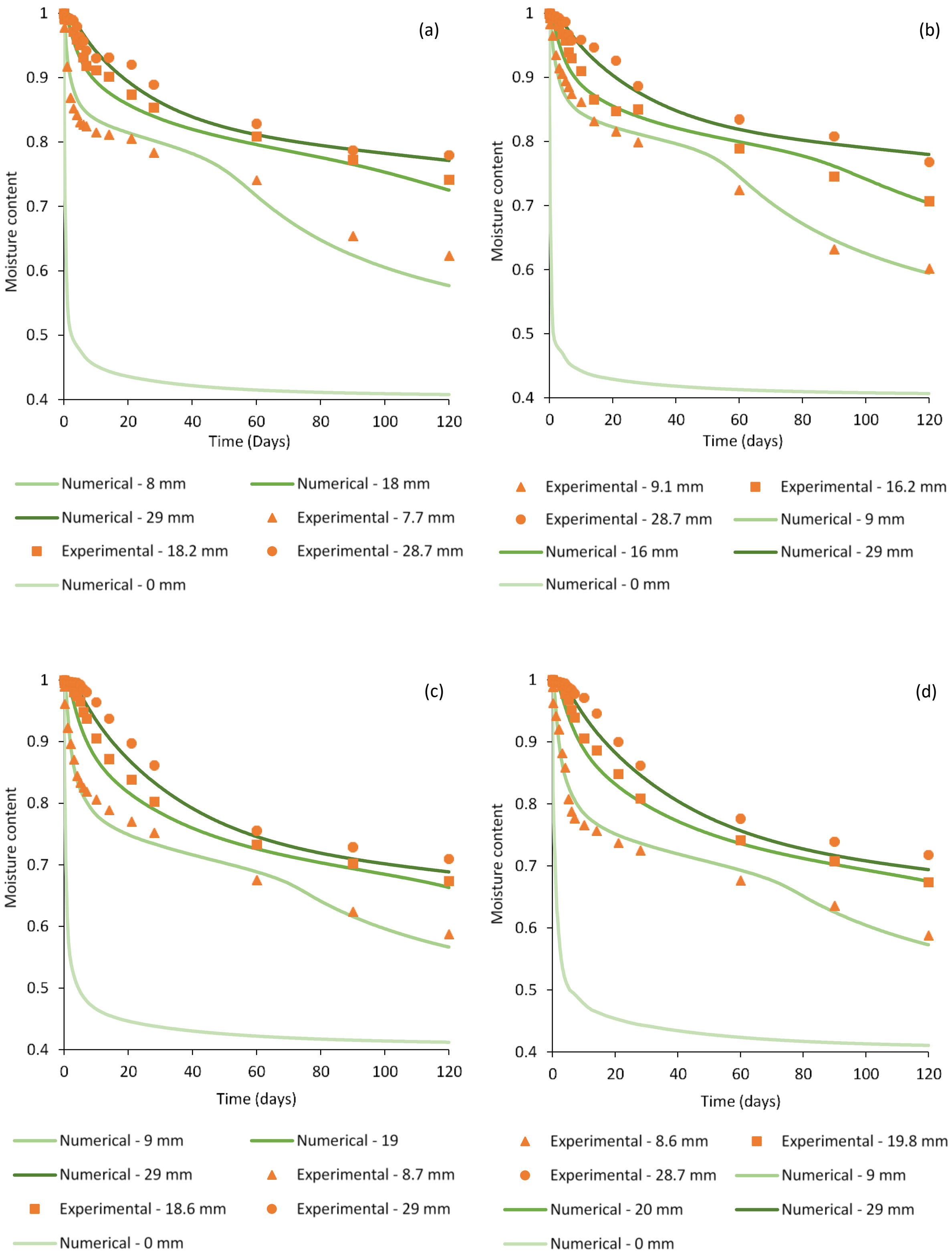

Figure 3.11. Numerical and experimental moisture profiles: (a) CSA; (b) FCSA; (c) RSC; (d) FRSC

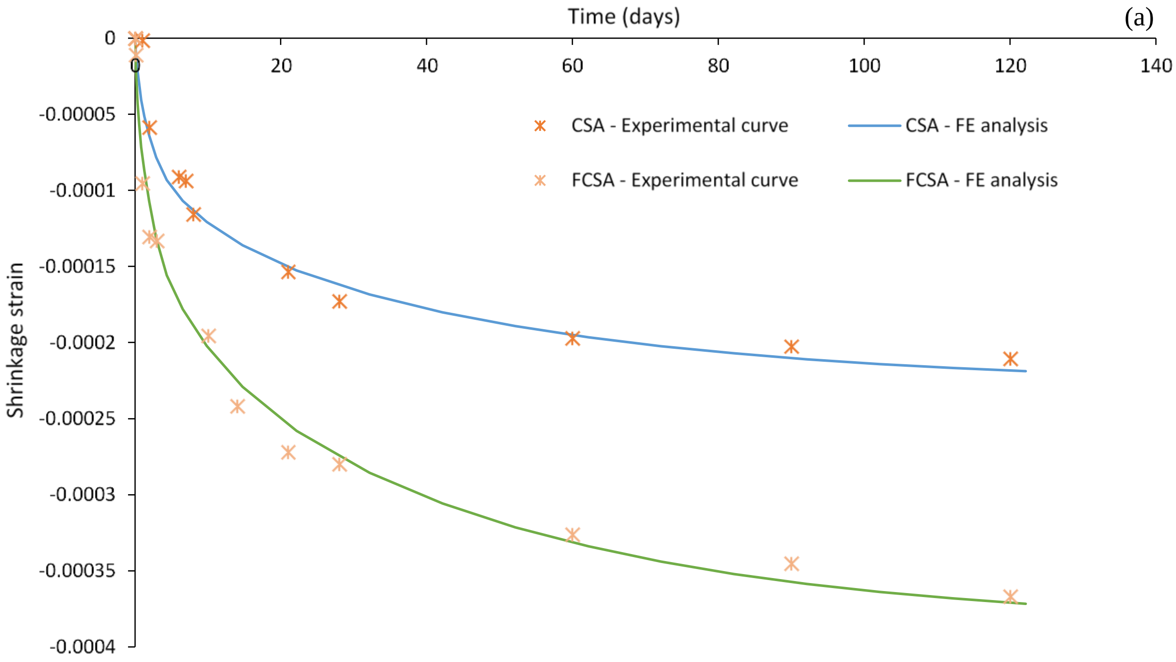

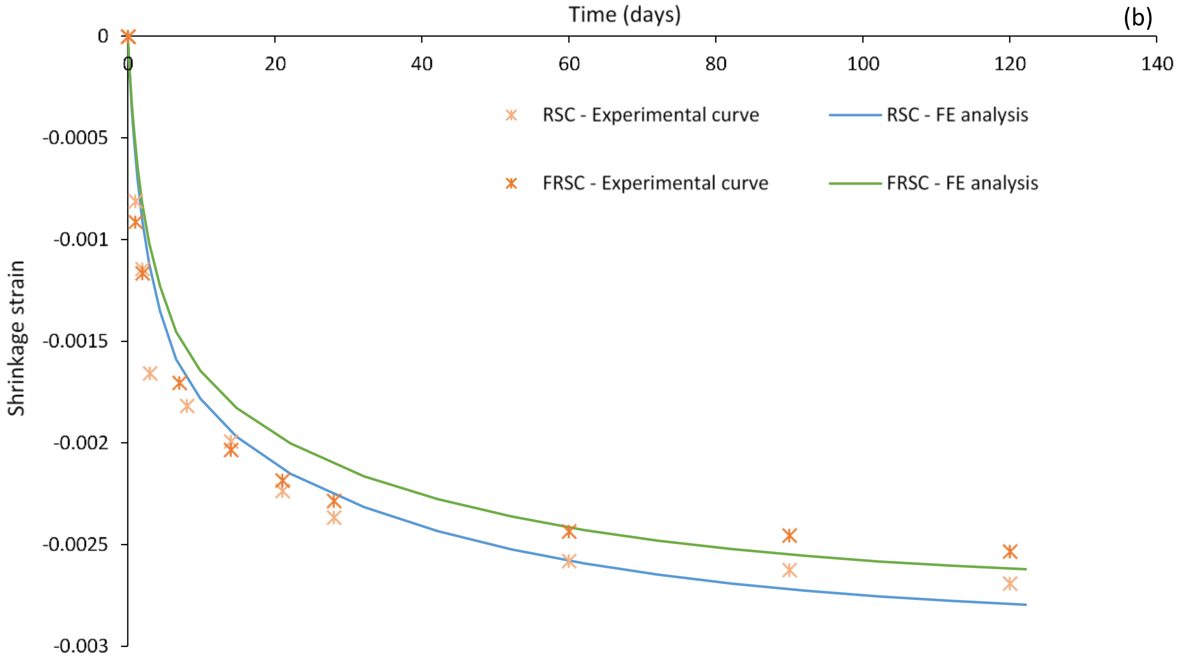

Figure 3.12. Numerical free shrinkage strain compared with experimental results: (a) CSA & FCSA; (b) RSC & FRSC

3.5.3 Comparison between numerical shrinkage and shrinkage predicted using MC, EC and ACI Code procedures

The parameters proposed for each code procedure to predict free shrinkage strain are used to obtain the free shrinkage of prisms of each mix with four different heights; 20, 30, 50 and 100 mm. The resulting curve for each mix, for a specific height, are compared with the FE predicted shrinkage (for that specific height) using the same parameters given in previous sections, Figure 3.13- Figure 3.16.

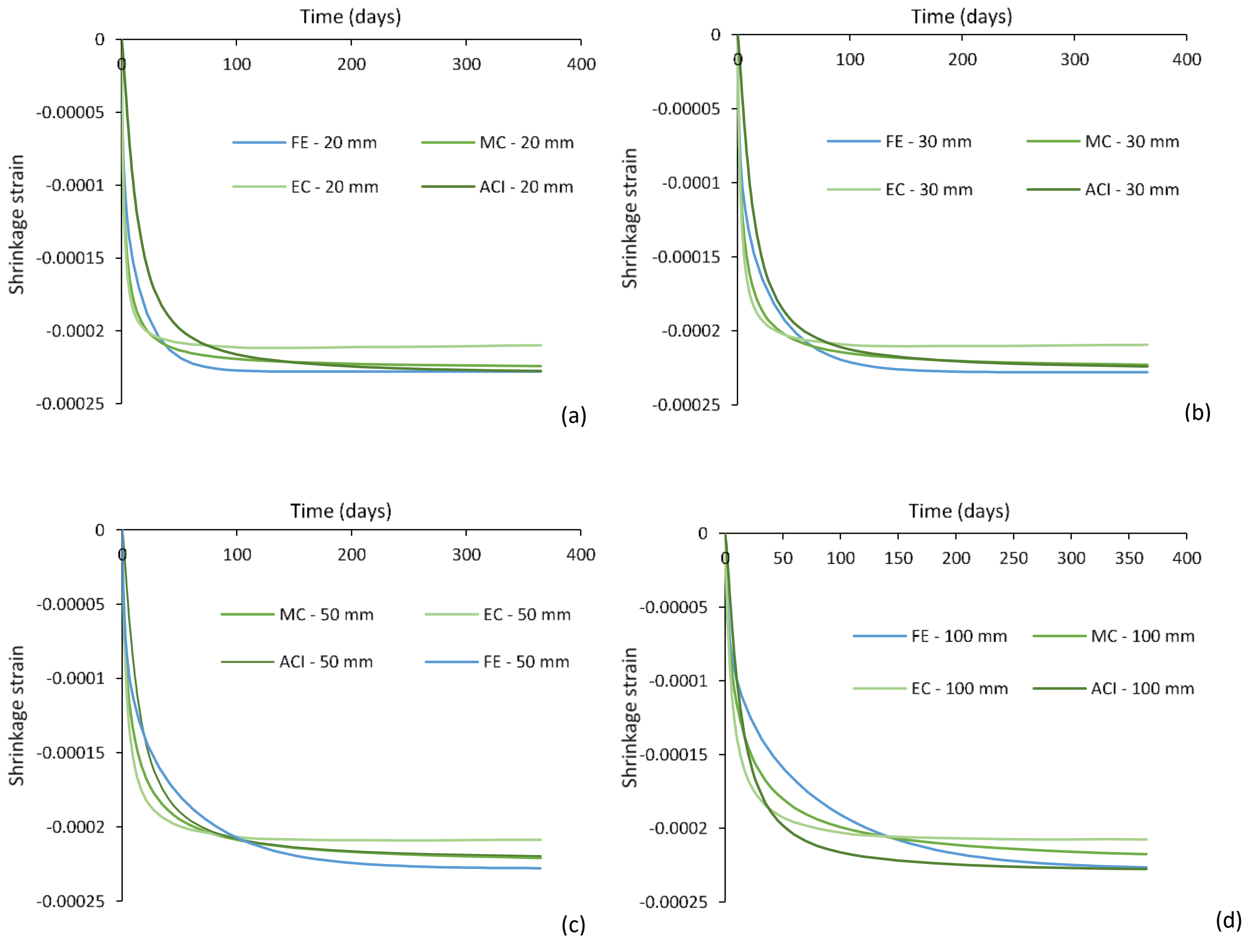

Figure 3.13. Numerical free shrinkage strain compared to shrinkage predicted using different codes for CSA prisms of heights: (a) 20 mm; (b) 30 mm; (c) 50 mm; (d) 100 mm

As seen in Figure 3.13 and Figure 3.14, the procedures are able to predict the shrinkage development of CSA and FCSA samples, respectively, over time with reasonable accuracy, especially for thinner sections.

The MC seems to offer the best estimate at both the beginning and the end of drying. However, EC appears to slightly overestimate the shrinkage at the beginning of drying while underestimates it towards the end of the testing period.

The estimated curves for total shrinkage development of RSC and FRSC over time against FE predicted curves are given in Figure 3.15 and Figure 3.16, respectively. It should be noted that EC was not used to predict shrinkage of RSC and FRSC mixes as it does not consider parameters for cement type in autogenous shrinkage prediction as it is the case in MC and, thus, was not used to model the shrinkage of RSC and FRSC mixes.

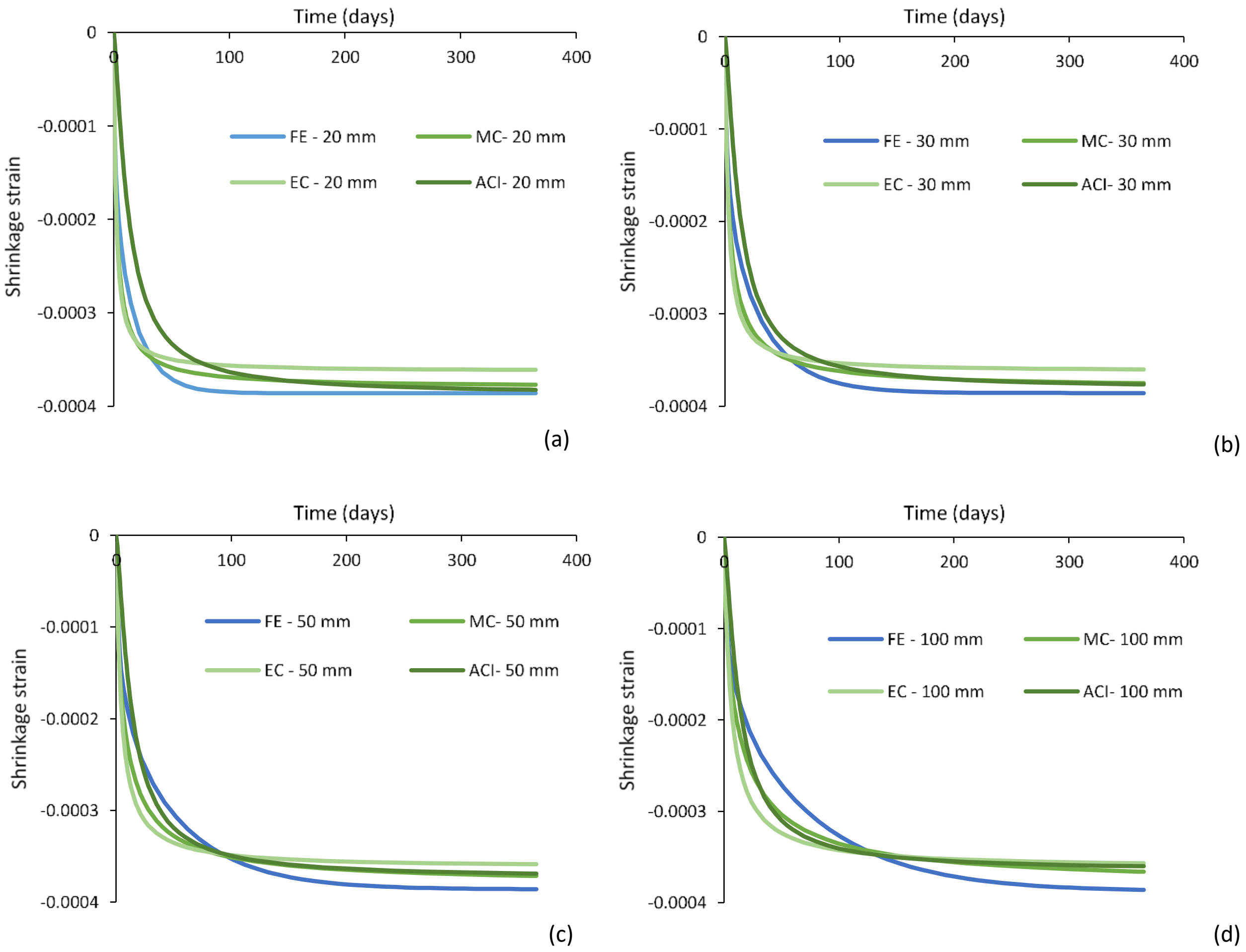

Figure 3.14 Numerical free shrinkage strain compared to shrinkage predicted using different codes for FCSA prisms of depths: (a) 20 mm; (b) 30 mm; (c) 50 mm; (d) 100 mm

As shown, for very thin sections, ACI offers slightly better predictions of shrinkage development with time compared to MC. At thicker sections, however, the MC seems to better capture the shrinkage history as ACI tends to overestimate the shrinkage development at the beginning of the testing and rather underestimates the shrinkage at later stages.

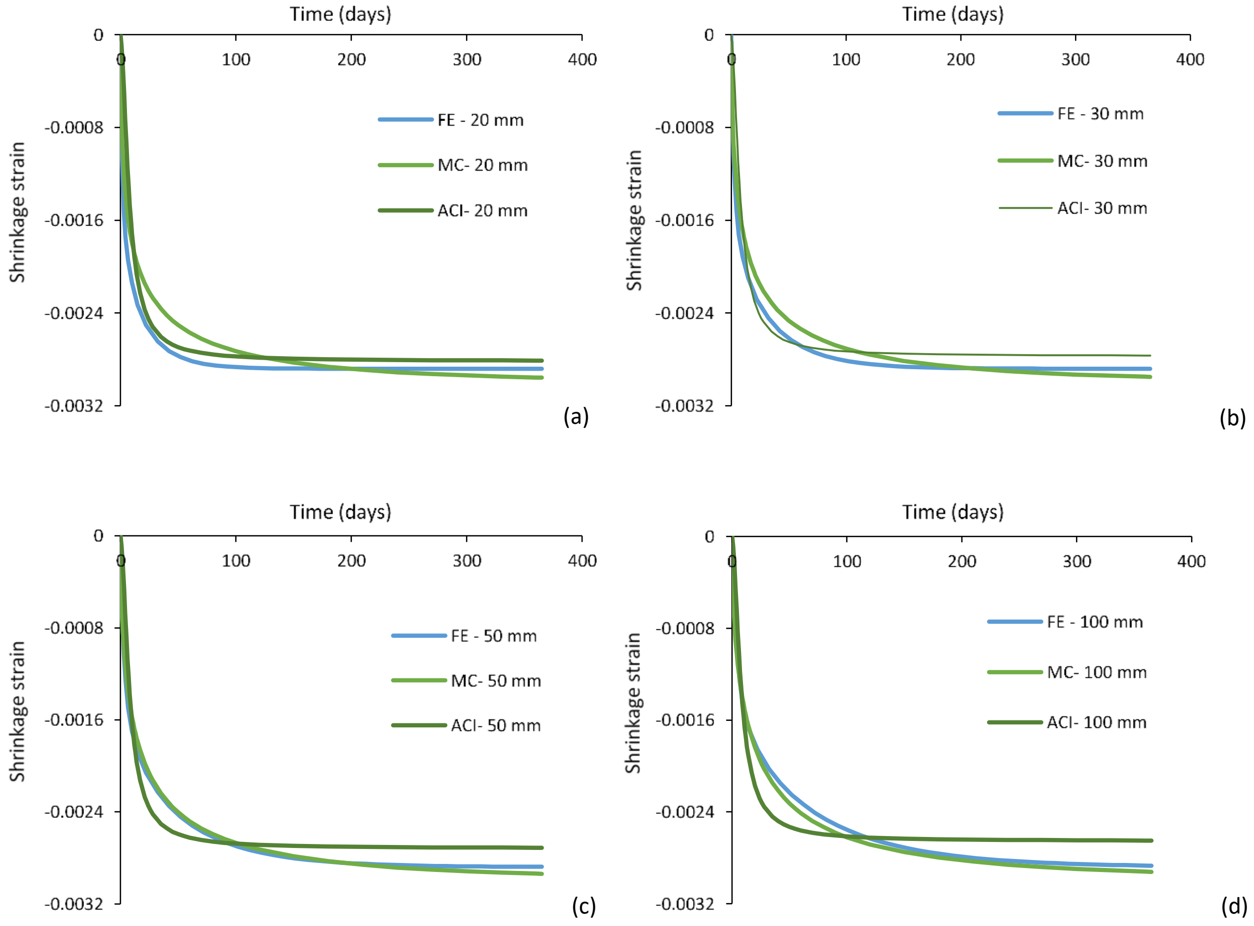

Figure 3.15. Numerical free shrinkage strain compared to shrinkage predicted using different codes for RSC prisms of heights: (a) 20 mm; (b) 30 mm; (c) 50 mm; (d) 100 mm

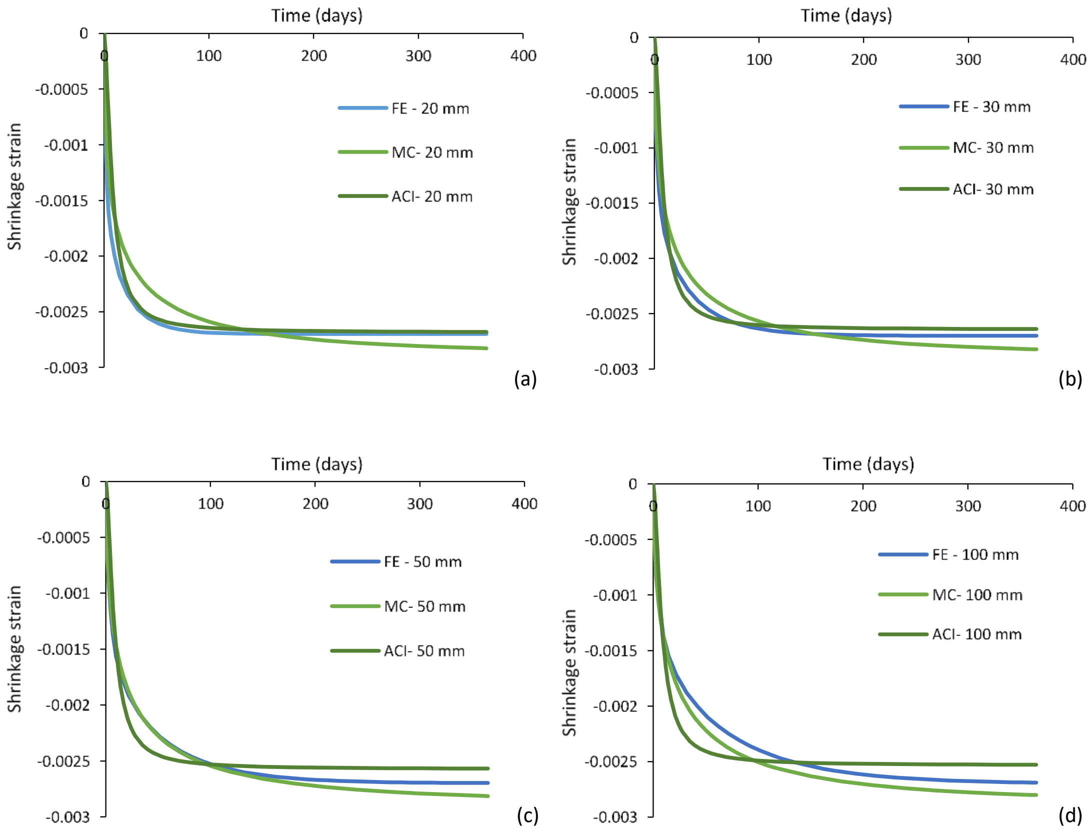

Figure 3.16. Numerical free shrinkage strain compared to shrinkage predicted using different codes for FRSC prisms of heights: (a) 20 mm; (b) 30 mm; (c) 50 mm; (d) 100 mm

3.6 Case studies

To assess the risk of cracking and/or delamination due to restrained shrinkage in repair layers prepared from the mixes developed in this study, the Silfwerbrand procedure [19] is followed. This requires knowing the free shrinkage of the overlay, the elastic modulus of the overlay layer and the substrate concrete as well as the tensile strength of the repair layer. The interface shear strength and the stiffness (K) should also be known.

To assess the risk of cracking and/or delamination, at one-year of age, the bonding conditions shown in Table 3.5 are considered. A layer with dimensions of 50*150*1000 mm is overlaid above an old concrete substrate with 200*150*1000 mm. The analysis is run twice for each mix; with and without creep in the overlay. When considering creep, the stresses were calculated by using the modulus of elasticity modified by creep coefficients (calculated based on the recommendations of MC 2010 [21]). The modulus of elasticity modified by creep is calculated as in Equation 3.10. As the substrate is already a few years old, it is considered conservative to neglect its creep deformations.

$$E_{cr} = \frac{E_c}{(1 + \theta_c)}$$

Equation 3.10

where, E_{cr} is the modulus of elasticity modified by creep; θ_c creep coefficient.

The calculated tensile stresses for CSA and FCSA overlaid prisms are shown in Figure 3.17 while the shear stresses that develop at the interface are presented in Figure 3.18 for different bond conditions (ranging from 1-100 to represent very weak to strong bond). The effect of creep is also shown (curves labelled -c).

Table 3.5 Material properties used for the case studies

Layer type	E_c (GPa)	E_{cr} (GPa)	*Tensile strength* (MPa)	λL	
Substrate	35	------	------		1
CSA	21.73	9.23	3.52		3
FCSA	28.00	12.80	4.00		10
RSC	20.56	10.55	3.02		30
FRSC	26.11	14.17	3.3		100

As shown in Figure 3.17 and Figure 3.18, neglecting creep leads to an overestimation of both tensile and shear stresses. When considering creep, for both CSA and FCSA overlays, the maximum tensile stress that develops at the interface is lower than the overlay tensile strength and thus it is predicted that cracking is unlikely to develop. However, for the strongest bond condition assumed (λL=100), high values of shear stresses develop with 6.11 MPa and 13.15 MPa for CSA and FSCA, respectively, at the edge of the composite prism, implying delamination if the shear strength at the interface is assumed to be similar to the tensile strength of concrete for well-prepared surfaces.

For RSC and FRSC overlays, cracking is predicted to occur for most bond conditions as the shrinkage strains are very high. The calculated shear stresses are also very high, indicating horizontal separation at the interface. However, in practice, as cracks develop, energy is released and shear stresses can drop.

The Silfwerbrand procedure does not clearly specify how to determine λL for different surface preparations and it is only useful in predicting cracking risk and, thus, the beneficial role of fibres cannot be quantified. Therefore, more experimental and analytical work is needed to understand how to accurately estimate λL and K for different bond conditions. Such work can help provide better predictions of cracking and delamination risks, quantify the role of fibres in materials with high shrinkage values (over 2500 με) and residual strength higher than the cracking strength and determine whether or not fibres have a beneficial role in resisting/delaying delamination.

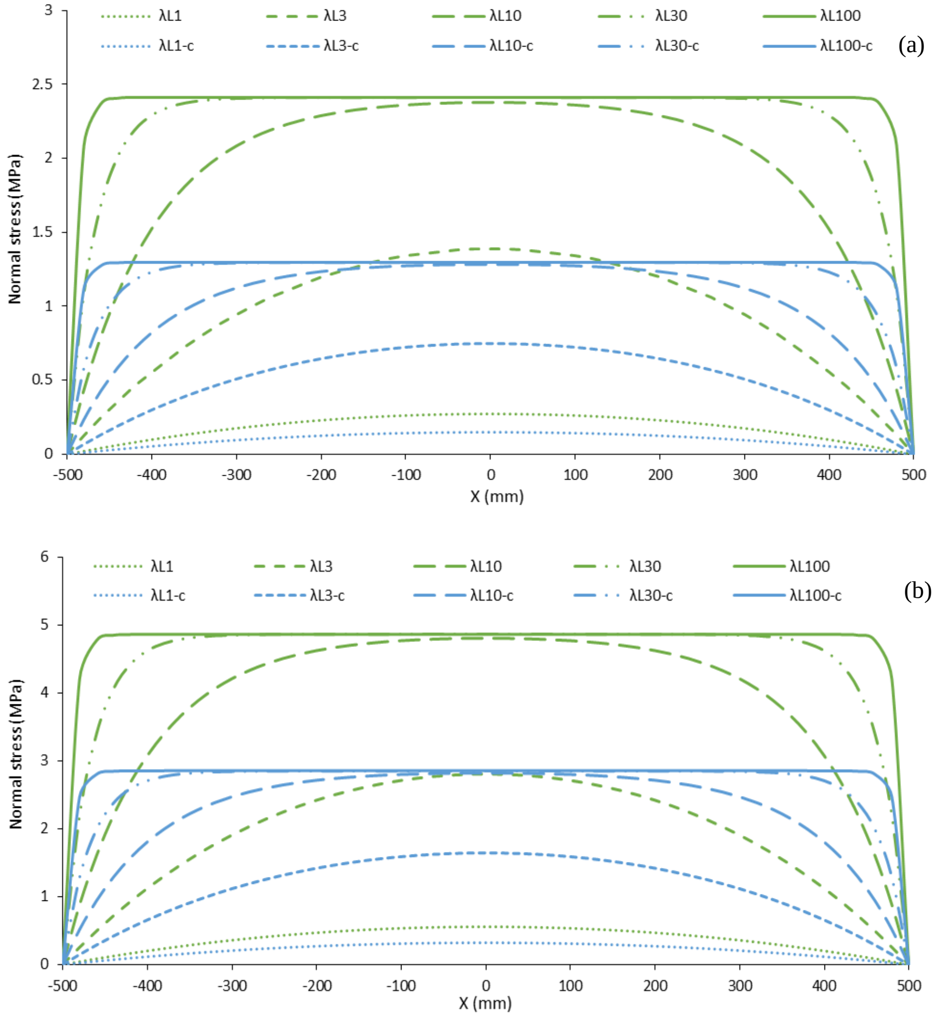

Figure 3.17. Normal stresses that develop at the interface between CSA overlay and substrate with and without creep for; (a) CSA overlay; (b) FCSA overlay

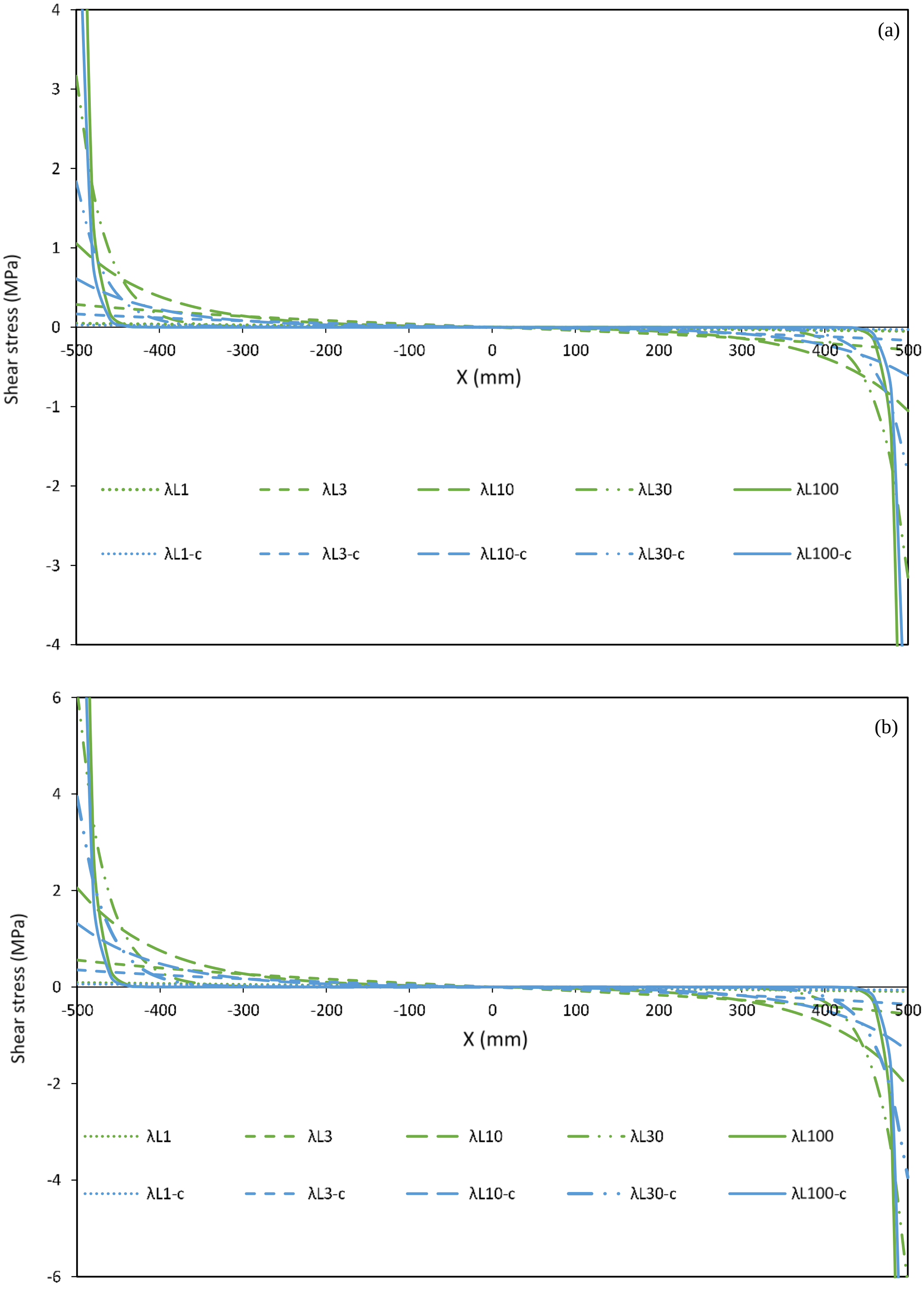

Figure 3.18. Shear stresses that develop at the interface between overlay and substrate with and without creep for; (a) CSA overlay; (b) FCSA overlay

3.7 Conclusions

This paper presents the main outcomes of a series of experimental and numerical studies on the time dependent transport properties of rapid hardening plain and fibre reinforced mortars for repair applications and on their shrinkage performance. Fibres are necessary to control crack widths in restrained conditions. The main findings of this study are:

- The fibre inclusion was confirmed not to have a major role on the moisture transport properties of rapid hardening mortar mixes, which allows the use of the MC equation, usually used to estimate the moisture diffusivity of plain concrete, to calculate their moisture diffusivities with good accuracy.
- Mixes with CSA cement showed much lower shrinkage strains (211 and 367 με) compared to mixes with RSC cement (2690 and 2532 με) at 120 days as CSA is expansive cement. Unlike CSA and FCSA, RSC and FRSC mixes showed considerable autogenous shrinkage which accounts for around 64 % and 71% of their total shrinkage at the age of 60 days possibly due to conversion.
- FE analyses were used in combination with experimental moisture distribution measurements to back calculate the moisture diffusivity of the tested mixes. It was found that the moisture diffusivities for mixes with rapid hardening cements are high at the beginning of drying (34.8 – 24.14 mm^2/day) and remain almost constant up to moisture contents of 85% - 75%, for different mixes, then sharply decreases upon further drying.
- There is a linear relationship between shrinkage and moisture loss for all the mixes with good correlation ratios.
- The hygral contraction coefficient, for each mix, were back calculated using inverse analysis for measured shrinkage strains. The coefficients range from 0.00038 to 0.0048 depending on the cement type and fibre inclusion.
- MC and ACI equations can be used to predict the shrinkage development with time provided appropriate coefficients for each cement type are used.

- Creep was found to play an important role in moderating tensile and shear stresses of the overlays.
- The Silfwerbrand procedure is used to determine normal and shear stresses in an overlay case study. Though the procedure is simple, it relies on parameters (λL and K) that are not easy to determine.

References

1. Beushausen, H., Alexander, M.G., (2006). Failure mechanisms and tensile relaxation of bonded concrete overlays subjected to differential shrinkage. *Cem. Concr. Res.* 36 (10), 1908-1914. Available at:

https://www.sciencedirect.com/science/article/pii/S0008884606001608.

2. Scrivener, K., (2003). Calcium Aluminate Cement. In Newman, J., Advanced Concrete Technology. 2/1-2/29. Oxford: ButterworthHeinemann.

3. Jewell, R., (2015). *Influence of Calcium Sulfoaluminate Cement on the Pullout Performance of Reinforcing Fibres: An Evaluation of the Micro-Mechanical Behavior*. PhD Thesis. University of Kentucky. Available at: http://uknowledge.uky.edu/ce_etds/27. [Accessed March 28, 2018].

4. Swamy, R.N., Stavrides, H., (1979). Influence of fiber reinforcement on restrained shrinkage and cracking. In *Journal Proceedings*. *ACI J.* 76(3), 443-460.

5. Graeff, A.G., Pilakoutas, K., Neocleous, K., Peres, M.V.N.N., (2012). Fatigue resistance and cracking mechanism of concrete pavements reinforced with recycled steel fibres recovered from post-consumer tyres. *Eng. Struct.* 45, 385–395. https://doi.org/10.1016/j.engstruct.2012.06.030.

6. Al-musawi, H., Figueiredo, F., Bernal, S.A., Guadagnini, M., Pilakoutas, K., (2019). Performance of rapid hardening recycled clean steel fibre materials. *Constr. Build. Mater.*, 195, 483-496.

7. Hu, H., Papastergiou, P., Angelakopoulos, H., Guadagnini, M., Pilakoutas K., (2018). Mechanical properties of SFRC using blended recycled tyre steel cords and recycled tyre steel fibres, *Constr. Build. Mater.*, 187, 553-564. Available at: https://www.sciencedirect.com/science/article/pii/S0950061818318750?via%3Dihub.

8. Banthia, N., Zanotti, C. and Sappakittipakorn, M., (2014). Sustainable fibre reinforced concrete for repair

applications. *Constr. Build. Mater*., 67 (PART C), 405–412. Available at: http://dx.doi.org/10.1016/j.conbuildmat.2013.12.073.

9. Xin, D., Zollinger, D.G., Allen, G.D., (1995). An approach to determine diffusivity in hardening concrete based on measured humidity profiles. *Adv*. *Cem*. *Based Mater*., 2(4), 138–144. Available at:

https://www.sciencedirect.com/science/article/pii/1065735595900144.

10. Bazant, Z.P., Najjar L.J., (1972). Nonlinear water diffusion in non-saturated concrete. *Mater*. *Struct*., 5, 3–20. Available at:

https://link.springer.com/article/10.1007%2FBF02479073.

11. Sakata, K., (1983). A study on moisture diffusion in drying and drying shrinkage of concrete. *Cem*. *Concr*. *Res*., 13(2), 216–224. Available at:

https://www.sciencedirect.com/science/article/pii/0008884683901047.

12. Selih, J., Sousa, A.C.M., Bremner, T.W., (1996). Moisture transport in initially saturated concrete during drying. Transp. Porous Media, 24, 81–106. Available at:

https://link.springer.com/article/10.1007%2FBF00175604.

13. Ayano, T., Wittmann, F.H., (2002). Drying moisture distribution, and shrinkage of cement-based materials. *Mater*. *Struct*., 35, 134–140. Available at:

https://link.springer.com/article/10.1007%2FBF02533581.

14. Shekarchi, M., Bonakdar, A., Bakhshi, M., Mirdamadi, A., Mobasher, B., (2010). Transport properties in metakaolin blended concrete. *Constr*. *Build*. *Mater*., 24 (11), 2217-2223. Available at:

https://www.sciencedirect.com/science/article/pii/S0950061810001558.

15. Bakhshi, M., Mobasher, B., (2011). Experimental observations of early-age drying of Portland cement paste under low-pressure conditions. *Cem*. *Concr*. *Compos*., 33(4), 474-484. Available at:

https://www.sciencedirect.com/science/article/pii/S0958946511000229.

16. Bakhshi, M., Mobasher, B., Soranakom, C., (2012). Moisture loss characteristics of cement-based materials under earlyage drying and shrinkage conditions. *Constr*. *Build*. *Mater*., 30, 413–425. Available at:

https://www.sciencedirect.com/science/article/pii/S0950061811006453?via%3Dihub.

17. Bakhshi, M., Mobasher, B. and Zenouzi, M., (2012). Model for early-age rate of evaporation of cement-based materials. *J*. *Eng*. *Mech*., 138 (11), 1372-1380.

18. Jafarifar, N., (2012). *Shrinkage behaviour of steel-fibre-reinforced-concrete pavements*. PhD thesis. University of Sheffield. Available at:

http://etheses.whiterose.ac.uk/7475/.

19. Silfwerbrand, J., (1997). Stresses and strains in composite concrete beams subjected to differential shrinkage. *ACI Struct*. *J*., 94(4), 347-353.

20. CEN, (2004). Eurocode 2: Design of concrete structures, Part 1-1: General rules and rules for buildings. European Committee for Standardization. Brussels, Belgium.

21. F.I. du Béton, (2013). Fib Model Code for Concrete Structures 2010, Wilhelm Ernst & Sohn, Berlin, Germany.

22. ACI, (2008). ACI 209.2R-08: guide for modeling and calculating shrinkage and creep in hardened concrete. American Concrete Institute, Farmington Hills.

23. Azenha, M., Maekawa, K., Ishida, T. and Faria, R., (2007). Drying induced moisture losses from mortar to the environment. Part I: experimental research. *Mater*. *Struct*., 40(8), 801-811. Available at:

https://link.springer.com/article/10.1617/s11527-007-9244-y.

24. Lura, P., Pease, B., Mazzotta, G.B., Rajabipour, F. and Weiss, J., (2007). Influence of shrinkage-reducing admixtures on development of plastic shrinkage cracks. *ACI Mater*. *J*., 104(2), 187-194.

25. Hall, C., Hoff, W.D. and Nixon, M.R., (1984). Water movement in porous building materials—VI. Evaporation and drying in brick and block materials. *Build*. *Environ*., 19(1), 13-20.

26. Hall, C. and Hoff, W.D., (2002). Water transport in brick, stone and concrete. New York: Taylor & Francis.

27. Vu T.H., (2006). *Influence of pore size distribution on drying behaviour of porous media by a continuous model*. MSc Dissertation. Germany: Otto-von-Guericke-Universität Magdeburg.

28. Huang, H., Garcia, R., Guadagnini, M. and Pilakoutas, K., (2017). Effect of section geometry on development of shrinkage-induced deformations in box girder bridges. *Mater*. *Struct*., 50:222. Available at:

https://link.springer.com/article/10.1617/s11527-017-1090-y.

29. Baluch, M.H., Rahman, M.K., Al-Gadhib, A.H., Raza, A. and Zafar, S., (2006). Crack minimization model for hot weather concreting. *Arabian J*. *Sci*. *Eng*., 31(1C), 77-91.

30. BS EN 13892-2, (2002). Methods of test for screed materials — Part 2: Determination of flexural and compressive strength.

31. JSCE-SF4, (1984). Standard for Flexural Strength and Flexural Toughness, Method of Tests for Steel

Fiber Reinforced Concrete, Concrete library of JSCE, Japan Concrete Institute (JCI), Japan.

32. ASTM C191, (2013). Standard Test Method for Time of Setting of Hydraulic Cement by Vicat Needle. *ASTM International*, (May), 1-8.

33. ASTM C 157, (2008). Test method for length change of hardened hydraulic cement mortar and concrete. *ASTM International*.

34. Pera, J., and Ambroise, J., (2004). New applications of calcium sulfoaluminate cement. *Cem. Concr. Res.*, 34(4), 671-676.

35. Winnefeld, F., and Lothenbach, B., (2010). Hydration of calcium sulfoaluminate cements—experimental findings and thermodynamic modelling. *Cem. Concr. Res.*, 40(8), 1239-1247.

36. Al-Kamyani, Z., Guadagnini M., and Pilakoutas, K., (2018). Predicting shrinkage induced curvature in plain and reinforced concrete. *Eng. Struct. J.*, 176, 468-480. Available at:

https://www.sciencedirect.com/science/article/pii/S014102961831023X.

37. Neville, A.M., (1995). *Properties of concrete* (4th ed.). London: Longman.

38. Wu, L., Farzadnia, N., Shi, C., Zhang, Z. and Wang, H., (2017). Autogenous shrinkage of high performance concrete: A review. *Constr. Build. Mater.*, 149, 62-75.

39. ABAQUS 2017 Documentation.

40. Bažant, Z.P. and Najjar, L.J., (1971). Drying of concrete as a nonlinear diffusion problem. *Cem. Concr. Res.*, 1(5), 461-473.

41. Kim, J.K. and Lee, C.S., (1999). Moisture diffusion of concrete considering self-desiccation at early ages. *Cem. Concr. Res.*, 29(12), 1921-1927.

Chapter 4: Effect of shrinkage on rapid hardening plain and recycled steel fibre concrete overlays

Al-musawi, H., Huang, H., Benedetti, M., Guadagnini, M., Pilakoutas, K., (2019). Effect of shrinkage on rapid hardening plain and recycled steel fibre concrete overlays. Submitted for publication.

Abstract

The durability and functionality of concrete overlay repairs are highly dependent on the extent of cracking and crack widths, which are difficult to predict. This article presents an experimental and analytical investigation on restrained shrinkage of overlays made with rapid hardening mortar mixes reinforced with recycled fibres. The investigated parameters include cement type (calcium sulfoaluminate cement-CSA and calcium aluminate cement-RSC), overlay depth, bond condition and fibre dosage. Sixteen composite prisms were tested to determine shrinkage strains and cracking development over time. Both plain (RSC) and fibre reinforced (FRSC) overlaid prisms made of calcium aluminate cement developed multiple cracks in less than 16 hours due to their high shrinkage values, but 60% lower crack widths developed in FRSC. An effective analytical model is derived to estimate the crack spacing of concrete overlays. As concrete crack width predictive models are shown to be deficient in predicting the crack width of materials with flexural hardening properties, a semi-empirical approach is adopted to quantify the effect of fibres in such matrices. The predicted crack widths are in a good agreement with the experimentally measured values. The suggested model is expected to make a contribution towards safer and more sustainable solutions for concrete repairs.

This chapter consists of a "stand alone" journal paper and includes a relevant bibliography at the end of the chapter. Additional information and further details are presented in Appendix C.

4.1 Introduction

Concrete overlays are increasingly used in both structural and non-structural repairs of concrete structures. Cracking and/or delamination are their main structural performance issues, due to tensile and shear stresses that develop as a result of restrained shrinkage [1]. Shrinkage in repair mortars (without expansive cements) is expected to be high since they are made with cement rich mixes, often with rapid hardening cements, and are laid on substrates that can easily absorb moisture. Thus, to preserve the durability and functionality of overlays, it is essential to limit crack widths and prevent delamination along the interface.

Manufactured steel fibres (MSF) are often used as a reinforcement to control shrinkage cracks [2,3]. An illustrative example on the beneficial role of fibres in controlling crack widths is a highway in Canada that was repaired with plain and fibre reinforced concrete overlays. While the plain sections deteriorated rapidly with big cracks and extensive delamination within less than 24 months in service, the fibre reinforced overlays showed much less debonding and limited crack widths for the duration of the 12-year monitoring period [4-7].

To promote the sustainability of repairs, suitable alternative recycled materials could be used in concrete repairs. Recent research studies at University of Sheffield [8,9] showed that concrete mixes reinforced with recycled clean steel fibres, extracted from pre-vulcanised rubber belt offcuts, can result in comparable or even better flexural performance than MSF reinforced concrete. These mixes exhibited flexural hardening properties even at dosages of 30 kg/m^3, indicating their efficiency in resisting loads even after significant cracking possibly due to high bond strength. Using such materials is expected to not only enhance functionality, but also promote the sustainability of repairs.

Al-Kamyani et al. [10] found that using 1% blends of MSF and post-consumer recycled tyre steel fibres (RTSF) can reduce crack widths by about 34% in structural beams reinforced with steel bars of about 0.42%. It was also shown that steel fibres contributed in reducing the transfer length between cracks by lowering the tensile strain in the horizontal reinforcement. However, the fibre effect on crack spacing may not be the same in overlays [2,11] as fine distributed cracks develop in well bonded overlays made with both plain concrete and SFRC, while in unbonded areas of overlays (the overlays are partially bonded), a single wide crack developed in which case fibres can help control the cracks [2].

To estimate crack widths in plain overlays, as for reinforced concrete, the crack spacing is multiplied by the concrete free shrinkage ε_{cs}. In the case of fibre reinforced overlays, the crack reduction attained by fibre bridging is often accounted for by utilising the FRC fracture characteristics. For instance, the Swedish Concrete Society, in report no 13 [12], considers the effect of fibres by introducing the material residual strength factor ($R_{10,20}$) (Equation 4.1):

$$\mathrm{w_{cr}} = \mathrm{S}.\,\varepsilon_{\mathrm{cs}}\,.\left(1 - \frac{\mathrm{R_{10,20}}}{100}\right) \qquad \textit{Equation 4.1}$$

where, w_{cr} is the crack width; S is the crack spacing and $R_{10,20}$ is the residual strength factor (further details on how to calculate this factor are given in [13]).

A similar approach is suggested by Kim et. al. [14] to predict the width of joint openings in thin FRC overlays, by utilising either the residual flexural strength factor calculated at (span/150) deflection or the fiber aspect ratio (l_f/d_f) as shown in Equation 4.2 & Equation 4.3:

$$\mathrm{w_{CR}} = \mathrm{C}_b.\,\mathrm{S}.\,(\alpha_\mathrm{t}\Delta\mathrm{T} + \varepsilon_{\mathrm{cs}})\{\mathrm{K_a} \text{ or } \mathrm{K_b}\} \qquad \textit{Equation 4.2}$$

$$\mathrm{K_a} = \frac{50}{\frac{\mathrm{l_f}}{\mathrm{d_f}}} \leq 1.0 \text{ or } \mathrm{K_b} = 1 - \frac{\mathrm{f_{res,FRC}}}{\mathrm{f_{mor,FRC}}} \qquad \textit{Equation 4.3}$$

where, C_b: is an adjustment factor to account for the subgrade restraint effect; S is the crack spacing, α_t: is a coefficient of thermal expansion of FRC; ΔT: is the temperature gradient; $f_{res,FRC}$: is residual strength of FRC obtained from a flexural prism test based on ASTM C1609/C1609M (MPa) [15]; $f_{mor,FRC}$: is a flexural strength of the mortar (MPa).

None of the above approaches can be used to predict crack widths in SFRC with flexural hardening characteristics, as their flexural residual strength factor will be over one, which surprisingly results in negative cracking values for such materials. It should be noted that the onset of cracking is rather related to the tensile strength of the matrix rather than their residual characteristics. In addition, the use of the residual strength at (span/150) 3 mm deflection (ultimate state) to predict the shrinkage crack widths may underestimate the contribution of shorter fibres. Short fibres from post-consumer recycled tyre steel fibres (RTSF) were found to control well restrained shrinkage cracks at serviceability limit states [10]. Furthermore, there is currently no universally accepted design approach to control crack widths or quantify accurately the effect of fibres on crack width and spacing of overlays. There are also no experimental data or analytical models that show the effect of RCSF on cracks in concrete and mortar repairs.

The other important aspect for durability and functionality of repairs is having sufficient bond. It is not only necessary to obtain distributed small shrinkage cracks [2,11], but it is also crucial to avoid delamination and subsequent deterioration. Surface cleaning and treatment, roughness, strength and stiffness of both layers and moisture level of the substrate [2, 16-18] were all found to have an impact on the quality of the bond. However, the role of fibres on the bond quality is inconclusive. Whilst some researchers [19] point out that fibres may not be beneficial in avoiding delamination, as by controlling crack widths less energy is released through cracks which means higher bond strengths are required to prevent delamination, others [20] argue that the inclusion of 0.5 - 1% (by volume) fibres increases the adhesive bond strength by 100%.

To address these issues, restrained shrinkage of overlays made of rapid hardening mortar mixes is investigated experimentally and analytically in this paper. The parameters examined include cement type (two types of rapid hardening cements), overlay depth, bond condition and fibre dosage.

This paper presents details on the experimental work on restrained shrinkage of overlaid prisms. By using the experimental results, a simple analytical model for predicting crack spacing is developed. The available methods of predicting the crack width are reviewed and a modified crack width prediction model is developed.

This chapter addresses objectives 7-10 of the thesis.

4.2 Experimental program

4.2.1 Mix proportions and mechanical properties

Two plain and two SFRC mixes with 45 kg/m^3 (V_f = 0.57%) of RCSF were investigated in this study, details of which are given Table 4.1. Two commercial cement types were used; calcium sulfoaluminate cement (CSA) and rapid setting calcium aluminate cement (RSC), each at 600 kg/m^3. River washed sand (0-5mm, SG=2.65) was used as fine aggregates. Recycled clean steel fibres (RCSF) were sourced from tyre cords extracted from un-vulcanised rubber belts. Their strength is reported to exceed 2600 MPa [8]. The length of the RCSF used in this study was 21 mm and the diameter 0.2 mm. Further details on the mixes and material characteristics are given elsewhere [9].

To characterize flexural performance, three 40*40*160 mm mortar prisms were tested according to BS EN 13892-2, (2002) [21], but using displacement control instead of load control, to better capture the post-peak behaviour. A specially designed aluminum yoke was mounted on the specimens to eliminate support movements. To assess the flexural behaviour over time, the prisms were tested at various ages, ranging from one hour up to one year. After flexural testing, the two fractured parts were tested under uniaxial compressive loading according to BS EN 13892-2, (2002) [21]. The results in terms of first cracking strength ($f_{ctm,fl}$) and compressive strength (f_{cu}) with their corresponding standard deviation values (listed in brackets) are shown in Table 4.1.

Table 4.1 Mix proportions and flexural strength ($f_{ctm,fl}$) and compressive strength (f_{cu}) for all mixes (MPa)

Mix	Fibre dosage (kg/m^3)	Sand (kg/m^3)	SP[a]	w/c ratio	1 hr	3 hrs	1 day	7 days	28 days	365 days
					$f_{ctm,fl}$ f_{cu}	$f_{ctm,fl}$ f_{cu}	$f_{ctm,fl}$ f_{cu}	$f_{ctm,fl}$ f_{cu}	$f_{ctm,fl}$ f_{cu}	$f_{ctm,fl}$ f_{cu}
CSA	0	1420	0.60	0.40	2.6 (0.2) 21.1 (3.0)	4.0 (0.2) 26.9 (2.8)	4.3 (0.2) 31.8 (2.5)	5.3 (0.3) 36.0 (3.0)	5.4 (0.3) 38.6 (2.3)	5.4 (0.3) 40.9 (2.3)
FCSA	45	1420	0.61	0.41	3.5 (0.4) 26.1 (4.6)	6.8 (0.5) 31.6 (3.7)	6.5 (0.5) 36.6 (2.3)	8.2 (0.8) 41.1 (3.3)	8.7 (0.9) 43.1 (3.2)	8.7 (1.0) 45.5 (3.0)
RSC	0	1300	0.20	0.35	2.5 (0.2) 17.2 (1.9)	2.9 (0.2) 24.2 (2.0)	3.5 (0.1) 33.0 (2.0)	4.2 (0.2) 40.4 (2.4)	4.4 (0.2) 46.5 (2.6)	4.5 (0.1) 48.1 (3.7)
FRSC	45	1300	0.21	0.36	3.5 (0.2) 21.3 (3.0)	3.5 (0.2) 28.3 (3.5)	5.0 (0.2) 37.9 (2.4)	5.5 (0.3) 46.2 (3.2)	5.7 (0.3) 51.5 (2.9)	5.6 (0.3) 54.5 (6.6)

[a] % by cement mass.

4.2.2 Restrained shrinkage

4.2.2.1 Construction of concrete substrates and overlays

For the concrete substrates, 16 prisms 500 mm long, 150 mm wide and with two different depths (120 and 130 mm) were cast in wooden moulds using conventional ready mixed concrete (CEM I 52,5N; 20 mm graded Limestone as coarse aggregate), details of which are given in

Table 4.2. The top surface of the prisms was mildly steel wire brushed, the day after casting, to expose aggregate surfaces. In some specimens (the prisms to be overlaid with RSC and FRSC layers), the top surface was further steel wire brushed to accomplish rougher surfaces so as to study the effect of surface texture. The specimens, then, were demoulded and kept in a mist chamber for 27 days. To accelerate their drying, the specimens were placed in an oven at 80 °C for a week and then left in a standard laboratory environment for a few days to cool down. Their top surfaces were thoroughly cleaned. A few hours before casting the overlay, water was sprayed on the substrate upper surface and let to dry out to achieve a saturated surface dry condition.

Each batch was used to cast two overlays (the final depths are listed in Table 4.3). After the estimated setting time, while still in the moulds, water was added to the top surface of the prisms which were then covered with plastic foil up to approximately one hour. They were then demoulded and placed in an environmental chamber with a relative humidity of 50 ± 5% and a temperature of 20 ± 2 °C.

Table 4.2 Mix proportions of substrate

Component	*Cement*	*GGBS*	*Sand*	*Gravel*	*w/c*	*Plasticiser*[a]
Amount (kg/m^3)	86	105	900	1060	0.5	1.14

[a] Pozzolith 324N Plasticiser (Litre)

Table 4.3 The depths of overlays and substrate layers (all dimensions are in mm)

Mixes	*1*		*2*		*3*		*4*	
	Substrate	*Overlay*	*Substrate*	*Overlay*	*Substrate*	*Overlay*	*Substrate*	*Overlay*
CSA	120	31	120	30	113	40	113	40
FCSA	117	35	125	30	112	42	112	42
RSC	122	28	117	33	116	37	110	40
FRSC	118	34	124	26	116	37	116	34

4.2.2.2 Restrained shrinkage measurements

The shrinkage measurements were recorded for the 16 composite prisms at frequent time intervals starting from the day of casting and up to approximately 4 months, using a 200 mm Demec gauge. Six measurements were taken for each prism; two at the top layer of the overlay (Top1 and Top 2 in Figure 4.1) and two readings at each side of the prism (R1 and R2) as shown in Figure 4.1. R1 is around 7-10 from the top while R2 is 5-7 mm from the interface. The prisms were also checked for cracks and their widths were recorded using a digital microscope with a 300 magnification. The same device was also used to check for any horizontal cracking or separation along the interface.

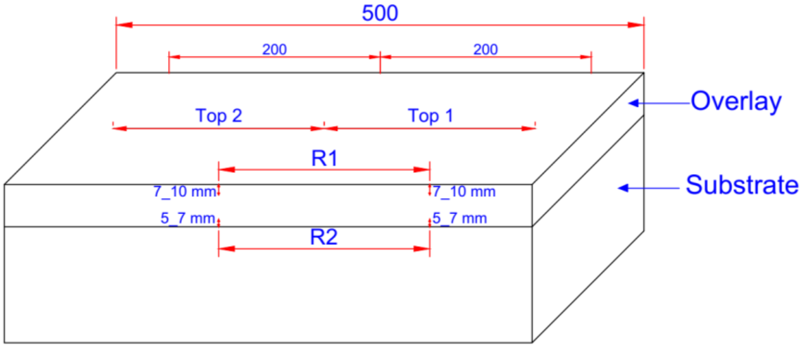

Figure 4.1. The locations of restrained shrinkage measurements for a composite prism

4.2.2.3 Flexural testing of composite prisms

After 18 months from casting the overlays, the prisms were tested under a 4-point bending arrangement using a 300 kN universal electromechanical testing machine. Central deflections were measured by using Linear Variable Differential Transducers (LVDTs) mounted on a yoke frame, first adopted by Japanese Society of Civil Engineers standard [22], to eliminate torsional and local crushing effects. The testing was displacement controlled at a rate of 0.3 mm/min until failure. Additional LVDTs were fitted at the interface of the opposite ends of each prism to measure any delamination between the interface and the substrate as shown in Figure 4.2. The prisms were flipped over so that the overlay is subjected to tension during the test. For fibre reinforced specimens, a clip gauge of 12.5 mm length was attached to the overlay at the centre to record the local extensions.

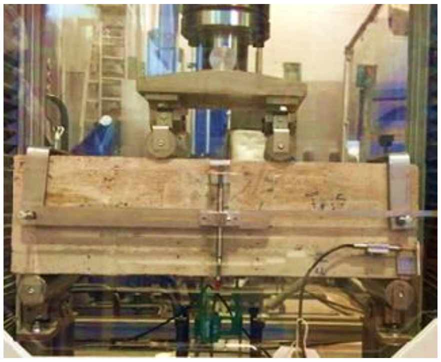

Figure 4.2. Flexural testing of overlaid prism

4.2.2.4 Shear tests on composite sections

There are several methods to measure the shear bond strength of repairs. A rather easy to preform test is the bi-shear test originally proposed by Momayez et al. [23] which is expected to result in low coefficients of variation. In this test, three-point loads are applied on composite cube specimens, where the repair layer roughly constitutes third of the cube volume, to produce a predominantly shear stress at the overlay interface. To avoid boundary effects (mainly due to fibre alignment), it was decided to cast a linear composite prism for each mix, similar to those used in shrinkage measurements. The prisms were kept in a mist room before testing. As the overlays for these testes were 40 mm deep, the prisms were reduced to a depth of 120 mm to comply with the requirements of the three-point test. Their overall dimensions were 120 ×150 × 150 mm (see Figure 4.3). Three specimens were produced from each prism. A 300 kN universal testing machine was used to apply the load. The tests were displacement controlled at a rate of 0.3 mm/min. One LVDT was used to measure the shear displacement, as a DIC system monitored the other side of the specimen.

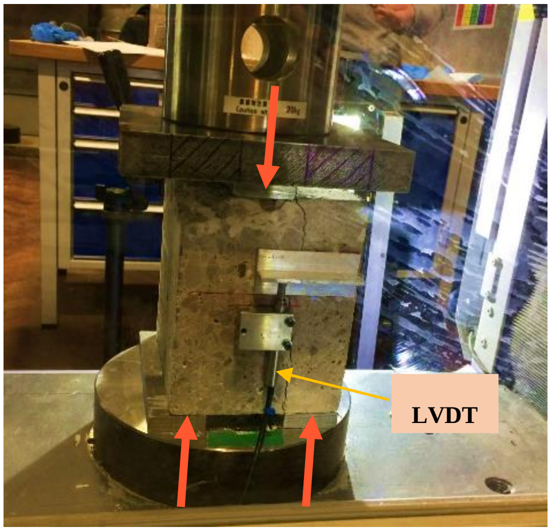

Figure 4.3. Shear specimen after testing

4.2.2.5 Experimental results and discussion

The shrinkage development with time for all prisms is shown in Figure 4.4 to Figure 4.7. The measurements at the top (Top_1 and Top_2) and sides (R_1-S_1 and R_1-S_2 [$R_{1\text{-avg}}$], R_2-S_1 and R_2-S_2 [$R_{2\text{-avg}}$]) were averaged for each prism. In Figure 4.4 to Figure 4.7, only the average readings (Top_{avg}, $R_{1\text{-avg}}$ and $R_{2\text{-avg}}$) are reported. For comparison purposes, the predicted free shrinkage strain of each overlay is shown in those Figures as well. Free shrinkage strain for each overlay can either predicted using numerical tools or estimated using code equations and parameters suggested in a previous work published by the authors [24]. Free shrinkage strain shown in these Figures is numerically predicted. As the pair CSA_1 and CSA_2 as well as the pair CSA_3 and CSA_4 have approximately the same dimensions and similar interface characteristics, their shrinkage values were averaged (see Figure 4.4). Overall, CSA prisms show less measured shrinkage strains (losses) compared to FCSA prisms (see Figure 4.4 and Figure 4.5), as the total free shrinkage of FCSA mix is higher than CSA. However, a direct comparison between CSA and FCSA composite prisms is not entirely possible due to different bond preparations for each mix. FCSA prisms had rougher interface surfaces than CSA prisms (see Figure 4.8) and thus, their interface stiffness is expected to be higher, resulting in bigger restraint of shrinkage of overlays. It should be noted that neither CSA nor FCSA overlaid prisms showed any cracks until flexural testing at one and a half years' time. On the other hand, cracks were developed on RSC and FRSC prisms in less than 16 hours after mixing. Further cracks appeared a few days after casting and no additional cracks were noticed 7 days after casting. The final crack locations are shown diagrammatically in Figure 4.9 for RSC and FRSC prisms. Hence, for the RSC and FRSC composite prisms, the strain measurements are heavily influenced by the presence of shrinkage cracks. Despite the higher free shrinkage strain of RSC mix (Figure 4.6), RSC composite prisms showed less shrinkage strains in comparison with FRSC prisms.

It is worth mentioning that only two RSC prisms showed local delamination at one end of the prism at nine months age. However, the horizontal cracks did not propagate into the inner parts of the prisms until testing in flexure.

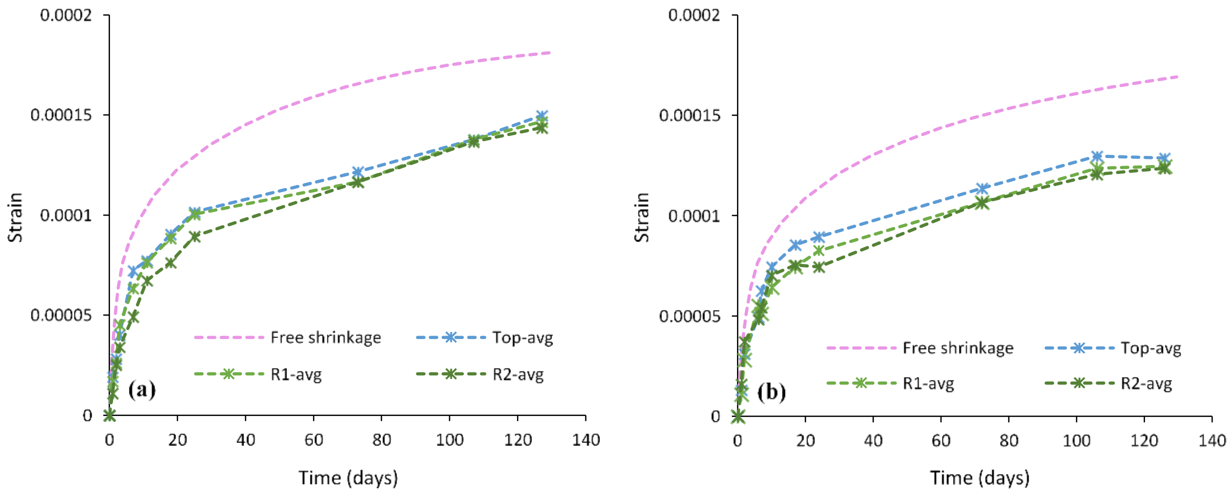

Figure 4.4. Shrinkage development with time for composite prisms: (a) Average of CSA$_1$ &CSA$_2$; (b) CSA$_3$ & CSA$_4$

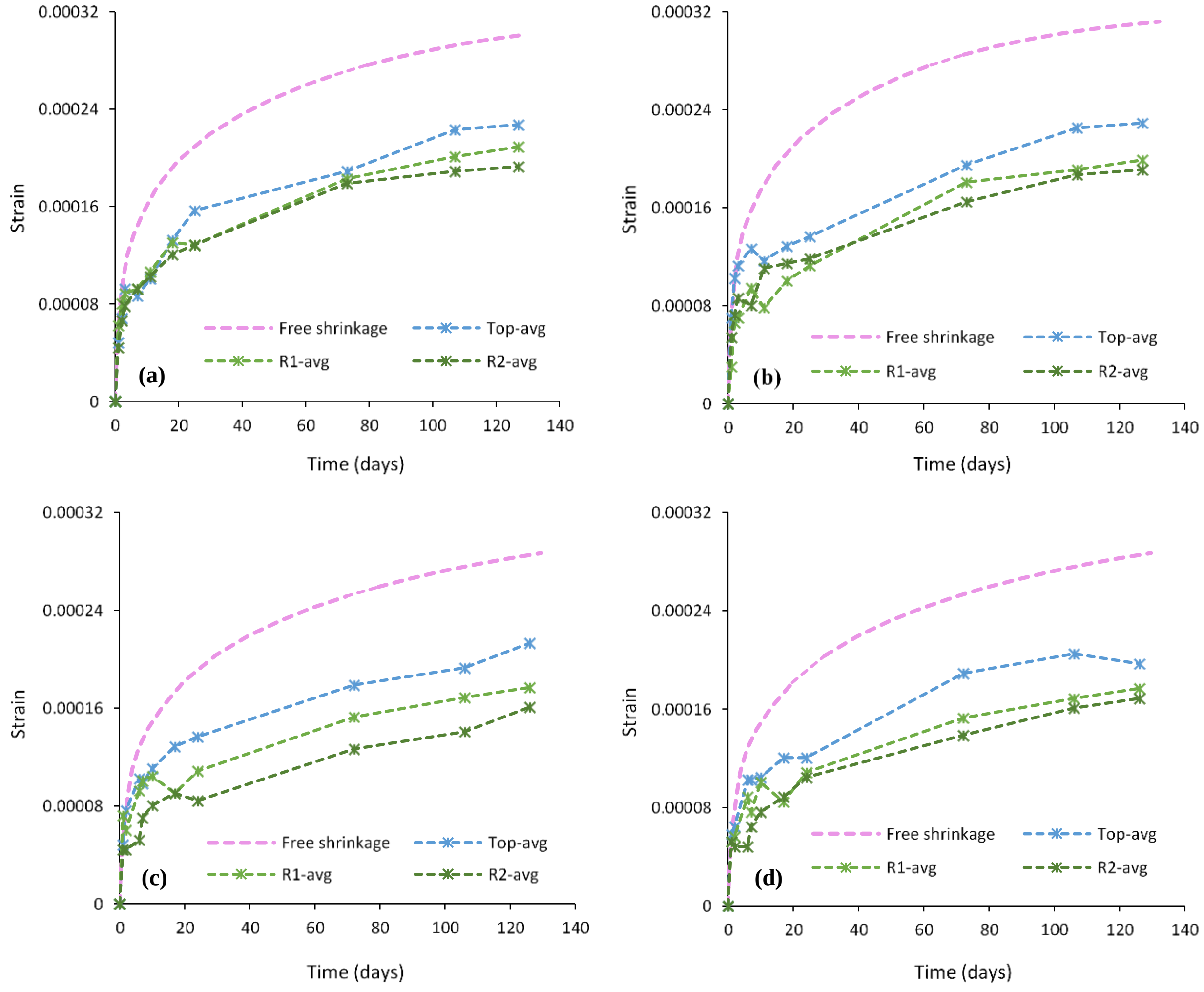

Figure 4.5. Shrinkage development with time for composite prisms: (a) FCSA$_1$; (b) FCSA$_2$; (c) FCSA$_3$; (d) FCSA$_4$

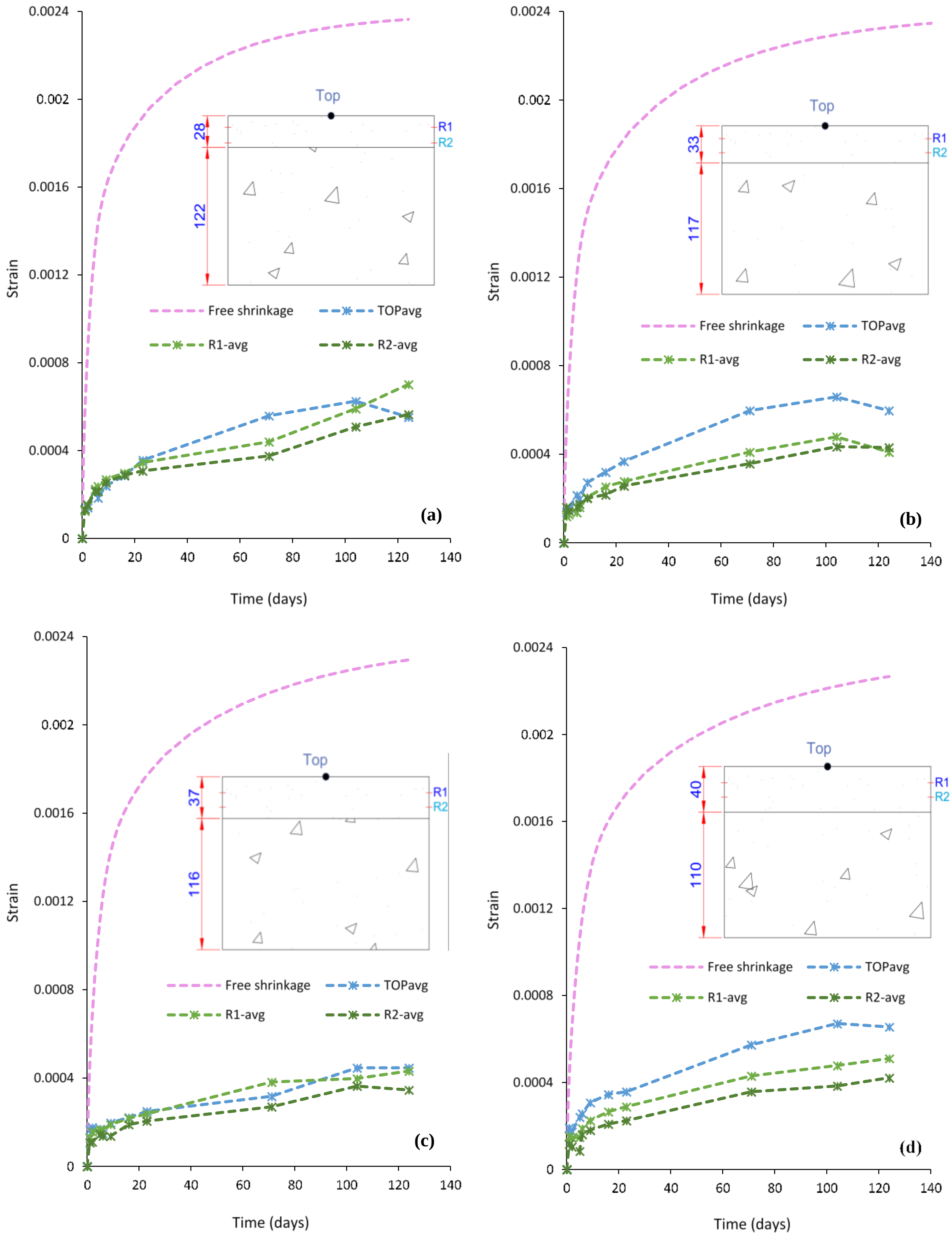

Figure 4.6. Shrinkage development with time for composite prisms: (a) RSC$_1$; (b)RSC$_2$; (c) RSC$_3$; (d) RSC$_4$

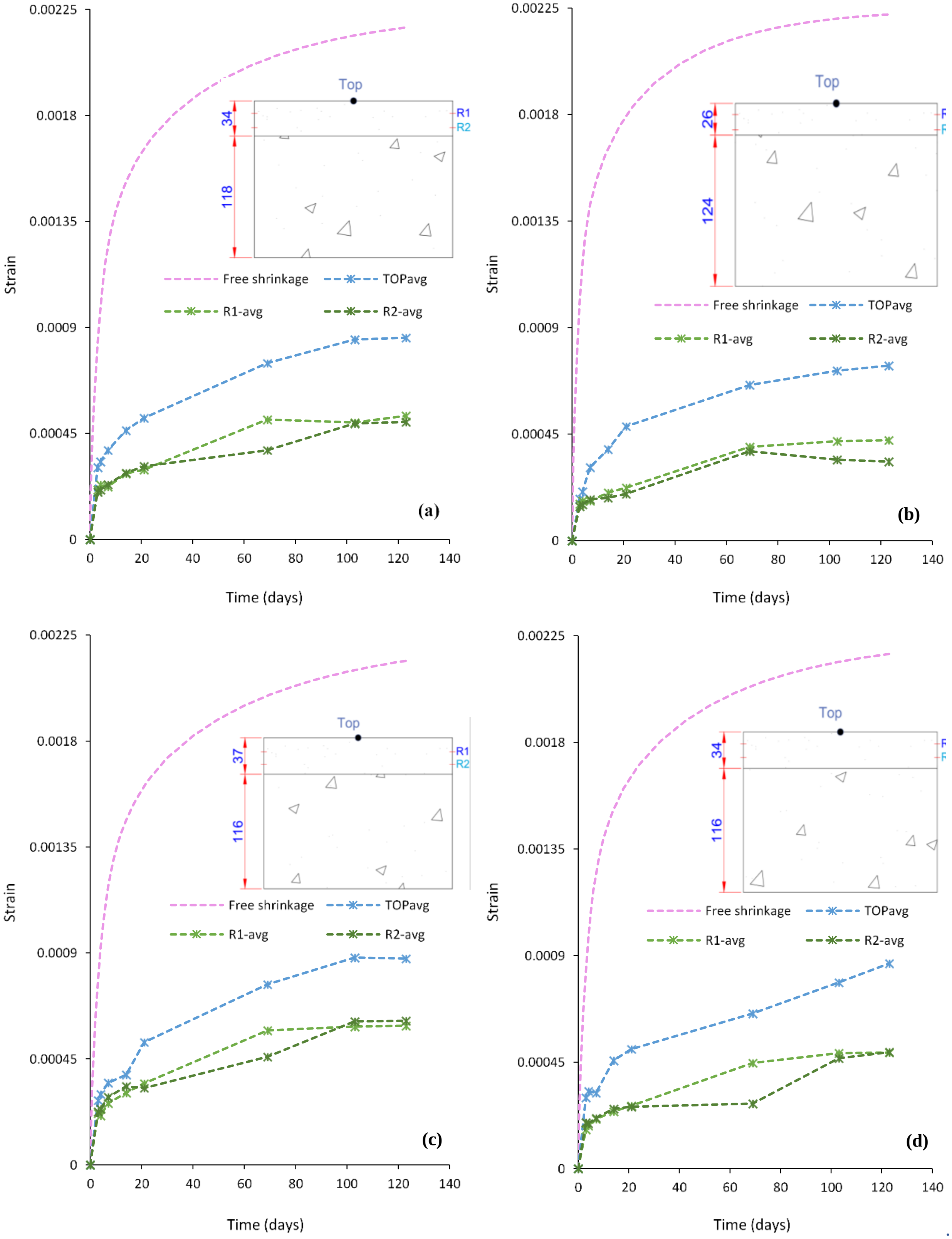

Figure 4.7. Shrinkage development with time for composite prisms: (a) FRSC$_1$; (b) FRSC$_2$; (c) FRSC$_3$; (d) FRSC$_4$

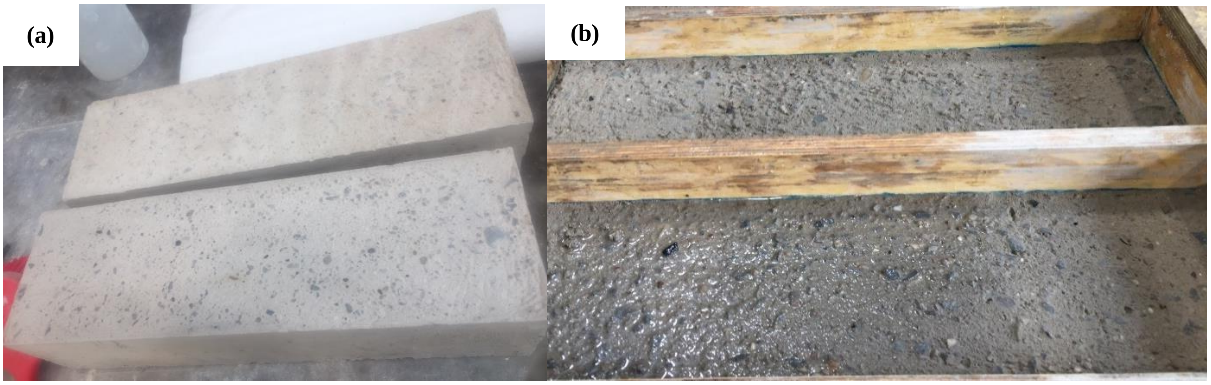

Figure 4.8. Substrate prisms to be overlaid with: (a) CSA prisms; (b) FCSA prisms

It should be noted that at the time of casting the overlays, the base prisms had approximately 50 % humidity. Although their top surfaces were moistened prior to overlying, it is expected that the base layer would absorb some moisture from the overlay. Therefore, the base layer can swell depending on the amount of moisture transferred from the overlay, creating a shrinkage gradient across the depth of the prism. This is because the overlay dries faster from the top surface than towards the substrate. This is exacerbated by the fact that the top layer tends to have more shrinkage than the lower layer due to non-uniform constituents' distribution (as more aggregate tend to settle in the lower part of the section) [25] and bleeding [26]. This can be noticed in the shrinkage strain results of the composite prisms, where the top layer shrinks more than the lower sides of the prisms. This is more pronounced in prisms with higher shrinkage strains. Differential shrinkage is expected to cause higher peak tensile stresses in the overlays compared with the simple uniform shrinkage distribution usually assumed in generic models for shrinkage estimation. Non-uniform shrinkage was also reported by Younis et al. [26] and Al-Kamyani et al. [27].

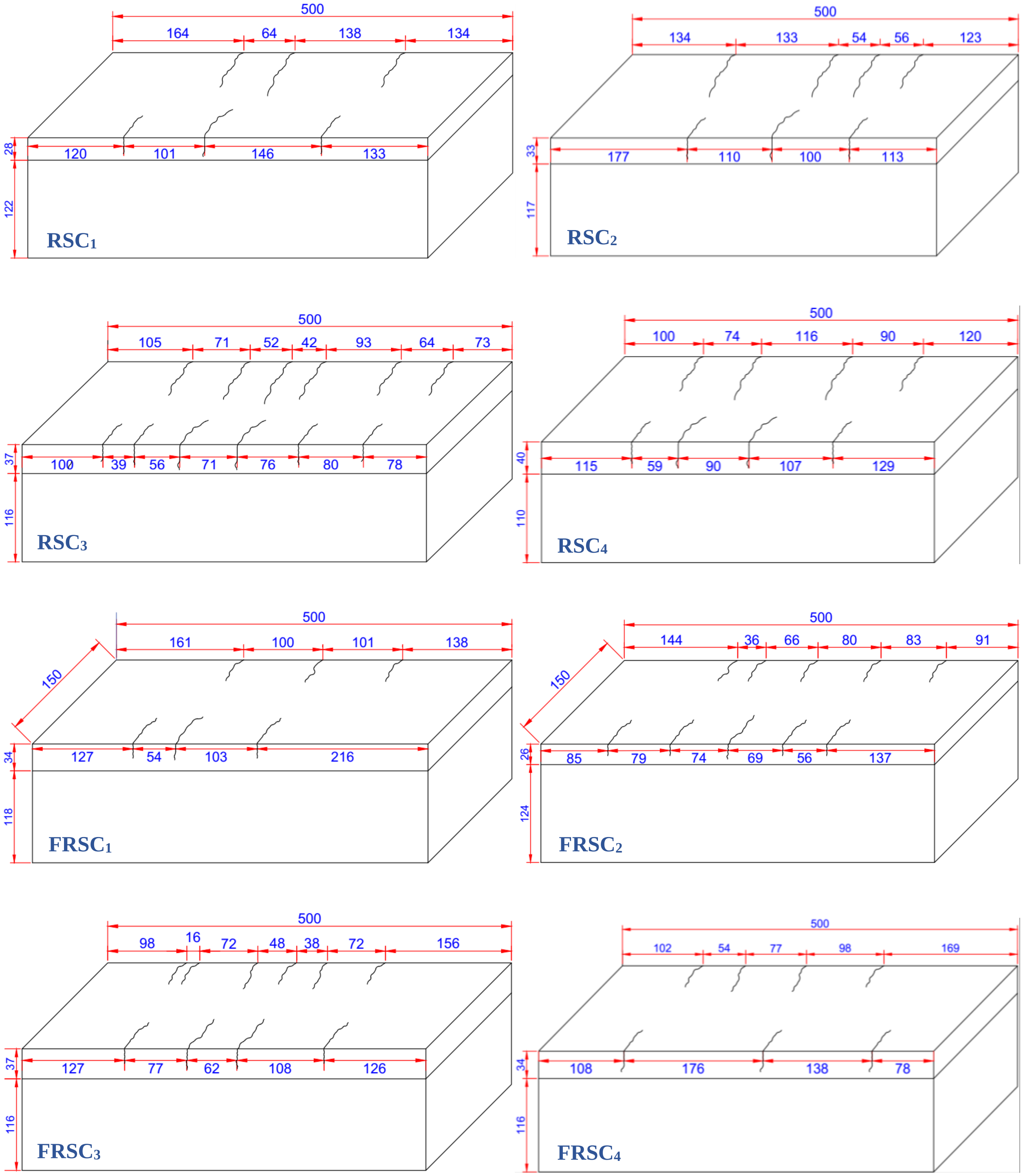

Figure 4.9. Crack spacing for composite prisms: (a) RSC$_1$; (b) RSC$_2$; (c) RSC$_3$; (d) RSC$_4$; (e)FRSC$_1$; (f)FRSC$_2$; (g) FRSC$_3$; (h)FRSC$_4$

4.3 Degree of restraint of the base layer

To understand the role of the base in restraining the overlay, Carlsward [2] calculated the degree of restraint (ψ) for various stiffness ratios m (m = E_b/E_o, where E_b is the modulus of elasticity of the base layer while E_o is the modulus of elasticity of the overlay layer) and geometrical relations α ($\alpha = h_o/H$ where h_o is the overlay depth and H is the total depth of the composite prism) based on Silfwerbrand [28], Equation 4.4:

$$\psi = \frac{m.(1-\alpha).(m.\ (1-\alpha)^3 +\ \alpha^2\ .(3+\ \alpha))}{m + (m-1).(m.(1-\alpha)^4 - \alpha^4\ )} \qquad \textit{Equation 4.4}$$

He concluded that the degree of restraint increases rapidly for α smaller than 0.15, while it is almost constant for α values in the range of approximately 0.15-0.75. For bigger α values, the restraint will diminish, see Figure 4.10.

The ψ values for RSC and FRSC prisms are plotted in Figure 4.11 using time dependent values of modulus of elasticity for both layers. As shown, the restraint levels range approximately between 0.71 – 0.81 at early ages and then decrease with time as the overlay stiffness evolves. It should be noted that those prisms developed cracks in less than 24 hours and thus, it can be assumed that the restraint levels were very high already from early ages.

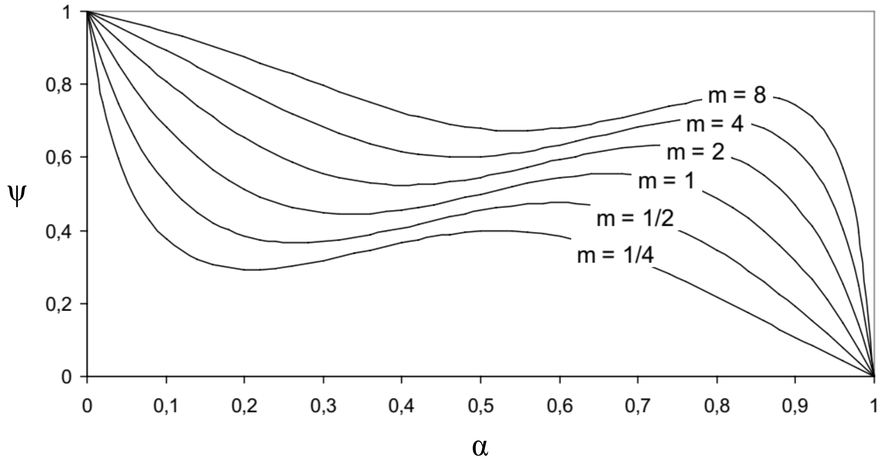

Figure 4.10. Degree of restraint ψ as a function of the relative overlay depth α for different stiffness relations between overlay and substrate m based on the Silfwerbrand model (after Carlsward [2]).

The degree of restraint offered by the reinforcement in conventional RC is much lower, in the level of 0.1 - 0.2, which means the crack spacings of overlays will be dominated by the total free shrinkage rather than the strain in the reinforcement. This means that the crack spacing and development will be different than in RC and more influenced by how fast the interface bond can develop the overlay tensile force.

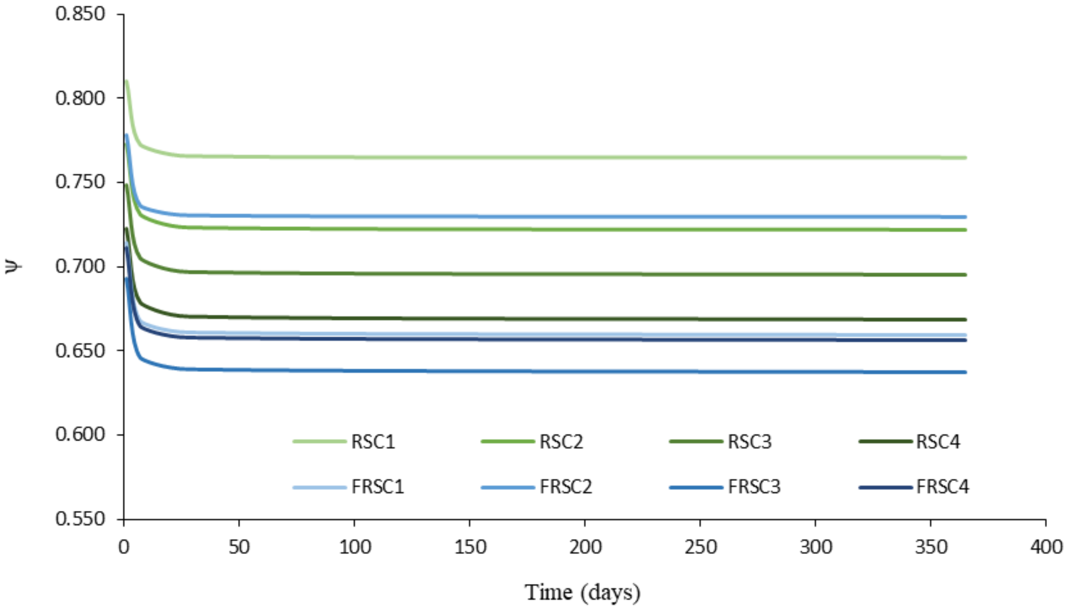

Figure 4.11. Degree of restraint ψ for RSC and FRSC prisms with time

4.4 Cracking Results

4.4.1 Crack spacing

4.4.1.1 Experimental crack spacings

The crack spacings of RSC and FRSC are shown in Figure 4.9. MC 2010 [16] adopts a value of 1.7 for the ratio between maximum and average crack spacing when calculating the crack widths of conventional reinforced structural concrete beams. To understand the relation between average and maximum crack spacing of overlays, their distribution should be examined first. After performing the normality tests in SPSS [29], the distribution of spacings and normalised spacings appear to follow the normal distribution curve despite some variation due to inhomogeneity of the materials. Figure 4.12 shows the frequency distribution of the measured crack spacings while Figure 4.13 shows the frequency distribution of the normalised measured crack spacing to the average crack spacing of all prisms. The calculated 5% exceedance value for the normalised distribution curve is 1.64. This value can be used to determine the ratio of the maximum crack spacing to the average crack spacing (S_{max}/S_{avg}) and is very close to the MC adopted value of 1.7 for the ratio between max and average crack spacing. Hence, it is reasonable and conservative to accept that MC value of **1.7** can be used to predict maximum crack widths for overlays.

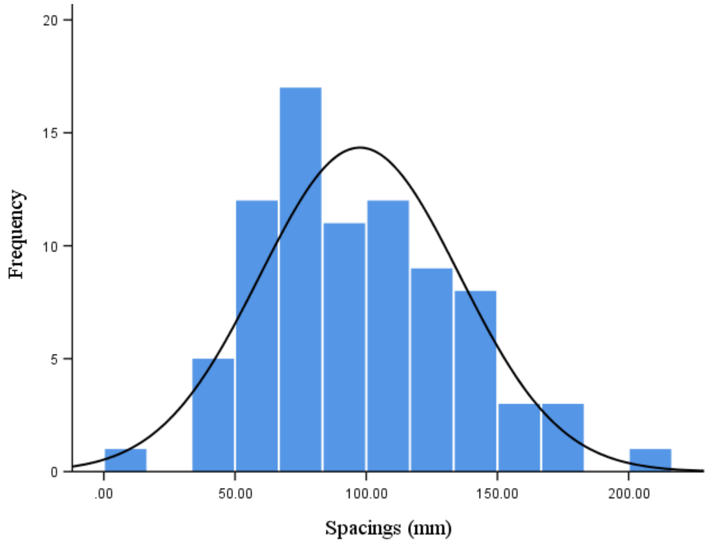

Figure 4.12. Frequency distribution of the measured crack spacings of all cracked prisms

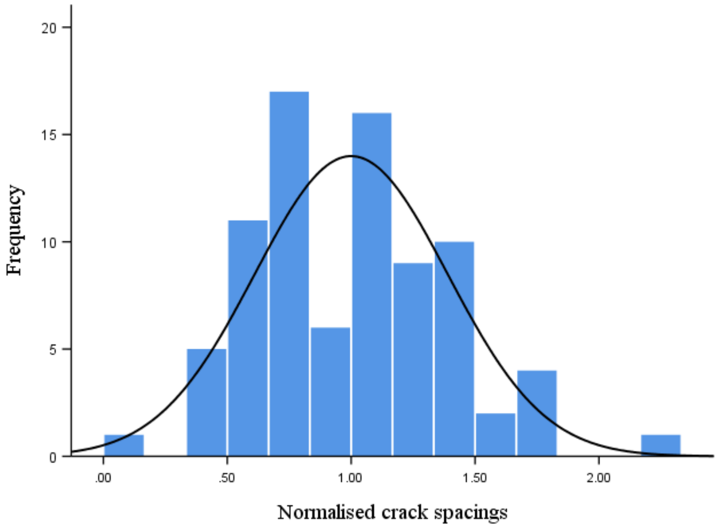

Figure 4.13. Frequency distribution of the normalised crack spacings

4.4.1.2 Predicting crack spacings

4.4.1.2.1 RC

To examine crack spacing in FRC overlays, it is worth examining the effect of fibres on cracks in conventional reinforced concrete (RC). The addition of fibres to RC is expected to reduce crack spacing compared with conventional RC without fibres, due to the reduction in the tensile stresses in the longitudinal bars at the cracked section [10, 30]. Assuming the bond stress along the bar is constant, the transfer length is expected to reduce to maintain equilibrium of forces between the cracked section and the no-slip section (Figure 4.14). It should be noted that the shear stress τ_{sm} is not uniform along the length of the bar, but the equilibrium principle is still valid when an average bond stress is assumed.

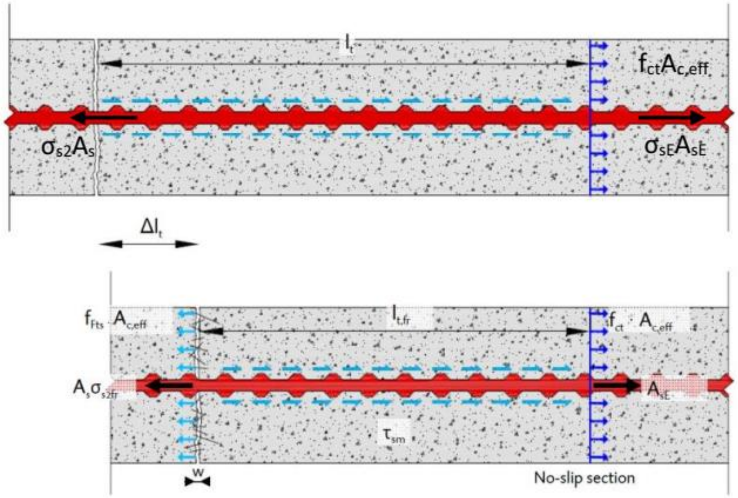

Figure 4.14. Effect of fibres in reducing transfer length, Groli (2014) [30].

4.4.1.2.2 No Fibres

Now, to understand the role of fibres on shrinkage crack spacing for composite concrete sections without conventional reinforcement, the crack spacing should be quantified for composite sections without fibres first.

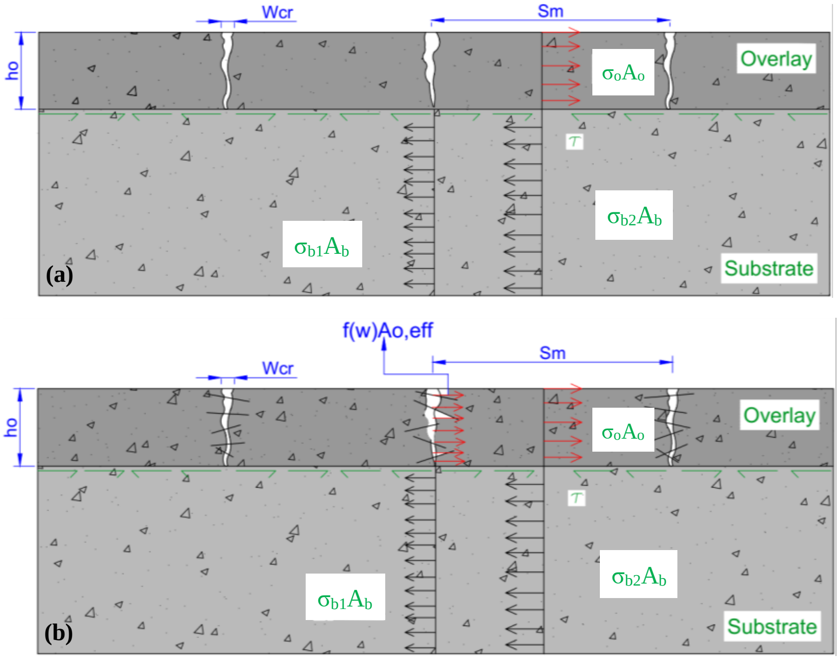

Figure 4.15. Concrete overly system with multiple cracks: (a) Plain overlay; (b) FRSC overlay

Figure 4.15shows a composite section with multiple cracks developed in an overlay layer due to shrinkage, as the base layer restrains the free shrinkage of the overlay through bond stress at the interface. As in the previous example, the stress levels shown in the figure along sections represent averages rather than the actual stress distributions which are more complex. In fact, the normal stress across the depth of each layer is not uniform due to shrinkage gradient and the shear stresses are also highly nonlinear. To facilitate calculations, average stresses and shrinkage strains are used.

To maintain equilibrium conditions between the cracked and free section, the following expressions are obtained:

$$\sigma_{b1}A_b = \sigma_{b2}A_b + \sigma_0 A_0$$

Equation 4.5

$$\sigma_{b1}A_b = \sigma_{b2}A_b + 0.5\, S_m \tau\, b$$

Equation 4.6

where, σ_{b1} is the nominal average stress of the base layer at the cracked section; A_b is the cross-sectional area of the base; σ_{b2} is the average stress of the base layer at the crack-free section; σ_o is the average stress of the overlay at the crack-free section; A_o is the cross-sectional area of the overlay; S_m is the average crack spacing; τ is the average shear stress at the interface between the overlay and the base; and b is the width of the overlay.

Since no reinforcement is added to the overlay, the contribution of the concrete layer is taken as zero at the cracked section. By using Equation 4.5 & Equation 4.6, the average crack spacing can be determined by:

$$S_m = \frac{2\sigma_0 h_0}{\tau} \quad \text{Equation 4.7}$$

4.4.1.2.3 With fibres

When fibre reinforced overlays crack, the stress at the crack locations does not drop to zero. Therefore, the shear stress at crack locations is expected to be smaller than the shear stress developed in plain overlays and the tensile contribution of the overlay, $f_{(w)}$ $A_{o,eff}$ (residual tensile strength multiplied by the effective area, see Figure 4.15.a) needs to be taken into account. This term should be included in Equation 4.5, resulting in Equation 4.8 for S_m of FRC overlays:

$$S_m = \frac{2\,(\sigma_o h_o - f_w\, h_{0,eff}\,)}{\tau} \quad \text{Equation 4.8}$$

Though the numerator is reduced, the average crack spacing is not anticipated to significantly decrease as the shear stress value will reduce as well. This is natural since the onset of cracking is dependent on the matrix tensile strength itself and not on the presence of fibres. This result differs from the case of conventional RC with fibres where the fibres are expected to reduce the crack spacing. In addition, the risk of delamination in FRSC overlays is lower as the developed shear stresses are smaller than in plain overlays. This may explain the absence of any delamination in the FRSC prisms examined in this study while two of the plain prisms locally debonded at their free edges.

Equation 4.7 and Equation 4.8 show that the crack spacing is proportional to the overlay depth and to the ratio of axial tensile stress to shear stress at the interface. Using these equations, the ratio of σ/τ is calculated using experimental crack spacings and the overlay depths, as shown in Table 4.4. The distribution of the calculated ratios rather follows the log normal distribution. If the average σ/τ value of 1.34 is used, then the average crack spacing of overlays is as in Equation 4.9:

$$S_m = 2.68\ h_o$$

Equation 4.9

Table 4.4 The calculated σ/τ using experimental crack spacings and the overlay depths

Spacing (mm)	Overlay depth (mm)	σ/τ	Spacing (mm)	Overlay depth (mm)	σ/τ	Spacing (mm)	Overlay depth (mm)	σ/τ
216	34	3.176	108	34	1.588	74	26	1.423
177	33	2.682	107	40	1.338	73	37	0.986
176	34	2.588	105	37	1.419	72	37	0.973
169	34	2.485	103	34	1.515	72	37	0.973
164	28	2.929	102	34	1.500	71	37	0.959
161	34	2.368	101	28	1.804	71	37	0.959
156	37	2.108	101	34	1.485	120	40	1.500
146	28	2.607	100	33	1.515	69	26	1.327
144	26	2.769	100	37	1.351	66	26	1.269
138	28	2.464	100	40	1.250	64	28	1.143
138	34	2.029	100	34	1.471	64	37	0.865
138	34	2.029	98	37	1.324	62	37	0.838
137	26	2.635	98	34	1.441	59	40	0.738
134	28	2.393	93	37	1.257	56	33	0.848
134	33	2.030	91	26	1.750	56	37	0.757
133	28	2.375	90	40	1.125	56	26	1.077
133	33	2.015	90	40	1.125	54	33	0.818
129	40	1.613	85	26	1.635	54	34	0.794
127	34	1.868	83	26	1.596	54	34	0.794
127	37	1.716	80	37	1.081	52	37	0.703
126	37	1.703	80	26	1.538	48	37	0.649
123	33	1.864	79	26	1.519	42	37	0.568
120	28	2.143	78	37	1.054	39	37	0.527
116	40	1.450	78	34	1.147	38	37	0.514
115	40	1.438	77	37	1.041	36	26	0.692
113	33	1.712	77	34	1.132	16	37	0.216
110	33	1.667	76	37	1.027			
108	37	1.459	74	40	0.925			

However, as the above result utilises average shear stress values, it is worth examining the expected shear distribution in cracked and uncracked overlays as high shear stresses could lead to delamination rather than cracking.

4.4.1.2.4 Shear distribution

For non-cracked prisms, the shear stress is expected to peak at the edges and substantially reduce towards the middle of the prism. The axial stresses are zero at the free edges and increase over a distance, defined as l_t, to a constant value ($\sigma_{x,max}$) (see Figure 4.16). When $\sigma_{x,max}$ exceeds the tensile strength of the overlay, the overlay section cracks and the tensile stress drops to zero and the shear stresses change accordingly. To quantify the stresses for non-cracked overlaid prisms, Jonasson [31,32] adopted the following equilibrium equations:

$$N_x = \int_{-H/2}^{-\frac{H}{2}+h_o} \sigma_x \, . \, dz \qquad \text{Equation 4.10}$$

$$\int_0^l \tau_{xz} \, . \, dx = N_x \qquad \text{Equation 4.11}$$

where, N_x is the normal force; σ_x is the overlay normal stress; τ_{xz} is the average shear stress along the interface; h_o is the overlay depth.

With the use of numerical analysis and assuming a triangular shear stress distribution with a maximum value of $\tau_{xz,max}$ at the free edge (Figure 4.17), Jonasson found that the shear distance (X_2) at which shear stresses reduce to zero is approximately three times the overlay depth ($3h_o$). As this distance leads to the peak normal stress σ_x, it means that this distance will eventually be the minimum crack spacing. This spacing value is slightly higher than the value of 2.68 found for the average spacing of the cracked overlay sections, which indicates that the triangular shear stress distribution is a conservative estimate.

For both RSC and FRSC, multiple cracks developed in the overlay layer (Figure 4.9) which indicates a strong bond condition. If the surfaces were not prepared well to develop good shear strength, then delamination might have occurred first. The recorded crack spacings approximately ranged between h_o and

$5h_o$. The results of this study agree with the observations of Laurence et al. [33] who noticed that, for 400 × 400 mm overlays, the crack pattern was rather related to the overlay depth, such that thicker overlays have bigger crack spacings and wider cracks. The reported spacings were of the order of 1-3 times the overlay depth. It should be remembered that smaller crack spacings are not necessarily an issue, as it is the maximum crack spacing that determines the maximum crack width.

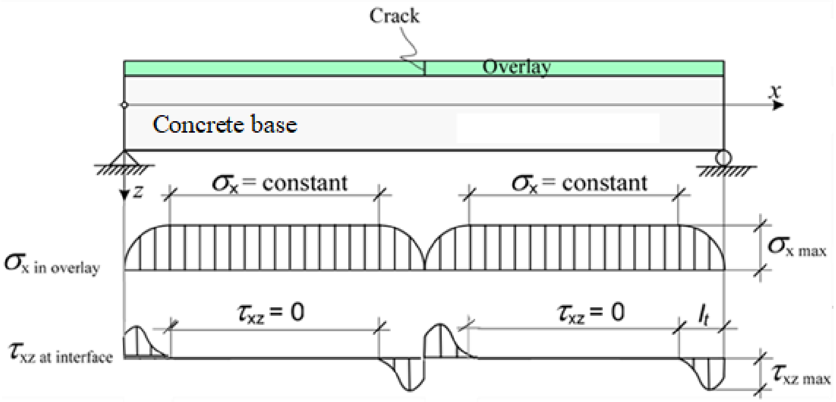

Figure 4.16. Assumed distribution of tensile stresses in the overlay and interfacial shear stresses (after Carlsward [2])

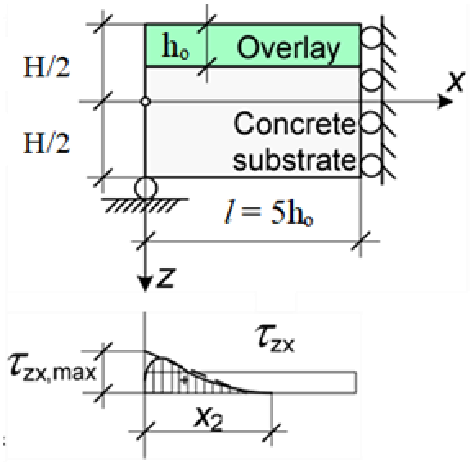

Figure 4.17. Interfacial shear stresses in the end zone due to normal stress σ_x at a distance l from the support, Jonasson [31]

It should also be noted that when assuming uniform shrinkage strain distribution and homogenous material properties, the crack is expected to start at the interface and propagate towards the upper layer of the overlay.

However, since the shrinkage distribution is in fact non-linear, with faster drying from the top layer that is relatively weaker, the crack starts at the top of the overlays and propagates downwards.

4.4.2 Restrained shrinkage

To estimate crack widths in overlays, the Swedish Concrete Society utilises the concrete free shrinkage strain ε_{cs} (see Equation 4.1). However, using the total free shrinkage strain will naturally overestimate the crack widths, as concrete is still restrained in between cracks.

The restrained shrinkage strain depends on the restraint level provided from the base (which can be quantified by using ψ). By using the restraint values shown in Figure 4.11, the predicted restrained shrinkage strain ($\varepsilon_{\mathrm{re}}$) versus the experimentally determined restrained strain values (obtained by subtracting the measured shrinkage strain on the top of the overlays from the free shrinkage strain) are given in Figure 4.18. It can be seen that using a constant ψ yields a fairly accurate value for the restrained shrinkage strain and can be adopted to predict crack widths in overlays. However, creep (ε_{cr}) should also be taken into account to obtain more accurate results.

It should be noted that the shrinkage at the top of the overlays should be used to predict crack widths due to restrained shrinkage. However, this is more difficult to obtain than the average shrinkage of free overlays with uniform shrinkage distribution, which can be easily obtained by using current code equations and parameters suggested by the authors in a previous study [24] or can be predicted numerically. A comparison between the two shrinkage values for RSC_1 is shown in Figure 4.19. Apart from the slight difference at the early ages, the uniform average shrinkage of overlays is accurate in predicting the shrinkage strain development at the top of restrained overlays and, hence, can be adopted in design.

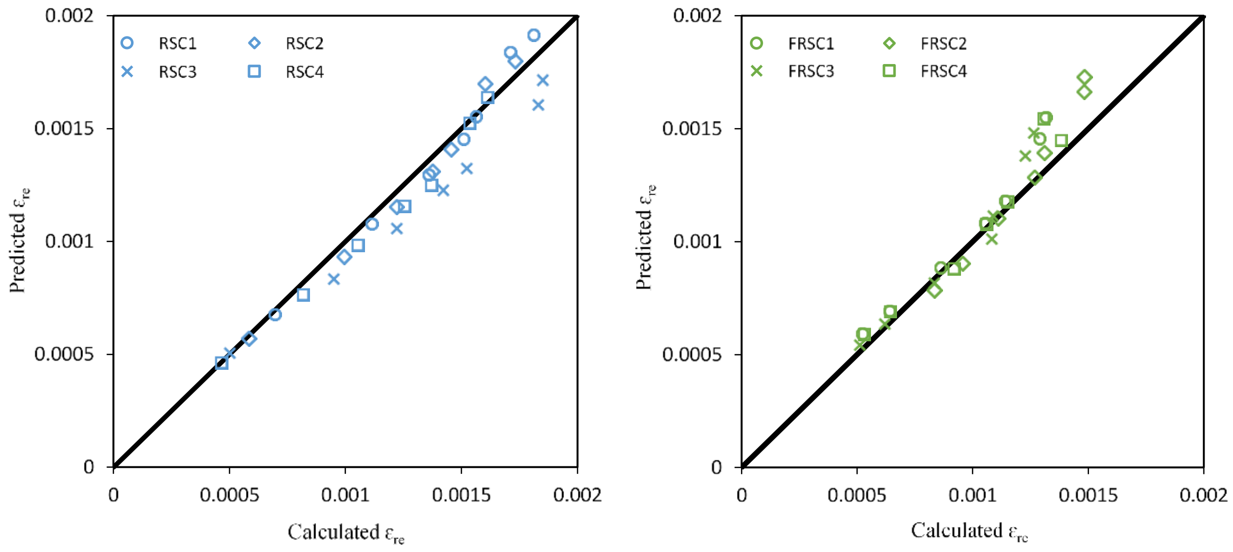

Figure 4.18. Calculated versus predicted restrained shrinkage of: (a) RSC; (b) FRSC prisms

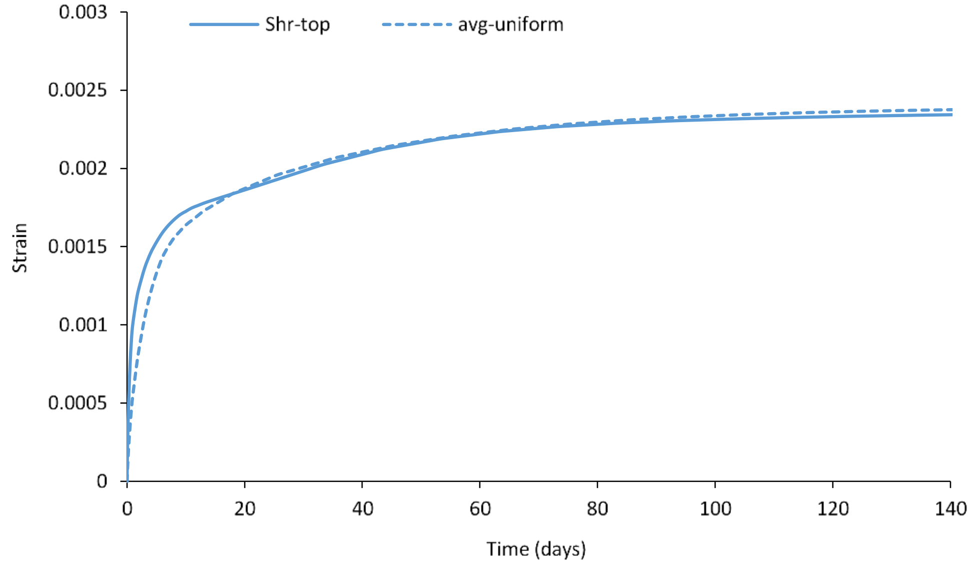

Figure 4.19. A comparison between shrinkage at the top of overlays and average shrinkage of RSC1

4.4.3 Crack width analysis

Based on the analytical crack spacing and experimental observations, the average crack width for unreinforced overlays can be roughly estimated as:

$$w_{cr,avg} = S_m \,.\, (\varepsilon_{cs} - \varepsilon_l - \varepsilon_{cr}) \qquad \text{Equation 4.12}$$

where, ε_{cs} is the free shrinkage strain; ε_l is the losses (unrestrained) strain and ε_{cr} is the creep strain. This equation can be written as:

$$w_{cr,avg} = S_m \,.\, (\psi.\, \varepsilon_{cs} - \varepsilon_{cr}) \qquad \text{Equation 4.13}$$

where, ψ is the restraint factor obtained using Equation 4.4.

The maximum crack width that develops in a plain overlay can be calculated by multiplying the average crack spacing by P (the percent of S_{max}/ S_{avg}, 1.7) . The maximum crack width thus can be estimated as:

$$w_{cr,max} = P.\, S_m \,.\, (\psi.\, \varepsilon_{cs} - \varepsilon_{cr}) \qquad \text{Equation 4.14}$$

For fibre reinforced overlays, the effect of fibres on cracking is normally considered by using the post-cracking flexural residual strength concept [12,14]. However, the flexural results of this study (see Figure 4.20) show a clear deflection hardening for all tests and, thus, the flexural residual strength factor will greater than one and negative cracking values will be predicted for such materials. Therefore, this concept should be adjusted to better consider the effect of fibres on shrinkage cracks.

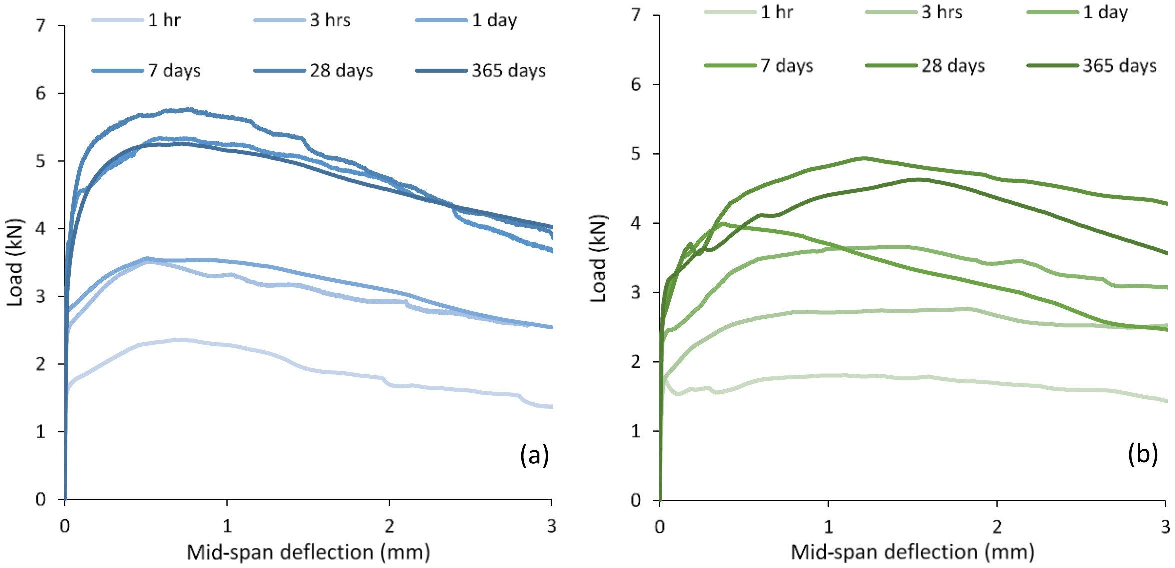

Figure 4.20. Load-deflection response of rapid hardening fibre reinforced mortars tested at different ages: (a) FCSA; (b) FRSC [9]

A close look at the tensile σ – ε relationships obtained by inverse analysis in a previous study conducted by the authors [9] (Figure 4.21) reveals that deflection hardening in the flexural test does not necessarily mean strain hardening in tension. Therefore, the tensile strength and post-cracking tensile stresses may offer a better material parameter to quantify the effect of fibres.

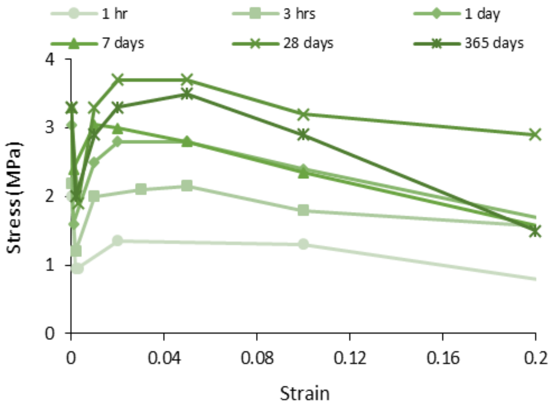

Figure 4.21. Tensile σ – ε curves for mixes at different ages for FRSC mixes

MC 2010 [16] uses the loss in stress f_{ctm}- f_{Ftsm} (where f_{ctm} is the concrete mean tensile strength and f_{Ftsm} is the average value of the residual strength of FRC) to consider the contribution of fibers in reducing crack widths in structural beams. Although the stress at the cracked section of FRC is a function of the crack width ($f_{(w)}$), it is reasonable to consider a constant stress value for serviceability limit checks.

Based on the above discussion, it is proposed that the maximum crack width of SFRC overlays is calculated by using the following equation:

$$\mathrm{w_{cr,max}} = \mathrm{P.s_m}.(\psi.\varepsilon_{cs}.-\varepsilon_{cr}).\left(1-\frac{\mathrm{f_{Ftsm}}}{\mathrm{f_{ct}}}\right) \qquad \textit{Equation 4.15}$$

MC 2010 [16] adopts the value of 0.45f_{R1} (residual flexural strength calculated at 0.5 mm CMOD) for f_{Ftsm}. This value, however, seems to overestimate the energy absorption capacity of FRSC at service loads for the mixes used in this study [9]. Similar observations were reported by Hu et al. [34] when modeling flexural results of concrete reinforced with industrial and post-consumer recycled steel fibres. Therefore, Hu et al. [34] suggested using 0.27f_{R1} for predicting the stress at the serviceability limits of concrete reinforced with blends of MSF and RTSF.

To determine the relationship between the actual tensile stress (σ_1) obtained from inverse analysis [9] at the serviceability limit and the residual strength (f_{R1}) for matrices reinforced with RCSF, it was decided to normalise σ_1 by f_{R1} obtained from flexural tests. As only one fibre dosage and one fibre length was used in this study, the results of Hu et al. [8], who tested concrete prisms reinforced with different RSCF and RTSF dosages, are also considered. Three mixes reinforced with 45 kg/m^3 of 60 mm RCSF, 30 kg/m^3 of 60 mm RCSF and a mix with 35 kg/m^3 of 60 mm and 10 kg/m^3 of post-consumer steel fibres are included. For the mixes tested in this study, only the results of mature mixes (at ages of 28 days and 365 days) are considered. The $\sigma_{1/}$ f_{R1} ratios for the five mixes are shown in Figure 4.22. As the value are characterised by a low scatter, the average value of $0.2f_{R1}$ is considered reasonable to calculate the f_{Ftsm} for matrices reinforced with RCSF.

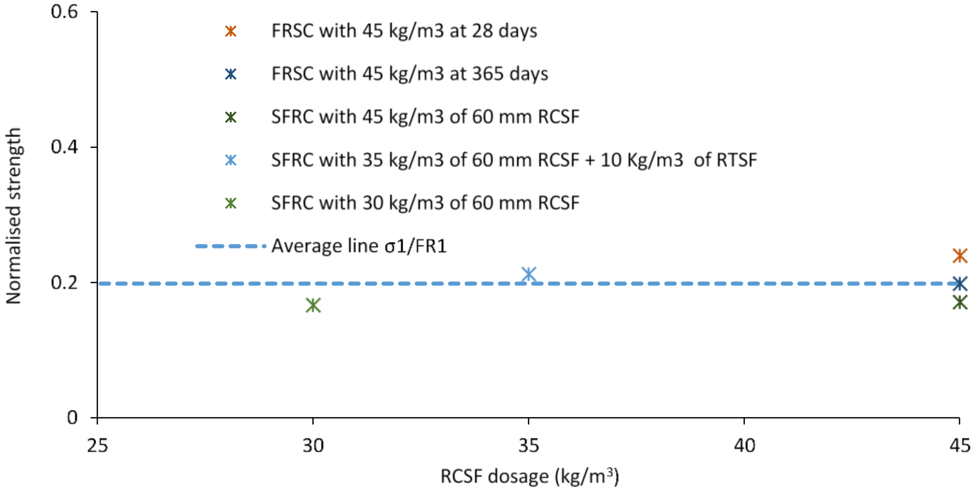

Figure 4.22. Relationship between RCSF dosage contained in each SFRC mix and σ_1/f_{R1} ratio

The predicted maximum crack widths of RSC and FRSC overlays using Equation 4.14 & Equation 4.15 versus the measured maximum crack widths are given in Figure 4.23. The average value for the ratio of predicted crack width to measured crack width is 1.08 and 1.06 for RSC and FRSC, respectively, while their corresponding standard deviations are 0.51 and 0.19. It can be seen that the proposed equations can predict the maximum crack widths fairly well.

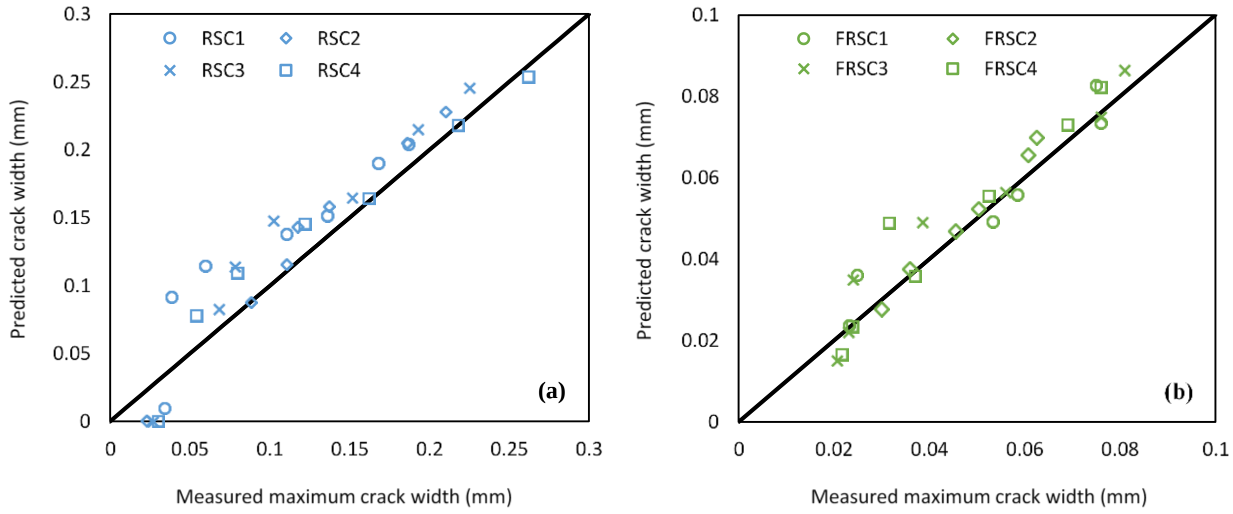

Figure 4.23. Predicted versus measured crack widths for overlays of: (a) RSC; (b) FRSC

4.5 Flexural behaviour of composite prisms

The load - deflection behaviour of all fibre reinforced composite prisms is shown in Figure 4.24. It should be kept in mind that RSC and FRSC prims were cracked prior to testing due to restrained shrinkage, while CSA and FCSA composite prisms were uncracked. The plain prisms failed directly after developing a major crack at the middle third part of the prism that started at the lower surface of the overlay and propagated into the substrate layer. For clarity, these results are not shown in Figure 4.24. The composite flexural load and the estimated capacity of the substrate layers alone (shown in brackets) are listed in Table 4.5. The RSC prisms presented the lowest loading capacity (very near the capacity of the overlay alone), while the FRSC specimens showed considerable resistance despite being cracked. Both FCSA and FRSC prisms continued to carry load after the peak load, but their capacity gradually decreased with increasing displacement. For RSC and FRSC prisms, the failure flexural crack always developed from a shrinkage crack. The flexural capacity of FCSA prisms is much higher than that of the cracked FRSC specimens. It should be noted that the two RSC prisms, which exhibited local debonding at the end of the drying period, did not show any further delamination upon loading and development of flexural cracking.

Table 4.5 Maximum load capacity for all composite prisms and their estimated substrate capacity (in brackets). All values are in kN.

Mix	*Prisms*			
CSA	*CSA₁*	*CSA₂*	*CSA₃*	*CSA₄*
	31.99 (22.19)	32.89 (22.19)	33.25 (19.99)	33.12 (19.99)
FCSA	*FCSA₁*	*FCSA₂*	*FCSA₃*	*FCSA₄*
	46.80 (21.24)	40.97 (23.83)	48.38 (19.69)	47.44 (19.69)
RSC	*RSC₁*	*RSC₂*	*RSC₃*	*RSC₄*
	23.56 (22.84)	23.42 (21.24)	25.13 (20.92)	18.50 (19.08)
FRSC	*FRSC₁*	*FRSC₂*	*FRSC₃*	*FRSC₄*
	32.34 (21.55)	35.87 (23.50)	37.16 (20.92)	37.15 (20.92)

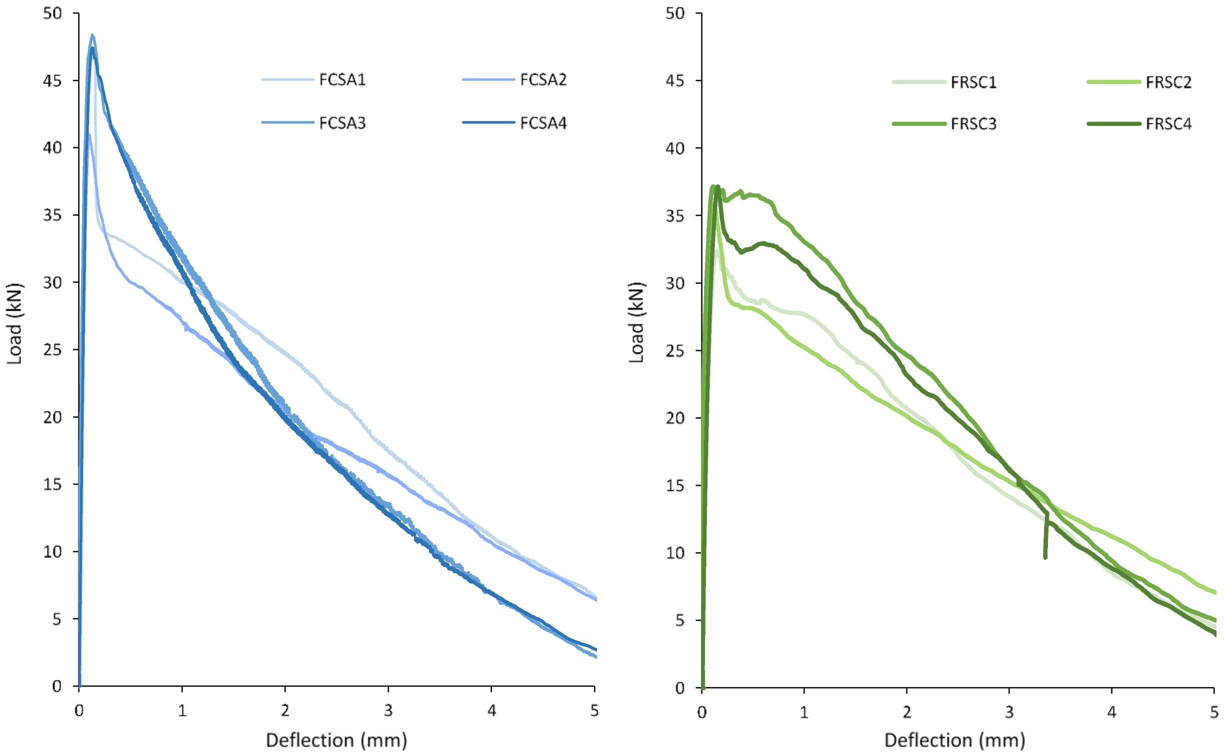

Figure 4.24. Load versus average deflection of composite prisms with: (a) FCSA; (b) FRSC overlays

In order to analyse a fully bonded composite beam, Gere [35] employed the classical beam theory concepts and derived the following expressions (Equation 4.16 & Equation 4.17):

$$E_1 \int_1 ydA + E_2 \int_2 ydA = 0$$ *Equation 4.16*

$$\sigma_2 = \frac{MyE_2}{E_1 I_1 + E_2 I_2}$$ *Equation 4.17*

where, σ_2 is the flexural stress of the lower layer; M is the applied bending moment; y is the distance from the bottom fibre to the neutral axis, E_1 & E_2 are the moduli of elasticity of the top and lower layer materials, respectively; I_1 & I_2 are the moments of inertia of the top and bottom layer materials with respect to the neutral axis, respectively.

The predicted capacity of the fully composite prisms, using these Equations, is given in Table 4.6. As can be seen, shrinkage has a considerable impact on the flexural capacity of overlays. However, the fibres reduced this effect after hygral cracking development. Therefore, it is expected that fibre reinforced overlaid pavements will withstand much higher fatigue loads than plain overlays.

Table 4.6 Tensile stresses that develop at the overlay bottom under the flexural loading (MPa)

Mix	*Prisms*				*Average stress*	$f_{ctm,fl}$	*Loss in flexural strength (%)*
CSA	CSA_1	CSA_2	CSA_3	CSA_4	3.52	5.40	34.8
	3.40	3.54	3.57	3.56			
FCSA	$FCSA_1$	$FCSA_2$	$FCSA_3$	$FCSA_4$	5.41	8.67	37.6
	5.62	4.68	5.72	5.61			
RSC	RSC_1	RSC_2	RSC_3	RSC_4	2.38	4.48	46.9
	2.42	2.48	2.60	2.03			
FRSC	$FRSC_1$	$FRSC_2$	$FRSC_3$	$FRSC_4$	4.16	5.63	26.11
	3.75	4.18	4.29	4.43			

4.6 Shear tests results

The max shear load, displacement and strength values of all specimens tested in shear are reported in Table 4.7 along with their standard deviation (listed in brackets). As the interface surface of all prisms was rough and clean when overlaid, the shear strength of these mixes was expected to be relatively high. It should be noted that several plain and fibre reinforced specimens developed two shear plane failures.

MC 2010 [16] suggests the following equation to predict the design shear strength of composite concrete sections without reinforcement crossing the interface:

$$V_u = C_h . f_{ctd} \qquad \text{Equation 4.18}$$

where, V_u is the ultimate shear strength, (MPa); C_h is a coefficient of cohesion, a value of 0.5 is suggested for an indented surface (shear keys).

If the tensile strength of the weakest surface is considered (substrate) (based on recommendations of MC [16]), then the predicted shear strength (using Equation 4.18) is around 1.5 MPa. This value is significantly lower than the experimental values obtained for well-prepared surfaces. It should also be mentioned that the fibres seems to have a positive effect on the shear strength of overlays.

Table 4.7 Maximum shear load (kN), displacement (mm) and strength (MPa) for different mixes

Specimen	$FCSA_1$	$FCSA_2$	$FCSA_3$	CSA_1	CSA_2	CSA_3
Load	126	117	154	96	140	139
Displacement	(0.007)	(0.006)	(0.014)	(0.002)	(0.015)	(0.009)
Shear mean load	132			125		
Shear strength	2.8	2.6	3.4	2.1	3.1	3.1
Mean	2.9 (0.4)			2.8 (0.6)		
Specimen	FRSC_1	FRSC_2	FRSC_3	RSC_1	RSC_2	RSC_3
Load	171	129	118	100	97	107
Displacement	(0.004)	(0.008)	(0.008)	(0.005)	(0.012)	(0.004)
Shear mean load	139			101		
Shear strength	3.8	2.9	2.6	2.2	2.2	2.4
Mean	3.1 (0.6)			2.2 (0.1)		

4.7 Conclusions

This paper presents an experimental and analytical investigation of on the evolution of hygral stresses, strains and cracking in rapid hardening plain and fibre reinforced mortar layers used for repairs. The main findings are:

- The measured shrinkage strain on composite prisms depends on the free shrinkage strain of the overlay mix and the relative dimensions of the layers.
- None of the CSA and FCSA overlays showed any cracking for the duration of the test. Although RSC

and FRSC overlays developed multiple cracks at the edges of the prisms in less than 16 hours, minimum or no delamination was observed. This is attributed to the good bond conditions developed by good surface preparations.

- Shrinkage strains are not uniform across the depth of the overlay as the top layer tends to have higher shrinkage values compared to the lower part of the overlay. This results in shrinkage gradient across the depth, and bigger shrinkage cracks at the top.
- It is shown that fibres have little effect on the crack spacing of concrete overlays and that the ratio between maximum and average crack spacings is approximately 1.7, which coincides well with the value suggested by MC 2010 to quantify the ratio of crack spacing for conventional RC. A simple analytical model is presented to estimate the spacing of cracks of overlays.
- None of the available approaches in literature can predict the contribution of RCSF on the crack width of overlays. A simple approach, based on tensile stress loss, is developed to predict the crack width of RCSF reinforced overlays. The predicted widths of cracks of RSC and FRSC composite prisms using the suggested approaches agree well with the measured experimental crack widths.
- RCSF was found to reduce the width of cracks by around 60% for fibre reinforced overlays compared to plain overlays.
- Restrained shrinkage and subsequent cracking have a negative impact on the flexural capacity of composite prisms. However, RSCF tend to mitigate this effect by bridging cracks and providing higher resistance to flexural loads. Therefore, the use of fibre reinforced concrete for the repair of structures is expected result in better durability and extended fatigue life.
- Fibres are found to have a positive effect on the interfacial shear strength of overlays.

References

1. Beushausen, H., Alexander, M.G., (2006). Failure mechanisms and tensile relaxation of bonded concrete overlays subjected to differential shrinkage. *Cem. Concr. Res.* 36 (10), 1908-1914. Available at: https://www.sciencedirect.com/science/article/pii/S0008884606001608.

2. Carlsward, J., (2006). *Shrinkage Cracking of Steel Fibre Reinforced Self Compacting Concrete Overlays*. Doctoral Thesis. Lulea University of Technology. Department of Civil and Environmental Engineering, Sweden.

3. Turatsinze, A., Granju, J.L., Bonnet, S., (2006). Positive synergy between steel-fibres and rubber aggregates: Effect on the resistance of cement-based mortars to shrinkage cracking. *Cem. Concr. Res.*, 36 (9), 1692-1697.

4. Lupien, C., Chanvillard, G., Aitcin, P-C., Gagne, R., (1995). Rehabilitation dune chaussee par resurfacage mince adherent en beton renforce de fibres dacier. Proceeding of AIPCR, comite C-7, Montreal, Canada. 246-250. Cited in: Bissonnette, B., Courard, L., Fowler, D.W. and Granju, J.L., (eds.), (2011). Bonded Cement-based Material Overlays for the Repair, the Lining or the Strengthening of Slabs or Pavements: State-of-the-art Report of the RILEM TC 193-RLS. Springer, Dordrecht.

5. Lupien, C., Chanvillard, G., Aitcin, P-C., Gagne, R., (1990). Rehabilitation dune chaussee en beton avec une chape mince en beton renforce de fibres dacier. In les techniques de transport au service de la qualite de vie, Expose des communications du 25 congres annuel de IAQTR. Montreal. 108-122. Cited in: Bissonnette, B., Courard, L., Fowler, D.W. and Granju, J.L., (eds.), (2011). Bonded Cement-based Material Overlays for the Repair, the Lining or the Strengthening of Slabs or Pavements: State-of-the-art Report of the RILEM Technical Committee 193-RLS. Springer, Dordrecht.

6. Chanvillard, G., Aitcin, P.C., Lupien, C., (1989). Field Evaluation of Steel-Fiber Reinforced Concrete Overlay with Various Bonding Mechanisms. Transportation Research Record, 1226, 48-56.

7. Chanvillard, G. and Aitcin, P.C., (1990). Thin bonded overlays of fiber-reinforced concrete as a method of rehabilitation of concrete roads. *Can. j. civ. Eng.*, 17(4), 521-527.

8. Hu, H., Papastergiou, P., Angelakopoulos, H., Guadagnini, M., Pilakoutas K., (2018). Mechanical properties of SFRC using blended recycled tyre steel cords and recycled tyre steel fibres, *Constr. Build. Mater.*, 187, 553-564. Available at: https://www.sciencedirect.com/science/article/pii/S0950061818318750?via%3Dihub.

9. Al-musawi, H., Figueiredo, F., Bernal, S.A., Guadagnini, M., Pilakoutas, K., (2019). Performance of rapid hardening recycled clean steel fibre materials. *Constr. Build. Mater.*,195, 483-496.

10. Al-Kamyani, Z., Guadagnini, M., Pilakoutas, K., (2018). Impact of Shrinkage on Crack Width and Deflections of Reinforced Concrete Beams with and without Steel Fibres. *Eng. Struct.*, Submitted for Publication.

11. Malmgren, L., Nordlund, E., Rolund, S., (2005). Adhesion strength and shrinkage of shotcrete. *TUNN UNDERGR SP TECH*, 20(1), 33-48.

12. Concrete Report No. 13, (2006). Draft version of the Swedish Concrete Society report on Industrial Floors (In Swedish). Swedish Concrete Society, Report no 13. Cited in: Carlsward, J., (2006). *Shrinkage Cracking of Steel Fibre Reinforced Self Compacting Concrete Overlays*. Doctoral Thesis. Lulea University of Technology. Department of Civil and Environmental Engineering, Sweden.

13. Concrete Report No 4, (1995). Steel fibre concrete – Recommendations for the design, construction and testing (In Swedish). Swedish Concrete Society, Report no 4. Cited in: Carlsward, J., (2006). *Shrinkage Cracking of Steel Fibre Reinforced Self Compacting Concrete Overlays*. Doctoral Thesis. Lulea University of Technology. Department of Civil and Environmental Engineering, Sweden.

14. Kim, M.O., Bordelon, A.C., Lee, N.K., (2017). Early-age crack widths of thin fiber reinforced concrete

overlays subjected to temperature gradients. *Constr. Build. Mater.*, 148, 492-503.

15. ASTM C1609/C16609M, (2012). Standard test method for flexural performance of fiber-reinforced concrete (using beam with third-point loading). ASTM International, West Conshohocken (PA), United States.

16. F.I. du Béton, (2013). Fib Model Code for Concrete Structures 2010, Wilhelm Ernst & Sohn, Berlin, Germany.

17. Santos, P.M., Julio, E.N., (2007). Correlation between concrete-to-concrete bond strength and the roughness of the substrate surface. *Constr. Build. Mater.*, 21(8), 1688-1695. Available at: https://www.sciencedirect.com/science/article/pii/S0950061806002005.

18. Santos, P.M., Julio, E.N., (2014). Interface Shear Transfer on Composite Concrete Members. ACI Struct. J., 111(1), 113-122.

19. Li, M., Li, V.C., (2006). Behavior of ECC/concrete layered repair system under drying shrinkage conditions. J. Restoration Build. Monuments, 12, 143-160.

20. Zanotti, C., Rostagno, G., Tingley, B., (2018). Further evidence of interfacial adhesive bond strength enhancement through fiber reinforcement in repairs. *Constr. Build. Mater.*, 160, 775-785.

21. BS EN 13892-2, (2002). Methods of test for screed materials — Part 2: Determination of flexural and compressive strength.

22. JSCE-SF4, (1984). Standard for Flexural Strength and Flexural Toughness, Method of Tests for Steel Fiber Reinforced Concrete, Concrete library of JSCE, Japan Concrete Institute (JCI), Japan.

23. Momayez, A., Ramezanianpour, A.A., Rajaie, H., Ehsani, M.R., (2004). Bi-surface shear test for evaluating bond between existing and new concrete. *ACI Mater. J.*, 101(2), 99-106.

24. Al-musawi, H., Figueiredo, F., Guadagnini, M., Pilakoutas, K., (2019). Shrinkage properties of plain and recycled steel–fibre-reinforced rapid hardening mortars for repairs. *Constr*. *Build*. *Mater*., 197, 369-384. Available at:

https://doi.org/10.1016/j.conbuildmat.2018.11.099.

25. Jeong, J.H., Park, Y.S., Lee, Y.H., (2015). Variation of Shrinkage Strain within the Depth of Concrete Beams. Materials, 8(11), 7780-7794.

26. Younis, K.H., Pilakoutas, K., (2016). Assessment of post-restrained shrinkage mechanical properties of concrete. *ACI Mater*. *J*., 113(3), 267-276.

27. Al-Kamyani, Z., Guadagnini M., and Pilakoutas, K., (2018). Predicting shrinkage induced curvature in plain and reinforced concrete. *Eng*. *Struct*. *J*., 176, 468-480. Available at: https://www.sciencedirect.com/science/article/pii/S014102961831023X.

28. Silfwerbrand, J., (1997). Stresses and strains in composite concrete beams subjected to differential shrinkage. *ACI Struct*. *J*., 94(4), 347-353.

29. IBM SPSS Statistics, Version 25.

30. Groli, G., (2014). *Crack width control in RC elements with recycled steel fibres and applications to integral structures: theoritical and experimental study*. PhD thesis. Madrid, Polytechnic University of Madrid.

31. Jonasson, J.-E. (1977). Computer programs for non-linear analyses of concrete in view of shrinkage, creep and temperature. (In Swedish), CBI Research Report 7:77, Swedish Cement and Concrete Institute, Stockholm, Sweden. Cited in: Carlsward, J., (2006). *Shrinkage Cracking of Steel Fibre Reinforced Self Compacting Concrete Overlays*. Doctoral Thesis. Lulea University of Technology. Department of Civil and Environmental Engineering, Sweden.

32. Jonasson, J.E., (1978). Analysis of creep and shrinkage in concrete and its application to concrete top layers. *Cem. Concr. Res.*, 8(4), 441-454.

33. Laurence, O., Bissonnette, B., Pigeon, M., Rossi, P., (2000). Effect of Steel Macro Fibres on Cracking of Thin Concrete Repairs. In Proceedings of the 5th International RILEM Symposium on Fibre-Reinforced Concretes (BEFIB 2000), Sep. 13-15, Lyon, France, RILEM Publications SARL, 213-222.

34. Hu, H., Wang, Z., Figueiredo, F., Papastergiou, P., Guadagnini, M., Pilakoutas, K., (2018). Post-cracking tensile behaviour of blended steel fibre reinforced concrete. *Struct. Concr*. Submitted for publication.

35. Gere, J.M., (2004). Mechanics of Materials, Brooks. Cole, Pacific Grove. SIXTH EDITION.

Chapter 5: A numerical study on the effect of restrained shrinkage on rapid hardening plain and recycled clean steel fibre concrete overlays

Al-musawi, H., Huang, H., Guadagnini, M., Pilakoutas, K., (2019). A numerical study on the effect of shrinkage on rapid hardening plain and recycled steel fibre concrete overlays. Submitted for publication.

Abstract

This article presents FE numerical studies on restrained shrinkage of plain and fibre reinforced rapid hardening mortars. Moisture diffusivity analysis is coupled with structural analysis to calculate the evolution of hygral stresses, strains and cracking over time. The numerical results are validated against results from analytical models and compared to measured experimental values. Parametric studies are carried out to examine the effect of the interface stiffness, moisture content of the substrate layer and overlay depth on restrained shrinkage strain and stresses of overlays. Fibre inclusion is shown to reduce the risk of deterioration by slowing down the evolution of local slippage and controlling crack widths. It is also found that the uniform shrinkage strain distribution that is assumed in analytical models underestimates the hygral tensile stresses of overlays compared to real non-linear strain distribution. A modification to account for this effect is proposed through shrinkage amplification factor. This approach is expected to provide a better estimation of the risk of cracking in overlays.

This chapter consists of a "stand alone" journal paper and includes a relevant bibliography at the end of the chapter. Additional information and further test results are presented in Appendix A, B and C.

5.1 Introduction

Restrained shrinkage can lead to cracking and/or delamination of concrete overlays and is a dominant mechanism in overlay deterioration. Modelling restrained shrinkage of concrete overlays is rather complex since it depends on multiple time-dependent properties relating to geometrical, hygral and material characteristics. Thus, for accurate prediction of shrinkage strain and concrete damage development with time, a time dependent fracture-based analysis that considers the stress-strain behaviour of the materials at different ages, accurate interfacial properties and moisture transfer characteristics should be used.

Groth [1] analysed the cracking performance of restrained shrinkage of concrete overlays of various depths using a fracture-based approach referred to as the inner softening band (ISB) method. The analysis shows that, for well bonded overlays, multiple cracks develop during the first week followed by selective crack growth in the weeks after. The density of cracks tends to increase for thinner overlays, for which the presence of fibres was found to be less important in distributing cracks. For thicker overlays, however, fibres were shown to play a dominant role in cracks distribution. However, in his study, the restraint from the substrate was assumed to be 100% and the effect of moisture transfer between the overlay and the base layer was not examined. These simplifications can lead to errors as even for very thin overlays, the restraint level is not expected to be 100% and there is always some moisture exchange with the base layer.

Kim and Bordelon [2] modeled FRC overlays constructed over hot mixed asphalt (HMA) pavements to investigate the effect of the fracture properties of the FRC overlay and the interface on joint opening width and interface delamination. Cohesive based surfaces with linear traction-separation behaviour were assigned for both contact areas across the joint location and along the interface between FRC overlays and HMA. The results show that for large slab sizes (3.35 m long), increasing the fracture energy of the FRC leads to reductions in joint crack width of 11%. The crack widths and debonding lengths at the interface reduce when the fracture energy of the FRC increases and when the interfacial tensile bond strength increases. However, the development of the fracture properties with time was not considered and the shrinkage and thermal strains were calculated using simple constant thermal loads applied at specific ages by using equivalent deflection.

Orta and Bartlett [3,4] presented investigations on the time dependent stress distributions in concrete bridge deck overlays due to restrained shrinkage. The drying humidity movement was modelled by using nonlinear application of Fick’s second law of diffusion, while the autogenous humidity loss was modelled by using an empirical equation. It was found that the moisture distribution, and consequently the shrinkage strain, is nonlinear across the depth of the overlay. The maximum shrinkage strains occurred at the top and bottom fibres while the maximum swelling strain for the substrate was at the interface (see Figure 5.1). Humidity profiles were found to depend on the overall depths of the overlay and the substrate layers. At early ages of drying, the overlay experiences large gradients of stresses at its top and bottom parts while maximum tensile stresses develop at mid-depth of the overlay at later ages (Figure 5.2). This approach can be used to assess the likelihood of cracking of plain concrete overlays. However, the beneficial role of fibres in controlling the width of cracking cannot be quantified as the overlay was assumed to be a linear elastic material.

This paper focuses on the numerical prediction of overlays performance under restrained shrinkage and subsequent deterioration, using non-linear time dependent material properties and variable moisture levels. Initially, a brief on experimental studies performed is presented. Then, the numerical modelling details and approaches are introduced, and the FE analysis results are validated using predictions from the Silfwerbrand analytical procedure [5]. Experimental results undertaken by the authors are modelled in Abaqus [6] and the numerical shrinkage evolution with time is compared with experimentally measured strains. Parametric studies are preformed to investigate the effect of overlay depth, mechanical and hygral properties of the interface and moisture content of the substrate on the shrinkage and cracking behaviour of rapid hardening overlays. Additional parametric studies are conducted to investigate the impact of non-linear shrinkage distribution across the depth of overlays on the development of tensile stresses and, thus, on the risk of cracking estimation. Finally, the experimental results of interfacial shear strength of small prismatic specimens are modelled and analysed.

This This chapter addresses objectives 11-13 of the thesis.

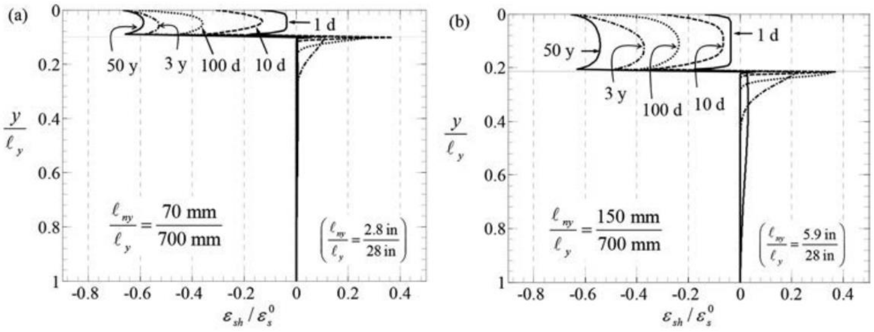

Figure 5.1. Humidity profiles at different drying times for: (a) 70 mm; (b) 150 mm overlay (after Orta and Bartlett)

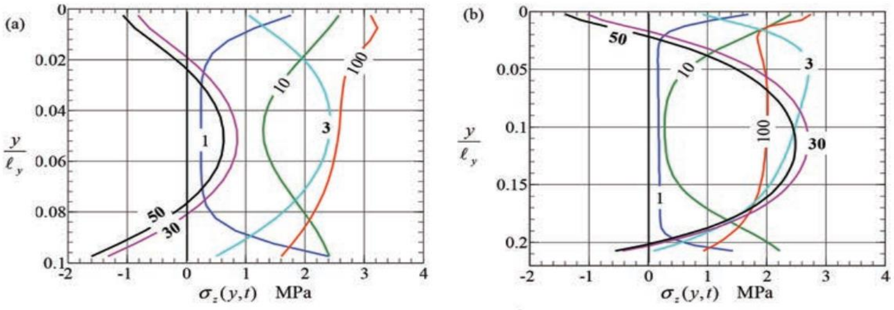

Figure 5.2. Overlay stress profiles for different overlay depths: (a) ℓny = 70 mm; (b) ℓny = 150 mm overlay (after Orta and Bartlett)

5.2 Experimental studies

5.2.1 Mix proportions, characteristics and mechanical properties

Two plain and two SFRC mixes are examined for overlay layers, details of which are presented in Table 5.1. Two commercial cement types are used; calcium sulfoaluminate cement (CSA) and rapid setting calcium aluminate cement (RSC), each at 600 kg/m^3. River washed sand (0-5mm, SG=2.65) is used as fine aggregate. Recycled clean steel fibres (RCSF) were sourced from tyre cords extracted from un-vulcanised rubber belts at a length of 21 mm and diameter of 0.2 mm. Further details on the mixes and material characteristics are given elsewhere [7]. For the concrete substrates (Sub, see Table 5.1), conventional ready mixed concrete (86 kg/m^3 of CEM I 52,5N; 105 kg/m^3 of GGBS, 1060 kg/m^3 of 20 mm graded Limestone as coarse aggregate and 900 kg/m^3 of fine aggregate) are used.

To characterize the flexural performance of overlay mixes, three 40*40*160 mm mortar prisms (Figure 5.3) were tested according to BS EN 13892-2, (2002) [8] in displacement control. To obtain net deflection, a specially designed aluminum yoke was mounted on the specimens. After flexural testing, the two fractured parts were tested under uniaxial compressive loading, according to BS EN 13892-2, (2002) [8]. The prisms were tested at various ages, ranging from one hour up to one year. The results of first cracking strength ($f_{ctm,fl}$) and compressive strength (f_{cu}), with corresponding standard deviation values (listed in brackets) are given in Table 5.1.

To determine the compressive strength of the substrate mix, 6 cubes of 150 mm were tested under uniaxial compressive loading according to BS EN 12390-3 (2009) [9] at the age of 28 days (see Table 5.1).

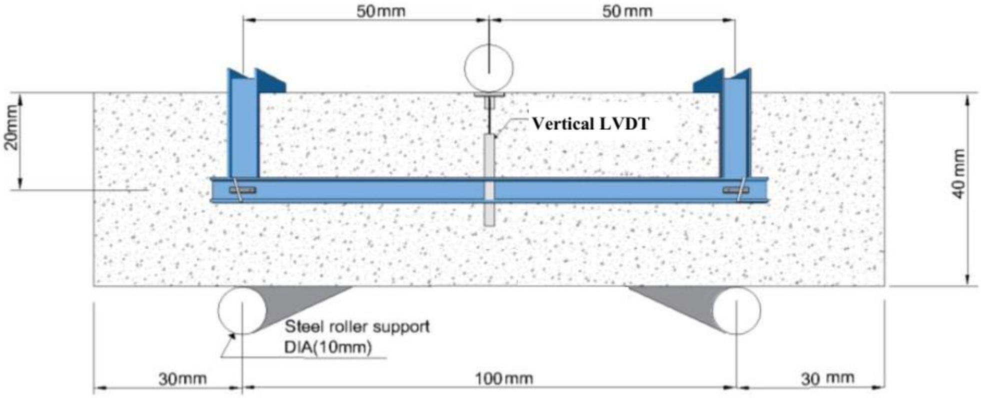

Figure 5.3. Flexural test set up of overlay mixes

Table 5.1 Mix proportions and flexural strength ($f_{ctm,fl}$) and compressive strength (f_{cu}) for all mixes (MPa)

Mix	*Fibre dosage (kg/m^3)*	*Sand (kg/m^3)*	*SP^a*	*w/c ratio*	*1 hr*	*3 hrs*	*1 day*	*7 days*	*28 days*	*365 days*
					$f_{ctm,fl}$ f_{cu}	$f_{ctm,fl}$ f_{cu}	$f_{ctm,fl}$ f_{cu}	$f_{ctm,fl}$ f_{cu}	$f_{ctm,fl}$ f_{cu}	$f_{ctm,fl}$ f_{cu}
CSA	0	1420	0.60	0.40	2.6 21.1 (0.2) (3.0)	4.0 26.9 (0.2) (2.8)	4.3 31.8 (0.2) (2.5)	5.3 36.0 (0.3) (3.0)	5.4 38.6 (0.3) (2.3)	5.4 40.9 (0.3) (2.3)
FCSA	45	1420	0.61	0.41	3.5 26.1 (0.4) (4.6)	6.8 31.6 (0.5) (3.7)	6.5 36.6 (0.5) (2.3)	8.2 41.1 (0.8) (3.3)	8.7 43.1 (0.9) (3.2)	8.7 45.5 (1.0) (3.0)
RSC	0	1300	0.20	0.35	2.5 17.2 (0.2) (1.9)	2.9 24.2 (0.2) (2.0)	3.5 33.0 (0.1) (2.0)	4.2 (0.2) 40.4 (2.4)	4.4 46.5 (0.2) (2.6)	4.5 48.1 (0.1) (3.7)
FRSC	45	1300	0.21	0.36	3.5 (0.2) 21.3 (3.0)	3.5 (0.2) 28.3 (3.5)	5.0 (0.2) 37.9 (2.4)	5.5 (0.3) 46.2 (3.2)	5.7 (0.3) 51.5 (2.9)	5.6 54.5 (0.3) (6.6)
Sub	0	900	1.14^b	0.5	-	-	-	-	27.0 (3.0)	-

^{a} % by cement mass, ^{b} Pozzolith 324N Plasticiser (Litre).

5.2.2 Moisture transfer and shrinkage properties

To obtain the time history of the moisture profile, needed to obtain the moisture diffusivity of the repair layers, a modified gravimetric method was used by the authors in a previous study [10]. The MC equation [11] that relates moisture diffusivity to relative humidity was used to obtain the first estimate of moisture diffusivity. These values were then used in heat transfer analysis (capitalising on the analogy between heat and moisture transfer analysis) to obtain the moisture distribution over time. The moisture diffusivity curve was determined through back analysis, until the numerical moisture profile approximately matches the experimental profile. The moisture diffusivity curve for each mix is shown in Figure 5.4. Free shrinkage was measured using the 40*40*160 mm prisms. The shrinkage evolution for each mix is shown in Figure 5.5. The hygral contraction coefficient (essential in shrinkage modeling in FE analysis) was back calculated by coupling thermal analysis with structural analysis. The obtained hygral contraction coefficient values were: 0.00038; 0.00065; 0.0048 and 0.0045 for CSA, FCSA, RSC and FRSC, respectively. Further details are given elsewhere [10].

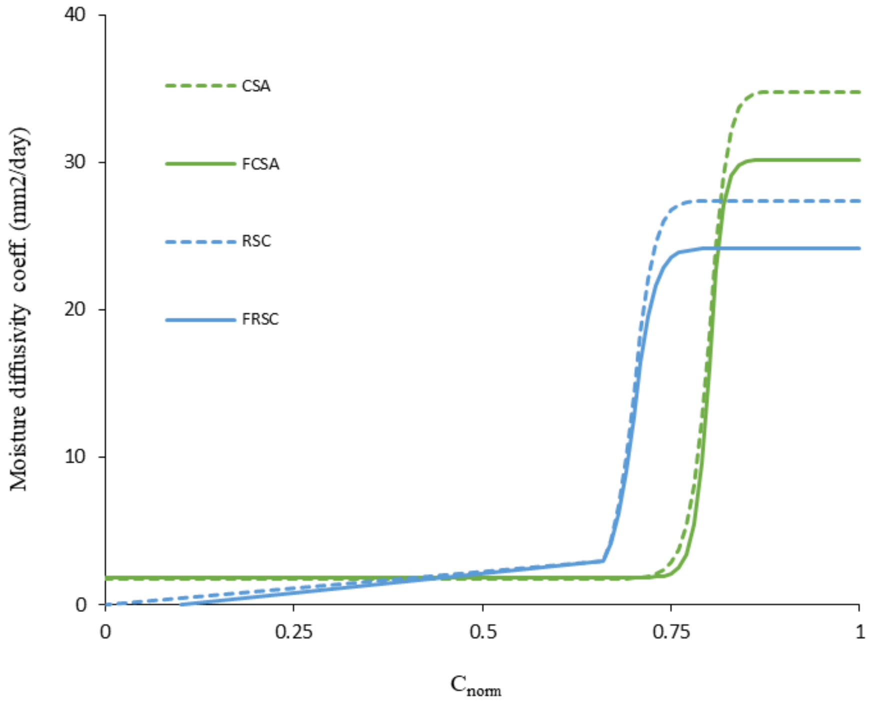

Figure 5.4. Moisture diffusivity versus normalized moisture content C_{norm}.

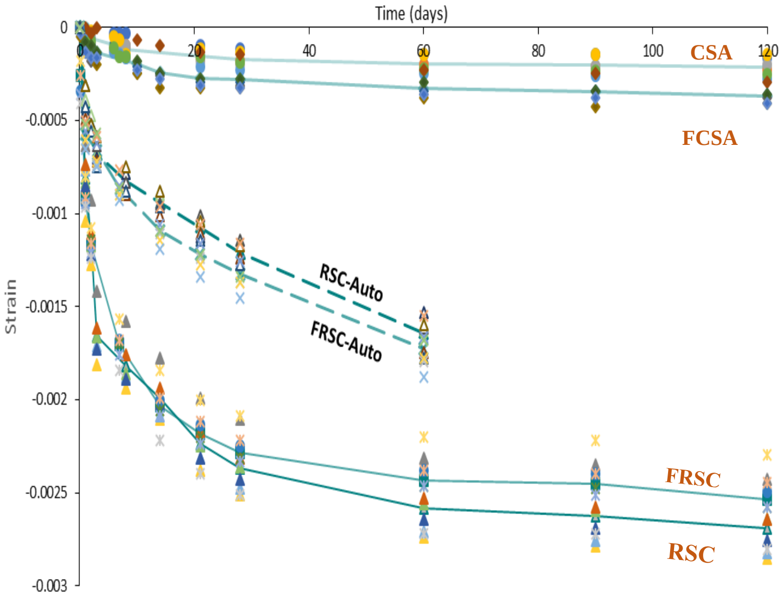

Figure 5.5. Experimental shrinkage development for all mixes with time (lines represent average for each mix)

5.2.3 Construction and restrained shrinkage of composite prisms

Sixteen concrete substrate prisms, 500 mm long, 150 mm wide and with two different depths (120 and 130 mm) were cast in wooden moulds. The top surface of the substrates was steel wire brushed, the day after casting, to expose aggregate surfaces. The top surface of prisms to be overlaid with RSC and FRSC layers was further steel wire brushed to accomplish rougher surfaces. After that, the specimens were kept in a mist chamber for 27 days and then dried in an oven at 80 °C for a week. Their top surfaces were thoroughly cleaned and saturated surface dry, just a few hours before overlaying. After overlay casting and setting, the specimens were kept moist for approximately one hour before they were demoulded and placed in an environmental chamber with a relative humidity of 50 ± 5% and a temperature of 20 ± 2 °C. The final depths of the overlay composite prism are listed in Table 5.2.

The shrinkage measurements were taken for the composite prisms at frequent time intervals using a 200 mm Demec gauge. Six measurements were recorded for each prism; two readings at the top layer of the overlay and two at each side of the prism as shown in Figure 5.6.

Table 5.2 The depths of substrate and overlays layers (all dimensions are in mm)

Prisms	1		2		3		4	
	Substrate	Overlay	Substrate	Overlay	Substrate	Overlay	Substrate	Overlay
CSA	120	31	120	30	113	40	113	40
FCSA	117	35	125	30	112	42	112	42
RSC	122	28	117	33	116	37	110	40
FRSC	118	34	124	26	116	37	116	34

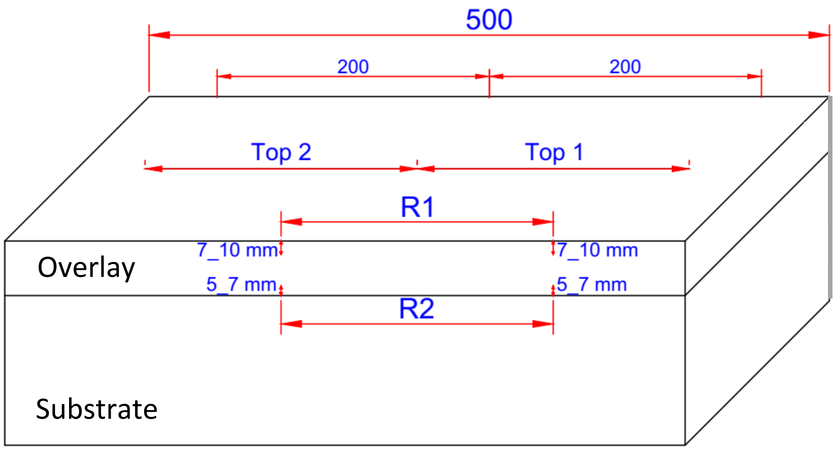

Figure 5.6. Location of shrinkage measurements for a composite prism

The shrinkage development over time for all prisms is shown in Figure 5.7 to Figure 5.10. The measurements at the top (Top$_1$ and Top$_2$) and the sides (R$_1$-S$_1$ and R$_1$-S$_2$ [R$_{1\text{-avg}}$], R$_2$-S$_1$ and R$_2$-S$_2$ [R$_{2\text{-avg}}$]) were averaged for each prism and only the average readings (Top$_{\text{avg}}$, R$_{1\text{-avg}}$ and R$_{2\text{-avg}}$) are reported. As the pair CSA$_1$ and CSA$_2$ as well as CSA$_3$ and CSA$_4$ have approximately the same dimensions and similar interface characteristics, their shrinkage values were averaged (Figure 5.7). Further details and discussion on shrinkage results are given elsewhere [12].

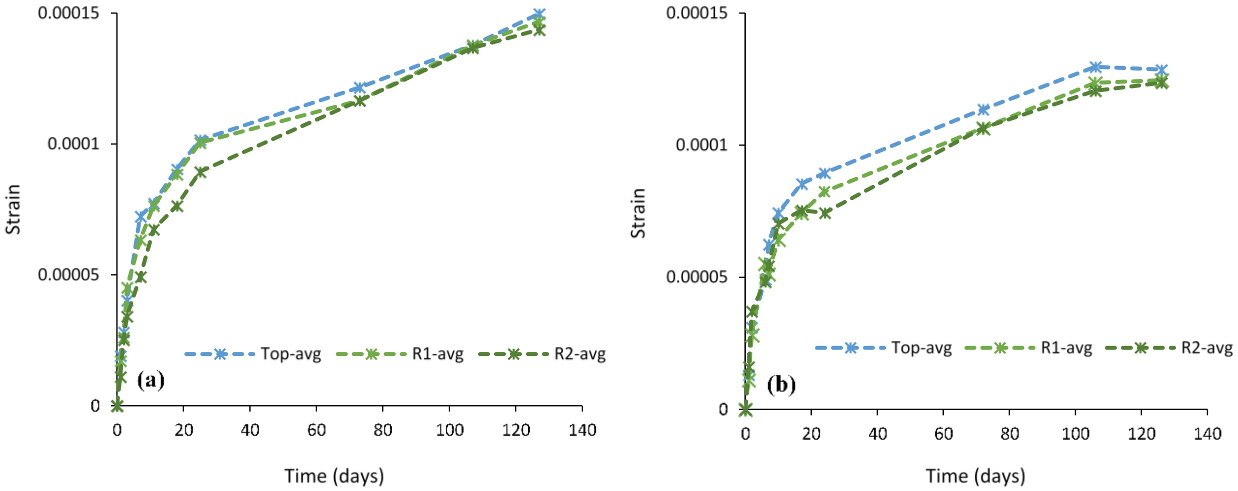

Figure 5.7. Shrinkage development with time for composite prisms: (a) Average of CSA$_1$ &CSA$_2$; (b) CSA$_3$ & CSA$_4$

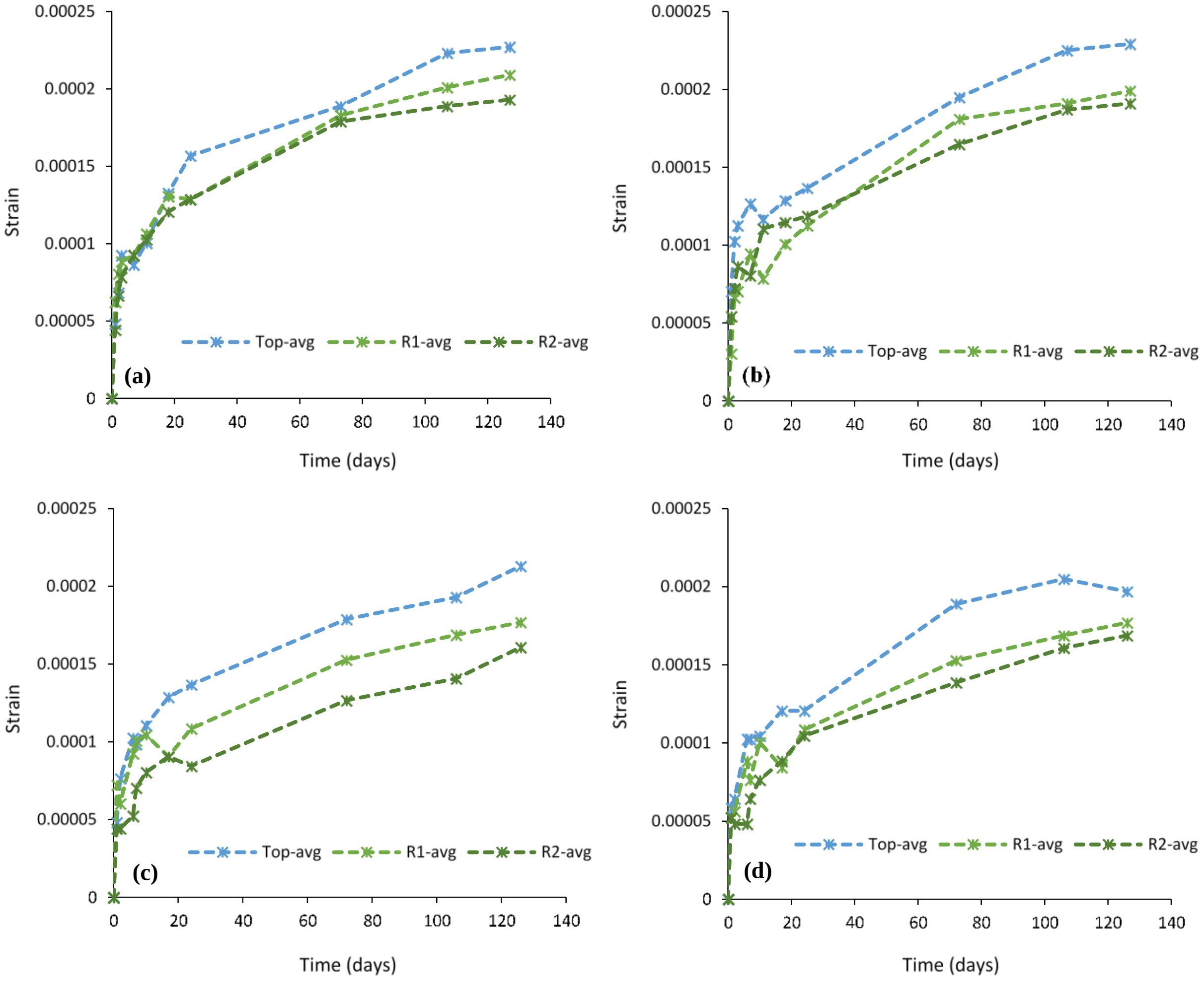

Figure 5.8. Shrinkage development with time for composite prisms: (a) FCSA$_1$; (b) FCSA$_2$; (c) FCSA$_3$; (d) FCSA$_4$

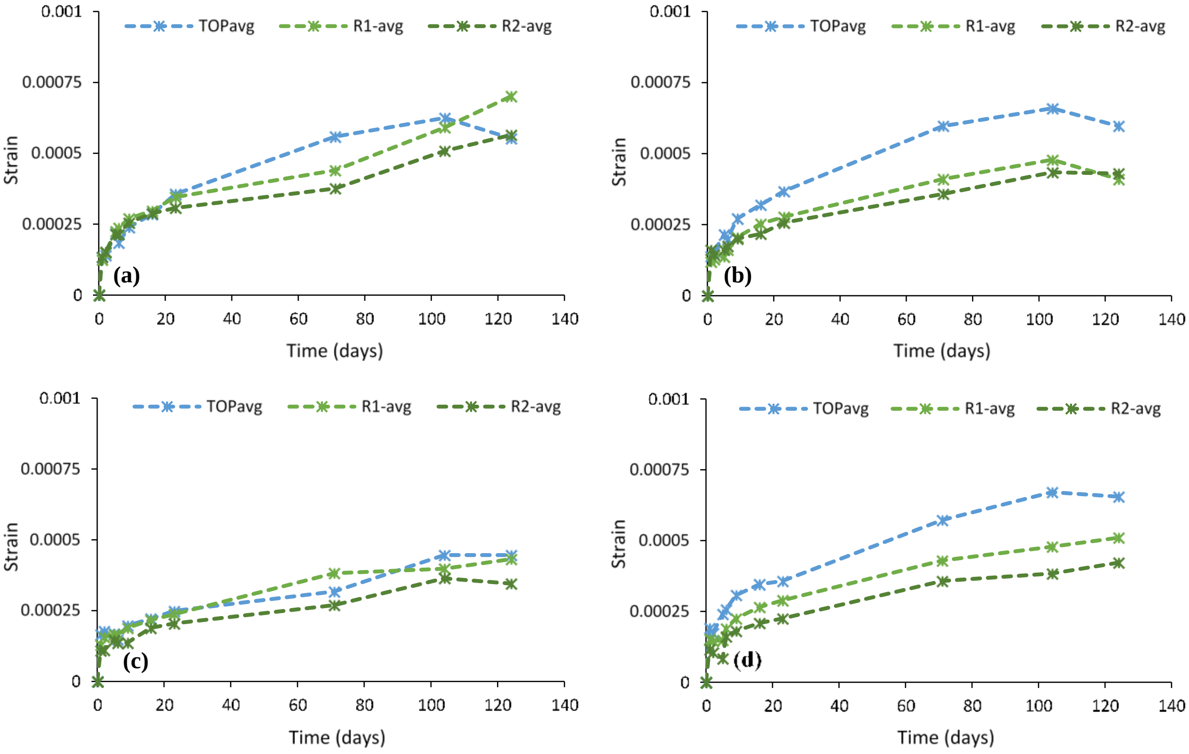

Figure 5.9. Shrinkage development over time for composite prisms: (a) RSC$_1$; (b)RSC$_2$; (c) RSC$_3$; (d) RSC$_4$

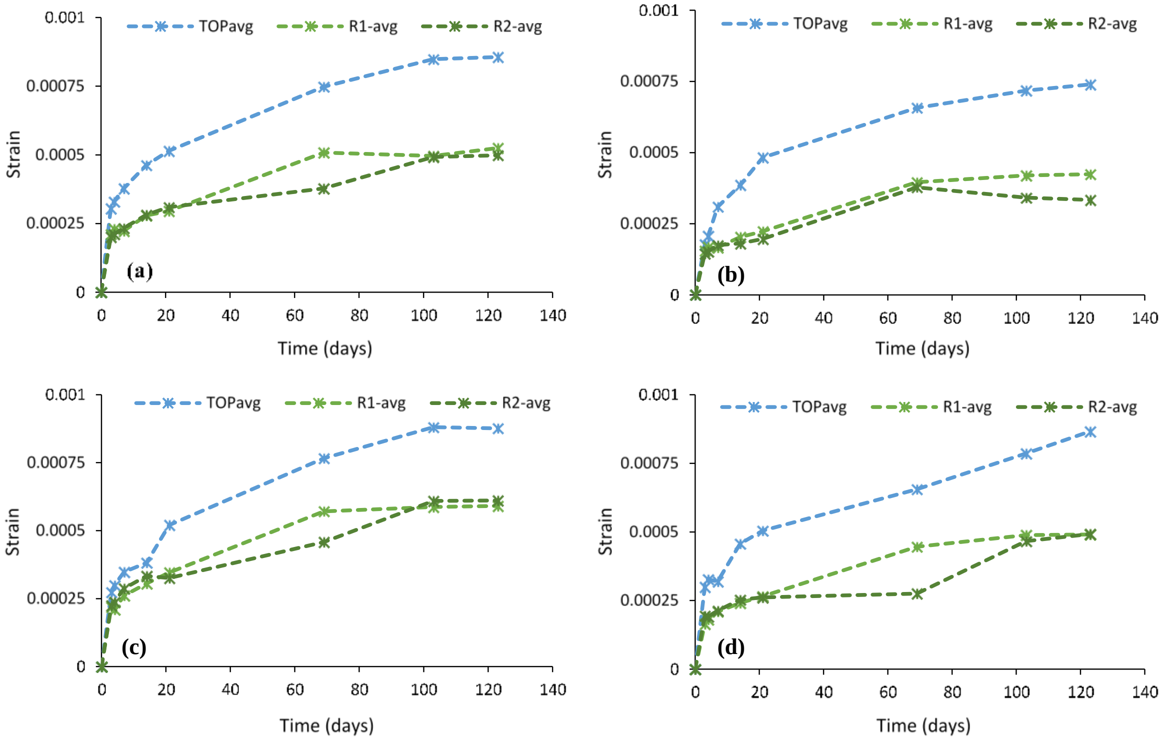

Figure 5.10. Shrinkage development over time for composite prisms: (a) FRSC$_1$; (b)FRSC$_2$; (c) FRSC$_3$; (d) FRSC$_4$

5.3 Numerical Studies

5.3.1 Modelling and validation

5.3.1.1 Material models and elements used

The FE package, Abaqus [6], was used to model each composite prism during the drying process. The analysis was performed by using the concrete damage plasticity (CDP) model. Moisture profiles as well as tensile and compressive properties are obtained from the experimental data using inverse analysis, details of which details are given elsewhere [7, 10]. Moisture analysis is performed first to obtain the spatial moisture distribution inside the repaired system with time. Conductivity properties were assigned to the interface so as to model the moisture transfer from the overlay to the substrate. Then, the moisture (thermal) analysis is coupled with structural analysis to obtain the time history of stresses and strains. The development of the material properties with time was incorporated into the structural analysis through the implementation of the user subroutine, USDFLD. Diffusive heat transfer 20-node quadratic brick elements (DC3D20) were used for the thermal analysis while C3D20R elements were used for the structural analysis. As no tensile cracks developed in the substrate layer, this layer was modelled as an elastic layer. The thermal and mechanical material properties for this layer were obtained by using values for normal concrete from Model Code 2010 (MC 2010) [11].

As 40 × 40 × 160 mm flexural prims without fibres (RSC and CSA prisms) failed without any softening or residual strength after cracking [7] and it was not possible to determine their post-peak stress characteristics. MC 2010 [11] proposed using bi-linear tension stiffening model for plain concrete. In this study, however, tri-linear model was adopted to avoid numerical convergence issues. (See Figure 5.11 for RSC).

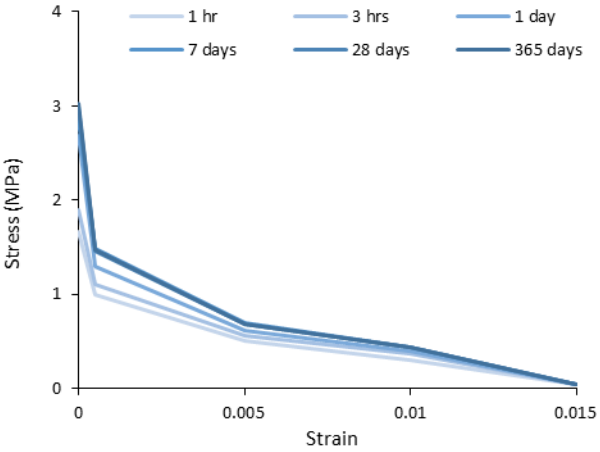

Figure 5.11. Tensile stress strain at different ages of RSC prisms

5.3.1.2 Interface modelling approach

Two approaches are adopted for modeling the interface between the overlay and the substrate. The first approach is cohesive surface based and is suitable for modelling bond when the interface thickness is quite small. Traction-separation constitutive laws defines the cohesive surface behaviour which initially has linear elastic behavior specified by an elastic constitutive matrix in which the normal and shear stresses are related to the normal and shear separations across the interface [6]. The model requires definition of the normal and tangential stiffness components (K_{nn}, K_{tt} and K_{ss}) for uncoupled traction-separation behavior. The degradation of the bond and the eventual delamination can be modeled by incorporating damage to the cohesive behaviour, through progressive degradation of the cohesive stiffness. The parameters for the initial cohesive behaviour, the criteria for damage initiation and the subsequent damage evolution law that specifies the rate of stiffness degradation have to be determined experimentally. This approach has been successfully used to model the interface between concrete and CFRP [13], steel and concrete [14] and concrete and asphalt layers [2].

The second approach is frictional based, utilising the concept of the classical isotropic Coulomb friction model. It allows the user to introduce a shear stress limit (τ_{max}), the maximum value of shear stress that the interface can carry before sliding begins. It also permits relative slippage (elastic slip) while the surfaces are in the “sticking” state. This approach has been exploited by Jafarifar et al. [15] to model the interface between a concrete slab and the base layer and by Baek [16] to model the interface between concrete and asphalt layers.

Based on the experimental observations of higher shrinkage strains at the top layer (from the experimental part of this study), it was decided to use a bigger surface factor for the top surface than for the other surfaces in the numerical analysis. This factor ranged from 9-12 mm/day while the surface factors for the other surfaces were the same as determined previously by inverse analysis in another study done by the authors [10]. At the beginning of drying, the moisture concentration throughout the overlay was 100% while the ambient relative humidity was considered constant at 50%. The substrate is assumed to be in equilibrium with the surrounding environment and, hence, initial humidity similar to humidity of the surrounding environment was given to the substrate. Due to symmetry, only a quarter of the composite prisms has been modelled.

5.3.1.3 Validation of numerical models using analytical predictions

The hygral stresses generated from the numerical modeling are compared with analytically predicted stresses obtained using the Silfwerbrand [5] procedure. This procedure assumes that both substrate and overlay have linear elastic properties and the shrinkage of the overlay is uniform across the depth. CSA_2 and CSA_3 were selected for the purposes of this comparison. Only the cohesive interface approach is used as it uses interface bond stiffness and allows a direct comparison with Silfwerbrand analysis. To achieve as uniform shrinkage across the section as possible, the top and bottom surfaces of CSA_2 and CSA_3 were assigned the same thermal properties (surface factor). Four different bond stiffnesses were used for each prism, ranging from 2.5 N/mm^3 and up to 50 N/mm^3. The numerical and analytical tensile stresses at the interface and at the top of overlaid prisms (CSA_2 and CSA_3) at 365 days are shown in Figure 5.12 and Figure 5.13, respectively, while the maximum shear stresses at the interface are listed in Table 5.3.

Table 5.3 The numerical and analytical shear stresses (MPa) at the interface

K (N/mm^3)	2.5		5		10		50	
	Analytical	Numerical	Analytical	Numerical	Analytical	Numerical	Analytical	Numerical
CSA_1	0.10	0.11	0.18	0.19	0.30	0.30	0.77	0.69
CSA_2	0.10	0.11	0.19	0.19	0.31	0.31	0.8	0.71

The results confirm that the numerical analysis is successful in predicting both the tensile and shear stresses that develop in the overlays due to restrained shrinkage for this simple case and can be used to analyse more complex cases. The results differ near the ends possibly due to stress concentrations and shear lag which distort the shape of the overlay in those locations.

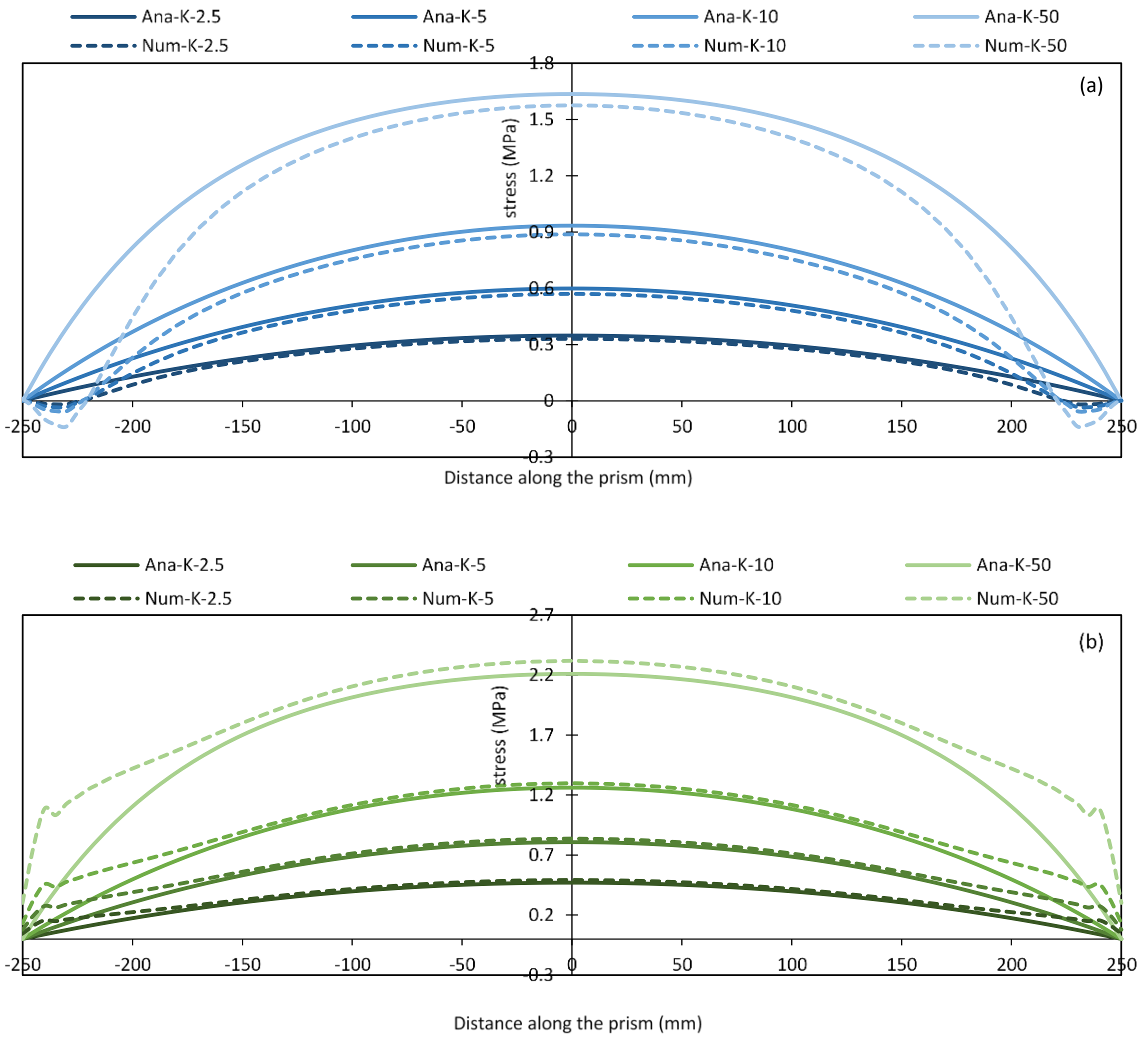

Figure 5.12. The numerical and analytical tensile stresses of CSA_2 at: (a) Top of the overlay; (b) The interface

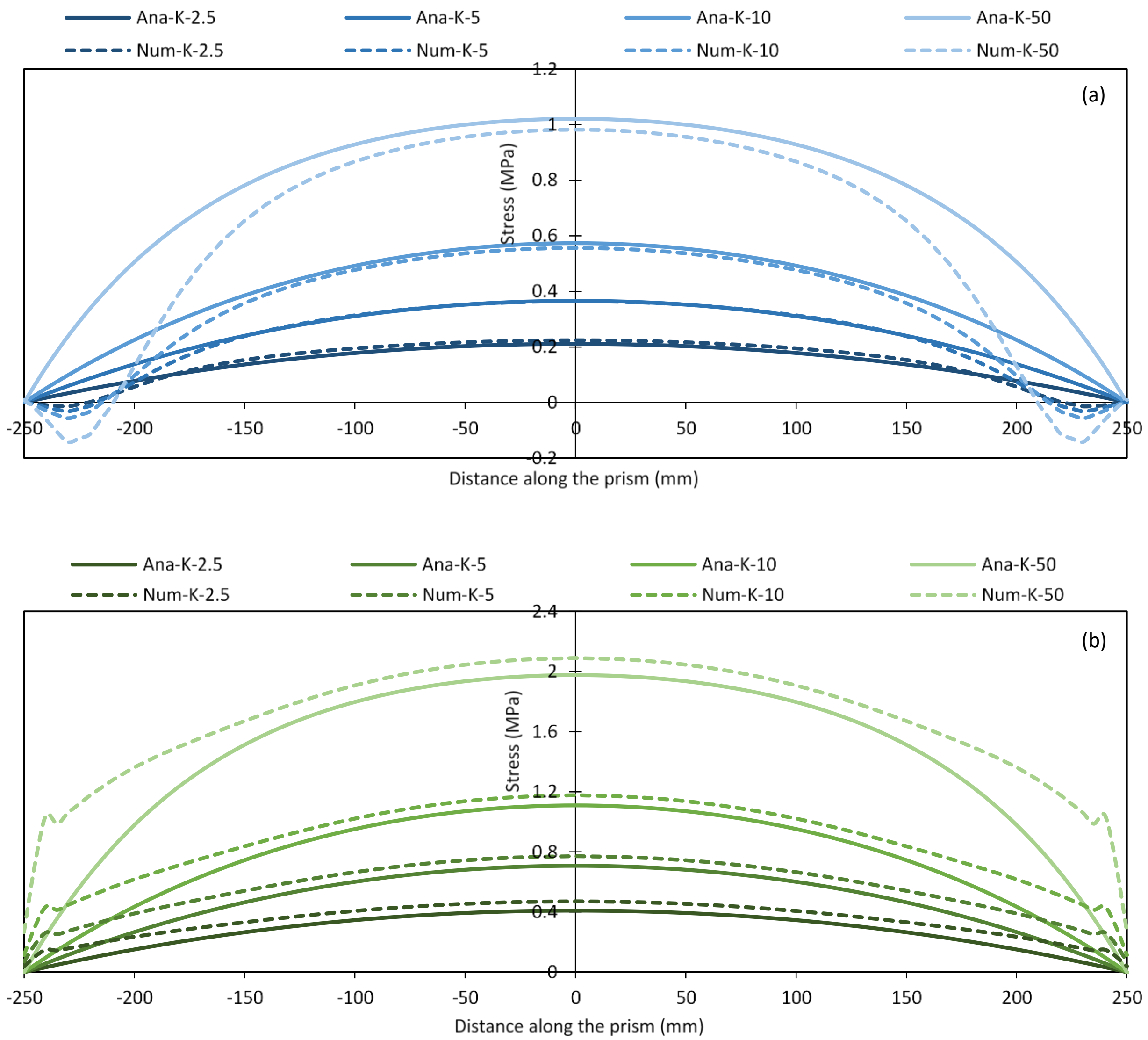

Figure 5.13. The numerical and analytical tensile stresses of CSA$_3$ at: (a) Top of the overlay; (b) The interface

5.3.2 Modelling interface parameters

A wide range of interface shear stiffnesses (0.5 – 95 N/mm^3) were determined by Tsioulou and Dritsos [17], for various interface conditions, based on results from experimental studies reported in literature [18-25]. Interface properties can be quantitatively estimated from the interface level of preparation [11]. A minimum coefficient of friction (μ) of 0.5 between concrete surfaces is suggested in BS EN 12812 (2008) [26] while the value of μ of 10 was reported to result in behaviour approximating monolithic for modelled columns strengthened by jacketed concrete [27].

As the mechanical properties of the interface are not known a-priori, they can be determined iteratively by considering the difference between the measured shrinkage strain of composite prisms to the free shrinkage strain predicted for overlays of the same dimensions, but without substrate. Stronger restraint conditions due to higher bond stiffness or higher coefficient of friction will result in lower shrinkage strain measured on the overlay layer compared to the free shrinkage strain. Using numerical back analysis, the interface properties for modelling purposes for all prisms were determined as shown in Table 5.4. As there is some moisture exchange through the interface, this parameter was also considered when modelling the interface, using a moisture (thermal) conductivity factor (value of 0.1), also obtained through back analysis.

Prims with overlay shrinkage strain values close to the free shrinkage values were given lower interface stiffnesses and lower coefficients of friction. Using the values listed in Table 5.4, the predicted shrinkage strain (using cohesive -coh and friction -fric approaches) against the experimental measured values are shown in Figure 5.14, Figure 5.15 and Figure 5.17 - Figure 5.19. The experimental shrinkage strain at the top and two side surfaces are shown in the graphs as Top, R_1 (near the top of the overlay) and R_2 (near the interface), respectively. For CSA and FCSA composite prisms, the numerical shrinkage development with time is shown in Fig. 6 and Fig. 7, respectively. It is clear from the graphs that both modeling approaches capture well the development of shrinkage strains with time. Overall, substrate prisms overlaid with CSA mixes had the smoothest interfaces and thus it is expected that they also have the lower interface characteristics (see Table 5.4). FCSA prisms, on the other hand, had rougher surfaces and higher restraint conditions.

MC 2010 [11] suggest values of 1.5-2.5 MPa for the mean interfacial strength for rough interfaces and 2.5-3.5 MPa for very rough interfaces, provided that the surfaces are clean and appropriate roughening are used. The back calculated values (τ_{max}, shown in Table 5.4) in this study are in well congruent with MC proposed values.

Table 5.4 Parameters used to model the interface of CSA and FCSA overlaid prisms

	Cohesive stiffnesses (N/mm^3)			Friction parameters		
	K_{nn}	K_{tt}	K_{ss}	μ	τ_{max} (MPa)	Elastic slip
CSA_1	3	3	3	1.3	1.0	0.04
CSA_2	3	3	3	1.3	1.0	0.04
CSA_3	4	4	4	1.4	1.3	0.04
CSA_4	4	4	4	1.4	1.3	0.04
$FCSA_1$	10	10	10	1.5	2.0	0.03
$FCSA_2$	14	14	14	2.2	2.0	0.02
$FCSA_3$	40	40	40	2	3.0	0.009
$FCSA_4$	25	25	25	2	3.0	0.015
RSC_1	75	75	75	---	---	----
RSC_2	75	75	75	---	---	---
RSC_3	75	75	75	---	---	---
RSC_4	65	65	65	---	---	---
$FRSC_1$	100	100	100	2.3	3.0	0.0065
$FRSC_2$	100	100	100	2.0	3.0	0.0055
$FRSC_3$	100	100	100	2.3	3.0	0.0078
$FRSC_4$	100	100	100	2.0	3.0	0.0065

The maximum principal plastic strain, in the CDP model, can be related to cracking occurrence. The maximum principal plastic strain for CSA_1 is shown in Figure 5.16. As the plastic strain is zero everywhere, this means that no cracking has developed in the numerical model, which agrees with the experimental observations. The FCSA prisms, however, despite not having cracked in the experiments, are predicted to develop some cracking at the upper edges of the prisms (Figure 5.16), where stresses are high, as the edges loose moisture faster than the inner parts of the prism. This indicates that there is a relaxing mechanism that relieves stresses. The analysis of those prims was repeated by considering the effect of creep, calculated using MC 2010 [11]. This was done was reducing the modulus of elasticity of the mixes (as given in Equation 3.10). In this case, the results of the maximum principal plastic strain of $FCSA_3$, shown in Figure 5.16, agree with the experimental observations that no cracking should occur. This shows that it is important to consider creep when calculating hygral stresses in repair materials.

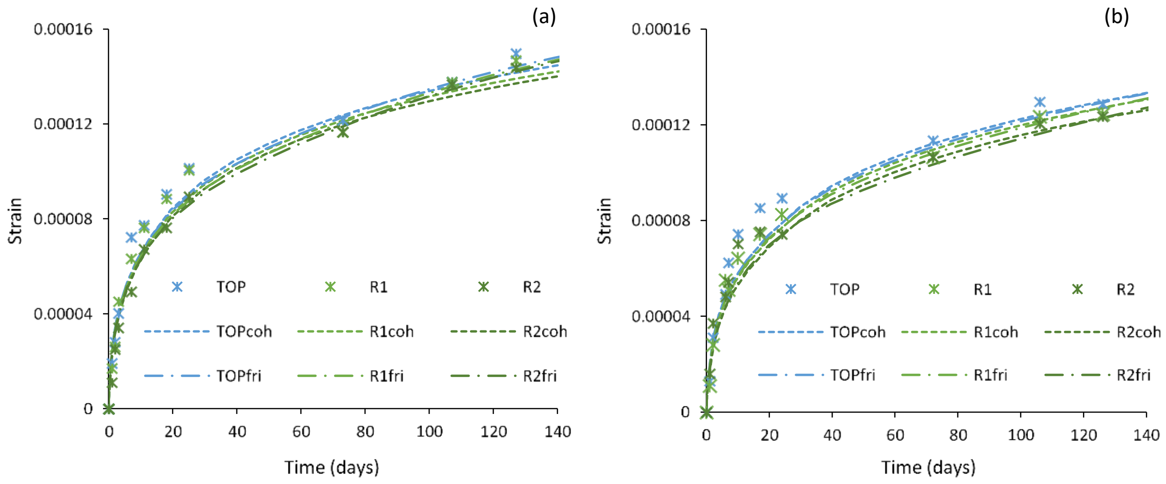

Figure 5.14. Experimental versus numerical shrinkage strain for overlays: (a) CSA_1 & CSA_2; (b) CSA_3 & CSA_4

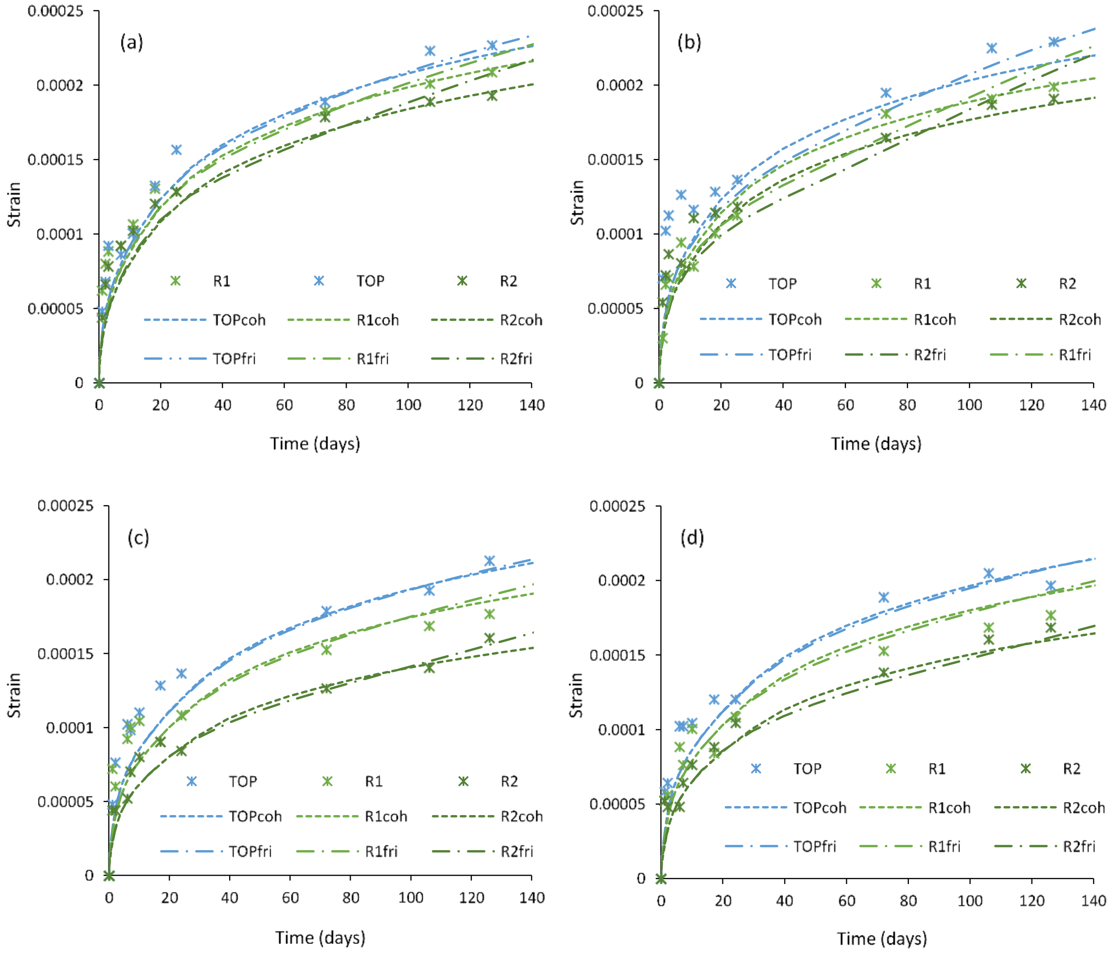

Figure 5.15. Experimental versus numerical shrinkage strain for overlays: (a) $FCSA_1$; (b) $FCSA_2$; (c) $FCSA_3$;(d) $FCSA_4$

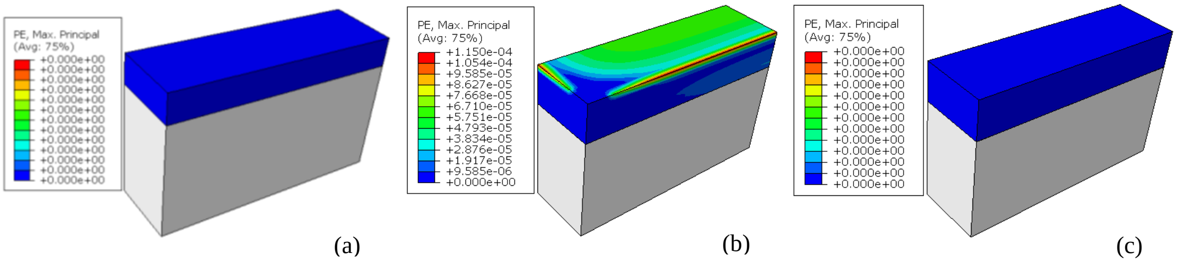

(a) (b) (c)

Figure 5.16. Max principal plastic strain of overlays: (a) CSA$_1$; (b) FCSA$_3$ without creep; (c) FCSA$_3$ with creep

The numerically predicted shrinkage strain development with time for FRSC$_1$ is presented in Figure 5.17. It can be seen that the use of constant interface stiffness overestimated the restraint of the overlay. This may be because at crack locations, in overlay composite prisms, there is high shear demand resulting in local slippage and as a result, the local interface stiffness decreases. As the numerical model utilises the smeared crack approach which averages this effect, the interface stiffness was decreased with crack development in the cohesive approach to consider the effect of slip adjacent to cracks using damage evolution. Details on the parameters determined for damage initiation and damage evolution are listed in Table 5.5. As expected, the damage evolution in FRSC prisms is much lower since crack openings are controlled by fibres and, hence, less slip is anticipated to occur and thus the reduction in interface stiffness is smaller.

Table 5.5 Damage parameters for cohesive interface of RSC and FRSC composite specimens (displacements are in mm)

Prisms	Damage initiation (Max separation)			Damage evolution		
	Normal	Shear-1	Shear-2	Displacement at failure	Softening	Parameter
RSC$_1$	0.005	0.005	0.005	0.4	exponential	9
RSC$_2$	0.006	0.006	0.006	0.41	exponential	8
RSC$_3$	0.0055	0.0055	0.0055	0.495	exponential	9
RSC$_4$	0.00535	0.00535	0.00535	0.5	exponential	4
FRSC$_1$	0.0065	0.0065	0.0065	1.1	exponential	2
FRSC$_2$	0.0055	0.0055	0.0055	1.0	exponential	2
FRSC$_3$	0.0078	0.0078	0.0078	0.9	exponential	2
FRSC$_4$	0.0065	0.0065	0.0065	1.2	exponential	2

The numerical shrinkage strain development with time against average experimental values for RSC and FRSC composite prisms using the parameters listed in Table 5.4 and Table 5.5 are shown in Figure 5.18

and Figure 5.19, respectively. As seen, the numerical models predict fairly well the shrinkage development of the tested prisms.

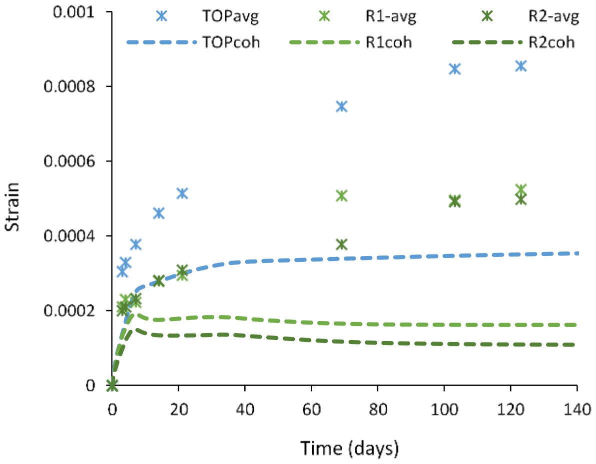

Figure 5.17. Experimental versus numerical shrinkage strain for FRSC$_1$ overlay (with constant interface stiffness)

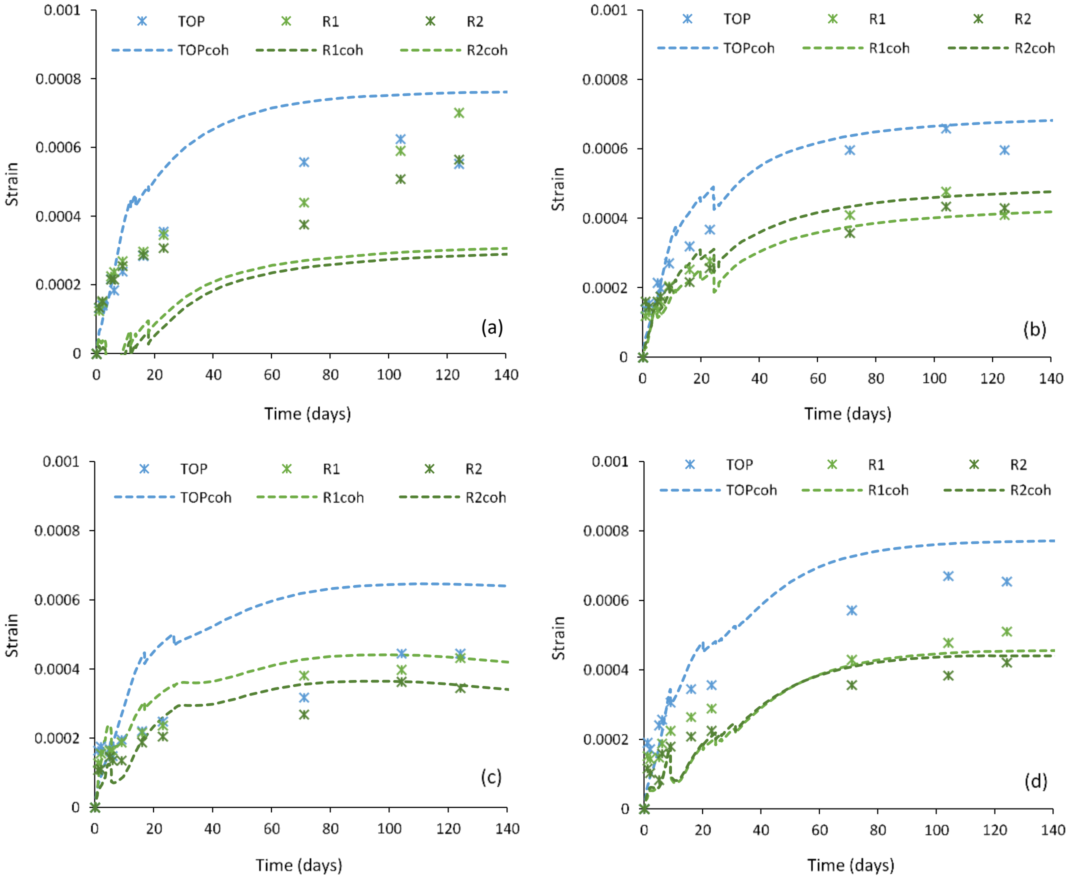

Figure 5.18. Experimental versus numerical shrinkage strain for overlays: (a) RSC1; (b) RSC2; (c) RSC3; (d) RSC4

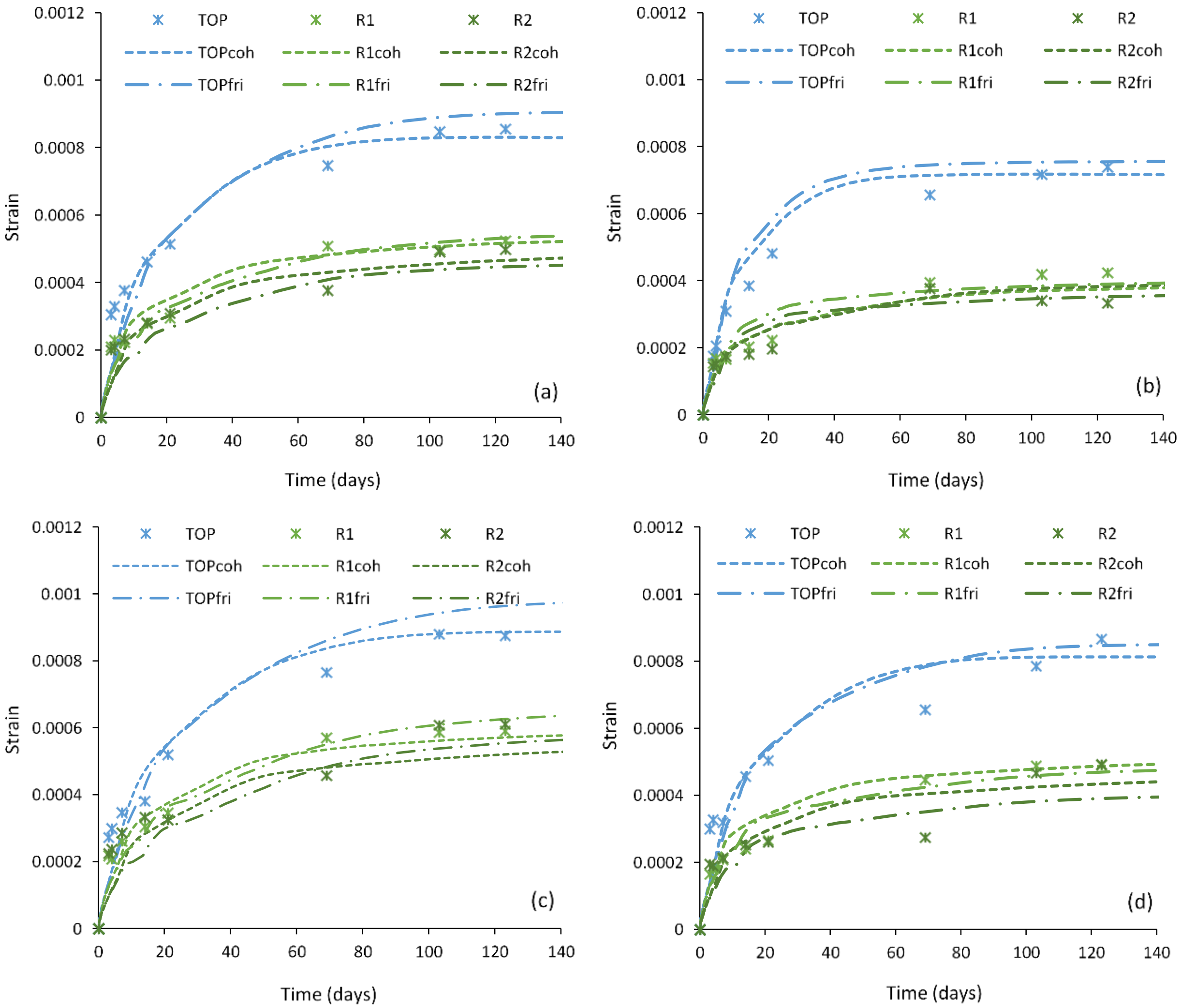

Figure 5.19. Experimental versus numerical shrinkage strain for overlays: (a) FRSC1; (b) FRSC2; (c) FRSC3; (d) FRSC4

5.4 Results of parametric Studies and discussion

The Silfwerbrand analytical procedure for crack risk analysis assumes that shrinkage is uniform across the section. However, there is an evidence that a shrinkage gradient developed in all prisms tested in the study, as the top layer tends to shrink more, since the rate of drying from the top surface to the environment is much higher than moisture absorption towards the base layer, and possibly due to non-uniform aggregate distribution [28] and bleeding [29]. Furthermore, the substrates can have various moisture content levels (depending on their age) and thus, different shrinkage states. To understand the effect of shrinkage gradient in the overlay and moisture conditions of the substrate layer on the tensile stress development in the overlays, a parametric numerical study was conducted. Eight CSA overlaid prisms were modelled with four moisture conditions and two interface stiffnesses (5 and 50 N/mm^3).

- The first condition assumes uniform shrinkage distribution across the overlay depth.
- The second condition neglects the moisture properties of the base and assumes no moisture interaction between the two layers, and therefore, the drying of the overlay occurs through the top surface only.
- The third condition assumes that the base layer has 75% humidity and the interface has moisture conductivity properties, allowing humidity transfer between the base and the overlay.

The last condition is as the third condition, except that the base layer has 50% humidity.

The depth of the overlay chosen is 50 mm and the depth of the base layer is 100 mm. The numerical results, in terms of tensile stress at the interface, are shown in Figure 5.20. It can be seen that the assumption of uniform shrinkage results in the lowest stress values while the conditions with shrinkage gradient and drier substrates yield the highest stress values. This means that the Silfwerbrand analytical equations, which only consider uniform shrinkage, underestimate the hygral stresses that develop in real overlays with different moisture conditions.

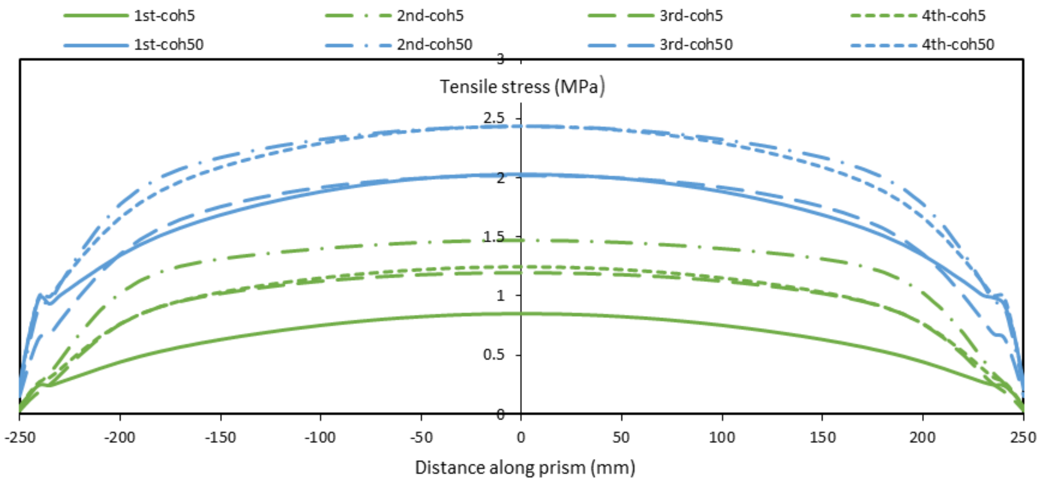

Figure 5.20. The tensile stresses of CSA overlaid prisms at the interface

To better investigate the issue of non-uniform shrinkage more, a parametric study is performed for CSA prisms with different depths ranging from 30-60 mm. The depth of the base layer was kept constant at 150 mm and the length of both layers is 1000 mm. As the risk of cracking is higher for composite prisms with high stiffness values, only stiffnesses of 50 and 100 N/mm^3 were considered in the analysis. The base layer was assumed to be relatively dry (has 50% relative humidity) as this condition is shown above (Figure 5.20) to be resulting in higher tensile stress values. The analysis results of this parametric study, in terms of the tensile stress at the interface, are shown in Figure 5.21. It is clear that the underestimation of the resulting tensile stresses is more pronounced for thicker overlays such as 50 and 60 mm compared to thin overlays (e.g. 30 mm). Therefore, to effectively use Silfwerbrand analytical equations in predicting the risk of cracking of concrete overlays, the effect of additional stresses due to non-uniform shrinkage has to be taken into account. One efficient yet easy solution to address this issue is to increase the free shrinkage strain of the overlay layer by a given amplification factor (AF). This factor is expected to increase with an increase in overlays depth as non-uniform shrinkage is more prominent in thicker overlays. The previous parametric study was extended to include different substrate depths and different lengths to determine the amplification factor for each case. By using regression analysis, the factor obtained for each overlay depth is listed in Table 5.6 and defined in Equation 5.1.

$$\mathrm{AF} = 1 + \left(\frac{\mathrm{h_o}}{100} - 0.2\right) \qquad \textit{Equation 5.1}$$

where, h_o: is the depth of the overlay in mm, $20 \leq h_o \leq 100$.

It can be seen that the factor increases linearly with an increase in overlay depth. The analytical stresses calculated using the adjusted shrinkage strains by using these the factors (for the same overlay dimensions mentioned above) against their predicted numerical values are given in Figure 5.22. It can be seen that the calculated stresses match much better their numerically predicted stress values. Therefore, it is suggested to use an adjusted shrinkage strain to assess the risk of cracking of overlays with rapid hardening materials.

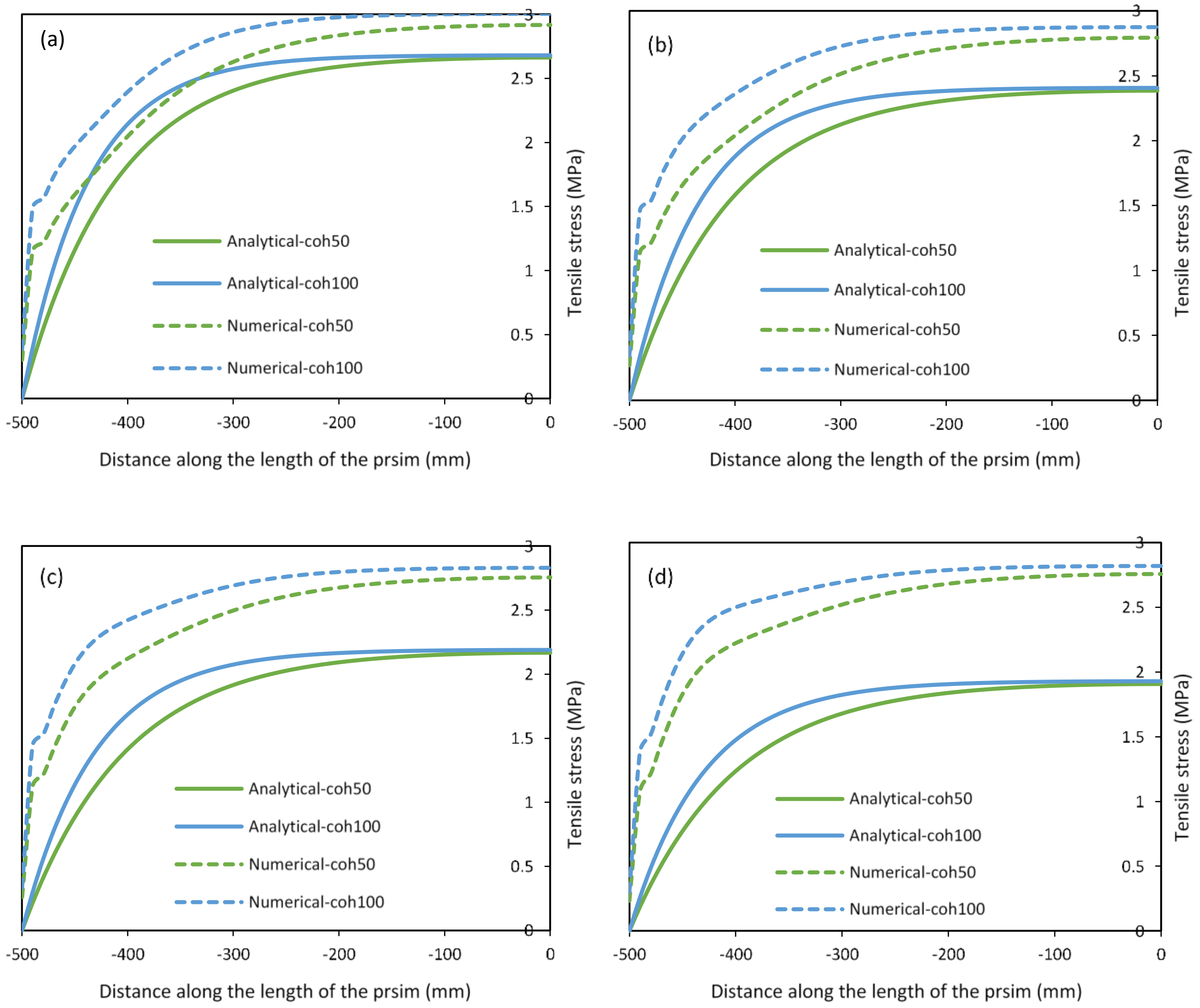

Figure 5.21. The tensile stresses at the interface of CSA overlaid prisms with depths of: (a) 30 mm; (b) 40 mm; (c) 50 mm; (d) 60 mm

Table 5.6 The calculated shrinkage factors for different overlay depths

Overlay depth (mm)	30	40	50	60
Shrinkage factor	1.1	1.2	1.3	1.4

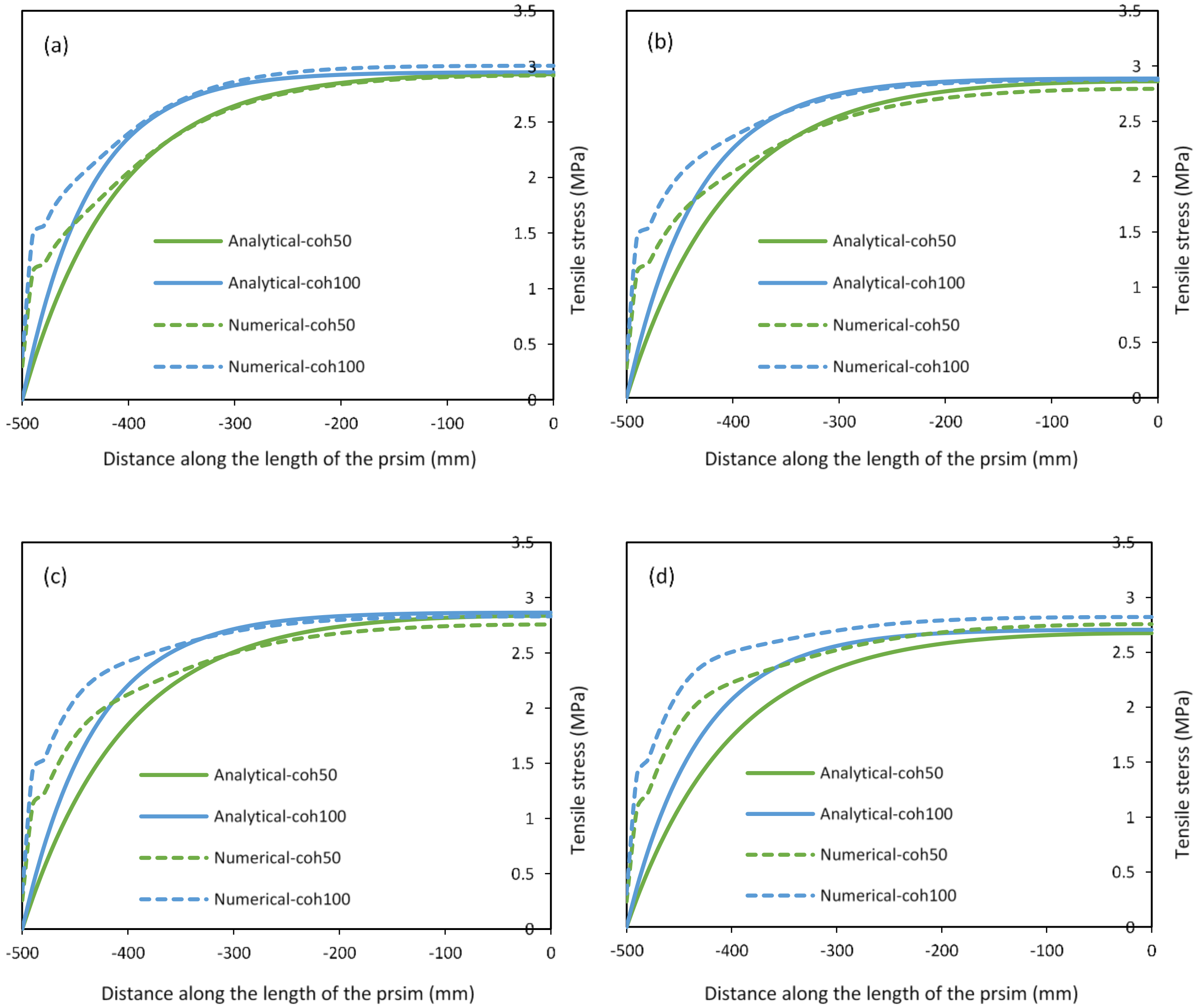

Figure 5.22. The tensile stresses using adjusted shrinkage strain at the interface of CSA overlaid prisms with depths of: (a) 30 mm; (b) 40 mm; (c) 50 mm; (d) 60 mm

5.5 Analysis of shear tests

Numerical analysis was performed on 12 composite specimens similar to the ones presented in a previous paper by the authors [12]. The analysis uses similar material models as in the previous numerical studies to have a better understanding on the shear behaviour of composite prisms. To define the contact properties at the interface, the cohesive approach is used. The properties of the interface were derived from experiments and are listed in Table 5.7. The initial stiffness was determined by dividing the shear strength values by the shear displacement values given in Table 4.7. The analysis assumes that the damage will initiate when the experimentally obtained shear strength is reached. Those values were given previously in Table 4.7 and listed here in Table 5.7. As in experiments, three-point loading was applied to the specimen through three steel plates (see Figure 5.23). The lower two plates are fixed while a downward displacement is applied on the top plate to create the shear forces. As the specimen is symmetrical along X-axis, only half of the prism is modelled. The results, in terms of the maximum load at failure, are given in Table 5.7. It can be seen that the numerical models are able to predict the maximum shear load with reasonable accuracy (5.3%) except for RSC which failed at a lower load (-22.4%) in the experiments. This may be due to material variabilities in the substrate. This analysis confirm that good preparation of the surface can lead to high shear strength which is essential to avoid delamination and to obtain distributed cracks in overlays. The stiffness values are rather high and bigger than the numerical obtained stiffness values for SFRC prisms (100 N/mm^3). It should be noted that due to restrained shrinkage in composite prisms, the interface undergoes creep and thus, the interface stiffness decreases over time, while the shear tests develop the stress rather quickly, hence no significant creep is expected to occur.

Table 5.7 Interface cohesive properties and analysis results

Specimen	Initial stiffness K (N/mm^3)	Damage parameters		Failure load (kN)	
		Shear 1	Shear 2	Experimental	Numerical
FCSA	330	2.94	2.94	132.1	132.6
CSA	470	2.78	2.78	124.9	131.5
FRSC	480	3.10	3.10	139.3	135.4
RSC	325	2.24	2.24	101.0	123.6

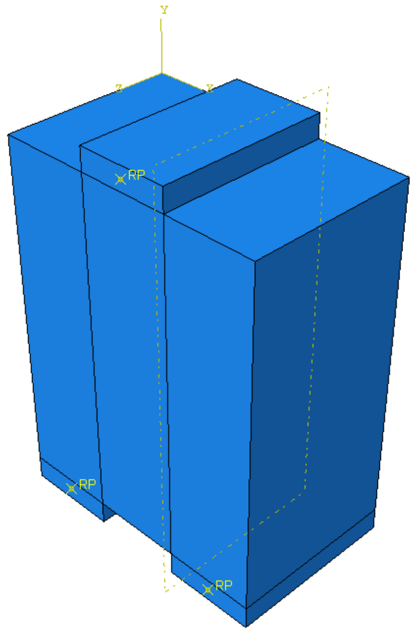

Figure 5.23. Shear assembly in FE analysis

5.6 Conclusions

- The numerical FE analysis (sequential heat analysis coupled with structural analysis to obtain the time history of stresses and strains) was demonstrated to successfully predict the shrinkage development with time for the tested composite prisms using both frictional and cohesive approaches.
- The numerical tensile and shear stresses developed at the interface are in good agreement with those estimated using Silfwerbrand analytical approach when assuming the shrinkage is uniform across the depth. However, this condition underestimates the stress development in overlays. A modification to consider this effect is introduced through a shrinkage amplification factor.
- The interface stiffness has a major role on restraining shrinkage of overlays, as with higher stiffness, more restraint is developed and possibly the risk of cracking increases. However, it is noticed that the well-prepared surfaces not only have high stiffness interface values but also high interfacial strengths which are shown to be a vital parameter in preventing the delamination especially when the shrinkage strains in overlays are very high. In cases of strong interface bond, tensile cracking is more likely to develop due to restrained shrinkage strain, rather than delamination, however, cracking can be

controlled by using fibres in the mix.

- Fibre inclusion in the mix is shown to slow down the evolution of local slippage at the interface when cracks are developed by controlling the cracking widths and, thus, can contribute in reducing the risk of delamination at crack locations. This was reflected in numerical models by introducing a slower damage evolution to interface stiffnesses.
- The moisture content of the substrate and interface absorption properties have an effect on restrained shrinkage and therefore on tensile stress development as drier substrates tend to absorb more moisture form the overlay layer.
- The cohesive approach is successful in predicting the shear capacity of composite prisms. The well-prepared surfaces are quite necessary to obtain high interfacial shear strength and to avoid the risk of delamination.
- The high interface stiffness increases the risk of cracking, but it reduces the risk of delamination as the interfacial strength for such surfaces are usually high. It should be mentioned that cracking is preferable to delamination as it is possible to control crack widths by adding fibres.

References

1. Groth, P., (2000). *Fibre reinforced concrete: fracture mechanics methods applied on self-compacting concrete and energetically modified binders*. PhD thesis. Department of Civil and Mining Engineering, Lulea University of Technology.
2. Kim, M.O., Bordelon, A.C., Lee, N.K., (2017). Early-age crack widths of thin fiber reinforced concrete overlays subjected to temperature gradients. Constr. Build. Mater., 148, 492-503.
3. Orta, L., Bartlett, F.M., (2014). Free Shrinkage Strains in Concrete Overlays. ACI Mater. J., 111(3), 263-272.
4. Orta, L., Bartlett, F.M., (2014). Stresses Due to Restrained Shrinkage in Concrete Deck Overlays. *ACI Mater. J.*, 111(6), 701-710.
5. Silfwerbrand, J., (1997). Stresses and strains in composite concrete beams subjected to differential shrinkage. *ACI Struct. J.*, 94(4), 347-353.
6. ABAQUS 2017 Documentation.
7. Al-musawi, H., Figueiredo, F., Bernal, S.A., Guadagnini, M., Pilakoutas, K., (2019). Performance of rapid hardening recycled clean steel fibre materials. *Constr. Build. Mater.*, 195, 483-496.
8. BS EN 13892-2, (2002). Methods of test for screed materials — Part 2: Determination of flexural and compressive strength.
9. BS EN 12390-3, (2009). Testing hardened concrete - Part 3: Compressive strength of test specimens. British Standards Institution, London, UK.
10. Al-musawi, H., Figueiredo, F., Guadagnini, M., Pilakoutas, K., (2019). Shrinkage properties of plain and recycled steel–fibre-reinforced rapid hardening mortars for repairs. *Constr. Build. Mater.*, 197, 369-384.
11. F.I. du Béton, (2013). Fib Model Code for Concrete Structures 2010, Wilhelm Ernst & Sohn, Berlin, Germany.

12. Al-musawi, H., Huang, H., Benedetti, M., Guadagnini, M., Pilakoutas, K., (2019). Effect of shrinkage on rapid hardening plain and recycled steel fibre concrete overlays. Submitted for publication.
13. Obaidat, Y.T., Heyden, S. and Dahlblom, O., (2010). The effect of CFRP and CFRP/concrete interface models when modelling retrofitted RC beams with FEM. *Com. Struct*., 92(6), pp.1391-1398. Available at: https://www.sciencedirect.com/science/article/pii/S0263822309004772.
14. Ooi, E.T., Yang, Z.J., (2011). Modelling crack propagation in reinforced concrete using a hybrid finite element–scaled boundary finite element method. *Eng. Fract. Mech*., 78(2), 252-273. Available at: https://www.sciencedirect.com/science/article/pii/S0013794410003590.
15. Jafarifar, N., Pilakoutas, K. and Bennett, T., (2016). The effect of shrinkage cracks on the load bearing capacity of steel-fibre-reinforced roller-compacted-concrete pavements. *Mater. Struct*., 49(6), 2329-2347. Available at: https://link.springer.com/article/10.1617/s11527-015-0652-0.
16. Baek, J., (2010). *Modeling reflective cracking development in hot-mix asphalt overlays and quantification of control techniques*. Doctoral dissertation. University of Illinois at Urbana-Champaign.
17. Tsioulou, O.T., Dritsos, S.E., (2011). A theoretical model to predict interface slip due to bending. *Mater. and struct.*, 44(4), 825-843.
18. Banta, T.E., (2005). *Horizontal shear transfer between ultra high performance concrete and lightweight concrete*. Master of Science in Civil Engineering. Virginia Polytechnic Institute and State University.
19. Dimitriadou, O., Kotsoglou, V., Thermou, G., Savva, A., Pantazopoulou, S., (2005). Experimental study of concrete interfaces in sliding shear. Tech. Chron. Sci. J. TCG, No 2–3, 123-136 (in Greek). Cited in Tsioulou, O.T., Dritsos, S.E., (2011). A theoretical model to predict interface slip due to bending. *Mater. and struct.*, 44(4), 825-843.
20. Dritsos, S., Vandoros, C., Agelopoulos, G., Antonogiannaki, E., Tzana, M., (1996). Shear transfer mechanism at interface between old and new concrete. In: Proceedings of the 12th Greek conference on concrete, Nicosia, Cyprus, 200–213 (in Greek). Cited in Tsioulou, O.T., Dritsos, S.E., (2011). A theoretical model to predict interface slip due to bending. *Mater. and struct.*, 44(4), 825-843.

21. Hanson, N.w., (1960). Precast-prestressed concrete bridges 2. Horizontal shear connections. *J. PCA Res. Dev. Lab.*, 2(2), 38–58.
22. Mattock, A.H., (1976). Shear transfer under monotonic loading, across an interface between concrete cast at different times. Technical Report, Department of Civil Engineering, University of Washington, Report SM 76-3.
23. Pauley, T., Park, R., Phillips, M.H., (1974). Horizontal construction joints in cast-in-plane reinforced concrete. Special Publication SP-42, *ACI*, 599-616.
24. Vassiliou, G., (1975). *An investigation of the behaviour of repaired RC elements subjected to bending*. PhD Thesis. Department of Civil Engineering, National Technical University of Athens (in Greek). Cited in: Tsioulou, O.T., Dritsos, S.E., (2011). A theoretical model to predict interface slip due to bending. *Mater. and struct.*, 44(4), 825-843.
25. Vintzeleou, E., (1984). *Load transfer mechanisms along reinforced concrete interfaces under monotonic and cyclic actions*. PhD Thesis. Department of Civil Engineering, National Technical University of Athens (in Greek). Cited in: Tsioulou, O.T., Dritsos, S.E., (2011). A theoretical model to predict interface slip due to bending. *Mater. and struct.*, 44(4), 825-843.
26. BS EN 12812, (2008). Falsework-performance requirements and general design. British Standards Institution, London, UK.
27. Lampropoulos, A., Tsioulou, O., Dritsos, S.E., (2003). Analytical prediction for the capacity of old-new concrete interfaces. Proceedings of the 4th International Conference on Earthquake Resistant Engineering Structures, Ancona.
28. Jeong, J.H., Park, Y.S., Lee, Y.H., (2015). Variation of Shrinkage Strain within the Depth of Concrete Beams. Materials, 8(11), 7780-7794.
29. Younis, K. H., (2014). *Restrained shrinkage behaviour of concrete with recycled materials*. PhD thesis. Sheffield, The University of Sheffield.

Chapter 6: Conclusions and Recommendations for Future Work

This chapter summarises the findings from all chapters and presents the main conclusion drawn from the work undertaken in this study. It also recommends some future research works for recycled materials aiming to better understand their behaviour and facilitate wider application of these materials.

6.1 Summary and conclusions

The study aims to contribute to a better understanding of fibres effect the shrinkage behaviour of overlays concrete made of rapid hardening concrete. In particular, the effect of recycled clean steel fibres on the crack widths of overlays so as to lead to better predictions that can enhance the functionality, durability and sustainability of repairs. The study utilised 100% recycled fibres only. The main findings can be summarised as follows.

6.1.1 Mechanical properties of rapid hardening mortars: Experimental and numerical findings

- The fibres have a positive effect on the strength of mortar prisms. FRC mixes showed a compressive strength increase of approximately 10% to 24% at different ages, with the highest strength increase of around 24% observed at one hour. No compressive strength reduction was observed for any of the mixes tested in this study up to the age of 365 days.
- The MC function $\beta_{cc(t)}$ underestimates the strength evolution of rapid hardening mixes at early ages by 100% as the strength evolves so rapidly. Therefore, new parameters are proposed to better predict the strength development with time for mixes with CSA and RSC cements. FCSA and FRSC mixes demonstrated a flexural strength increase of approximately 36% to 70% and 24% to 41% respectively. For E_{fm}, an increase of around 25% to 29% was found for FCSA and FRSC mixes tested at different ages.
- Flexural strength of both plain and fibre reinforced specimens evolves rapidly, e.g. 90% of their one-year strength achieved in one day. The specimens made with CSA cement showed higher flexural strength compared to mixes made with RSC cement tested at the same age.
- The flexural residual strength for both FCSA and FRSC specimens continued to increase with bigger CMOD ($CMOD_4$). FCSA prisms show higher flexural residual strength than FRSC prisms for the same crack width. The values of f_R continue to increase with time for both fibre reinforced mixes and reach their peak values at 28 days. However, there is a slight strength reduction at the age of one year

compared to 28 days. Strong correlations are found between f_{R1} and f_{R2}, f_{R1} and f_{R3}, f_{R1} and f_{R4} with $R^2 \geq 0.98$ and $R^2 \geq 0.92$ for FCSA and FRSC, respectively.

- FE-predictions using the tensile constitutive laws based on RILEM TC 162-TDF, CEB FIB MODEL CODE 2010, Barros et al. [1] overestimate the loading capacity of FCSA and FRSC specimens. Conversely, the use of the models proposed by Hu et al. [2] leads to underestimation.
- Numerical analyses using $\sigma - \varepsilon$ curves obtained from inverse analysis were successful in modelling the global load-displacement behaviour as well as capturing the cracking widths of FRC tested prisms.

6.1.2 Moisture and free shrinkage properties findings

- The fibre inclusion in rapid hardening mortar mixes was shown not to have a major role on the moisture transport properties of these mixes, which allows the use of the MC equation for plain concrete to calculate their moisture diffusivities with a good accuracy.
- Mixes with RSC cement showed much higher shrinkage strains (2690 and 2532 $\mu\varepsilon$) compared to mixes with CSA cement (211 and 367 $\mu\varepsilon$) at 120 days. Unlike CSA and FCSA, RSC and FRSC mixes showed considerable autogenous shrinkage which accounts for around 64 % and 71% of their total shrinkage at the age of 60 days.
- The moisture diffusivity of the tested mixes was back calculated by using a combination of FE analyses and experimental moisture distribution measurements. It was found that the moisture diffusivities for the mixes are high at the beginning of drying (34.8 – 24.14 mm^2/day) and remain almost unchanged up to moisture contents of 85% - 75%, for different mixes, then sharply decrease with further drying.
- A linear relationship was found between shrinkage and moisture loss for all the mixes with good correlation ratios.
- The back calculated hygral contraction coefficient, for each mix, range from 0.00038 to 0.0048 depending on the cement type and fibre inclusion.
- New appropriate coefficients for each cement type are proposed to predict the shrinkage development with time using MC and ACI equations.

- Although the Silfwerbrand procedure, used to determine normal and shear stresses in overlay case studies, is rather simple, it relies on parameters (λL and K) that are not easy to determine, and it assumes uniform shrinkage distribution through the depth of the layer which may not be true.

6.1.3 Restrained shrinkage of overlays: Experimental and analytical findings

- The restrained shrinkage of composite prisms depends on the free shrinkage strain of the mix and level of restraint. CSA composite prisms showed less measured shrinkage strains compared to FCSA composite prisms due to the lower free shrinkage strain of CSA mix.
- CSA and FCSA prisms showed no cracking for the duration of the test. However, RSC and FRSC mixes developed multiple cracking at the outer edges of the prisms in less than 16 hours. It should be noted though that only two RSC prisms showed local debonding at one end which did not propagate further under flexural testing.
- There a shrinkage gradient across the depth of an overlay with higher shrinkage strains at the top layer compared to the lower part of the overlay. This gradient resulted in bigger cracks at the top of the layer.
- A simple analytical model for estimating crack spacings of overlays is presented. Fibres are found not to have a significant effect on the crack spacing of concrete overlays. It was found that the ratio between maximum and average crack spacings is approximately 1.7. This value is well consistent with the ratio suggested by MC for the ratio of crack spacing in conventional RC.
- The available approaches in literature to estimate the crack widths of FRC overlays fail to predict the contribution of RCSF on the crack width of overlays. A simple approach, based on stress loss rather than flexural post cracking, is proposed to consider the effect of RSCF fibres on the width of cracks and evaluated. A good agreement between the measured experimental crack widths of RSC and FRSC composite prisms and those predicted using the suggested approaches is obtained.
- Both plain and fibre reinforced overlays showed multiple cracking due to restrained shrinkage, however, around 60% smaller widths are measured on FRSC prisms.

- Restrained shrinkage has a negative effect on the flexural capacity of composite prisms. However, RSCF are found to mitigate this effect by bridging cracks and providing higher resistance to flexural loads. Therefore, repaired structures with fibre reinforced concrete are expected to have a better durability and extended fatigue life.
- Fibres are found to insignificantly affect the interfacial shear strength of overlays. Nevertheless, as the fibres carry loads at the cracked sections along the overlay, the resulting shear stresses at the interface are expected to be smaller than those at the interface of plain prisms, and thus, reduce the risk of delamination after cracking development.

6.1.4 Restrained shrinkage of overlays: Numerical findings

- The sequential heat analysis coupled with structural analysis is successful in predicting the shrinkage development with time for the tested composite prisms. Both the frictional and cohesive approaches examined are efficient in modelling the interface between concrete layers. The CSA prisms showed no cracking in numerical modeling as it is the case in experimental study. FCSA prisms showed minor cracking at the edges which disappear when incorporating creep in the FE analysis. This highlights the important role of creep in estimating hygral stresses of concrete repairs.
- The FE predicted tensile and shear stresses were consistent with those estimated using Silfwerbrand analytical approach when assuming uniform shrinkage across the depth of the overlay. However, it is shown that the uniform shrinkage strain assumption underestimates the tensile stresses that develop in overlays. An empirical approach to consider this effect in the Silfwerbrand approach is proposed.
- The interface stiffness has a considerable effect on restrained shrinkage of overlays, as more restraint is developed for interfaces with higher stiffness values, therefore, bigger risk of cracking. However, for well-prepared surfaces, both interfacial stiffness and strength values are shown to increase. Having sufficient bond strength is crucial to prevent the delamination, especially when the shrinkage strains are very high.
- Fibres are demonstrated to slow down the evolution of local slippage at the interface at crack locations

by controlling the cracking widths and, thus, can contribute in reducing the risk of delamination. This was considered in numerical models by introducing a slower damage evolution to interface stiffnesses.

- The moisture content of the substrate and interface absorption properties are shown to have an effect on restrained shrinkage of overlays and, therefore, on tensile stress development as drier bases tend to absorb more moisture from overlays.

6.2 General conclusions

The overall aim of this research was to quantify the fibre effect on the width of cracks of overlays under restrained shrinkage conditions, in particular, the effect of RCSF. This was successfully achieved.

6.3 Recommendations for Future Work

Based on the investigation and findings of this study, the following issues should be further investigated:

- The effect of different fibre dosages on the fresh and mechanical properties of the mixes. Based on the results, σ-ε tensile models for design purposes can be developed.
- The behaviour of other supplementary cementitious materials (e.g. GGBS, geopolymer and fly ash).
- Investigate further the autogenous shrinkage of RSC and FRSC mixes.
- Investigate shear stress distribution after crack development and the evolution of interfacial shear strength.
- Establish a relationship between the level of preparation at the interface, in terms of interface roughness, and the interfacial strength and stiffness.
- Investigate the creep of rapid hardening materials.
- Investigate further the non-uniform shrinkage strain across the depth of overlays and provide analytical predictions to consider its effect.
- Study the fatigue behaviour of overlays reinforced with RCSF.

References

1. Barros, J.A.O., Cunha, V.M.C.F., Ribeiro, A.F., Antune J.A.B., (2005). Post-Cracking Behaviour of Steel Fibre-Reinforced Concrete. *Mater. Struct.*, 38, 47-56.
2. Hu, H., Wang, Z., Figueiredo, F., Papastergiou, P., Guadagnini, M., Pilakoutas, K., (2018). Post-cracking tensile behaviour of blended steel fibre reinforced concrete. *Struct. Concr.*, Submitted for publication.

Appendix: A

This appendix presents more detailed photos and raw data for the experimental work described in Chapter 2 of the thesis.

Figure A. 1 Semi-adiabatic test

Figure A. 2 Casting CSA flexural prisms

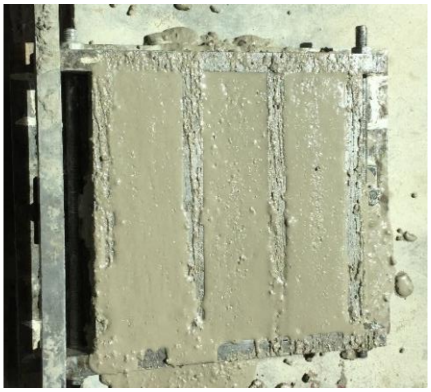

Figure A. 3 Casting RSC flexural prisms

Figure A. 4 RCSF used in this study

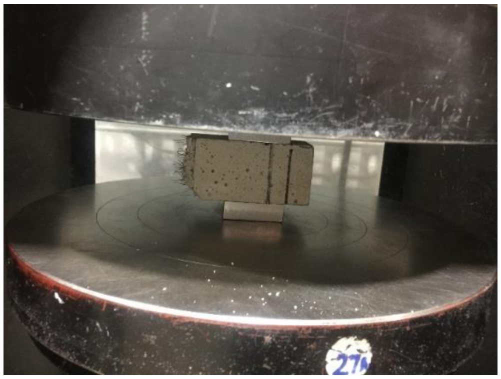

Figure A. 5 Compressive strength test of fractured prisms

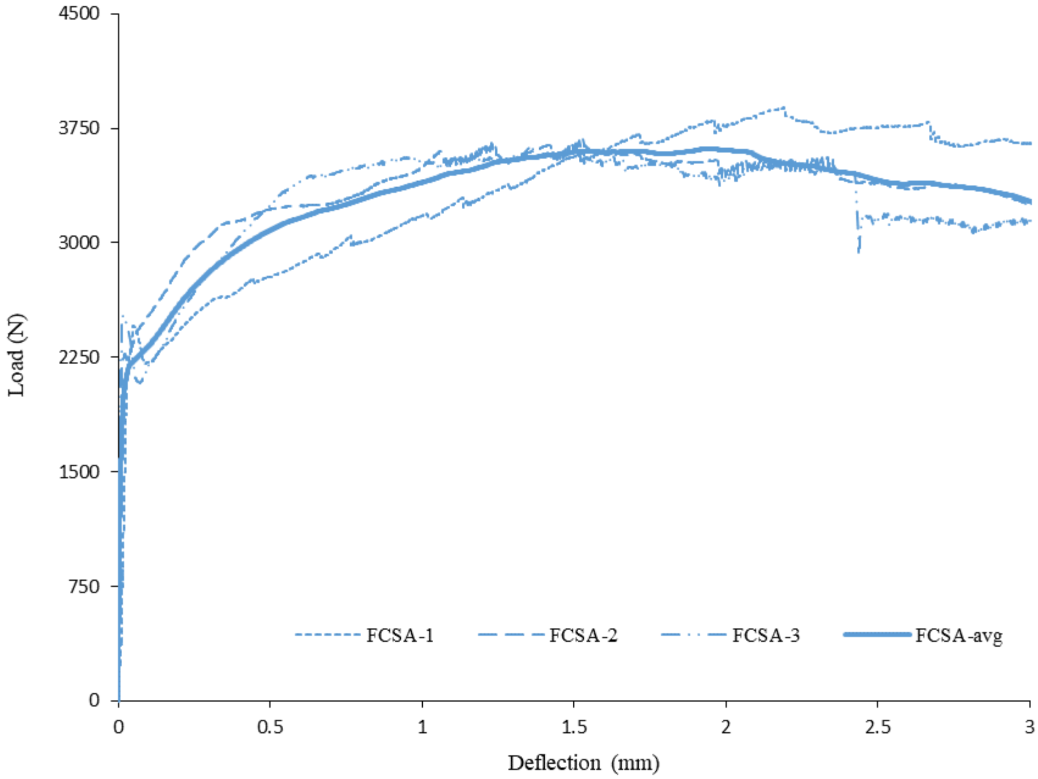

Figure A. 6 Load deflection curve of FCSA prisms at the age of two days

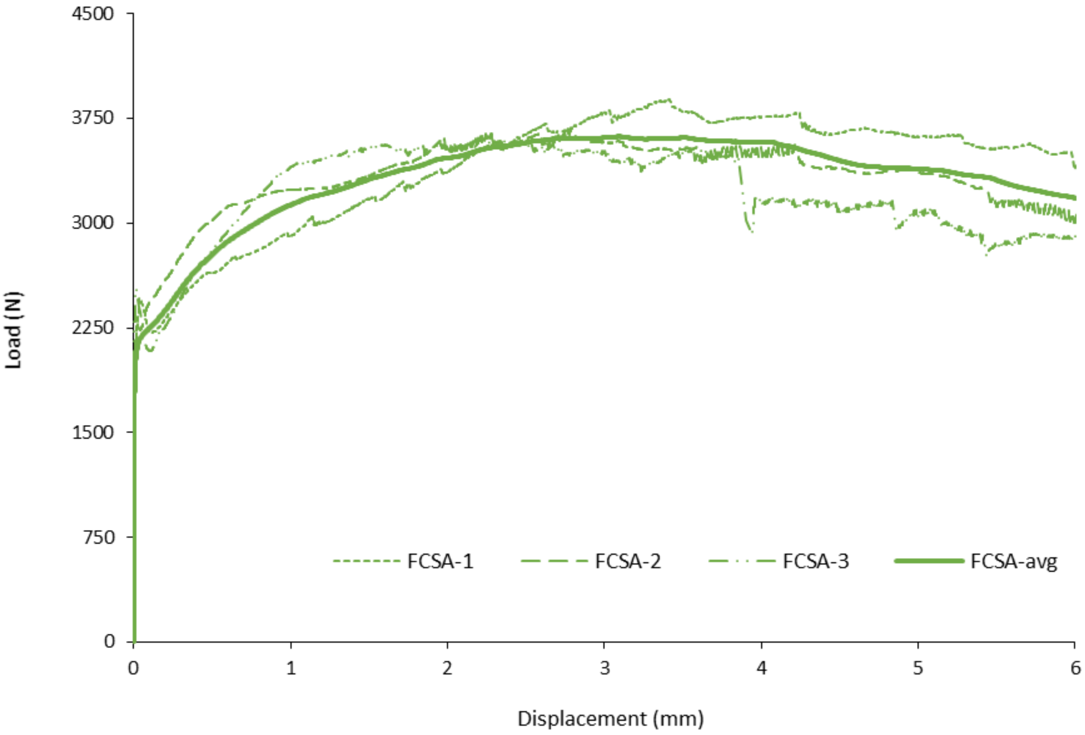

Figure A. 7 Load CMOD curve of FCSA prisms at the age of two days

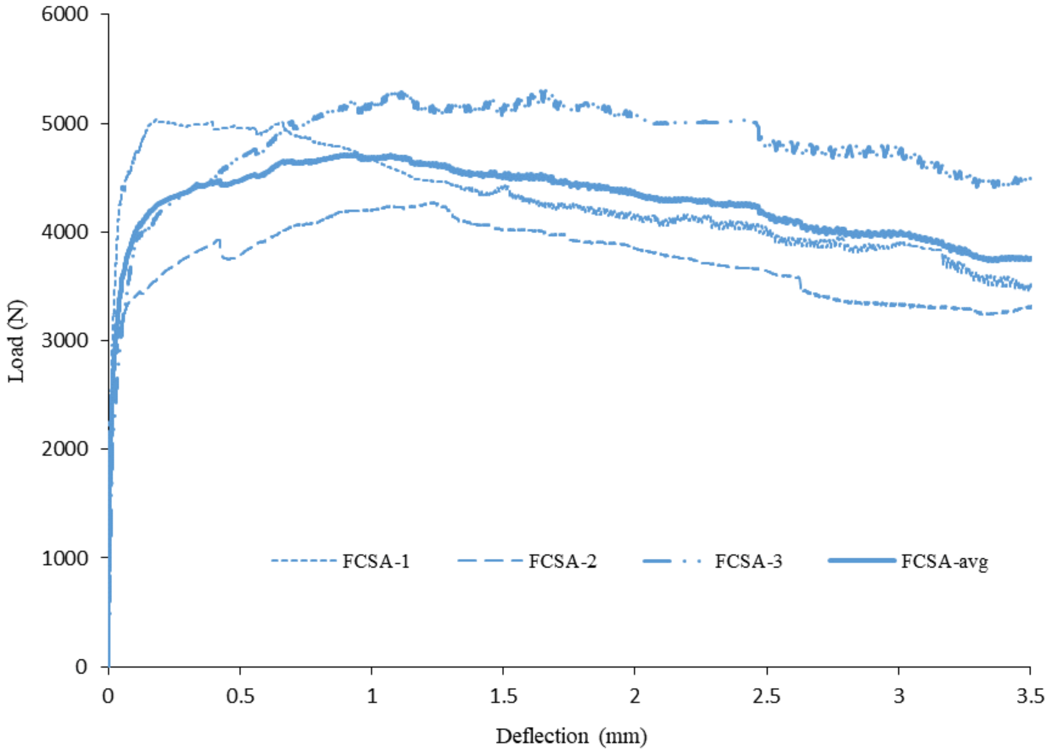

Figure A. 8 Load deflection curve of FCSA prisms at the age of seven days

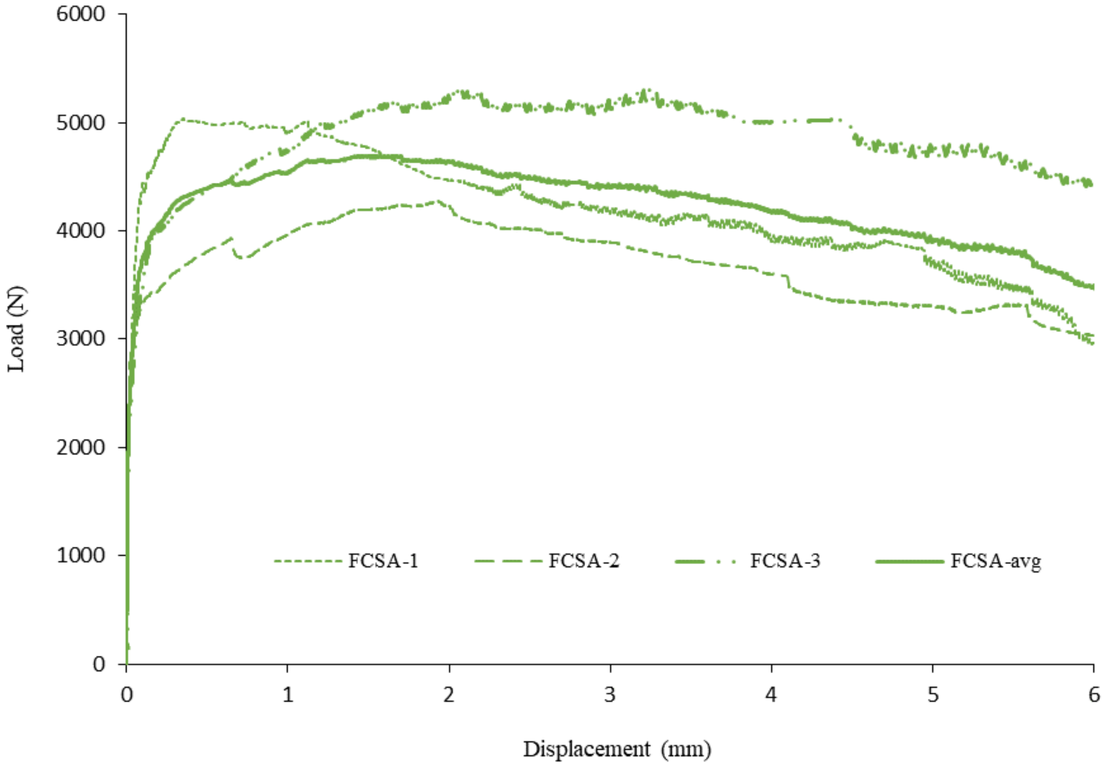

Figure A. 9 Load CMOD curve of FCSA prisms at the age of seven days

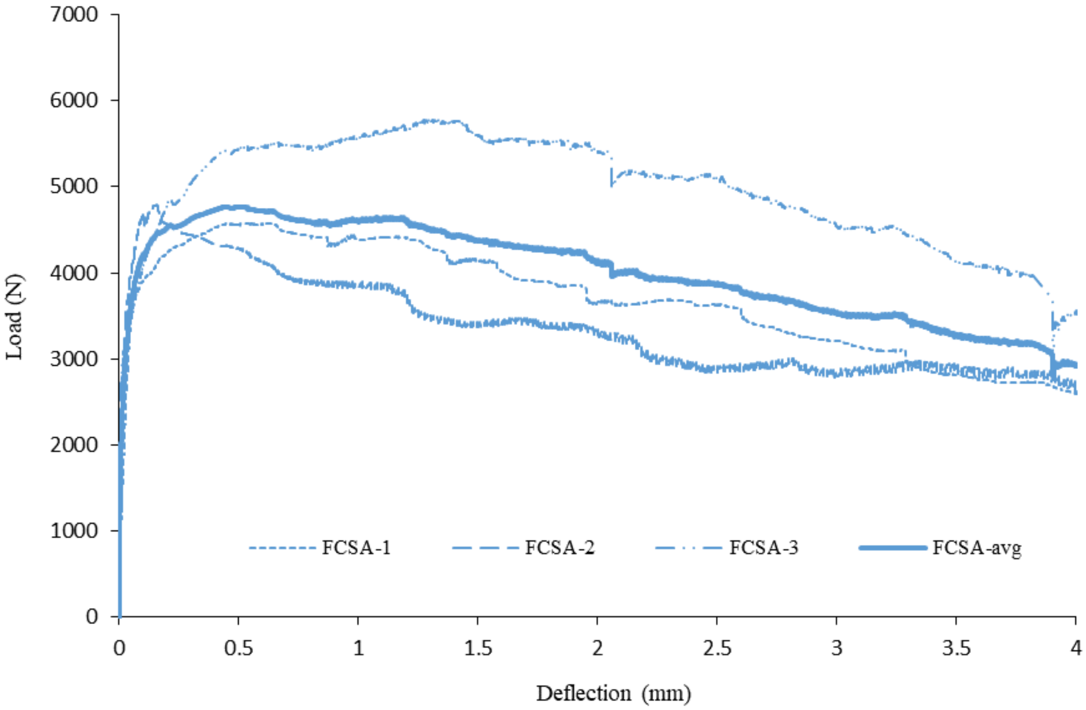

Figure A. 10 Load deflection curve of FCSA prisms at the age of 28 days

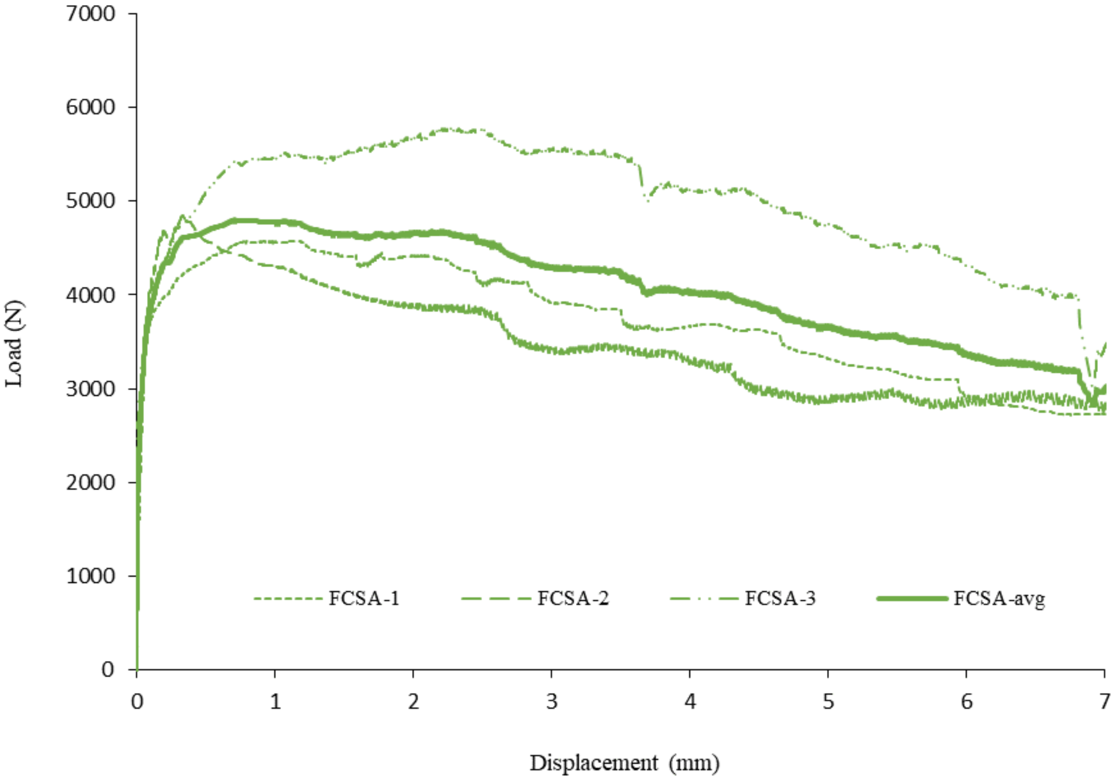

Figure A. 11 Load CMOD curve of FCSA prisms at the age of 28 days

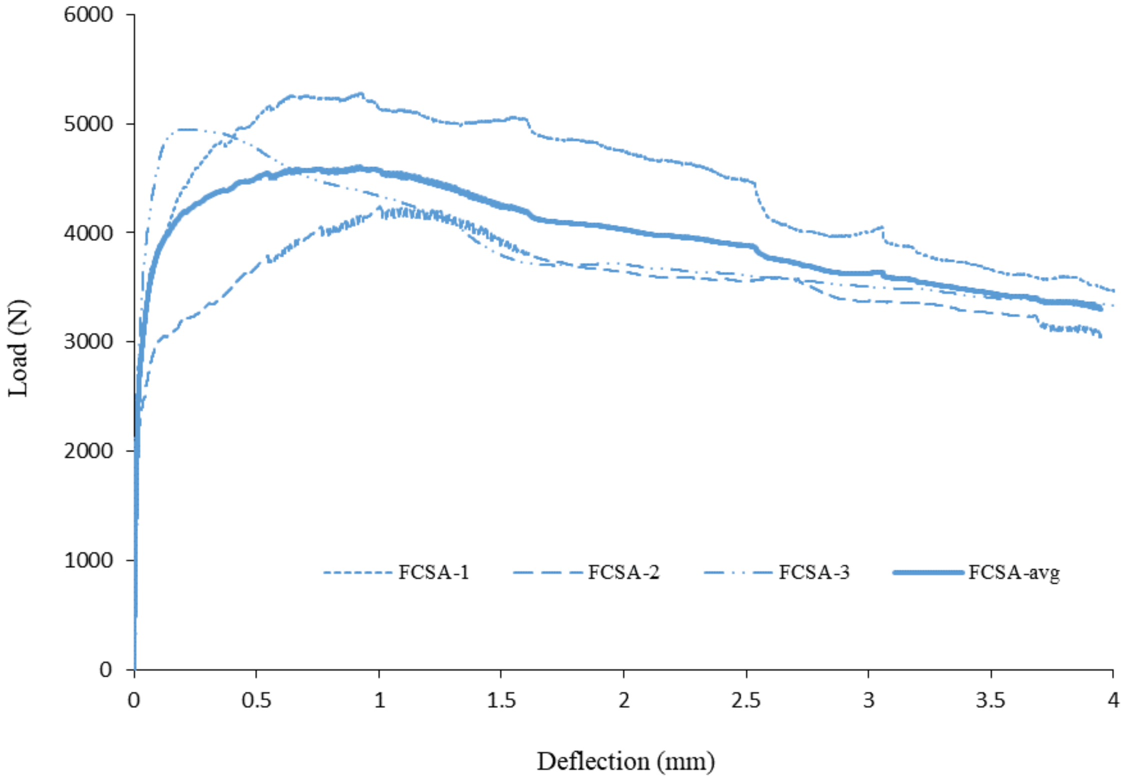

Figure A. 12 Load deflection curve of FCSA prisms at the age of 365 days

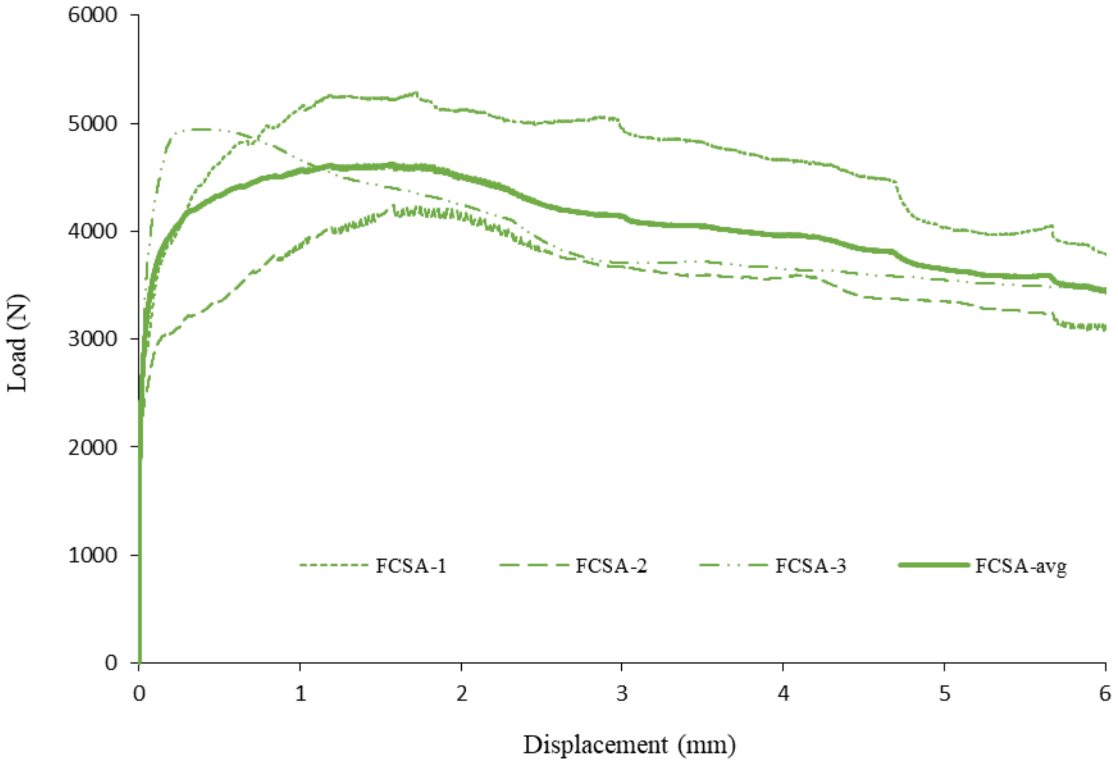

Figure A. 13 Load CMOD curve of FCSA prisms at the age of 365 days

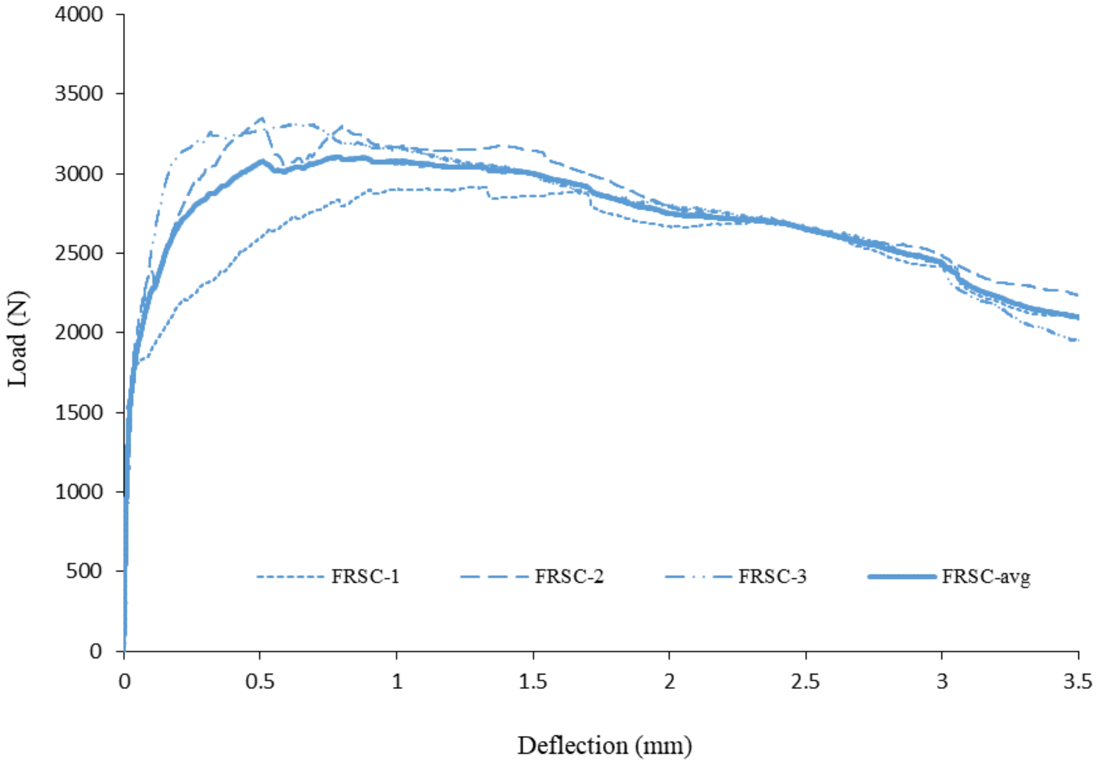

Figure A. 14 Load deflection curve of FRSC prisms at the age of two days

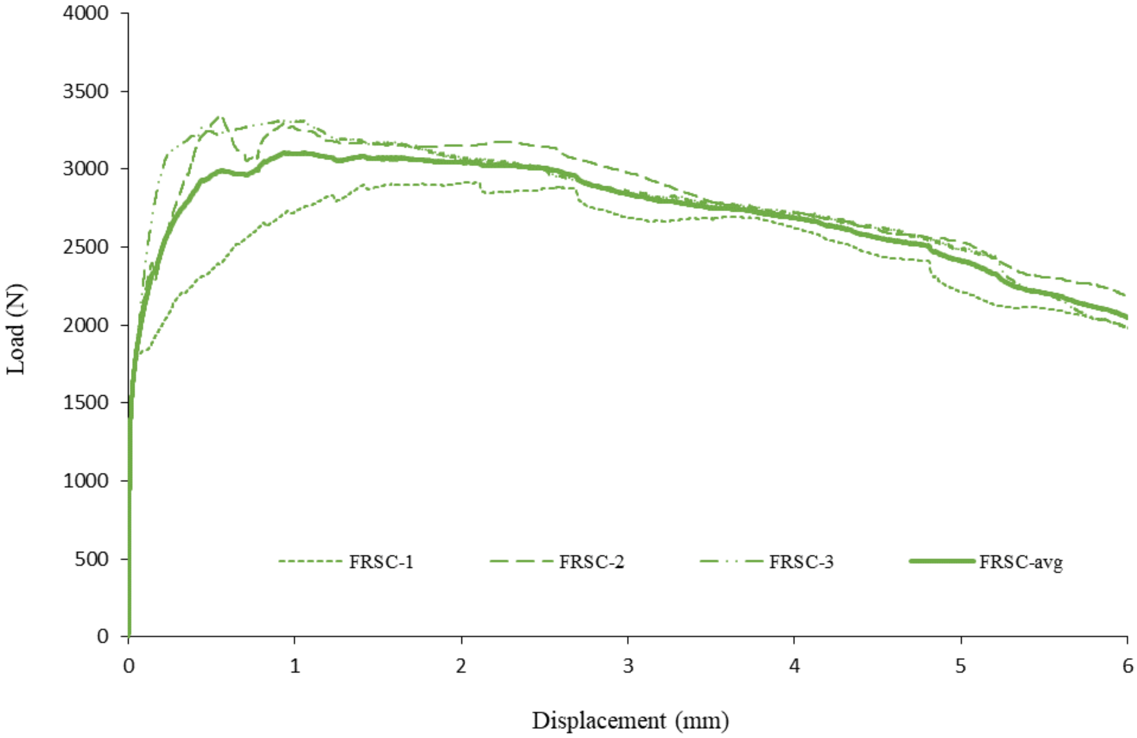

Figure A. 15 Load CMOD curve of FRSC prisms at the age of two days

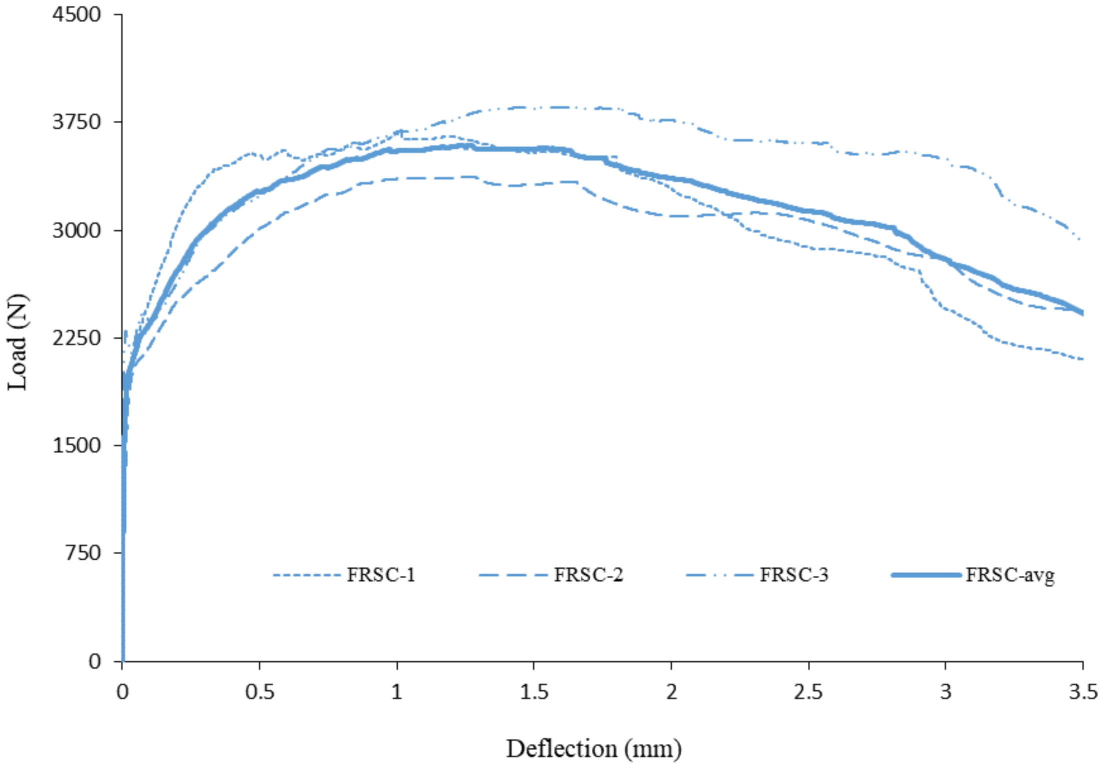

Figure A. 16 Load deflection curve of FRSC prisms at the age of seven days

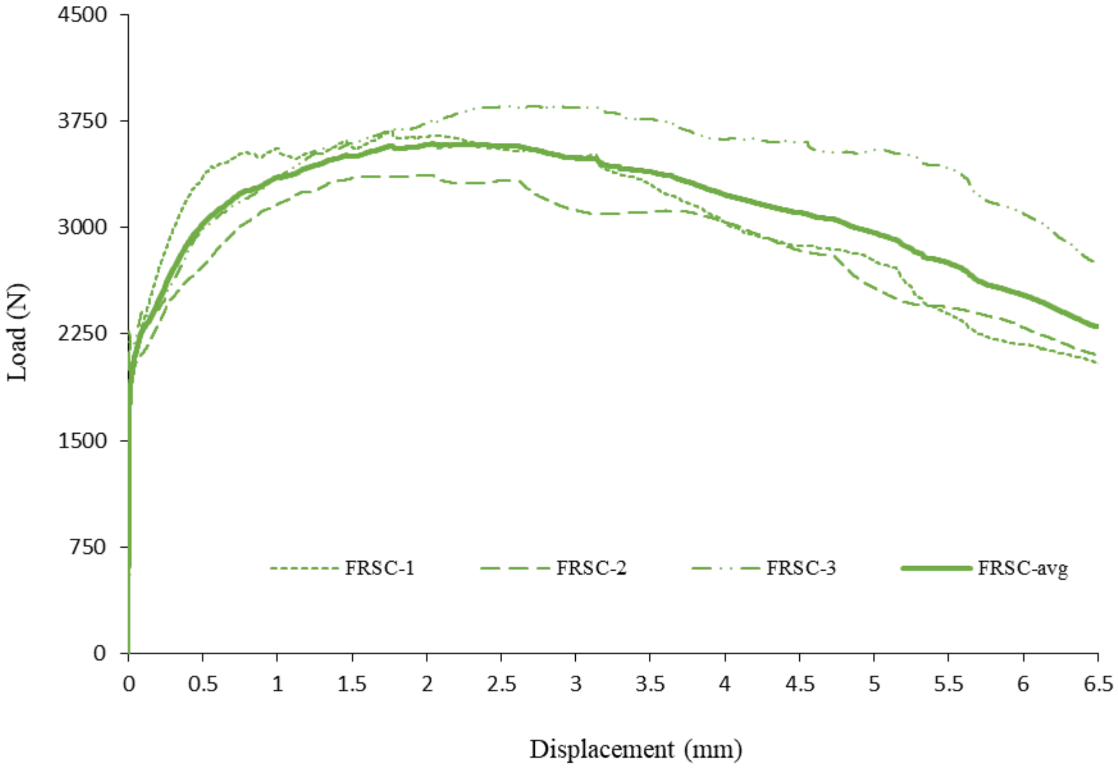

Figure A. 17 Load CMOD curve of FRSC prisms at the age of seven days

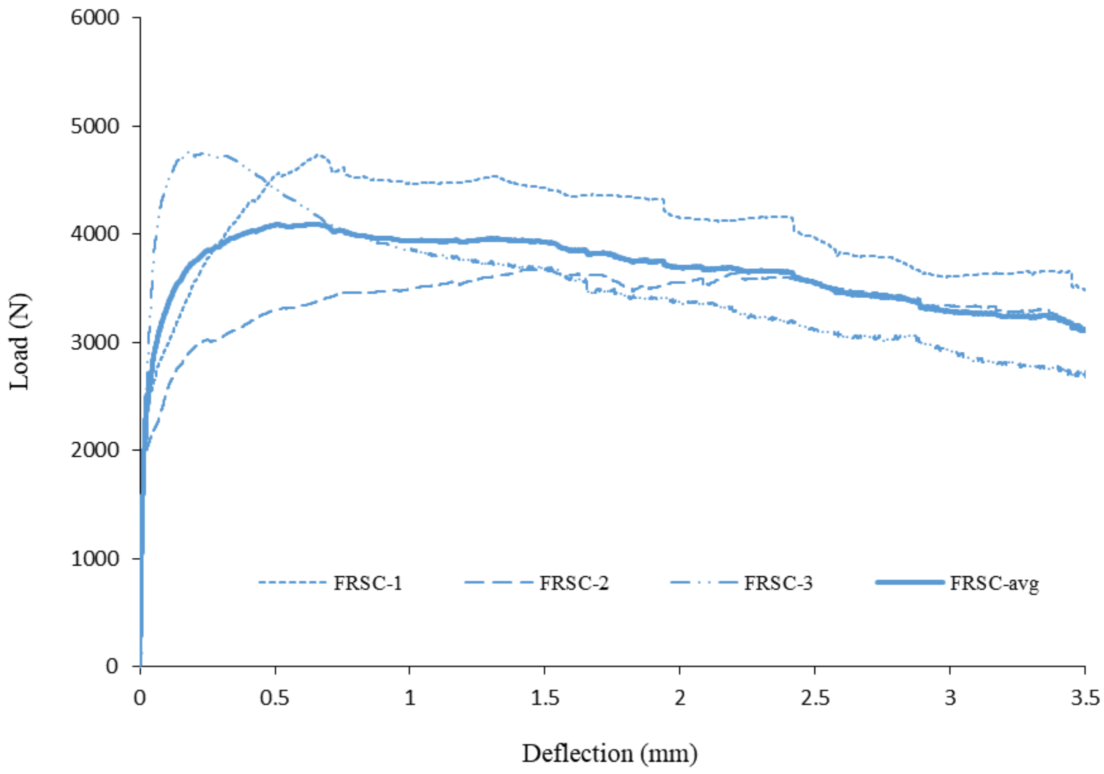

Figure A. 18 Load deflection curve of FRSC prisms at the age of 28 days

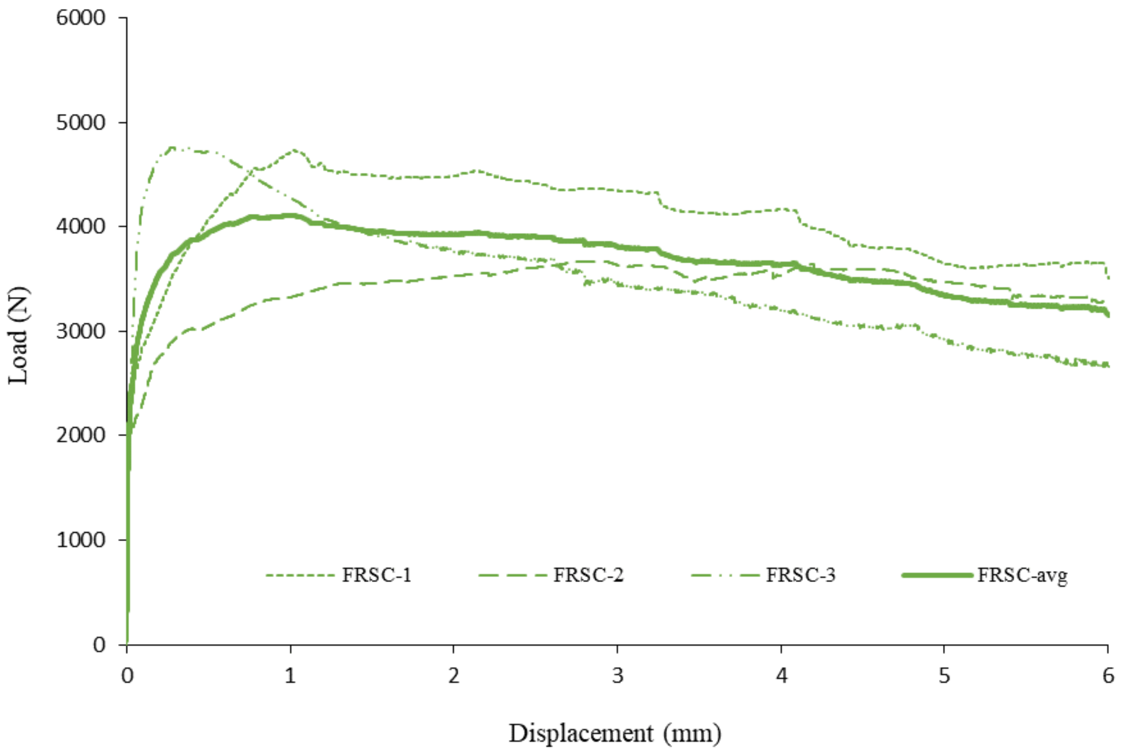

Figure A. 19 Load CMOD curve of FRSC prisms at the age of 28 days

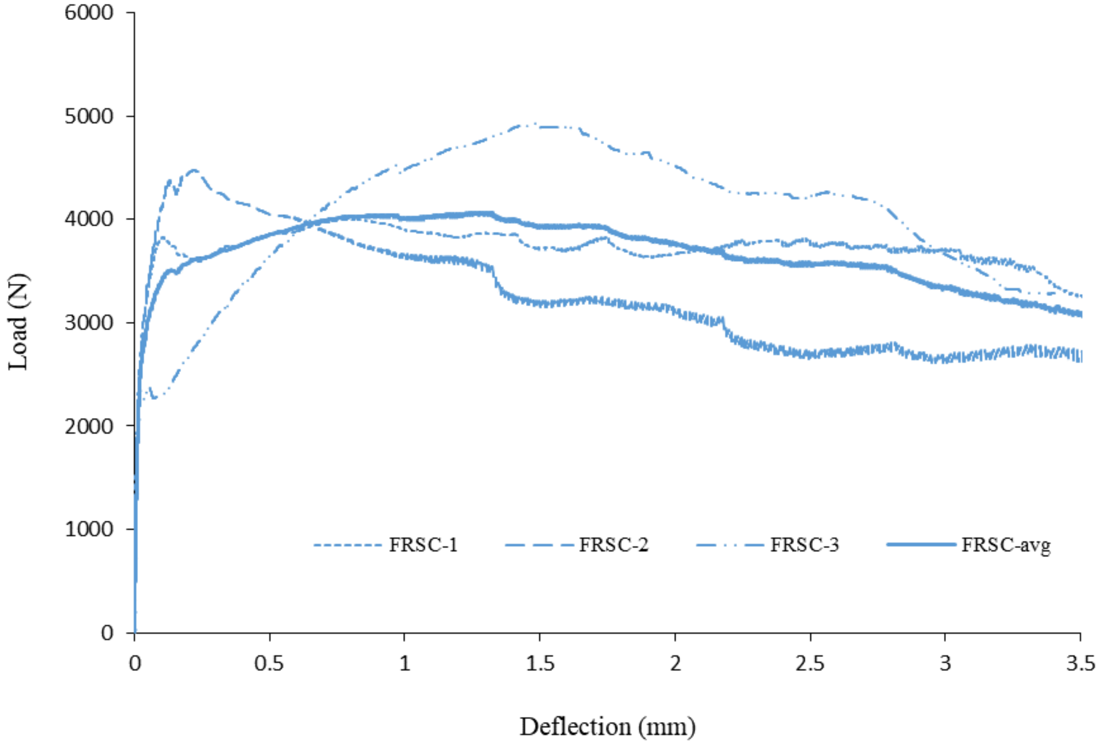

Figure A. 20 Load deflection curve of FRSC prisms at the age of 365 days

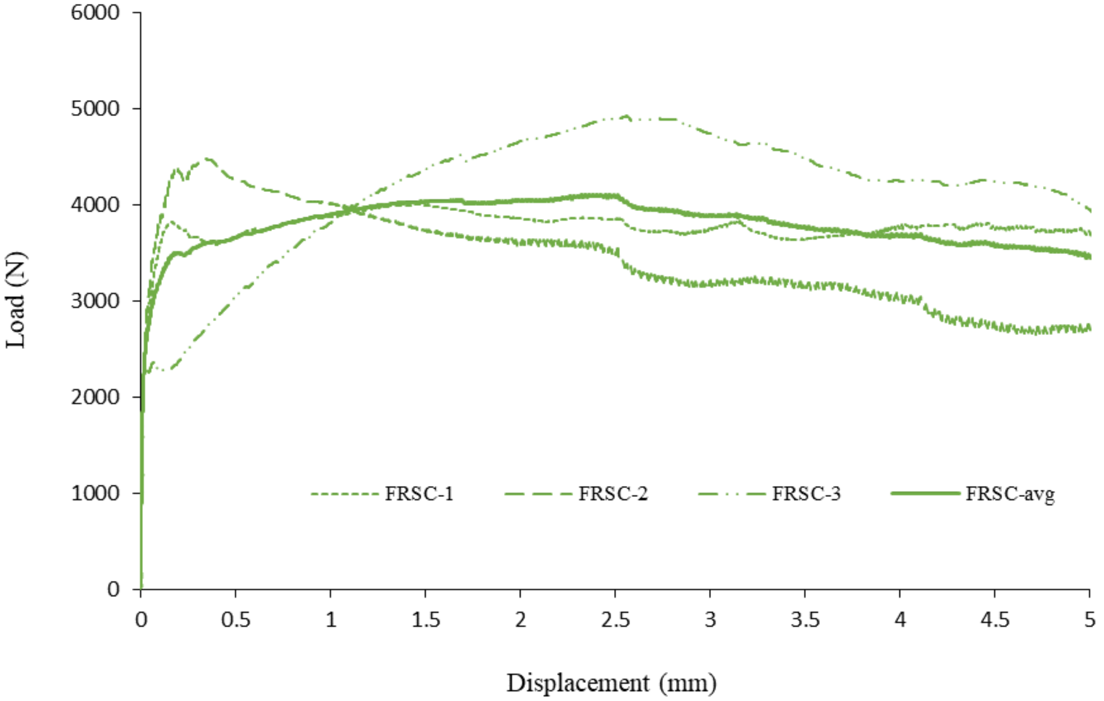

Figure A. 21 Load CMOD curve of FRSC prisms at the age of 365 day

Table A. 1 Compressive strength of the mixes f_{cu} at different ages (MPa)

Time (days)		0.04167	0.125	1	7	28	365
FCSA	1	18.9	25.7	36.6	35.9	41.1	41.6
	2	22.8	29.1	40.0	39.0	45.7	42.5
	3	26.0	34.7	38.5	43.2	48.2	45.1
	4	29.6	35.6	33.9	41.4	39.5	49.2
	5	28.5	33.0	36.0	41.6	42.4	46.4
	6	31.1	31.2	34.9	45.2	41.9	48.1
	Avg.	26.1	31.6	36.6	41.1	43.1	45.5
CSA	1	17.0	23.0	34.9	31.9	39.2	38.9
	2	18.3	26.5	33.5	34.4	42.0	39.6
	3	22.0	24.9	28.0	40.0	35.4	45.3
	4	22.6	27.2	29.8	38.4	36.8	40.0
	5	25.0	30.4	32.5	34.2	39.2	40.5
	6	22.0	29.5	31.8	36.9	39.1	41.1
	Avg.	21.1	26.9	31.8	36.0	38.6	40.9
FRSC	1	16.8	28.6	41.5	41.9	51.4	61.1
	2	19.4	33.2	40.0	43.6	55.3	57.4
	3	25.7	31.7	37.1	48.6	46.9	50.7
	4	21.0	25.0	34.9	50.5	49.9	43.0
	5	22.7	26.3	36.7	47.1	52.7	55.8
	6	22.5	24.9	37.3	45.3	52.9	59.0
	Avg.	21.3	28.3	37.9	46.2	51.5	54.5
RSC	1	14.7	23.1	35.8	39.3	48.6	52.1
	2	15.6	20.5	33.1	37.3	50.2	49.1
	3	20.1	24.7	33.1	44.2	46.7	50.9
	4	17.6	25.4	34.4	42.2	45.5	49.5
	5	18.3	26.1	30.4	40.1	43.0	43.2
	6	17.0	25.2	31.2	39.3	45.0	43.7
	Avg.	17.2	24.2	33.0	40.4	46.5	48.1

Table A. 2 Load at limit of proportionality of the mixes at different ages (N)

Time	FCSA				CSA			
	1	2	3	Avg.	1	2	3	Avg.
0.04167	1509.8	1666.8	1330.9	1502.5	1185.3	1010.0	1105.1	1100.1
0.125	3095.4	2689.9	2871.9	2885.7	1790.5	1645.2	1660.7	1698.8
1	2990.6	2592.8	2681.3	2754.9	1795.7	1929.1	1835.3	1853.4
7	3835.1	3479.8	3150.2	3488.4	2411.0	2155.8	2218.4	2261.7
28	4112.1	3303.2	3688.3	3701.2	2438.1	2264.4	2170.1	2290.9
365	4160.0	3630.3	3302.2	3697.5	2201.2	2419.1	2285.4	2301.9
Time	FRSC				RSC			
	1	2	3	Avg.	1	2	3	Avg.
0.04167	1360.6	1472.8	1669.1	1500.9	1142.6	998.8	1096.3	1079.3
0.125	1361.0	1478.4	1686.3	1508.6	1149.4	1282.4	1230.5	1220.8
1	2331.7	1939.6	2105.6	2125.6	1519.6	1554.3	1461.2	1511.7
7	2680.0	2379.7	2030.4	2363.4	1821.9	1863.8	1716.0	1800.5
28	2407.8	2818.4	2000.1	2408.8	1799.0	1955.8	1869.7	1874.9
365	2360.1	2781.2	2062.3	2401.2	1962.4	1900.7	1870.9	1911.3

Table A. 3 Modulus of elasticity of the mixes at different ages (GPa)

Time (days)	FCSA				CSA			
	1	2	3	Avg.	1	2	3	Avg.
0.04167	13.83	17.58	15.59	15.67	13.12	11.80	11.29	12.07
0.125	16.26	19.00	17.38	17.54	14.44	13.41	12.90	13.59
1	24.59	20.10	22.19	22.29	18.25	17.62	16.78	17.55
7	22.12	24.21	28.75	25.03	21.56	18.96	18.56	19.69
28	32.11	25.28	25.31	27.57	23.56	21.43	19.50	21.50
365	30.95	25.91	27.12	28.00	24.17	19.15	21.88	21.73
Time (days)	FRSC				RSC			
	1	2	3	Avg.	1	2	3	Avg.
0.04167	11.80	13.65	11.28	12.24	9.02	10.65	9.26	9.64
0.125	15.89	13.72	12.52	14.04	12.23	10.23	11.06	11.18
1	20.54	15.81	17.52	17.96	16.06	13.15	12.66	13.96
7	25.70	22.08	22.97	23.58	20.02	18.03	16.82	18.29
28	30.32	22.03	25.56	25.97	22.62	19.60	18.85	20.36
365	26.01	23.00	29.32	26.11	23.91	18.27	19.51	20.56

Appendix: B

This appendix presents more detailed photos and raw data for the experimental work described in Chapter 3 of the thesis.

Table B. 1 Moisture measurement test results of CSA mix

Net weight of each sample during drying (unsealed weight) (gr)*										
Specimen No.		**S1-1**	**S1-2**	**S1-avg.**	**S2-1**	**S2-2**	**S2-avg.**	**S3-1**	**S3-2**	**S3-avg.**
Height of each sample (mm)		7.52	7.84	7.68	18.71	17.75	18.23	29.47	28.01	28.74
Drying time (days)	0	160.23	169.27	164.75	403.60	390.42	397.01	632.18	623.66	627.92
	0.08	160.08	169.20	164.64	403.49	390.08	396.79	631.85	623.49	627.66
	0.16	159.95	169.03	164.49	403.34	389.92	396.63	631.71	623.27	627.49
	1	159.16	168.39	163.78	402.58	389.24	395.91	630.96	622.45	626.71
	2	158.41	168.01	163.21	402.02	388.57	395.30	630.29	621.85	626.07
	3	158.25	167.78	163.02	401.54	388.10	394.82	629.81	621.28	625.55
	4	158.14	167.66	162.90	401.30	387.71	394.51	629.36	620.82	625.09
	5	158.02	167.49	162.76	401.04	387.42	394.23	628.63	620.48	624.56
	6	157.97	167.46	162.72	400.66	387.10	393.88	628.24	619.96	624.10
	7	157.95	167.42	162.69	400.44	386.83	393.64	627.69	619.55	623.62
	10	157.83	167.33	162.58	400.19	386.65	393.42	627.32	619.09	623.21
	14	157.79	167.29	162.54	399.90	386.52	393.21	627.15	618.89	623.02
	21	157.71	167.22	162.47	399.39	386.01	392.70	626.35	618.31	622.33
	28	157.42	167.00	162.21	398.68	385.53	392.11	625.23	617.19	621.24
	60	156.98	166.44	161.71	397.64	384.13	390.89	623.49	614.61	619.05
	90	155.70	165.67	160.69	395.96	382.59	389.28	621.48	612.05	616.77
	120	155.41	165.25	160.33	395.11	381.75	388.43	620.33	611.26	615.80
Weight after drying in the oven (gr)		150.93	155.09	153.01	376.12	363.62	369.87	590.15	582.01	586.08

Table B. 2 Moisture measurement test results of FCSA mix

Weight of each sample during drying (unsealed weight) (gr)*										
Specimen No.		**S1-1**	**S1-2**	**S1-avg.**	**S2-1**	**S2-2**	**S2-avg.**	**S3-1**	**S3-2**	**S3-avg.**
Height of each sample (mm)		9.29	8.91	9.10	15.27	17.09	16.18	27.42	29.99	28.71
Drying time (days)	0	203.99	196.03	200.01	352.98	363.48	358.23	614.31	634.69	624.50
	0.08	203.86	195.94	199.90	352.85	363.37	358.11	614.19	634.55	624.37
	0.16	203.71	195.78	199.75	352.65	363.18	357.92	613.92	634.42	624.17
	1	203.52	195.43	199.48	352.35	362.90	357.63	613.58	634.08	623.83
	2	203.08	194.95	199.02	351.82	362.48	357.15	613.11	633.55	623.33
	3	202.76	194.66	198.71	351.40	362.04	356.72	612.64	633.05	622.85
	4	202.62	194.53	198.58	351.11	361.79	356.45	612.24	632.69	622.47
	5	202.46	194.36	198.41	350.83	361.51	356.17	611.99	632.38	622.19
	6	202.29	194.23	198.26	350.48	361.16	355.82	611.19	631.71	621.45
	7	202.12	194.08	198.10	350.28	360.84	355.56	610.72	631.30	621.01
	10	201.92	193.89	197.91	349.89	360.41	355.15	610.40	630.86	620.63
	14	201.44	193.46	197.45	349.02	359.39	354.21	609.28	629.64	619.46
	21	201.20	193.22	197.21	348.67	358.86	353.77	608.41	628.82	618.62
	28	200.92	192.97	196.95	348.41	358.67	353.54	607.46	627.79	617.63
	60	199.80	191.84	195.82	346.65	356.84	351.75	603.78	625.89	614.84
	90	198.36	190.45	194.41	344.92	354.79	349.86	601.41	623.46	612.44
	120	197.94	189.96	193.95	344.06	353.90	348.98	599.66	621.92	610.79
Weight after drying in the oven (gr)		189.89	182.15	186.02	329.96	337.92	333.94	570.11	592.15	581.13

Table B. 3 Moisture measurement test results of RSC mix

Weight of each sample during drying (unsealed weight) (gr)*										
Specimen No.		**S1-1**	**S1-2**	**S1-avg.**	**S2-1**	**S2-2**	**S2-avg.**	**S3-1**	**S3-2**	**S3-avg.**
Height of each sample (mm)		8.11	9.24	8.68	18.01	19.11	18.56	29.49	28.57	29.03
Drying time (days)	0	189.12	196.45	192.79	415.13	425.88	420.51	640.82	650.96	645.89
	0.08	189.02	196.33	192.68	415.01	425.69	420.35	640.67	650.79	645.73
	0.16	188.74	196.04	192.39	414.69	425.43	420.06	640.39	650.46	645.43
	1	188.38	195.60	191.99	414.24	424.96	419.60	639.88	650.03	644.96
	2	188.13	195.31	191.72	414.01	424.74	419.38	639.71	649.75	644.73
	3	187.86	195.04	191.45	413.58	424.29	418.94	639.32	649.23	644.28
	4	187.58	194.78	191.18	413.26	423.94	418.60	639.01	648.84	643.93
	5	187.44	194.67	191.06	413.05	423.68	418.37	638.69	648.62	643.66
	6	187.38	194.57	190.98	412.76	423.41	418.09	638.28	648.30	643.29
	7	187.32	194.49	190.91	412.57	423.20	417.89	638.04	648.02	643.03
	10	187.20	194.36	190.78	412.04	422.74	417.39	637.36	647.28	642.32
	14	187.03	194.17	190.60	411.52	422.10	416.81	636.47	646.34	641.41
	21	186.82	193.99	190.41	410.91	421.53	416.22	635.39	645.25	640.32
	28	186.62	193.81	190.22	410.33	420.89	415.61	634.32	644.19	639.26
	60	185.85	192.98	189.42	409.03	418.94	413.99	631.42	641.20	636.31
	90	185.30	192.48	188.89	408.15	418.05	413.10	630.16	640.02	635.09
	120	184.97	192.04	188.51	407.37	417.38	412.38	629.23	639.02	634.13
Weight after drying in the oven (gr)		178.94	185.88	182.41	393.21	403.69	398.45	608.12	619.15	613.64

Table B. 4 Moisture measurement test results of FRSC mix

Weight of each sample during drying (unsealed weight) (gr)*										
Specimen No.		**S1-1**	**S1-2**	**S1-avg.**	**S2-1**	**S2-2**	**S2-avg.**	**S3-1**	**S3-2**	**S3-avg.**
Height of each sample (mm)		8.49	8.79	8.64	19.31	20.33	19.82	28.29	29.14	28.72
Drying time (days)	0	192.05	200.77	196.41	446.99	456.92	451.96	647.87	663.94	655.91
	0.08	191.92	200.66	196.29	446.87	456.78	451.83	647.73	663.82	655.78
	0.16	191.64	200.38	196.01	446.55	456.49	451.52	647.40	663.52	655.46
	1	191.45	200.12	195.79	446.30	456.26	451.28	647.12	663.28	655.20
	2	191.22	199.87	195.55	446.04	456.01	451.03	646.87	663.03	654.95
	3	190.82	199.45	195.14	445.59	455.53	450.56	646.37	662.54	654.46
	4	190.56	199.21	194.89	445.17	455.09	450.13	645.93	662.10	654.02
	5	190.03	198.64	194.34	444.47	454.41	449.44	645.21	661.31	653.26
	6	189.81	198.44	194.13	444.03	453.98	449.01	644.80	660.78	652.79
	7	189.70	198.31	194.01	443.72	453.71	448.72	644.45	660.41	652.43
	10	189.58	198.19	193.89	443.15	453.11	448.13	643.79	659.73	651.76
	14	189.47	198.10	193.79	442.76	452.76	447.76	643.13	659.09	651.11
	21	189.26	197.89	193.58	442.04	452.00	447.02	641.89	657.83	649.86
	28	189.13	197.76	193.45	441.36	451.31	446.34	640.80	656.72	648.76
	60	188.63	197.23	192.93	439.89	449.86	444.88	638.37	654.33	646.35
	90	188.19	196.78	192.49	438.98	448.96	443.97	637.03	653.03	645.03
	120	187.64	196.32	191.98	437.97	448.01	442.99	635.80	651.82	643.81
Weight after drying in the oven (gr)		181.46	189.81	185.64	422.96	432.55	427.76	613.32	629.15	621.24

Table B. 5 Free shrinkage records at front side (S-F) and rear side (S-R) of each CSA specimen

Time (days)	Shrinkage records (με)						
	S_1-F	S_1-R	S_2-F	S_2-R	S_3-F	S_3-R	S-avg.
1	48.9	16.3	-16.3	-32.6	-32.6	8.1	-1.4
2	-97.8	-16.3	-65.2	-65.2	-32.6	-73.3	-58.4
6	-32.6	-48.9	-114.1	-130.4	-114.1	-105.9	-91.0
7	-32.6	-65.2	-65.2	-146.7	-97.8	-154.9	-93.7
8	-32.6	-146.7	-97.8	-163.0	-97.8	-154.9	-115.5
21	-97.8	-114.1	-163.0	-211.9	-179.3	-154.9	-153.5
28	-114.1	-130.4	-179.3	-228.2	-195.6	-187.5	-172.5
60	-146.7	-146.7	-195.6	-244.5	-228.2	-220.1	-197.0
90	-146.7	-146.7	-211.9	-260.8	-211.9	-236.3	-202.4
120	-163.0	-146.7	-228.2	-277.1	-195.6	-252.6	-210.5

Table B. 6 Shrinkage records at front side (S-F) and rear side (S-R) of each FCSA specimen

Time (days)	Shrinkage records (με)						
	S_1-F	S_1-R	S_2-F	S_2-R	S_3-F	S_3-R	S-avg.
1	0.0	-97.8	-130.4	-81.5	-130.4	-130.4	-95.1
2	-32.6	-146.7	-179.3	-97.8	-163.0	-163.0	-130.4
3	0.0	-146.7	-163.0	-130.4	-195.6	-163.0	-133.1
8	-65.2	-211.9	-244.5	-179.3	-244.5	-228.2	-195.6
14	-97.8	-244.5	-260.8	-244.5	-326.0	-277.1	-241.8
21	-130.4	-293.4	-293.4	-277.1	-326.0	-309.7	-271.7
28	-146.7	-293.4	-309.7	-277.1	-326.0	-326.0	-279.8
60	-228.2	-342.3	-358.6	-293.4	-374.9	-358.6	-326.0
90	-244.5	-342.3	-342.3	-342.3	-423.8	-374.9	-345.0
120	-293.4	-358.6	-374.9	-358.6	-407.5	-407.5	-366.8

Table B. 7 Shrinkage records at front side (S-F) and rear side (S-R) of each RSC specimen

Total shrinkage records (με)	Time (days)	S_1-F	S_1-R	S_2-F	S_2-R	S_3-F	S_3-R	S-avg.
	1	-1043.2	-847.6	-766.1	-733.5	-831.3	-635.7	-809.6
	2	-1271.4	-1222.5	-1157.3	-1108.4	-1173.6	-929.1	-1143.7
	3	-1809.3	-1727.8	-1711.5	-1613.7	-1662.6	-1418.1	-1657.2
	8	-1939.7	-1890.8	-1874.5	-1760.4	-1858.2	-1581.1	-1817.5
	14	-2102.7	-2021.2	-2086.4	-1939.7	-2021.2	-1776.7	-1991.3
	21	-2379.8	-2314.6	-2314.6	-2167.9	-2249.4	-1988.6	-2235.8
	28	-2510.2	-2428.7	-2477.6	-2314.6	-2363.5	-2102.7	-2366.2
	60	-2738.4	-2640.6	-2705.8	-2526.5	-2559.1	-2314.6	-2580.8
	90	-2787.3	-2689.5	-2754.7	-2575.4	-2591.7	-2347.2	-2624.3
	120	-2852.5	-2754.7	-2819.9	-2640.6	-2640.6	-2428.7	-2689.5
Autogenous shrinkage records (με)	Time (days)	S_1-F	S_1-R	S_2-F	S_2-R	S_3-F	S_3-R	S-avg.
	1	-391.2	-309.7	-456.4	-309.7	-489.0	-423.8	-396.6
	2	-472.7	-554.2	-521.6	-521.6	-554.2	-554.2	-529.8
	3	-684.6	-635.7	-700.9	-586.8	-717.2	-749.8	-679.2
	8	-782.4	-831.3	-782.4	-749.8	-896.5	-880.2	-820.4
	14	-896.5	-945.4	-961.7	-880.2	-1010.6	-961.7	-942.7
	21	-1026.9	-1010.6	-1124.7	-1043.2	-1108.4	-1141.0	-1075.8
	28	-1173.6	-1141.0	-1271.4	-1173.6	-1238.8	-1271.4	-1211.6
	60	-1597.4	-1613.7	-1532.2	-1597.4	-1744.1	-1776.7	-1643.6

Table B. 8 Shrinkage records at front side (S-F) and rear side (S-R) of each FRSC specimen

Total shrinkage records (με)	Time (days)	S_1-F	S_1-R	S_2-F	S_2-R	S_3-F	S_3-R	S-avg.
	1	-945.4	-912.8	-945.4	-912.8	-961.7	-798.7	-912.8
	2	-1173.6	-1141.0	-1206.2	-1157.3	-1238.8	-1075.8	-1165.5
	7	-1678.9	-1695.2	-1760.4	-1678.9	-1841.9	-1564.8	-1703.4
	14	-2004.9	-2053.8	-2086.4	-1988.6	-2216.8	-1841.9	-2032.1
	21	-2135.3	-2200.5	-2233.1	-2119.0	-2396.1	-2004.9	-2181.5
	28	-2249.4	-2314.6	-2330.9	-2216.8	-2510.2	-2086.4	-2284.7
	60	-2379.8	-2461.3	-2461.3	-2379.8	-2722.1	-2200.5	-2434.1
	90	-2396.1	-2477.6	-2510.2	-2396.1	-2722.1	-2216.8	-2453.2
	120	-2493.9	-2575.4	-2575.4	-2445.0	-2803.6	-2298.3	-2531.9
Autogenous shrinkage records (με)	Time (days)	S_1-F	S_1-R	S_2-F	S_2-R	S_3-F	S_3-R	S-avg.
	1	-554.2	-603.1	-505.3	-652.0	-603.1	-521.6	-573.2
	3	-619.4	-717.2	-586.8	-749.8	-733.5	-570.5	-662.9
	7	-847.6	-896.5	-766.1	-929.1	-896.5	-863.9	-866.6
	14	-1059.5	-1141.0	-961.7	-1189.9	-1108.4	-1092.1	-1092.1
	21	-1157.3	-1271.4	-1059.5	-1336.6	-1238.8	-1222.5	-1214.4
	28	-1255.1	-1369.2	-1157.3	-1450.7	-1369.2	-1336.6	-1323.0

	60	-1662.6	-1776.7	-1548.5	-1874.5	-1793.0	-1678.9	-1722.4

Figure B. 1 The process of slicing moisture transport specimens

Figure B. 2 Free shrinkage specimens

Appendix: C

This appendix presents more detailed photos and raw data for the experimental work described in Chapter 4 of the thesis.

Figure C. 1 Substrate concrete casting

Figure C. 2 Overlaid prisms that kept in the control room for restrained shrinkage measurements

Figure C. 3 Shear samples before testing

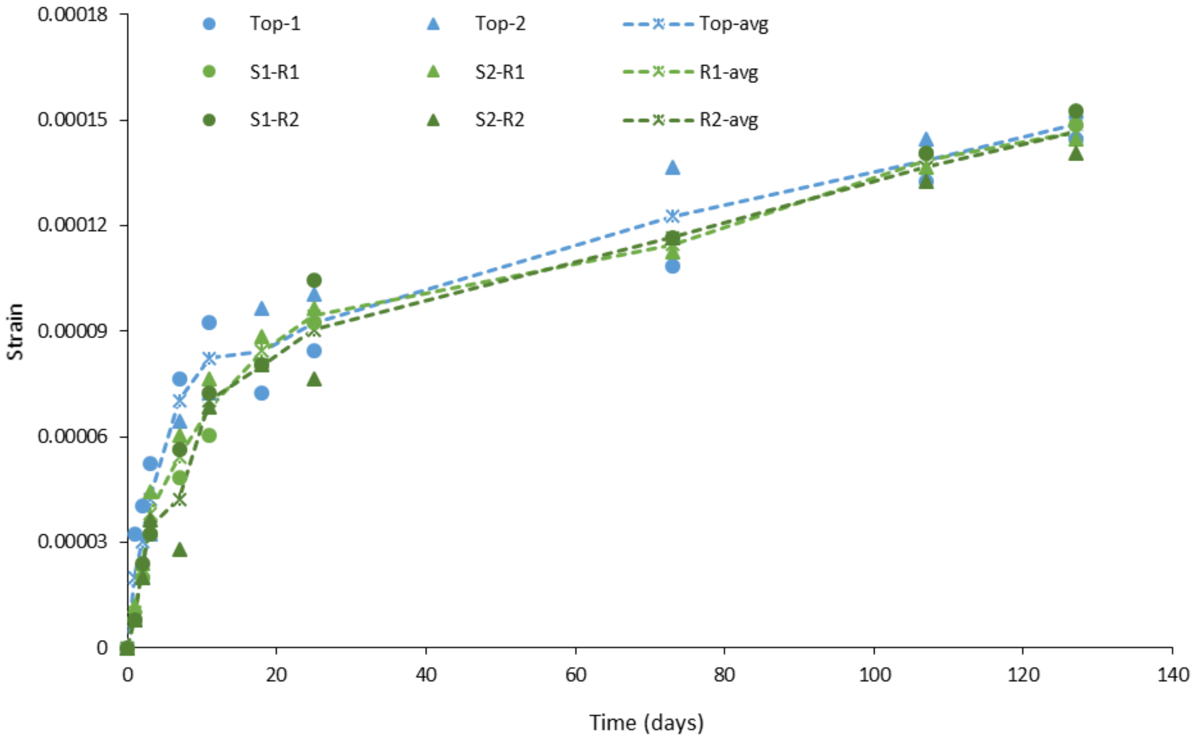

Figure C. 4 Shrinkage development with time for composite prisms with CSA$_1$

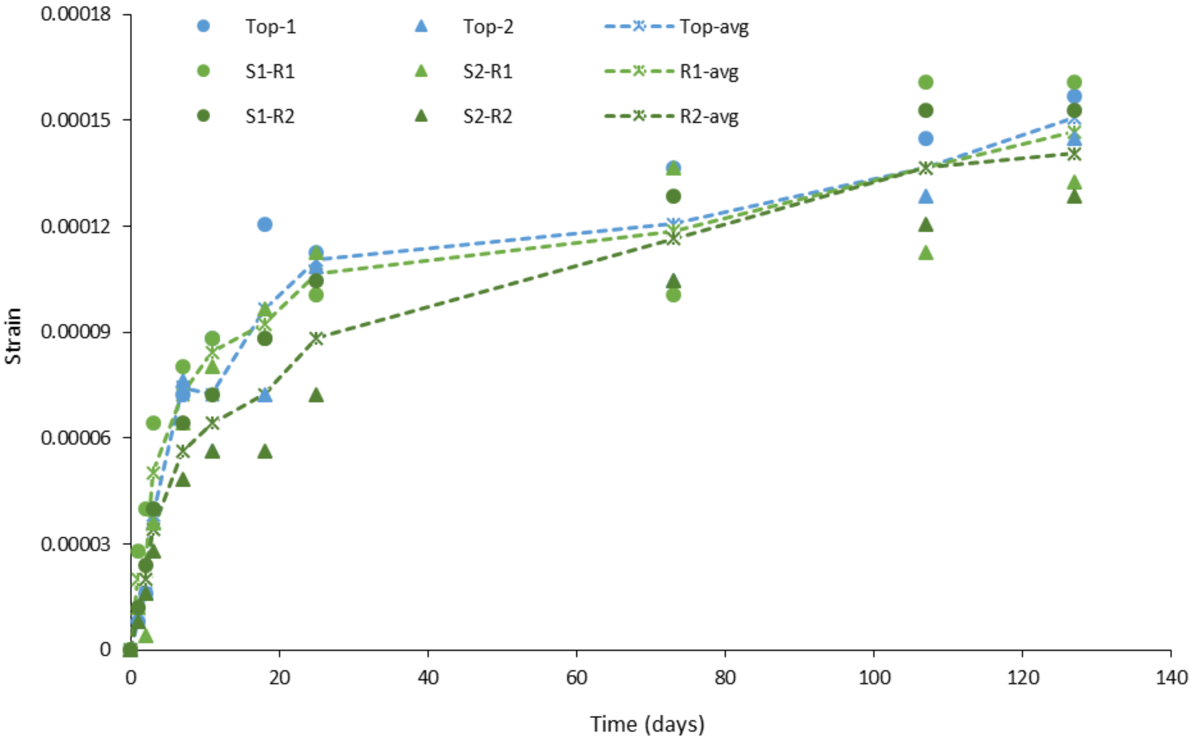

Figure C. 5 Shrinkage development with time for composite prisms with CSA$_2$

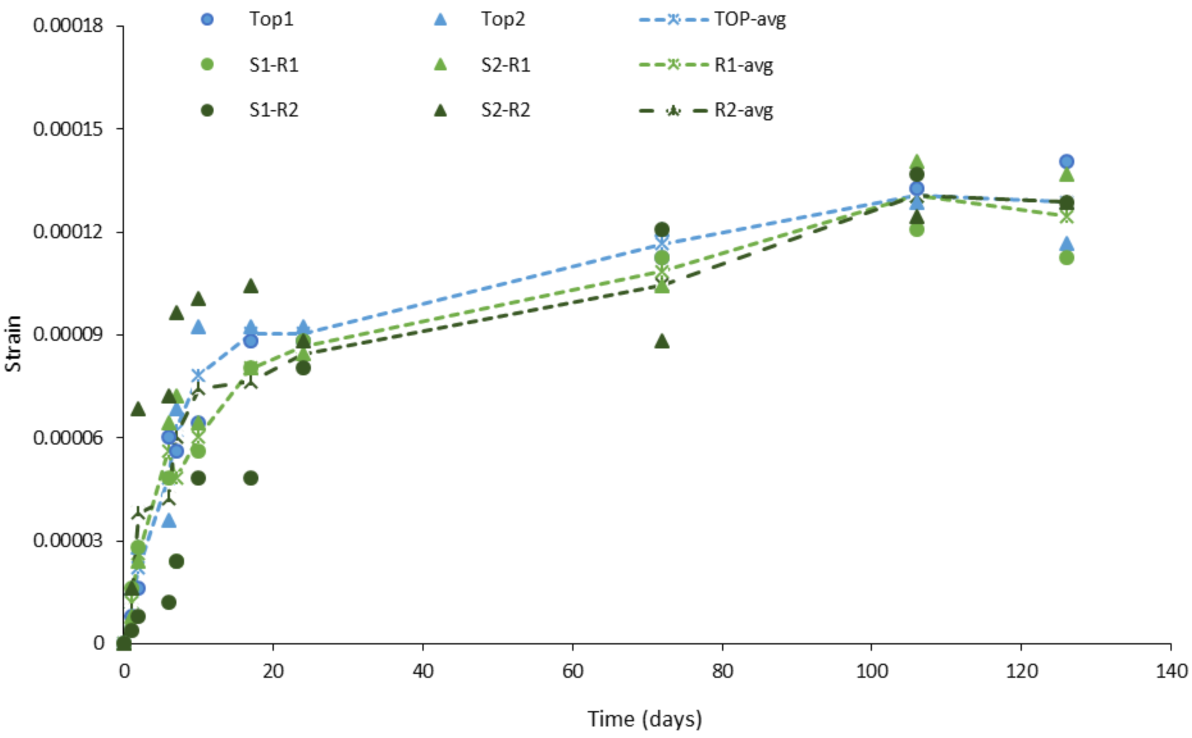

Figure C. 6 Shrinkage development with time for composite prisms with CSA_3

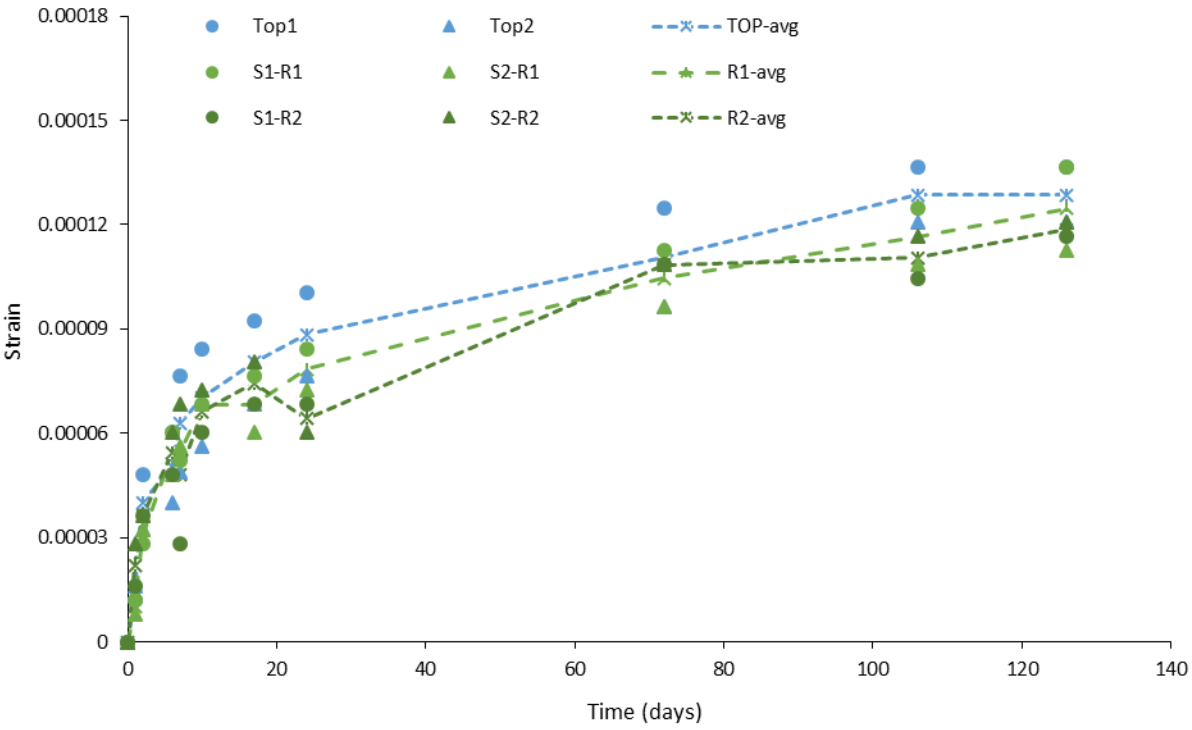

Figure C. 7 Shrinkage development with time for composite prisms with CSA_4

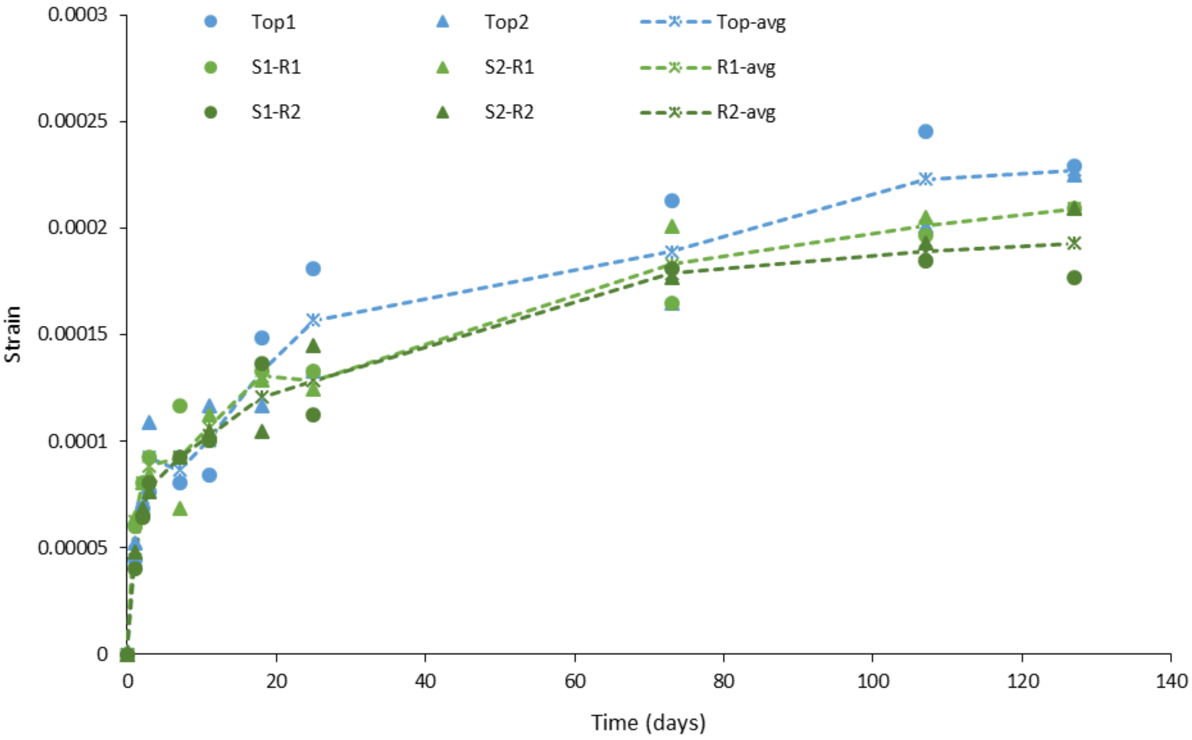

Figure C. 8 Shrinkage development with time for composite prisms with FCSA$_1$

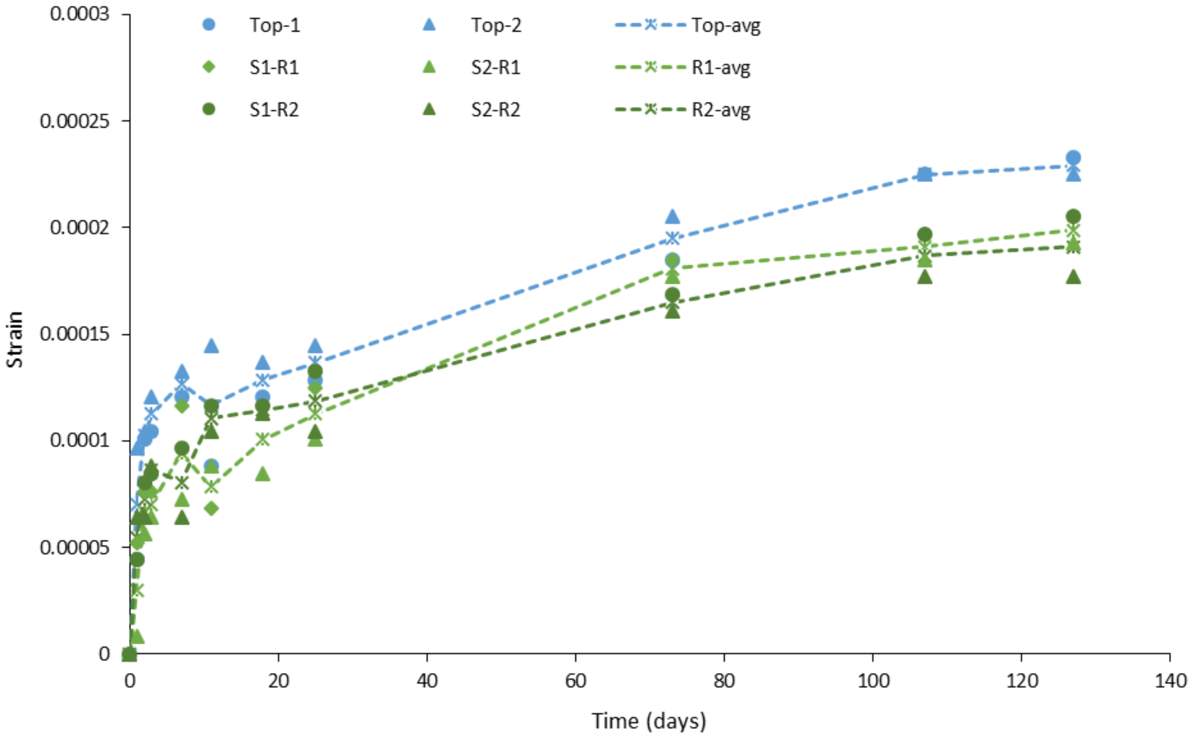

Figure C. 9 Shrinkage development with time for composite prisms with FCSA$_2$

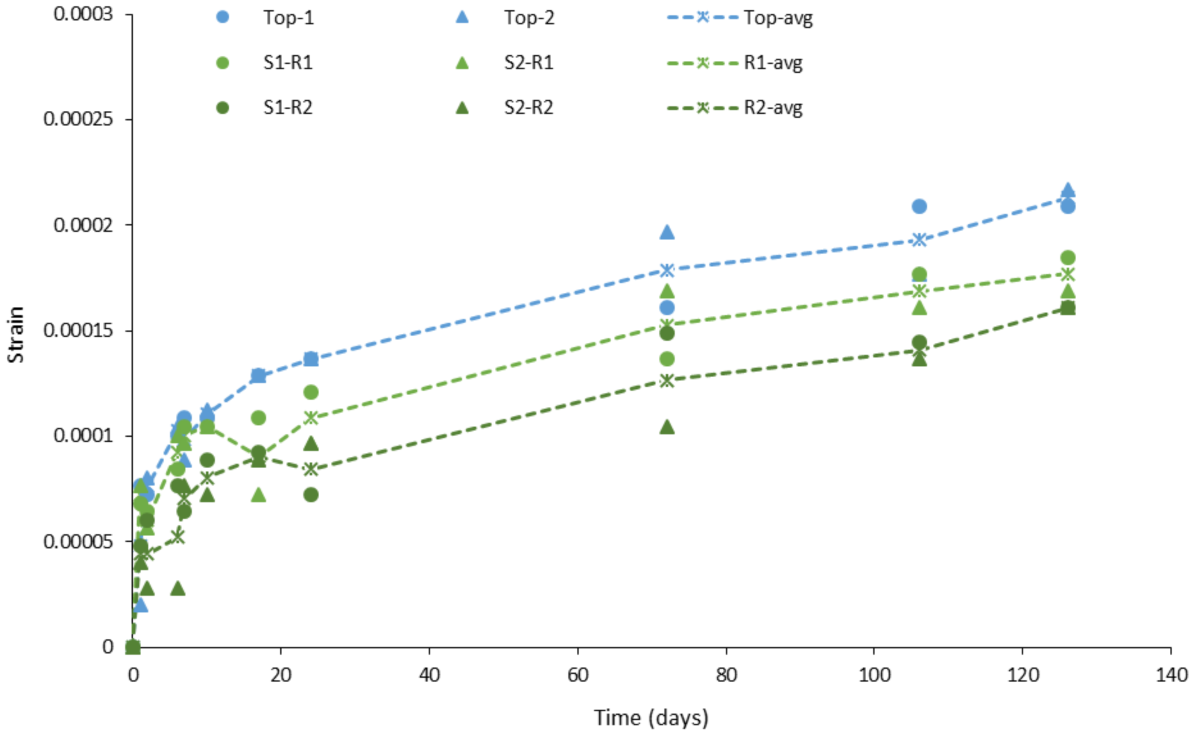

Figure C. 10 Shrinkage development with time for composite prisms with $FCSA_3$

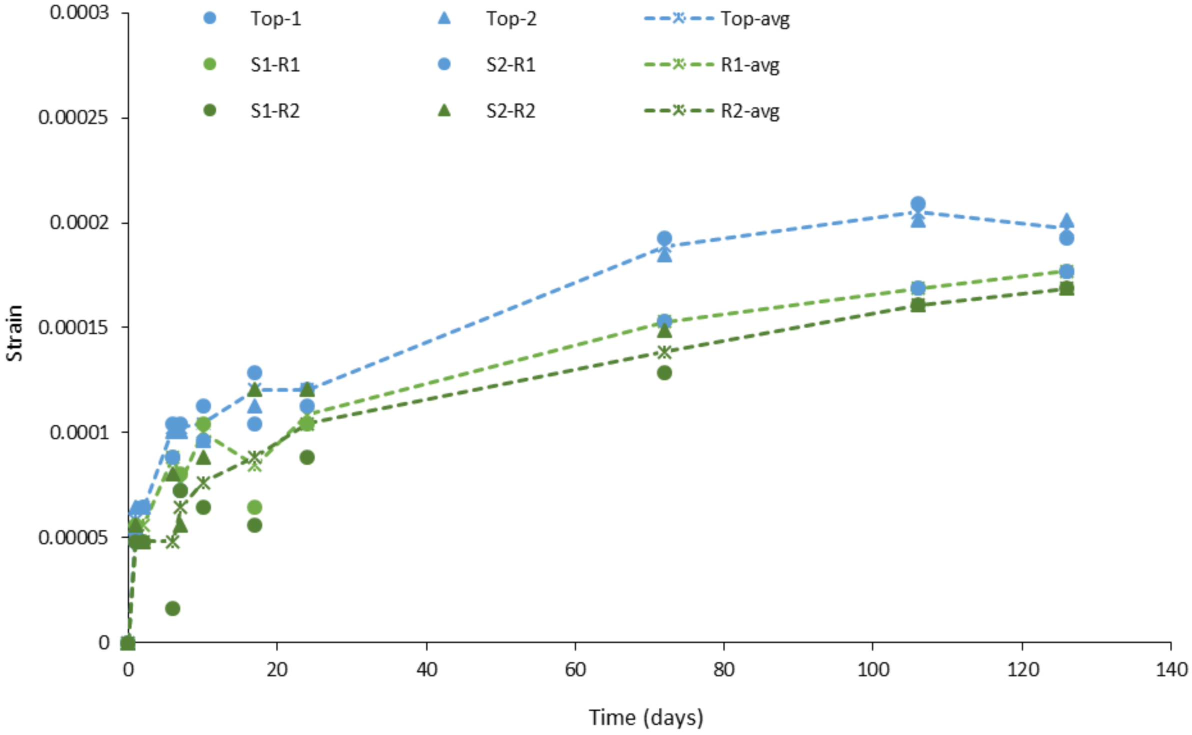

Figure C. 11 Shrinkage development with time for composite prisms with $FCSA_4$

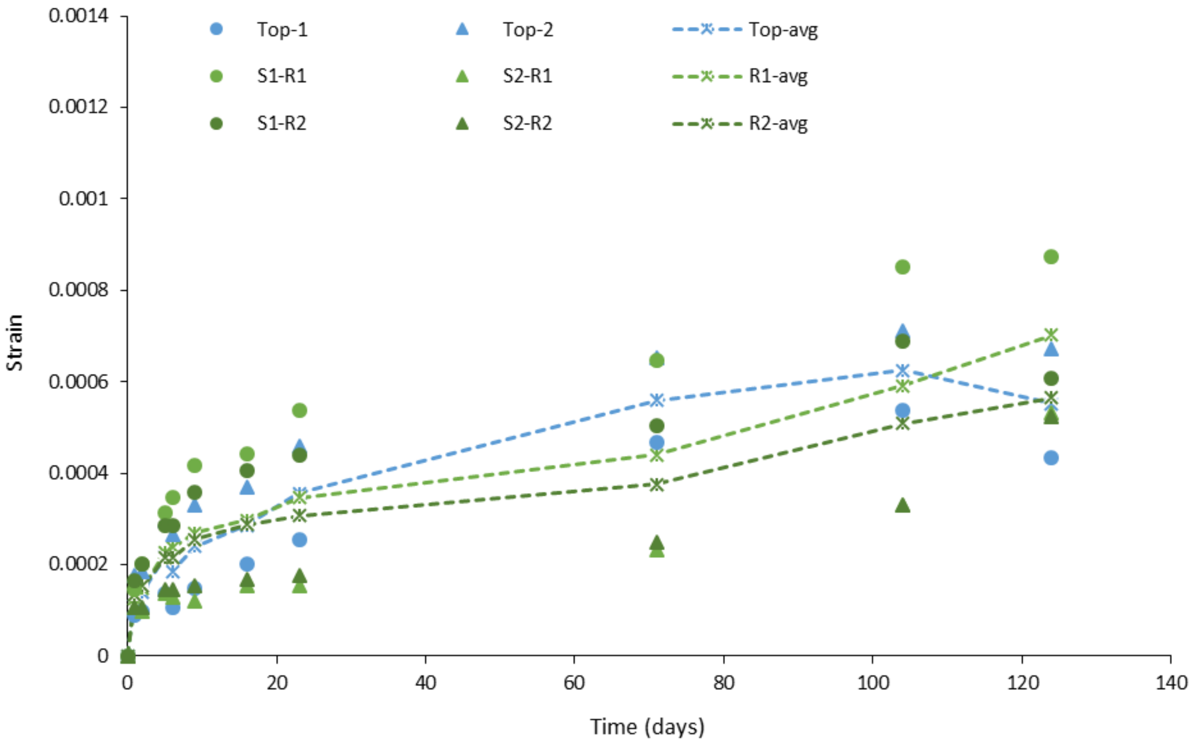

Figure C. 12 Shrinkage development with time for composite prisms with RSC_1

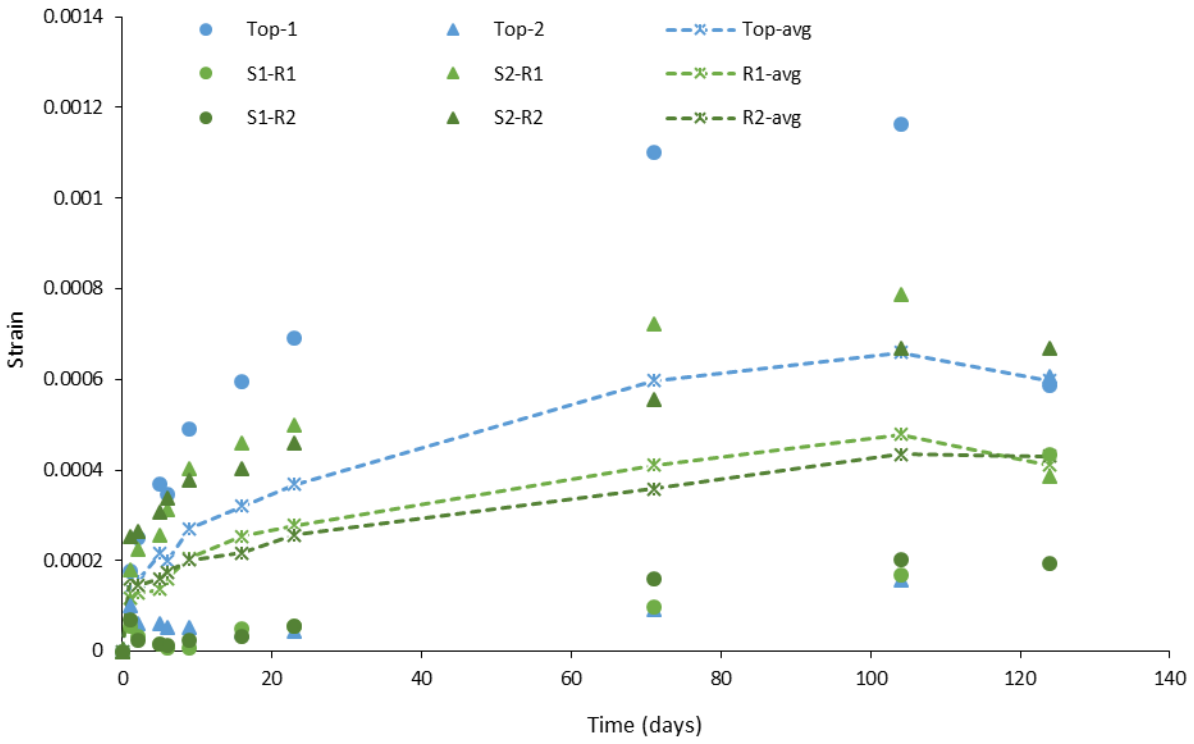

Figure C. 13 Shrinkage development with time for composite prisms with RSC_2

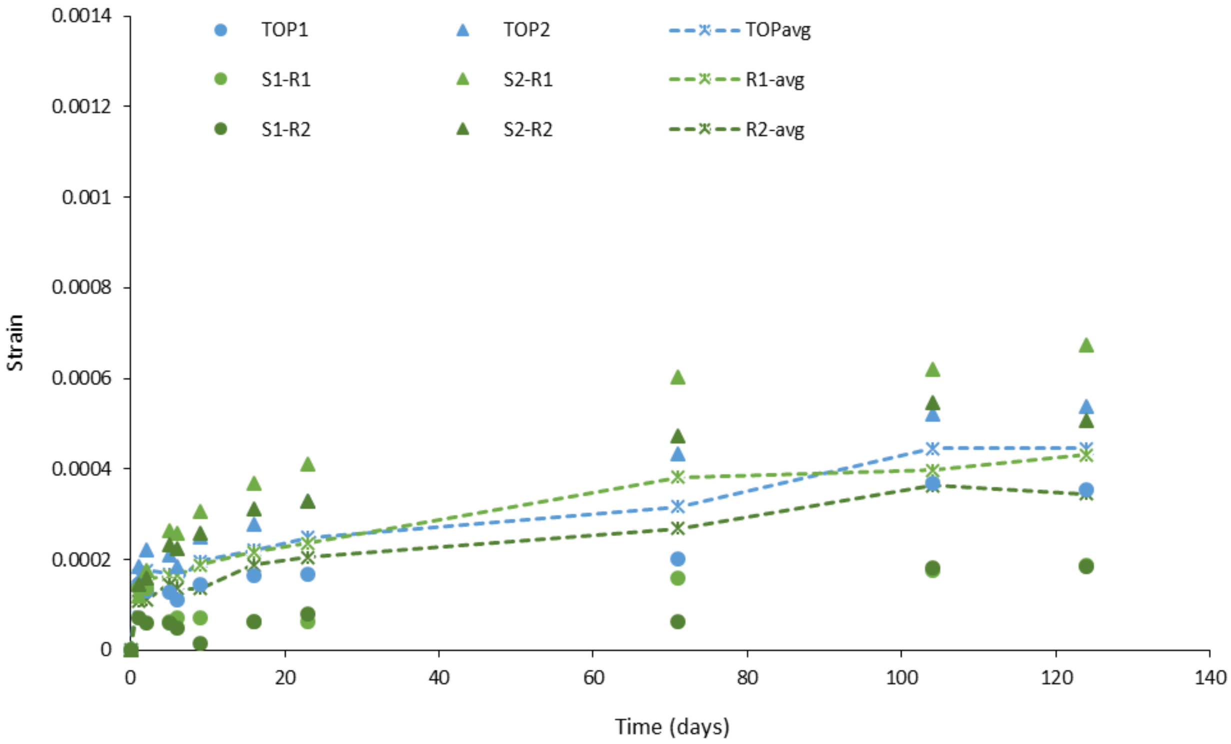

Figure C. 14 Shrinkage development with time for composite prisms with RSC$_3$

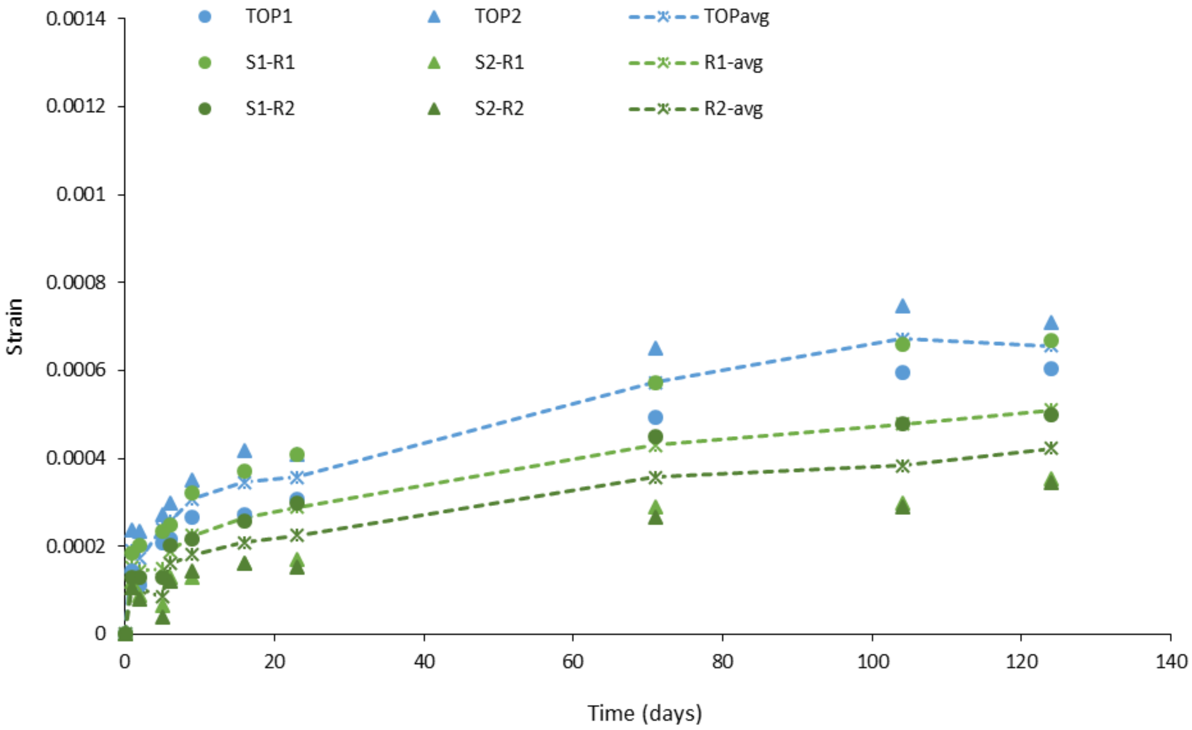

Figure C. 15 Shrinkage development with time for composite prisms with RSC$_4$

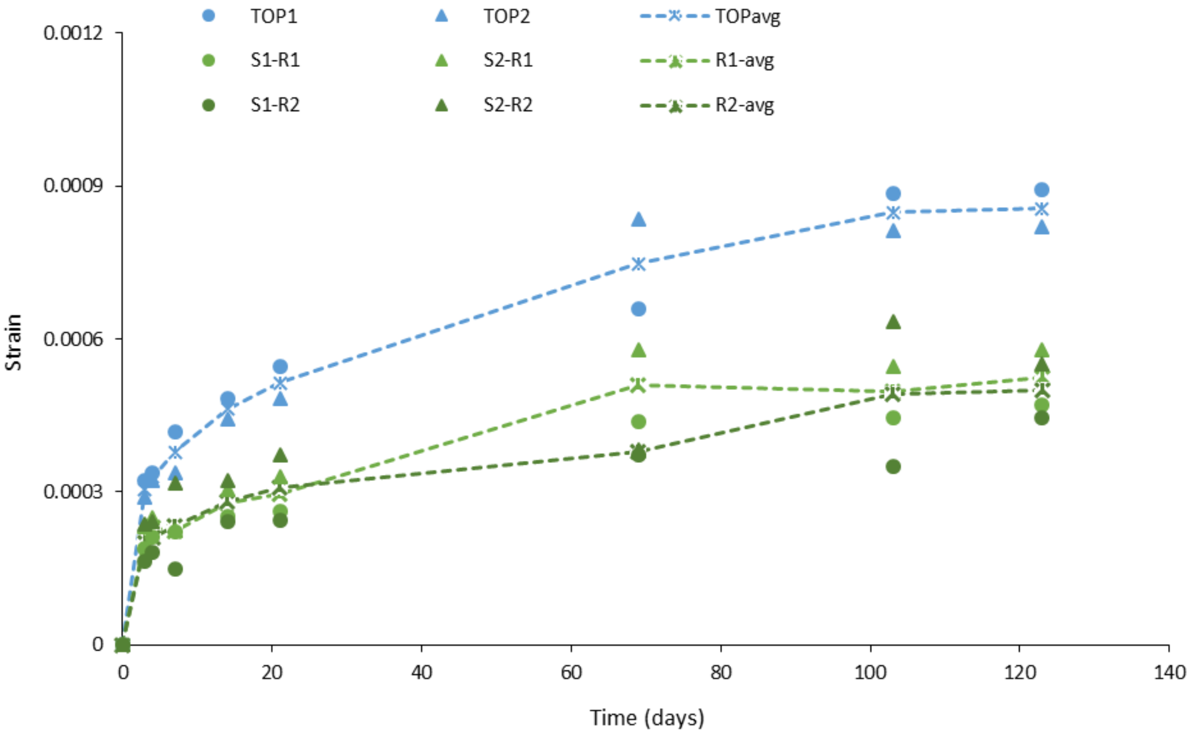

Figure C. 16 Shrinkage development with time for composite prisms with FRSC$_1$

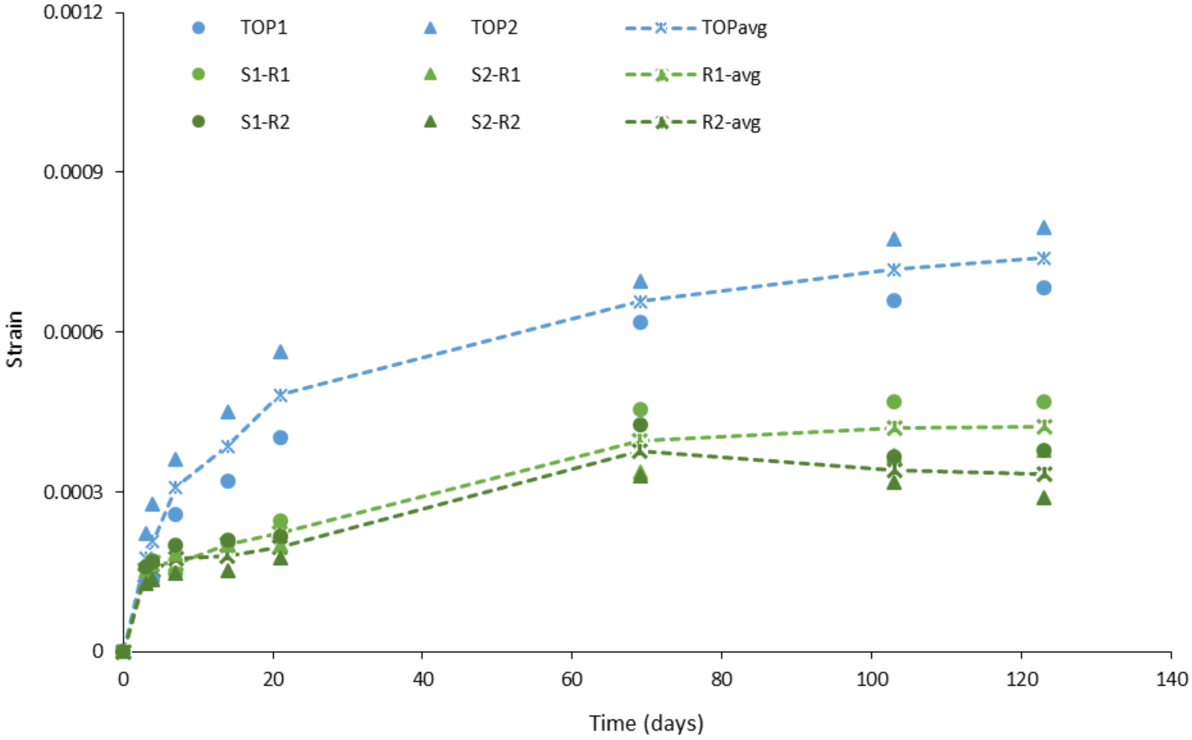

Figure C. 17 Shrinkage development with time for composite prisms with FRSC$_2$

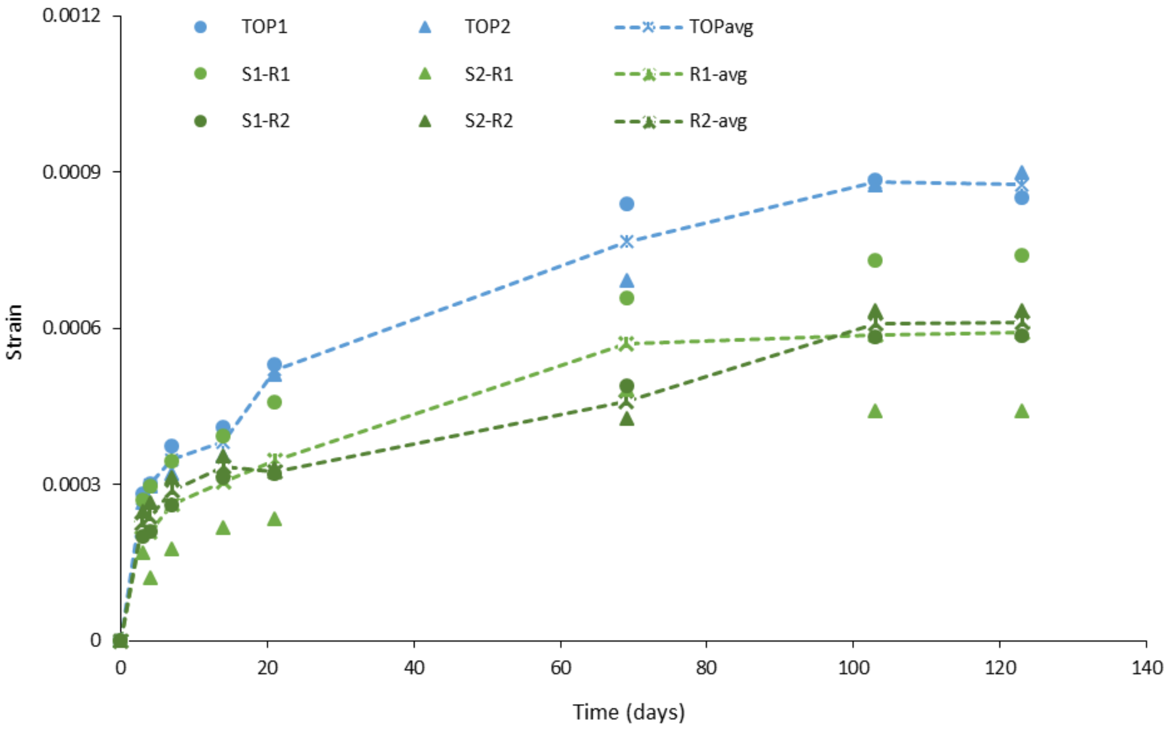

Figure C. 18 Shrinkage development with time for composite prisms with FRSC$_3$

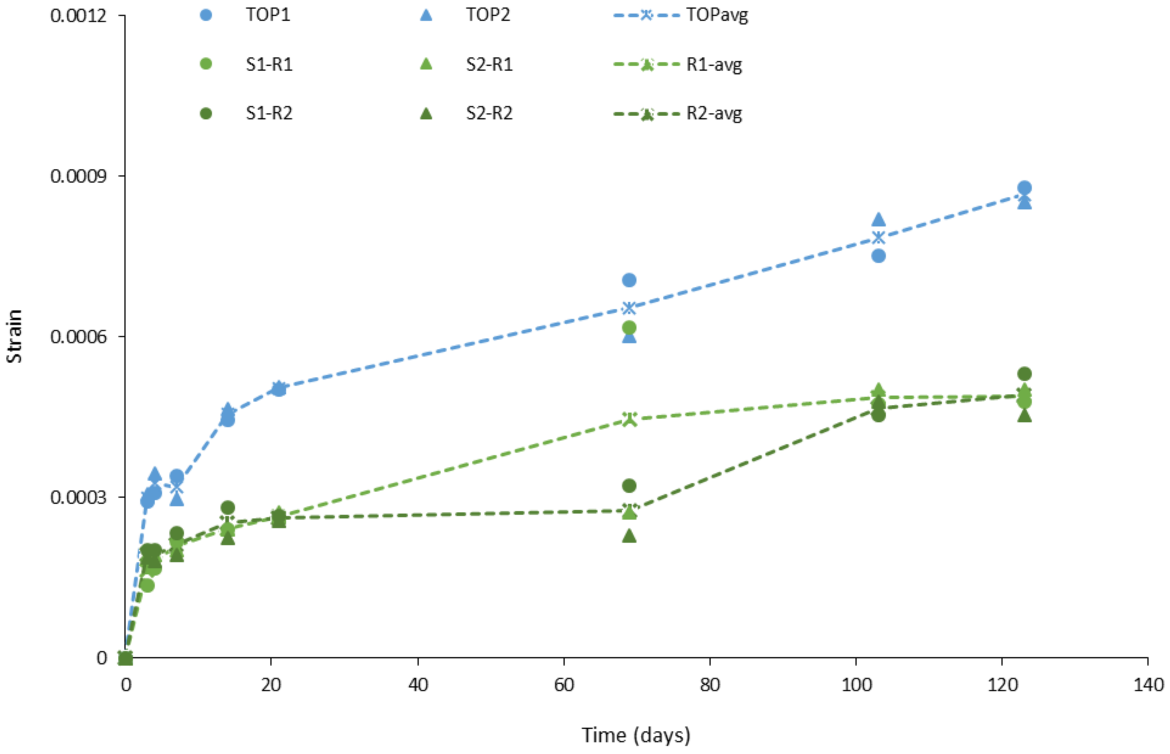

Figure C. 19 Shrinkage development with time for composite prisms with FRSC$_4$

Table C. 1 Tests of normality In SPSS package for crack spacings and normalized crack spacings

Tests of Normality

	Kolmogorov-Smirnov[a]			Shapiro-Wilk		
	Statistic	df	Sig.	Statistic	df	Sig.
Crack spacings	0.093	82	0.079	0.980	82	0.234
Normalised crack spacing	0.093	82	0.079	0.980	82	0.234

[a] Lilliefors Significance Correction